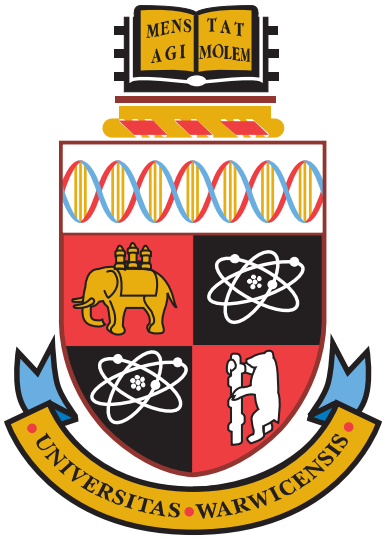

Trivalent cation substitution of β-tricalcium phosphate

by

Martin Mee

Thesis

Submitted to the University of Warwick

for the degree of

Doctor of Philosophy

Department of Physics

June 2011

THE UNIVERSITY OF WARWICK

Contents

List of Tables

List of Figures

Acknowledgments

There have been many people who have influenced both myself and my work during the course of my PhD and I'd like to thank all of them.

Most of all I'd like to thank my supervisor, Diane Holland, without whom this thesis almost certainly would not have been possible. She has been an enormous help in every aspect of my work and her patience with me has been undeservedly unending.

Secondly I have to thank the people at AWE for their funding and support, especially Shirley, Lee, Phil, Brian and Ian, all of whom have been a great help. In my work at Warwick I'd like to thank Andy Howes, Ray Dupree, Kevin Pike and Tom Kemp for their invaluable assistance with everything NMR, to David Walker for his help with x-ray diffraction and to Dave Hammond and Keith Briggs for making sure that everything in our little world on the ground floor runs smoothly. I am also grateful to Zhehong Gan for the NMR experiments he ran and to Steve Feller for being a great host for me over in Coe College. Thanks also to Alex Hannon and Emma Barney for their knowledge and experience when it comes to neutron diffraction. I'd also like to thank the many undergraduate students I have supervised and who have contributed to this work.

The postgrads of both the Glass and Crystallography groups, past and present, must also be acknowledged, each of whom has aided me in some way. Enormous thanks go to (mostly in chronological order): my predecessor Ben, Emma, Dean, Dan, Rabaah, Kaustuv, Meng, my old drinking partner Iain, Aoife, my protégé Andy, Ollie, Steve, Sam and most of all Robin, who helped me with many problems throughout my PhD and especially for his help with LaTeX.

Thanks must also be given to all the members of Warwick Student Cinema, old and new, who have continued to be a large part of my life throughout my 8 years at Warwick. Of those, special thanks have to go to my best friend, supreme chef and projectionist extraordinaire Rachel, who has put up with me as a housemate for the past 4 years and always had faith in my abilities.

Finally I'd like to thank my parents and the rest of my family for all the support they've given me and their continued interest in my work on 'glass'.

Declaration and published work

I declare that the work presented in this thesis is my own except where stated otherwise, and was carried out entirely at the University of Warwick, during the period of July 2007 to June 2011, under the supervision of Dr. D. Holland. The research reported here has not been submitted, either wholly or in part, in this or any other academic institution for admission to a higher degree.

M. Mee

June 2011

Abstract

The mineral β-tricalcium phosphate (β-TCP), $Ca_3(PO_4)_2$, is currently of interest in the immobilisation of nuclear wastes, along with various biomedical applications. Several substituted forms of β-tricalcium phosphate have been produced with the general formula $Ca_9M_x^{3+}(PO_4)_{6+x}$, where M^{3+} is a trivalent metal ion, with Ga, Al and La being the main focus of study here, and x generally falling between 0 and 1. The aim of this study has been to investigate the substitution mechanisms of ions into β-tricalcium phosphate along with the effects which substitution has on its structure. This has mainly been carried out by nuclear magnetic resonance on many of the available nuclei, along with x-ray and neutron diffraction of the materials produced.

It has been shown that substituted β-tricalcium phosphate can be readily produced, although with additional phases present in some samples, generally upon high levels of substitution, and especially in the Al case. Rietveld refinements of x-ray and neutron diffraction patterns show the β-TCP structure remains intact throughout the samples produced, with Ga thought to substitute onto the Ca(5) site, La onto the Ca(3) site and Al onto both the Ca(4) and Ca(5) sites. However, values determined for the Ca site occupancies have in some cases deviated from those expected and often have large errors associated with them. Part of this is due to problems with the peak shape used with the x-ray diffraction data, but it is also thought that disorder may be present in the substituted samples, causing unexpected values in the refinements. Total correlation functions have also been produced from the neutron diffraction data and again show the β-TCP structure to remain relatively unchanged in most cases with 6-coordinated Al and Ga present in samples containing those ions. The addition of Al does, however, change the structure considerably, possibly through distortions of the sites involved due to the smaller size of the Al ions.

^{31}P NMR has been performed on all samples and appears extremely sensitive to changes in the Ca site occupancies. Fitting has been performed on spectra from the Ga system, with fits produced consistent with substitution onto the Ca(5) site. The method of substitution for the Al and La systems has proven to be too complex for fitting of the ^{31}P spectra to be practical in these cases. Natural abundance ^{43}Ca NMR has been performed on some of the samples and, although having poor signal to noise ratios, the spectra produced can be fitted according to the method of site substitution predicted. ^{27}Al NMR on the Al containing samples has produced interesting spectra, with an additional feature being present in addition to the expected 6-coordinated resonance. This feature lies within the range associated with AlO_6 or $Al(OP)_5$ environments and is thought to be due to distortion of one of the Ca sites that the Al is substituting into, probably the smaller Ca(4) site.

Glossary and abbreviations

β-TCP	β-tricalcium phosphate
ADP(s)	Anisotropic displacement parameter(s)
FID	Free induction decay
GEM	General materials diffractometer
GOF	Goodness of fit
HLW	High level (nuclear) waste
ILW	Intermediate level (nuclear) waste
LLW	Low level (nuclear) waste
MAS NMR	Magic-angle-spinning nuclear magnetic resonance
ND	Neutron diffraction
NMR	Nuclear magnetic resonance
TOF	Time of flight
XRD	X-ray diffraction

Chapter 1

Introduction

1.1 Overview

Since the start of the nuclear age, a growing problem has developed in the form of long term storage of radioactive waste. These wastes can come from a diverse number of sources such as power, medical, military and may be in many different forms, the combination of which poses a major problem in safe, long term storage. For short term storage these wastes are processed in a variety of ways which almost all lead to a liquid waste for which many precautions need to be taken [1]. Immobilisation of this liquid waste is the goal for long term storage with the main candidates for the immobilisation being glasses, ceramics or cements with the objective of providing a solid, durable and stable material. Once immobilised, the waste can then be stored for the rest of its active life in underground repositories without worry of escape into the biosphere.

Immobilisation is usually accomplished by either dissolution of the waste into a host lattice or encapsulation within an inert matrix. Numerous materials have been found to deal with the diverse variety of wastes, including borosilicate glasses for some high level wastes. There are however many other complex types of waste for which there is no current storage solution. Existing methods, when employed with certain waste streams, result in problems such as less durable wasteforms which can leach hazardous materials into the water table. This means new methods of storage need to be found.

There is a need for radically different storage solutions to accommodate these materials depending on the constituents of the waste in question. Reprocessing of plutonium can create a chlorine-rich waste for which extra care needs to be taken in its treatment due to the possibility of chlorine leaching out of the final wasteform [2]. Some success has been achieved by storage of these chlorine-rich wastes in calcium phosphate based ceramics, particularly chlorapatite ($Ca_5Cl(PO_4)_3$) and spodiosite ($Ca_2Cl(PO_4)$) [3]. These are both minerals found naturally in the earth and are known to be stable

over long geological time periods. Studies have been carried out by AWE using chlorapatite to store a simulated waste stream by calcining the waste with $CaHPO_4$. This resulted in phases identified by x-ray powder diffraction as chloride substituted fluorapatite ($Ca_5(PO_4)_3F_{0.9}Cl_{0.1}$) and β-tricalcium phosphate ($Ca_3(PO_4)_2$) [3].

1.2 Aim of the work

The aim of this study is to investigate the substitution mechanisms of ions into β-tricalcium phosphate (β-TCP) and the effects on its structure. In order to achieve this, samples of β-TCP have been produced containing a range of different atoms substituting onto the Ca sites. By looking at β-TCP doped with just one other element, the substitution mechanisms can more easily be determined and extended to other cases first by substitution of two complementary ions through to the behaviour of complex waste streams immobilised in β-TCP.

Nuclear magnetic resonance will be used to identify changes in the local structure of the material. ^{43}Ca NMR can be used to identify changes in the Ca environments directly. It is however a difficult nucleus to look at, partly due to the low natural abundance of ^{43}Ca. Therefore ^{31}P NMR will be used to measure changes in the Ca sites indirectly through the changes in P environments. In other systems, with substitution of NMR active nuclei, such as Al, additional experiments can be performed on these nuclei to complement the other techniques.

X-ray diffraction will also be used, initially to check phase purity of samples produced and also in order to perform Rietveld refinement of the data to determine site occupancies. This will be backed up with neutron diffraction studies which will both aid the refinement and also provide total scattering data which can be used to give a better insight into the atomic environments in the material.

1.3 Structure of thesis

This thesis contains nine chapters which are outlined here to give a summary of the presented work.

Chapter 2 gives an overview of the field of nuclear waste immobilisation, encapsulation and storage and addresses the problems and possible solutions in the immobilisation of waste with a high chlorine content, particularly with respect to that produced from the reprocessing of plutonium at AWE.

Chapter 3 describes the general structure of β-tricalcium phosphate along with previous work in the area and possible substitution mechanisms into the structure including how these may be represented through experiments.

Chapter 4 details the theory and practice of the experimental techniques used. These include x-ray and neutron diffraction, Rietveld refinement and nuclear magnetic resonance.

Chapters 5 to 7 present the preparation of Ga, Al and La substituted β-tricalcium phosphate along with results and discussion of data obtained.

Chapter 8 deals with substitution of other cations into β-tricalcium phosphate and their relationship with the general understanding of the system.

Chapter 9 provides discussion and general conclusions for all the systems presented in the study along with future work that may be possible to aid in the understanding of β-tricalcium phosphate.

Chapter 2

Nuclear wastes and immobilisation

2.1 Introduction

Nuclear waste is produced from a wide range of sources and can be present in many different forms, the combination of which can produce wastes with potentially very different compositions and, as such, many precautions need to be taken in the identification and disposal of these wastes. The combination of different radionuclides present, along with the actual composition of the waste, means that disposal methods generally have to be tailored to a specific waste. Half-lives of the main long-lived radionuclides, which are often present in wastes, are shown in table 2-1. Although wide ranging, the wastes can however be broadly categorised into three different groups; these being low, intermediate and high level wastes.

2.1.1 High level wastes

High level wastes (HLW), as the name suggests, are the most dangerous types of waste, generally consisting of isotopes separated from the processing of spent fuel rods. Due

Table 2-1 Half lives of the main long-lived radionuclides [4].

Radionuclide	Half-life (y)	Radionuclide	Half-life (y)
^{79}Se	7×10^4	^{237}Np	2.14×10^6
^{90}Sr	28	^{238}Pu	87.7
^{93}Zr	1.5×10^6	^{239}Pu	2.41×10^4
^{99}Tc	2.1×10^5	^{240}Pu	6569
^{107}Pd	6.5×10^6	^{241}Pu	14.4
^{126}Sn	10^5	^{242}Pu	3.7×10^5
^{129}I	1.57×10^7	^{241}Am	432.2
^{135}Cs	2×10^6	^{243}Am	7380
^{137}Cs	30	^{244}Cm	18.1
^{151}Sm	93	^{245}Cm	8500

to their high level of activity these wastes can build up large amounts of heat for many years, if not decades, and care needs to be taken to dissipate this heat until the stability of the waste reaches an acceptable level for long term disposal. Initially these are usually processed into liquid wastes which are then stored in large inert tanks, with active cooling, until they can be processed into a suitable form where they can be left to cool in the air until safe for long term immobilisation and disposal.

2.1.2 Intermediate level wastes

Intermediate level wastes (ILW) come from a variety of sources and can be composed of many different isotopes depending on the nature and history of the waste and are all to some degree dangerously radioactive. They are however relatively stable in contrast to HLW, having a fairly predictable behaviour with respect to the decay chains of the nuclei present. These wastes do not need the cooling required with HLW and can, when methods are more fully developed, be immediately disposed of. They can often contain materials with very long half-lives (up to millennia or more) and therefore need to be disposed of adequately over these long time periods. These wastes generally consist of materials which have been in close proximity to nuclear reactors, such as shielding removed from power stations or as some kind of by-product from the reprocessing or treatment of nuclear fuel or HLW.

2.1.3 Low level wastes

Low level wastes (LLW) generally consist of materials which may have come into contact with active materials, such as clothing, paper, tools, and as such usually have a low level of radioactivity and relatively short half-lives. They do however contain enough radioactivity to make disposal with ordinary landfill wastes potentially hazardous. The classification of LLW is such that the level of activity for the waste should not exceed 4 GBq/t of alpha activity or 12 GBq/t for beta and gamma activity [5]. The danger of LLW is not in its initial radioactivity but in its potential to transit into the environment and build up into large amounts. Careful disposal and monitoring in environmentally isolated areas can ensure that LLW does not pose a problem, with another method of disposal for some types of LLW being deep ocean dumping where the dilution of the

waste brings the activity to acceptable levels. LLW in the UK is disposed of at the Drigg repository near Sellafield where it is compacted into steel containers before being placed in engineered concrete vaults.

2.2 Storage methods of nuclear wastes

There are four main methods used in the storage of high and intermediate level wastes, these being immobilisation as a glass, ceramic or glass-ceramic wasteform or alternatively encapsulation [1].

Vitrification of wastes is a well established process used in a number of countries across the world. In this method the waste is usually dissolved into a glass host which must therefore be compatible with the waste and able to withstand the conditions arising from the materials present, be they radioactive or chemically volatile. One of the main problems of vitrification is thermal stability. Due to most glasses having a relatively low glass transition temperature (the temperature above which the solid can be thought of as being a supercooled liquid), care must be taken so that the wasteform does not undergo excessive heating such that its structure could be compromised. The majority of glasses used are borosilicate and phosphate based glasses, with the exact composition dependent on the composition of the waste and often modified to reduce the melting temperature in an effort to reduce costs associated with immobilisation.

Immobilisation as a ceramic is not currently a widely used technique due to the more complex production route and the generally higher temperatures needed. A benefit of ceramics however is their improved thermal stability and chemical durability over glasses. Production of these wasteforms would be done either by simple grinding and sintering of the constituent materials or via wet chemistry methods. Wet chemistry techniques mean that temperatures required for formation can be reduced but they are generally much more complex than simple powder methods and can involve the use of highly volatile or dangerous compounds. There are many different families of ceramics which have been studied, each favoured for a specific kind of waste but generally found naturally in the earth and known for their compositional variance and stability over geological time periods making them ideal for nuclear waste hosts.

Glass-ceramic wasteforms provide the improved durability of ceramics whilst re-

ducing the possibility of additional phases being present in the final wasteform and the additional handling precautions necessary. Glass-ceramics are produced by the controlled crystallisation of a glass, meaning they can be made much more easily than using normal ceramic preparation methods. A disadvantage of this is that it is effectively a two stage process, resulting in an increase in the processing facilities needed and the costs associated with them.

Encapsulation simply consists of encapsulating the waste within an inert matrix. This can be done using a range of materials including glasses, polymers, ceramics and cements. Encapsulation can be performed on the raw waste itself but is also used to encapsulate the already immobilised waste. This is usually to produce a monolithic wasteform from ceramic powders or glass beads and is an effective method of reducing the surface area of the waste and provides a more easily manageable wasteform along with an additional barrier of containment.

Once immobilised into a solid wasteform the most popular proposed method for long term storage is currently to seal the wasteform in steel cans which are then stored deep underground in geologically stable locations. Once stored underground, these cans are further encased, in a material such as concrete, to restrict transport of radioactive elements and, when full, the entire compound is backfilled with a suitable material for the surroundings, which may be concrete or clay, for the foreseeable future.

2.3 Immobilisation of chlorine containing wastes

Most of the current accepted storage methods have been designed for the immobilisation and disposal of waste originating from nuclear reactors. There are however other wastes where these methods may not be suitable. At the Atomic Weapons Establishment (AWE) pyrochemical reprocessing of plutonium produces very different kinds of waste containing both actinide and chloride ions [2]. The chloride in this waste is highly reactive with some of the current immobilisation materials, such as borosilicate glass, with both the actinide and chloride ions also suffering from low solubility in most materials, potentially causing breakdown of these materials and resulting in transport of the waste components into the environment.

This pyrochemical reprocessing produces four different ILW streams, one of which

Table 2-2 Compositions of non-radioactive simulated waste streams [3].

Component (mass %)	Waste Stream Type			
	I	II	III	IV
Oxides				
HfO_2	-	20.7	62.2	11.4
Ga_2O_3	-	28.0	9.4	10.5
Al_2O_3	-	9.8	1.7	2.2
Sm_2O_3	-	4.6	11.7	1.0
MgO	-	6.3	-	10.1
FeO	-	1.5	-	0.7
Ta_2O_5	-	1.3	-	0.7
NiO	-	1.3	-	0.7
ZnO	-	-	-	35.7
SiO_2	-	-	-	0.8
B_2O_3	-	-	-	0.8
Halides				
$CaCl_2$	80.0	-	-	-
$SmCl_3$	20.0	-	-	-
CaF_2	-	10.4	5.0	8.5
KCl	-	16.3	10.0	16.9

contains a high chloride concentration (Type I) [3]. The other three are currently intended to undergo further aqueous reprocessing in order to convert the bulk of the waste into low level wastes, leaving three actinide and chloride containing intermediate level waste streams (Types II-IV) for immobilisation [6]. Therefore materials need to be found that can accommodate the high actinide and chloride content present along with satisfying the necessary prerequisites for an immobilisation host. Work has been done based on simulated waste streams consisting of non-radioactive analogues of the active atoms that may be present as shown in Table 2-2, where Hf is a surrogate for Pu^{4+} and Sm is a surrogate for Am^{3+} and Pu^{3+}.

One group of materials proposed for the safe immobilisation of waste with a high chlorine content are calcium phosphates. They can be found naturally in many different forms, a number of which are known to accommodate a range of ions within their structure. Studies have been undertaken using a variety of waste compositions after being sintered with $CaHPO_4$. Depending on starting composition and elements involved, substituted forms of the minerals apatite ($Ca_5(Cl,F,OH)(PO_4)_3$), spodiosite ($Ca_2Cl(PO_4)$) and whitlockite ($Ca_3(PO_4)_2$) are seen to be produced along with some unreacted oxides depending on the substitution level and elements present. The target phases for the

immobilisation of actinides and halides are whitlockite and apatite respectively.

Once sintered with the $CaHPO_4$, the majority of the waste-stream should be chemically immobilised within its ceramic host. There is however still a problem since the resulting wasteform will be a polycrystalline powder which could be easily dispersed. The solution to this is to encapsulate this new wasteform within a glass matrix. The chosen glass must also fulfil several requirements: it must have a relatively low melting point to keep processing costs down, it must ideally be inert with respect to the wasteform components and it too must be proven to be stable and durable over long time periods and under potential radiation damage. Sodium aluminophosphate glasses used for HLW immobilisation in the USSR fulfil these criteria and are being investigated for this purpose.In addition, they have increased chlorine solubility when compared to borosilicate glasses. They do however appear to react with the wasteform constituents producing another variable to be accounted for.

2.4 β-tricalcium phosphate as an immobilisation host

β-tricalcium phosphate, $Ca_3(PO_4)_2$, (β-TCP) is naturally present in the earth in a form known as whitlockite. This mineral contains Fe, Mg, H and traces of other impurities substituting for calcium within the structure and whitlockite has been seen to accommodate many different ions into its structure. It is because of this ability and the fact that whitlockite is known to be a durable mineral, stable over long time periods that β-TCP is also being considered as a host for immobilising a range of ions.

If β-TCP is to be used as a storage mechanism for the waste then there are a few problems which need to be addressed. Firstly it needs to be shown that the β-TCP structure can accommodate the different constituent ions present in the waste. It has been reported in the literature that β-TCP can be made with a variety of ions substituting onto the calcium sites and so this looks very promising. Secondly, if the different ions involved in the waste are able to be accommodated into the β-TCP structure, the maximum substitution level of the different atoms will need to be determined as any non-reacted waste is a potential hazard. Finally, much work needs to be done on optimising the level of substitution whilst taking into account possible variations in the composition of the waste stream to ensure all waste will be reacted.

The final stages of this will need to be done with actual waste or simulated waste streams which are representative of the actual waste. The use of actual waste streams is of course impractical and could be potentially hazardous in the early stages of the investigation and so some thought needs to be given about the starting point. One solution is to use surrogates for the radioactive elements, mimicking certain properties such as valency or ionic radius. For instance, a good surrogate for americium in certain circumstances could be samarium, since Sm^{3+} has the same valence and similar ionic radius to Am^{3+}. One element present in moderate quantities in the waste is gallium. Since gallium is not toxic or radioactive, Ga^{3+} would be a good candidate for use in initial experiments.

Chapter 3

β-tricalcium phosphate and cation substitution

3.1 Introduction

β-tricalcium phosphate (β-TCP, $Ca_3(PO_4)_2$) is a naturally occurring mineral usually found in the form of whitlockite, which contains Fe, Mg, H and other impurities substituting for Ca in the structure. Whitlockite is also present in samples brought back from lunar missions along with other calcium phosphate species [7], further indicating its prevalence of formation. It has also been of high interest for biomedical applications [8, 9], specifically in the field of bone repair due to the high biocompatibility of calcium phosphates.

3.2 Structure of β-tricalcium phosphate

β-tricalcium phosphate crystallises in the rhombohedral space group R3c with unit cell parameters a/b $\approx$ 10.41 Å and c $\approx$ 37.39 Å. The crystal structure of β-tricalcium phosphate comprises a hexagonal network of A and B columns with each A column surrounded by 6 B columns (Fig. 3-1). The B columns consist of two phosphorus sites, P(2) and P(3), arranged in PO_4 tetrahedra, along with three calcium sites, Ca(1,2,3). The A columns contain a repeating structure of one PO_4 group, P(1), along with two calcium sites, Ca(4) and Ca(5). The structure is further complicated however by partial occupancy of the Ca(4) site, effectively doubling the c-axis.

Of the calcium sites, Ca(1) is 7 co-ordinated, Ca(2) and Ca(3) are 8 co-ordinated, with the Ca(2) site having two slightly longer bonds and Ca(4) and Ca(5) are 6 co-ordinated. Ca-O bond lengths are shown in table 3-1 where it can be seen that the Ca(4) site is quite unusual in that it has three short bonds and three very long bonds, possibly

Table 3-1 Ca–O bond lengths for the different Ca sites in β-TCP.

		length (Å)			length (Å)			length (Å)
Ca(1)	O(3)	2.5117	**Ca(2)**	O(1)	2.4077	**Ca(3)**	O(1)	2.6877
	O(4)	2.4706		O(2)	2.4167		O(2)	2.6004
	O(4)	2.4517		O(3)	2.3741		O(3)	2.3542
	O(5)	2.3883		O(5)	2.7020		O(5)	2.3926
	O(6)	2.3274		O(6)	2.7438		O(6)	2.5450
	O(8)	2.4184		O(7)	2.4254		O(8)	2.6227
	O(9)	2.4634		O(7)	2.4230		O(8)	2.5676
				O(9)	2.4331		O(10)	2.5739
	Average	2.4331		Average	2.4811		Average	2.5430
Ca(4)	O(1)	2.3518	**Ca(5)**	O(4)	2.2101			
	O(1)	2.3518		O(4)	2.2101			
	O(1)	2.3518		O(4)	2.2101			
	O(9)	3.1191		O(7)	2.3116			
	O(9)	3.1191		O(7)	2.3116			
	O(9)	3.1191		O(7)	2.3116			
	Average	2.8255		Average	2.2609			

explaining the half occupancy of this site.

Tricalcium phosphate can be observed in three different phases, the β phase being the stable room-temperature phase. At 1120 °C there is a phase transition into the monoclinic α phase which, if rapidly cooled, is retained at room temperature. At 1470 °C an $\bar{\alpha}$ phase is formed which is stable up until its melting point at 1800 °C, although unstable at room temperature [10].

3.3 Possible substitution mechanisms

The actual method for substitution of ions into β-TCP is not yet fully understood, however various models have been suggested including one by Yoshida *et al.* [11] based on charge balancing (Fig. 3-1). In this model the ions are substituted for the Ca on the Ca(4) and Ca(5) sites depending on the charge on the substituent ions. Monovalent ions go onto the Ca(4) sites, substituting equally for both the Ca ions and filling vacancies present. Divalent ions substitute directly for the Ca ions since they have equal charge. The case is slightly more complicated for trivalent ions where the model suggests that two trivalent ions and one vacancy substitute for one Ca(4) and two Ca(5) ions to pre-

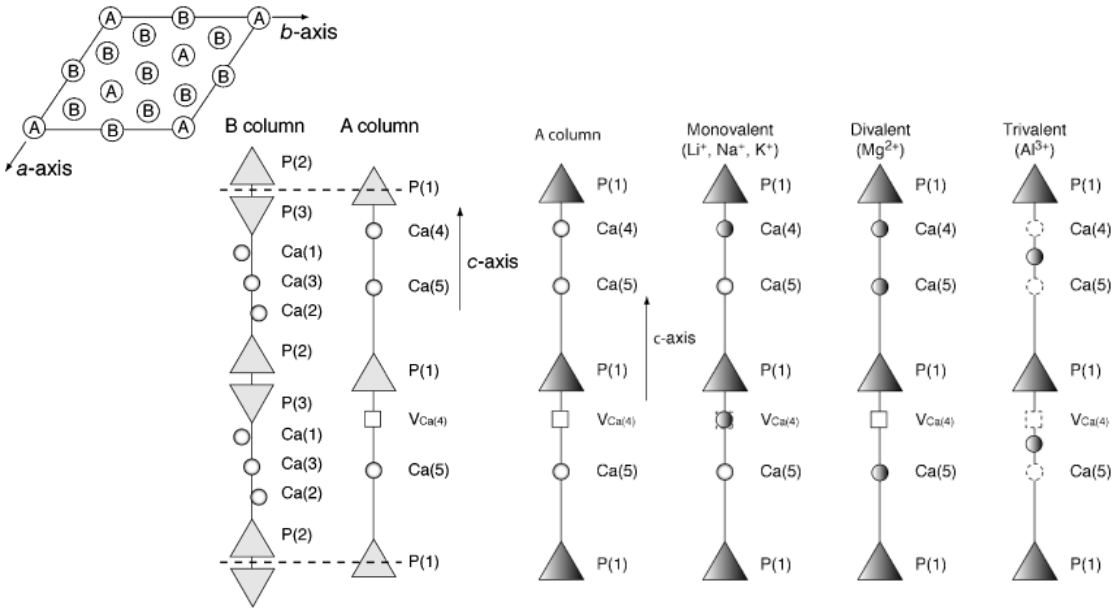

Figure 3-1 Structure of β-tricalcium phosphate including Yoshida model of substitution mechanisms for monovalent, divalent and trivalent ions [11].

serve charge neutrality.

Further studies by Golubev and Lazoryak [12, 13] suggest that substitution can take place on any of the Ca sites and is partially dependent on the radius of the substituent ions due to the effective sizes of the different Ca sites within β-TCP. For trivalent ions, the Ca will still be replaced as $3\,Ca^{2+} \rightarrow 2\,R^{3+} + \square$ where R^{3+} is a trivalent cation and $\square$ denotes a vacancy. The ions involved having radii comparable to Ca^{2+} occupy the Ca(1), Ca(2) and Ca(3) positions. Ions with radii larger than Ca^{2+} may predominantly occupy the larger Ca(3) polyhedra whereas slightly smaller ions may predominantly substitute into the smaller Ca(1) and Ca(2) polyhedra. However, ions with atomic radii much smaller than that of Ca are thought to substitute into the significantly smaller Ca(4) and Ca(5) sites, with a preference generally for the Ca(5) site due to the distorted environment of the Ca(4) sites. The metal–oxygen distances for the normal oxidation states and site substitution preferences for a range of elements are shown in table 3-2.

3.4 Relevance of NMR

Nuclear magnetic resonance (NMR) is an experimental technique used to probe the local environments of specific atoms within a material with each chemical environ-

Table 3-2 Metal–oxygen distances and site preferences for different elements in β-TCP.

Element	M^{n+}–O distance (Å) [14]	Site preference
Al	1.651	Ca(5) [15]
Cu	1.679	Ca(5) [16], Ca(4/5) [17]
Mg	1.693	Ca(5) [13], Ca(4/5) [18, 19]
Zn	1.704	Ca(4/5) [18]
Cr	1.724	Ca(5) [15]
Ga	1.73	Ca(5) [15]
Fe	1.759	Ca(5) [20]
Mn	1.76	Ca(5) [13]
Na	1.8	Ca(4) [21]
Sc	1.849	Ca(5) [15]
In	1.902	Ca(5) [15, 22]
Ca	**1.967**	
Sb	1.973	Ca(2) [15]
Eu	2.076	Ca(1/2/3) [12, 13]
La	2.172	Ca(3) [12]

ment producing a distinct resonance, further details can be found in section 4.1. There exist NMR 'active' isotopes for most elements although low natural abundance and receptivity can make some elements difficult or impossible to observe without isotopic enrichment or exotic NMR techniques being used.

3.4.1 ^{43}Ca nuclear magnetic resonance

Since substitution is thought to take place solely on the Ca sites, ^{43}Ca NMR would be an obvious choice as a technique to use in order to determine which Ca sites are affected. ^{43}Ca, however, is a very NMR insensitive nucleus with a low natural abundance (0.135 %), requiring very high fields to fully resolve the sites.

Interpreting ^{43}Ca NMR spectra should be fairly straightforward, with each calcium site corresponding to one resonance in the spectrum. Relative occupancies of each calcium site within the structure can simply be determined by the relative intensities of the peaks resulting from each site. The relative intensities expected for phase-pure β-TCP can be found in table 3-3.

Work done by Gervais *et al.* [23] suggests a link between Ca–O bond length and chemical shift of the associated Ca sites in ^{43}Ca NMR. They suggest a roughly lin-

Table 3-3 Fractional intensity of ^{43}Ca sites in β-TCP.

Site	Ca(1)	Ca(2)	Ca(3)	Ca(4)	Ca(5)
Fractional Intensity	28.6%	28.6%	28.6%	4.8%	9.5%

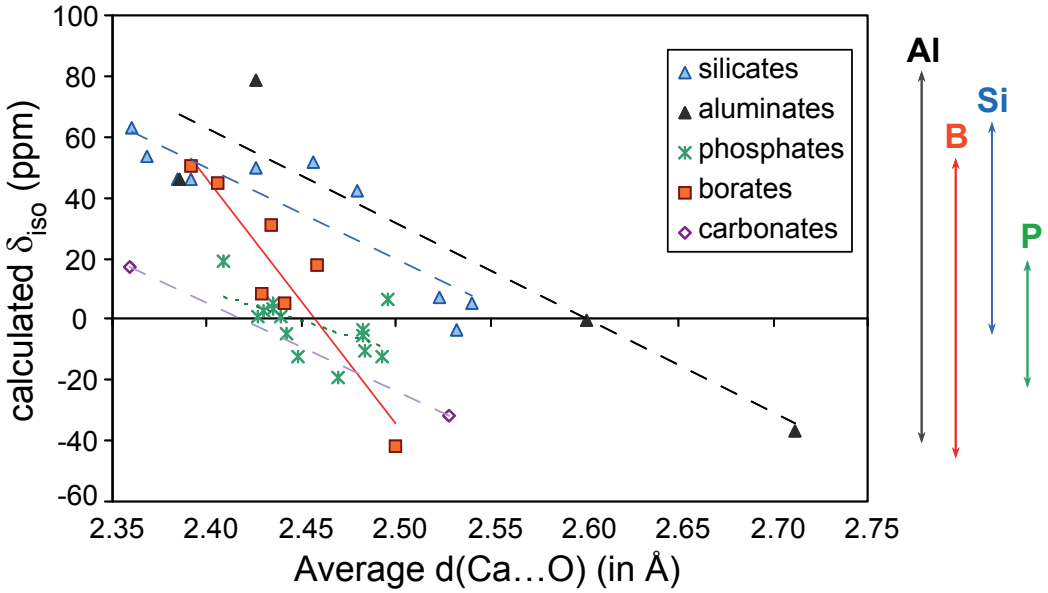

Figure 3-2 Correlation between ^{43}Ca isotropic chemical shifts and mean Ca–O bond distance in a series of calcium inorganic species [23].

ear variation of increasingly negative chemical shift with Ca–O distance at a rate of $-190\,\text{ppm}\,\text{Å}^{-1}$ for phosphates as shown in figure 3-2. By looking at the average Ca–O bond lengths for each Ca site (table 3-1), the order of the peaks in the ^{43}Ca spectra may be determined.

3.4.2 ^{31}P nuclear magnetic resonance

Substitution on the Ca sites will also affect the local environments of the different P sites, therefore ^{31}P NMR is another tool which may be used to measure changes in the different Ca sites indirectly. The three P sites each have different coordination with the Ca sites, especially the Ca(4) and Ca(5) sites which may be the most interesting according to the Yoshida model. Each P site has several Ca(1,2,3) next-nearest neighbours and, in addition, P(1) has one Ca(4) next-nearest neighbour, P(2) has both a Ca(4) and a Ca(5) next-nearest neighbours and P(3) has just an additional Ca(5) next-nearest neigh-

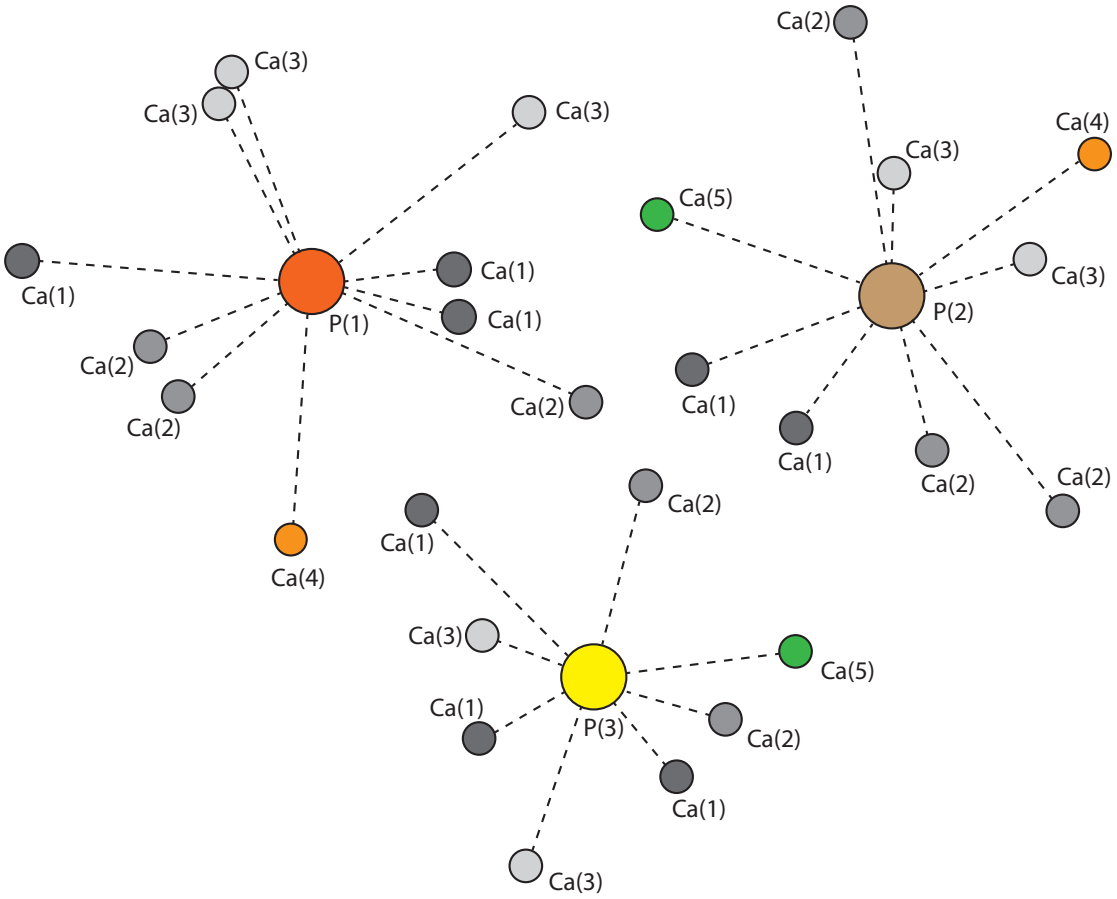

Figure 3-3 Second co-ordination spheres of P sites in β-tricalcium phosphate [24].

bour (Fig. 3-3). This difference of coordination makes ^{31}P NMR somewhat sensitive to changes in the P coordination spheres due to substitution onto the Ca(4) and Ca(5) sites.

The three P sites have relative occupancies 1:3:3 which would suggest that three resonances should be present with the same corresponding ratio of intensities. This is further complicated however by the partial occupancy of the Ca(4) site. Since P(3) has no Ca(4) next-nearest neighbour, the resonance corresponding to those sites will be unaffected by the state of the Ca(4) site. Both the P(1) and P(2) sites have Ca(4) next-nearest neighbours and, as such, the resonances from these sites should be split into two equally intense resonances due to the half occupancy of the Ca(4) site. This splitting will give rise to a ratio of intensities of the different resonances of 1:1:3:3:6 (Table 3-4).

As substitution occurs in the material, it will cause further splitting of the resonances due to partial occupation of the Ca sites by other ions along with a possible change in the number of vacancies. A splitting of the composition of one of the Ca sites will

Table 3-4 Relative intensities of the different ^{31}P NMR resonances as given by Jakeman *et al.* [18].

Site:	P(1)		P(2)		P(3)
Intensity:	1/2	1/2	3/2	3/2	3
Relative intensity (%):	7	7	21.5	21.5	43

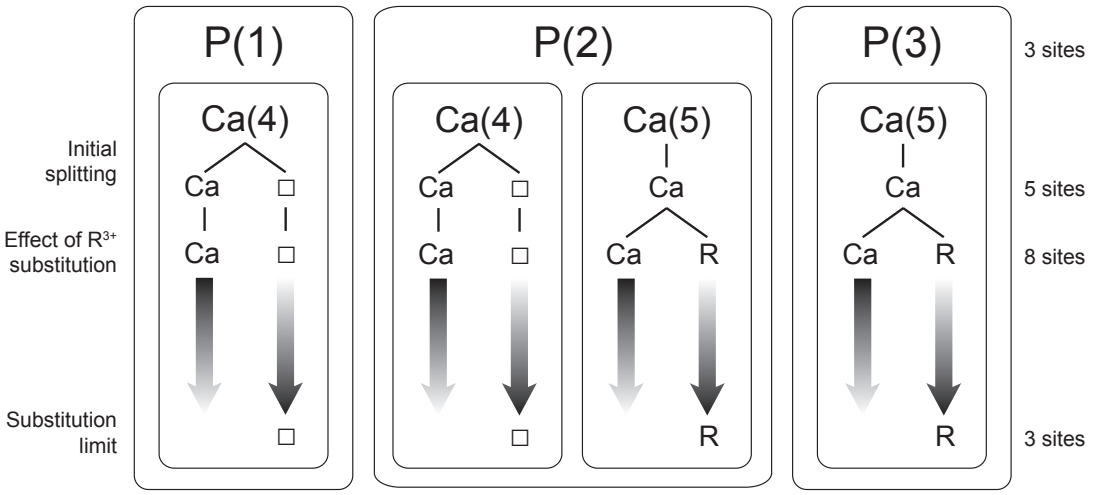

Figure 3-4 Possible effect on P sites of R^{3+} substitution into Ca(5) sites.

result in a doubling of the multiplicity of the number of distinct P environments of the corresponding P next-nearest neighbours. A schematic of the possible influence of R^{3+} substitution into Ca(5) sites is shown in figure 3-4, resulting in a maximum of 8 distinct resonances. However, upon reaching the substitution limit, the Ca(5) site will be fully occupied by the substituent ion and the Ca(4) site will be vacant, therefore no splitting will take place and there should be a single peak resulting from each of the three P sites.

If it is assumed that substitution takes place solely on the Ca(5) site with additional vacancies appearing on the Ca(4) site for charge balancing, i.e. $3\,Ca^{2+} \rightarrow 2\,R^{3+} + \square$, then there should be a linear change in the site occupancies with substitution. For substitution of the form $Ca_9R_x(PO_4)_{6+x}$, the substitution limit would be at x=1 where the Ca(4) site is fully vacant and the Ca(5) site contains only R^{3+} ions. This means that on the Ca(4) site, as x increases from $0 \rightarrow 1$, the Ca occupancy will go from $0.5 \rightarrow 0$ and the proportion of vacancies will go from $0.5 \rightarrow 1$. For the Ca(5) site it will be $1 \rightarrow 0$ for Ca occupancy and $0 \rightarrow 1$ for R occupancy.

Table 3-5 Distinct P environments present along with relative intensities of their ^{31}P NMR resonances under R^{3+} substitution.

P environment	Relative intensity
P(1) Ca(4)	$0.14(1/2 - x/2)$
P(1) □(4)	$0.14(1/2 + x/2)$
P(2) Ca(4) Ca(5)	$0.43(1/2 - x/2)(1 - x)$
P(2) Ca(4) R(5)	$0.43(1/2 - x/2)x$
P(2) □(4) Ca(5)	$0.43(1/2 + x/2)(1 - x)$
P(2) □(4) R(5)	$0.43(1/2 + x/2)x$
P(3) Ca(5)	$0.43(1 - x)$
P(3) R(5)	$0.43x$

To relate this to ^{31}P NMR spectra, the different P environments present need to be determined along with their relative proportions. Since, in this case, substitution is only affecting the Ca(4) and Ca(5) sites then it is only changes in these that need to be investigated. For example, on the P(1) site there is only a Ca(4) next-nearest neighbour which means there will be two distinct environments, one from Ca on the site and one from a vacant site. The fraction of these environments will change with substitution as shown above.

Quantitative values for the relative intensities of each site may be obtained quite simply by multiplying the fractional occupancy of the P(n) site by the fractional occupancies of the neighbouring Ca sites for each permutation on each P site. The distinct P environments present, and the equations showing how the relative intensities of ^{31}P NMR peaks depend on composition in this model, are shown in table 3-5 with a graphical representation shown in figure 3-5.

If the trivalent ions also substituted onto the Ca(4) sites, then this would cause a further increase in the number of P environments and hence also the number of peaks present in ^{31}P NMR spectra. By increasing the number of distinct environments associated with the Ca(4) site the maximum number of peaks present in the spectra will increase to 11.

Determining the impact which substitution has on ^{31}P NMR spectra can become much more complicated under substitution onto the Ca(1,2,3) sites. This is due to each P atom having multiple Ca(1,2,3) next-nearest neighbours, each giving slightly different

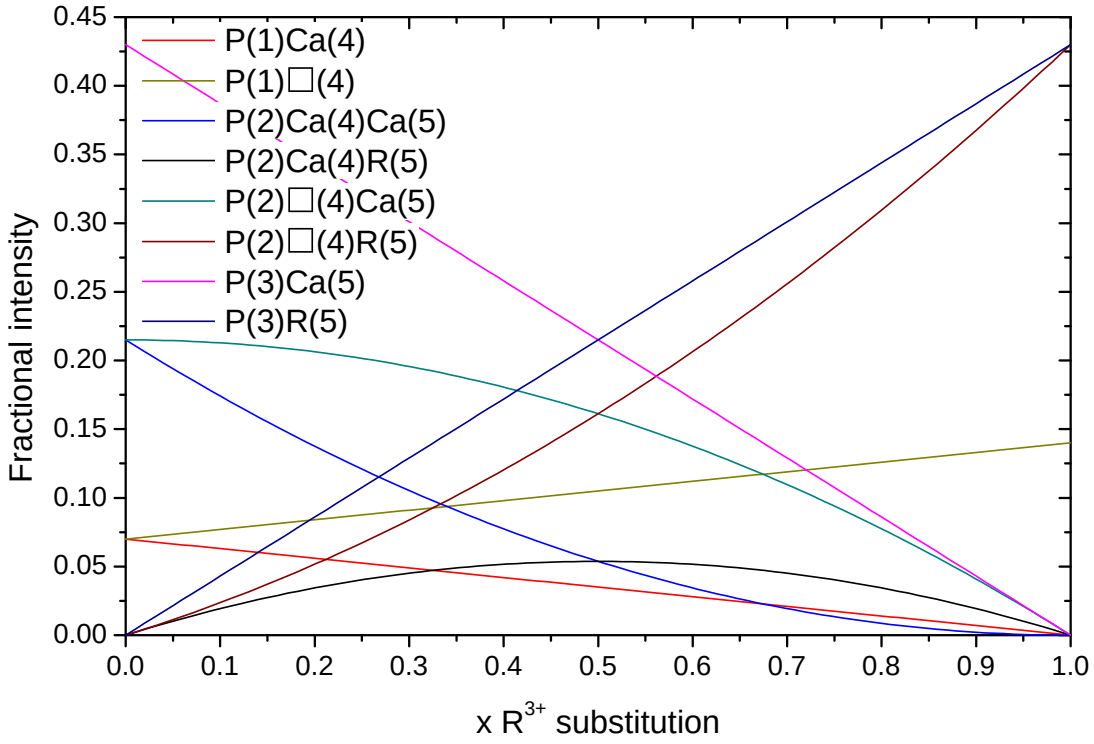

Figure 3-5 Predicted relative intensities of ^{31}P NMR resonances under R^{3+} substitution onto Ca(5) site.

P environments which, in the case of substitution solely onto the Ca(3) site, would give rise to a total of 13 different resonances, some of which could potentially be very similar in frequency and could make resolving them using ^{31}P NMR very difficult.

Chapter 4

Experimental theory and practice

4.1 Nuclear magnetic resonance

Nuclear magnetic resonance (NMR) is a technique which exploits the spin of nuclei and as such can be used as a local probe of structure. Nuclei with even mass and charge number have zero nuclear spin and thus cannot be observed via NMR. For all other nuclei their spin is a function of the spin quantum number of the nucleus, I, which can take integer or half-integer values. The signals obtained using NMR come from the fact that, in a magnetic field, the different spin states of a nucleus will be split into different energy levels (Zeeman splitting), with the energy required to induce transitions between these levels generally requiring photons in the radio-frequency range. The reason NMR is so sensitive to atomic environments is due to the surrounding atoms creating different effective fields around the nuclei via electronic shielding, causing the energy levels to change.

For nuclei with non zero spin, the nuclear magnetic moment, μ, is given by

$$\underline{\mu} = \gamma\hbar\underline{I} \tag{4-1}$$

where γ is the gyromagnetic ratio for that nucleus, $\hbar$ is the reduced Planck constant, equal to approximately 1.055×10^{-34} J s and $\underline{I}$ is the total spin angular momentum. Because angular momentum is quantised, there can be only $2I + 1$ different values that the z-component of the spin angular momentum can take and therefore $I_z = m\hbar$ where m takes the values $+I$, $(+I-1)$, through to $-I$. This leads to a z-component of the magnetic moment of

$$\mu_z = \gamma I_z = \gamma m\hbar \tag{4-2}$$

The simplest case to observe is for spin $1/2$ nuclei, such as ^{31}P. In the absence of an external magnetic field, and at thermal equilibrium, the nuclei will have $2I + 1 = 2$ degenerate energy levels which will therefore both contain the same number of nuclei.

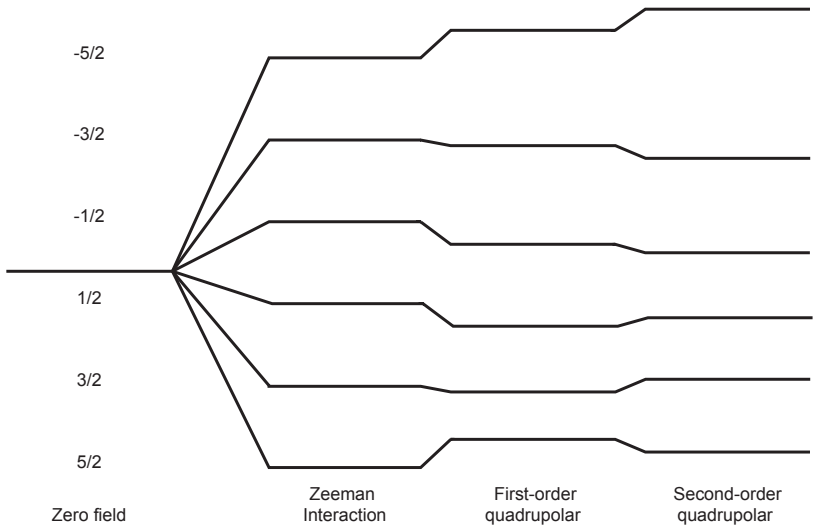

Figure 4-1 Zeeman splitting for spin 5/2 nuclei [25].

If the nuclei are now subject to an external magnetic field, $\underline{B}$, there will be an energy associated with the interaction of the nuclear magnetic moments with the field, given by

$$E = -\underline{\mu}.\underline{B} = -\gamma\hbar\underline{I}.\underline{B} \tag{4-3}$$

If the field is in the z-direction the energy can be shown to be

$$E = -\mu_z B_0 = -\gamma m\hbar B_0 \tag{4-4}$$

This implies an energy difference $\gamma\hbar B_0$ between the $+1/2$ and $-1/2$ spin states and gives rise to a population difference between the two states. For quadrupolar nuclei (those with spin $I > 1/2$), the number of spin states, and hence the number of energy levels available, is increased as $2I + 1$ (Fig. 4-1). Along with the additional splitting to produce a greater number of accessible energy levels, the electric quadrupole moment of quadrupolar nuclei causes a further shift in the energy levels of the spin states along with a broadening and shift of spectra obtained.

In a magnetic field, the magnetic moments of the nuclei will precess about the magnetic field direction at an angular frequency characteristic of a given nucleus known as the Larmor frequency,ω_0, where

$$\omega_0 = \gamma \left|\underline{B}\right| \tag{4-5}$$

Due to the random orientation of magnetic moments they will appear to form cones about the magnetic field axis giving rise to a net magnetisation $\underline{M}$ aligned with the direction of the magnetic field $\underline{B}$.

If a plane polarised r.f. pulse at the Larmor frequency is now applied to the nuclei in the x-direction, the nuclei will interact with this energy and their spins will rotate around the y-axis resulting in a change in the direction of the net magnetic moment within the material. The net magnetisation will now be seen to rotate about the z-axis at the Larmor frequency, with the angle from the z-axis, known as the tip angle, increasing with increasing pulse duration.

A weak r.f. signal will now be detectable from the nuclei as they precess about a different axis. The characteristics of this signal can be used to give details of the environments of the individual nuclei present in the sample. Over time, thermal motion will remove the coherence of the precessing nuclei and the signal will decay to an extent proportional to $\exp(-t/T_2)$ where T_2 is known as the transverse (or spin-spin) relaxation time. Also, since the system is in an excited state, the net magnetic moment of the system will gradually decay back to the equilibrium state. This will occur at a rate proportional to $\exp(-t/T_1)$, where T_1 is known as the longitudinal (or spin-lattice) relaxation time and therefore the net magnetisation along the z-axis can be given by

$$M_z = M_0\left(1 - \exp\left(\frac{-t}{T_1}\right)\right) \tag{4-6}$$

In pulsed NMR, a short r.f. pulse at the Larmor frequency is directed at the sample and the response detected. This response is observed as a free induction decay (FID), the signal in time space, consisting of a range of frequencies present in sample around the Larmor frequency and decaying proportional to T_2. In order to extract the frequency data out of this, the FID is Fourier transformed producing the NMR spectrum.

There are many interactions which can affect the local field of nuclei, the main ones being; chemical shift, quadrupole coupling, dipole-dipole coupling and J-coupling [26]. Chemical shift is dependent on the electronic environment produced by the neighbouring atoms and the magnetic field they create, meaning crystallographically similar sites within a material should, in most cases, give the same chemical shift. Quadrupole coupling involves the electric quadrupole moment, eQ, of a nucleus interacting with the electric field gradient, $\mathbf{V}$, produced by surrounding electrons. The interaction can be described by the quadrupole coupling constant, C_Q, where $C_Q = e^2qQ/h$ and $eq = V_{zz}$ [27]. Another important parameter is η, which describes the asymmetry of the electric field gradient and is given by $\eta = (V_{yy} - V_{xx})/V_{zz}$. Quadrupole coupling is only ob-

served for quadrupolar ($I > 1/2$) nuclei and only those in asymmetric environments. Dipole-dipole coupling is an effect produced by the through-space interaction of dipole moments of neighbouring atoms. J-coupling is due to an indirect coupling of dipole moments through bonding electrons in the material.

In many cases, the most important interaction is chemical shift as it is an easy way of observing the local environment of the atoms, where the shifts observed can often be related to specific configurations of atoms. Since the absolute chemical shift will change with different magnetic fields, a reference material is used to standardise the chemical shift values obtained. The reference material usually has a high concentration of the target nucleus and is either in solution or highly symmetric, leading to well-resolved, narrow lines. Chemical shift, δ, is usually calculated as the shift in the observed frequency from that of a reference material according to the formula

$$\delta = \frac{\nu_{sample} - \nu_{reference}}{\nu_{reference}} \tag{4-7}$$

Most interactions which affect NMR spectra, such as electronic shielding and dipole-dipole interactions are dependent on crystallite orientation. In a liquid the timescale on which the atoms move around is small compared to that of most of the interactions affecting the signal, therefore all orientations are effectively observed at once and as such this orientational dependence disappears.

This is obviously not the case when looking at polycrystalline powders which most solid state NMR entails. Here the distribution of crystallite orientations causes a broadening of the peaks in the observed spectra. The orientational dependence of some of the interactions (dipole-dipole, 1^{st} order quadrupole) is of the form $3\cos^2\theta - 1$, where θ is the angle between the vector describing these interactions and the external field. By exploiting this dependence via a technique known as magic angle spinning (MAS), this angular dependence can be removed. The basis of MAS is to spin the rotor containing the sample about an axis oriented at the 'magic angle' of 54.74° to the direction of the applied field. This is the angle which satisfies $3\cos^2\theta - 1 = 0$.

Two important parameters when performing NMR experiments are the duration of the applied pulse(s), or the pulse length, and the delay between pulse sequences, referred to here as the pulse delay. The pulse length determines to what extent the net magnetic moment is rotated about the z-axis, with a linear behaviour of tip angle with increasing pulse length. The pulse delay is the time between consecutive experiments,

the period in which the spins are allowed to relax back to their equilibrium state. This must be of sufficient duration, otherwise, if environments with differing longitudinal relaxation times are present, the observed spectra may not be fully representative.

A technique which can be used where spectra are expected to contain broad features is a spin echo. This involves applying a 180° pulse once the initial FID has died away which causes the spins to flip, meaning the dephased spins will begin to rephase giving what appears to be back to back FIDs. The main advantage of using a spin echo is being able to access the short time components of the FID, corresponding to broad features in the Fourier transformed spectra, usually lost for experimental reasons. However, by taking the measurement much further into the FID the magnetisation will have decayed and the signal obtained will be less intense. In order to perform a spin echo, T_1 needs to be much greater than T_2 so that the 'echoes' can be fully measured. Spin echoes can also be more difficult to perform as the 90°/180° pulse lengths need to be accurately determined otherwise additional dephasing may be observed.

Further background on NMR theory can be found in specialised books on the subject, such as those by Mackenzie and Smith [25], Levitt [26] and Duer [28].

4.2 X-ray diffraction

X-ray diffraction uses x-rays as a probe of the bulk structure of materials via constructive interference of diffracted waves. In order for constructive interference to occur, Bragg's law,

$$2d \sin\theta = n\lambda \tag{4-8}$$

must be satisfied where d is the interplanar spacing of atoms in the sample, θ is the angle of the x-rays incident on the scattering planes, λ is the wavelength of the incident x-rays and n is an integer related to the order of the interference (usually 1) (Fig. 4-2). By measuring over a range of angles a diffraction pattern can be built up from which structural details can be extracted from the position and shape of the Bragg reflections. In order to obtain the diffraction pattern, coherent scattering needs to be observed.

The positions of the peaks in the diffraction patterns produced are governed by the structure of the material and will mainly depend on the size of the unit cell along with the allowed Bragg reflections based on the symmetry of the unit cell. Intensities are

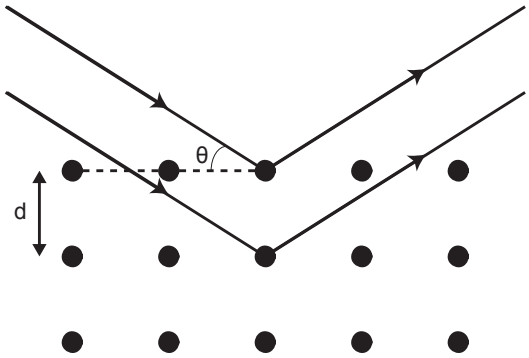

Figure 4-2 Schematic of x-ray scattering illustrating terms used in Bragg's law.

partially dependent on these conditions but also strongly on the atoms involved in the x-ray scattering with scattering from heavier elements being greater than that from light elements due to the increased number of electrons present. Intensities can also be affected if there is a preferred orientation of the sample in the holder. The peak shape of diffraction patterns can also give additional information about the system being examined such as thermal motion of atoms and size/strain defects.

Small imperfections within a crystal lattice will cause multiple scattering events to take place resulting in extinction of the x-rays at longer path lengths. This extinction effect may result in a reduction in intensity of higher order reflections due to the longer path lengths. If a large amount of extinction is present for a material it will also mean that the resulting pattern will have a larger contribution from the surface of the material.

If vacancies or defects are present in a material, as is the case in β-TCP, then the diffraction pattern may show additional reflections not normally allowed for the structure. If the defects are randomly distributed then little indication of their presence will be detected, only a slight change in intensity of the reflections involving that site. However, if ordering occurs then they may be more easily detected with periodic defects resulting in a change in the intensity of the reflections involving that site.

4.3 Neutron diffraction

In its simplest form neutron diffraction can be seen as an analogue to x-ray diffraction using neutrons instead of x-rays for the scattering. The interactions however differ due to the nature of the incident rays; x-rays will scatter from electrons, meaning the intensity of the diffracted beam increases with atomic number, whereas neutrons scatter from nuclei, the extent of which is largely independent of atomic number with different isotopes often having drastically different, and even negative, scattering factors. It is this difference in scattering that makes x-ray and neutron diffraction very complementary techniques.

One advantage of neutron over x-ray diffraction is that there is no angular dependence of the intensity of the diffracted beam, whereas x-rays scatter with an intensity which decreases with incident angle. A major drawback however is that some isotopes will absorb neutrons, making detection of these isotopes more difficult and producing radioactive samples. In most cases the radionuclides produced are short-lived with only a brief period required before they cool down to normal levels.

Thermal neutrons are the most widely used in scattering experiments, where the temperature of the moderator used in the production of the neutrons is in the order of room temperature, with ~290 K corresponding to an energy of 25 meV [29]. This gives a velocity of ~2.20 km s^{-1} and therefore a de Broglie wavelength of ~1.8 Å (Eq. 4-9). This wavelength is comparable to interatomic distances, making thermal neutrons an effective source for neutron diffraction.

$$\lambda = \frac{h}{m_n v} \tag{4-9}$$

In a neutron diffraction experiment the quantity measured is the differential cross section, $\frac{d\sigma}{d\Omega}$, a measure of the scattering per solid angle, which gives details of the total scattering from the sample. This is made up of two components, a self scattering term, $I^S(Q)$, and a distinct scattering term, $i(Q)$. It is this distinct scattering that is of most interest in an experiment. The differential cross section is given by [30]

$$\frac{d\sigma}{d\Omega} = I(Q) = I^S(Q) + i(Q) \tag{4-10}$$

The self scattering term can be approximately calculated from details of the sample (elements involved, number of each atom, temperature) and of the beamline and

spectrometer (flight path, detector efficiency, flux). The self scattering term can then be subtracted from the measured total scattering to give the distinct scattering.

This reciprocal space diffraction pattern can be converted into real space by Fourier transforming the distinct scattering. This neutron correlation function, $T(r)$, is given by [30]

$$T(r) = T^0(r) + \frac{2}{\pi}\int_0^\infty Qi(Q)M(Q)sin(rQ)dQ \tag{4-11}$$

where $T^0(r)$ is the average density contribution to the correlation function and $M(Q)$ is a modification function used to reduce termination ripples due to truncation of the integral at Q_{max}. The total correlation function is dependent on the properties and fractions of the elements involved and is made up of a weighted sum of partial correlation functions, $t_{ll'}$ [31]

$$T(r) = \sum_l \sum_{l'} c_l \overline{b}_l \overline{b}_{l'} t_{ll'}(r) \tag{4-12}$$

where $\overline{b}_l$ and $\overline{b}_{l'}$ are the coherent scattering lengths for elements l and l' and c_l is the atomic fraction of element l. From the total correlation function information can be extracted about the local structure of a material. Each peak will be due to a correlation between a specific pair of atoms of separation r as shown in Figure 4-3. From this the coordination number, $n_{ll'}$, can also be calculated according to [32]

$$n_{ll'} = \frac{r_{ll'}A_{ll'}}{(2-\delta_{ll'})c_l\overline{b}_l\overline{b}_{l'}} \tag{4-13}$$

where $A_{ll'}$ is the area of the peak in the total correlation function at position $r_{ll'}$ and $\delta_{ll'}$ is the Kronecker delta.

Two main neutron sources are used in experiments; either a nuclear reactor or spallation using accelerated particles. Neutron experiments in this work were carried out at the accelerator-based source at ISIS, specifically on the GEM diffractometer.

At ISIS a linear accelerator is used to accelerate H^- ions up to 70 MeV before being injected into a synchrotron. As the H^- ions enter the synchrotron they pass through thin alumina foil which strips away the electrons leaving a beam of protons. These protons are then accelerated in the synchrotron up to 800 MeV before being extracted. This process is repeated 50 times per second and delivers a 200 μA current to the targets.

The proton beam then collides with a tungsten target, producing neutrons via spallation. Moderators, such as water, liquid methane or liquid hydrogen are then used to slow down the fast neutrons produced to the required speeds.

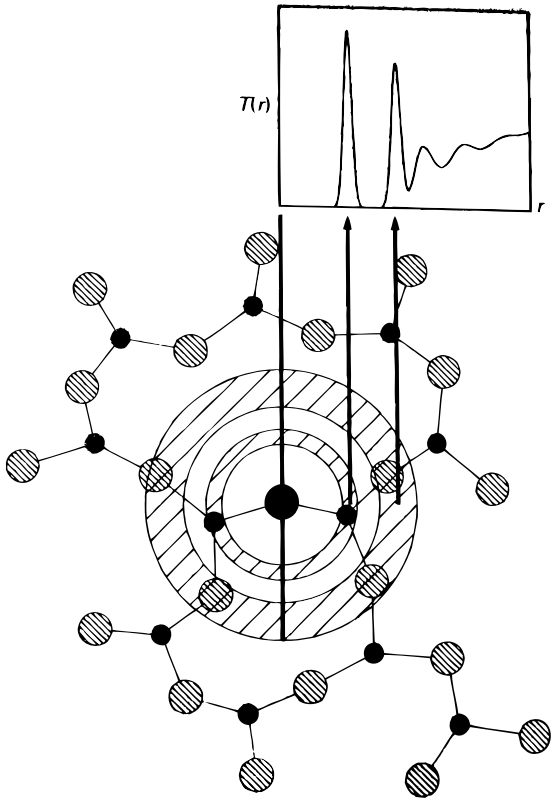

Figure 4-3 A simulated neutron correlation function, $T(r)$, together with a fragment of an A_2X_3 network, showing how the peaks in the correlation function arise from the interatomic distances [31].

The GEneral Materials (GEM) diffractometer at ISIS receives ~9 meV thermal neutrons from a liquid methane moderator at 110 K. The detectors cover a wide range in scattering angles (1.2° to 171.4°) and the long flight path gives a relatively high resolution in reciprocal space and therefore also in real space. The diffractometer detector array consists of 8 banks covering the different angular ranges, the detector layout of GEM is shown in Figure 4-4.

4.4 Rietveld refinement

In some cases simply indexing the diffraction peaks and relating them to their space group and lattice parameters is all the information that may be required from powder diffraction data. If however there is a need to determine the full structure of a material, the technique of Rietveld refinement may be used. This method was pioneered in the late 1960s by Hugo Rietveld [33, 34] and in simple terms involves using parameters

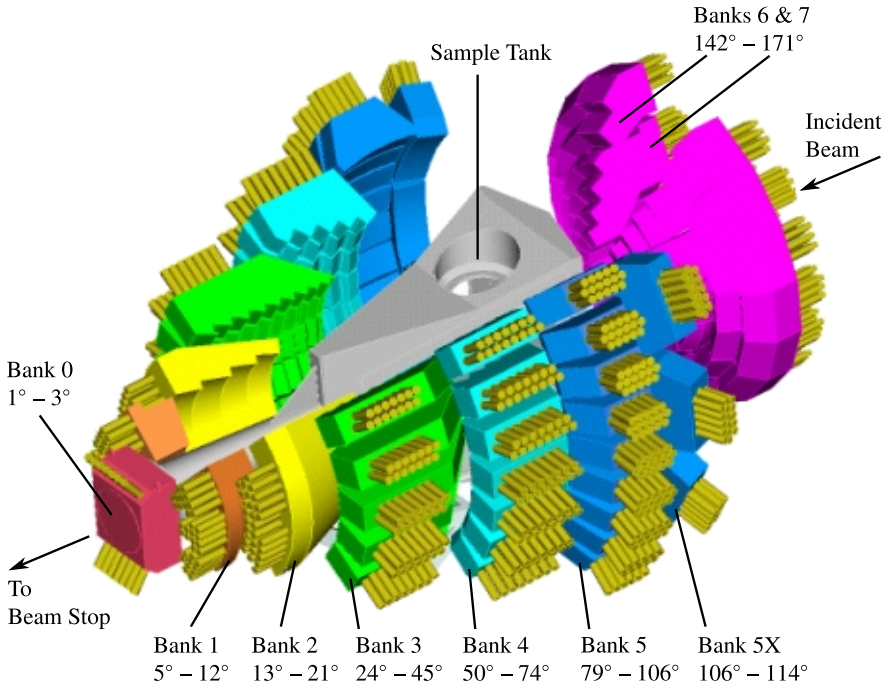

Figure 4-4 Layout of the GEM diffractometer [30].

of a postulated structure along with experimental conditions, including the optics used, to produce a simulated diffraction pattern. From this simulated pattern, parameters are varied in order to obtain a better fit to the observed data. This is done through iterative displacement of the parameters in order to reduce the residual, usually quantified by least-squares techniques, with the aim of reaching the global minimum of the system.

In Rietveld refinement, the diffraction pattern is split into i increments and least-squares refinement is performed in order to minimise the residual, S_y [35]

$$S_y = \sum_i w_i (y_{oi} - y_{ci})^2 \tag{4-14}$$

where w_i is a weighting factor equal to $1/y_{oi}$, y_{oi} is the observed intensity at the i^{th} step and y_{ci} is the calculated intensity at the i^{th} step. y_{ci} is calculated from the structure and experimental parameters according to the equation [35]

$$y_{ci} = s \sum_K L_K |F_K|^2 \phi(2\theta_i - 2\theta_K) P_K A + y_{bi} \tag{4-15}$$

where s is the scale factor, K represents the Miller indices, h, k, l, for a Bragg reflection, L_K contains the Lorentz polarization and multiplicity factors, ϕ is the reflection profile function, P_K is the preferred orientation function, A is an absorption factor, F_K is the structure factor for the K^{th} Bragg reflection and y_{bi} is the background intensity at the i^{th} step.

Table 4-1 Goodness of fit equations for Rietveld refinement, taken from Topas Academic technical reference [36].

Name	Function
R-pattern	$R_p = \sqrt{\frac{\sum \lvert y_{oi} - y_{ci} \rvert}{\sum y_{oi}}}$
R-weighted pattern	$R_{wp} = \sqrt{\frac{\sum w_i (y_{oi} - y_{ci})^2}{\sum w_i y_{oi}^2}}$
R-expected	$R_{exp} = \sqrt{\frac{\sum (M - P)}{\sum w_i y_{oi}^2}}$
Goodness of fit	$GOF = \chi^2 = \frac{R_{wp}}{R_{exp}} = \sqrt{\frac{\sum w_i (y_{oi}^2 - y_{ci}^2)}{(M - P)}}$
R-Bragg	$R_B = \frac{\sum \lvert I_{ok} - I_{ck} \rvert}{\sum I_{ok}}$

Least-squares refinement leads to a set of equations which involve derivatives of the calculated intensities, y_{ci}, with respect to each variable. These equations can then be solved by inversion of the normal matrix M_{ij} [35], where

$$M_{ij} = -\sum_i 2w_i \left[(y_{oi} - y_{ci}) \frac{\partial^2 y_{ci}}{\partial x_j \partial x_k} - \left(\frac{\partial y_{ci}}{\partial x_j} \right) \left(\frac{\partial y_{ci}}{\partial x_k} \right) \right] \tag{4-16}$$

where x_j and x_k are the adjustable parameters. Therefore, for a refinement involving m refined parameters, an m by m matrix must be inverted. Since the residual is non-linear, an iterative approach must be taken to find the solution where the shifts, Δx_k, are

$$\Delta x_k = \sum M_{jk}^{-1} \frac{\partial S_y}{\partial x_k} \tag{4-17}$$

In order to quantify how well the pattern has been modelled, goodness of fit parameters are often stated. Definitions of common parameters are shown in Table 4-1, where the previously undefined parameter M is the number of steps in the pattern, P is the number of refined parameters and I_{ok} and I_{ck} are the observed and calculated intensities of the k^{th} Bragg reflection.

R-pattern and R-weighted pattern are measures of how well the calculated pattern fits the data, based on the residual at each step. R-expected is the value for the theoreti-

cally best fit that can be produced from the model and data, determined by the number of steps in the data and number of parameters refined. Goodness of fit is the ratio of the R-weighted profile and R-expected and gives a measure of how well the data have been fit, with a goodness of fit of 1 meaning the data have been perfectly modelled and no more information can be extracted. R-Bragg relates only to the goodness of fit of the Bragg reflections in the structure being modelled, meaning any second phases present will be disregarded.

4.5 Experimental details

4.5.1 Sample preparation

Samples were generally produced according to the formula $Ca_9R_x(PO_4)_{6+x}$ with x = 0, 0.2, 0.4, 0.6, 0.8, 1.0. Precursors were ground and then calcined in air at 1050 °C for 4 h. The resulting powders were then reground and calcined further times to ensure phase purity. Further details for each system can be found in the relevant chapters.

4.5.2 Nuclear magnetic resonance

Acquisition details for each nucleus are shown below. After acquisition, spectra were processed using Bruker TopSpin 2.1 software [37], which involved Fourier transforming the FIDs before phasing and baseline correction were performed. Any fitting was performed using the fitting package within TopSpin, with spectra generally fitted to the Gaussian/Lorentzian peakshape provided.

4.5.2.1 ^{23}Na NMR ($I = 3/2$)

^{23}Na MAS-NMR spectra were obtained using a 500 MHz Bruker Avance III NMR spectrometer and 11.75 T cryomagnet, corresponding to a resonant frequency for ^{23}Na of 132.29 MHz. 4 mm rotors were used operating at approximately 10 kHz MAS frequency. A single pulse program was used with a 10 s pulse delay and 4 µs pulse length, with spectra referenced to solid NaCl at 7.2 ppm.

4.5.2.2 ^{27}Al NMR ($I = 5/2$)

^{27}Al MAS-NMR spectra were obtained using a 500 MHz Bruker Avance III NMR spectrometer and 11.75 T cryomagnet, corresponding to a resonant frequency for ^{27}Al of 130.31 MHz. 4 mm rotors were used operating at approximately 10 kHz MAS frequency. A single pulse program was used with a 1 s pulse delay and 0.5 µs pulse length, with spectra referenced to YAG at 0.7 ppm.

4.5.2.3 ^{31}P NMR ($I = 1/2$)

^{31}P MAS-NMR spectra were mainly obtained using a 500 MHz Bruker Avance III NMR spectrometer and 11.75 T cryomagnet, corresponding to a resonant frequency for ^{31}P of 202.45 MHz. 4 mm rotors were used operating at approximately 10 kHz MAS frequency. A single pulse program was used with a 60 s pulse delay and 2 µs pulse length, with spectra referenced to ammonium dihydrogen phosphate at 0.9 ppm.

^{31}P MAS-NMR spectra were also obtained using a 360 MHz Chemagnetics CMX 360 NMR spectrometer and 8.5 T cryomagnet, corresponding to a resonant frequency for ^{31}P of 145.77 MHz. 6.5 mm rotors were used operating at approximately 11 kHz MAS frequency. A single pulse program was used with a 30 s pulse delay and 2 µs pulse length, with spectra referenced to ammonium dihydrogen phosphate at 0.9 ppm.

4.5.2.4 ^{43}Ca NMR ($I = 7/2$)

^{43}Ca MAS-NMR spectra were obtained using an 850 MHz Bruker Avance III NMR spectrometer and 20 T cryomagnet, corresponding to a resonant frequency for ^{43}Ca of 57.2 MHz. 7 mm rotors were used operating at approximately 5 kHz MAS frequency. Signal enhancement was achieved using the rotor-assisted population-transfer (RAPT) sequence, where polarization associated with satellite transitions is transferred to the central transition [38]. Spectra were acquired using a 1.5 µs pulse length and a 5 s or 8 s pulse delay, with spectra referenced to 2M aq. $CaCl_2$ solution at 0 ppm.

^{43}Ca MAS-NMR spectra were also obtained using a 600 MHz Varian NMR spectrometer and 14.1 T cryomagnet, corresponding to a resonant frequency for ^{43}Ca of 40.4 MHz. 9.5 mm rotors were used operating at approximately 3.5 kHz MAS frequency. Spectra were acquired using a 6 µs pulse length and 5 s pulse delay, with spectra referenced to 2M aq. $CaCl_2$ solution at 0 ppm.

Additional ^{43}Ca MAS-NMR spectra were obtained by Zhehong Gan at the national high magnetic field laboratory (NHMFL), Tallahassee, using a 820 MHz Bruker Avance II+ NMR spectrometer and 19.3 T cryomagnet, corresponding to a resonant frequency for ^{43}Ca of 56.1 MHz. 7 mm rotors were used operating at approximately 5 kHz MAS frequency. Signal enhancement was achieved using RAPT. Spectra were acquired using a 3 μs pulse length and 8 s pulse delay, with spectra referenced to 2M aq. $CaCl_2$ solution at 0 ppm.

4.5.2.5 ^{71}Ga NMR ($I = 3/2$)

^{71}Ga MAS-NMR spectra were obtained by Zhehong Gan at NHMFL, using a 820 MHz Bruker Avance II+ NMR spectrometer and 19.3 T cryomagnet, corresponding to a resonant frequency for ^{71}Ga of 254.11 MHz. 1.8 mm rotors were used operating at approximately 27 kHz MAS frequency. Spectra were acquired using a 0.25 s pulse delay and 1 μs pulse length, with spectra referenced to $Ga(NO_4)$ solution at 0 ppm.

4.5.3 X-ray diffraction

Unless stated otherwise, all x-ray diffraction measurements were taken using a PANalytical X'Pert Pro MPD with focussed Cu$K\alpha_1$ radiation from a source at 45 kV–40 mA. A PANalytical PIXcel detector in Bragg-Brentano geometry was used with 255 channels covering an angular range of 3.347°. Runs were performed at room temperature over an angular range within the region 7–85° using a 0.02° step size.

Some measurements were alternatively taken on a Bruker D5005 diffractometer with a 12 mm footprint on the sample from a Cu K_α source at 40 kV–30 mA. Runs were performed at room temperature over an angular range within the region 10–80° using a 0.02° step size.

Once obtained, x-ray diffraction patterns were analysed using X'Pert HighScore Plus [39] and the ICDD PDF-4+ database [40] to determine the phases present. Rietveld refinement was also performed on some of the XRD data using Topas Academic [36], where the Thompson Cox Hastings (TCHZ) modified pseudo-Voigt peak type [41] and a simple axial model were used to describe the diffraction peaks.

4.5.4 Neutron diffraction

Neutron diffraction data were measured using the GEM diffractometer at the ISIS neutron source at the Rutherford Appleton Laboratory, UK. Samples were contained in either 5 mm or 8.3 mm diameter vanadium cans with 25 μm thick walls. Samples were measured until ~800 μA h of data had been acquired. Measurements of the empty diffractometer, empty vanadium cans and a vanadium rod were also taken to use in the processing of data.

Data were then processed using the GUDRUN program [42] in order to clean up, normalise and correct the data. Corrections need to be made based on the instrument parameters and incident beam along with subtracting the contributions to the measured cross section from the cans and spectrometer.

OpenGENIE [43] was then used to calculate the self scattering for the samples and obtain the distinct scattering. Banks were then merged and an approximation made to the low Q regions before being Fourier transformed to give total correlation functions.

Chapter 5

Ga substitution

5.1 Sample preparation and characterisation

Samples were prepared by Dr. Shirley Fong at AWE by grinding, under acetone, stoichiometric amounts of $CaH(PO_4)$, $CaCO_3$ and Ga_2O_3 according to the general formula $Ca_9Ga_x(PO_4)_{6+x}$ with samples of x=0, 0.2, 0.4, 0.6, 0.8 and 1.0 being produced. The resulting mixture was then heated at a rate of 10 °C/min up to 1050 °C and held for 4 h. This was then repeated a further two times to help ensure phase purity.

5.2 X-ray diffraction

X-ray diffraction patterns were collected for the entire composition range and are shown in Figure 5-1. The x-ray diffraction pattern taken of the 'pure' β-TCP sample appears to be consistent with the structure published by Yashima *et al.* [24], although there is some shift in the pattern observed. There is also a small amount of second phase present, thought to be hydroxyapatite ($Ca_5(PO_4)_3(OH)$). The x=1.0 sample also appears to have a small amount of additional phases present, identified as $GaPO_4$ and β-$Ca_2P_2O_7$. Upon addition of Ga^{3+} into the structure, a progressive shift of the diffraction peaks to increasing 2θ can be seen (Fig. 5-2), indicating a contraction of the unit cell. This contraction is consistent with Ga^{3+} having a much smaller 6-coordinated ionic radius (0.620 Å) than Ca (1.00 Å) [44] and can been seen in the reduction in all of the lattice parameters (Fig. 5-3), determined using Rietveld refinement. Another feature observable as substitution occurs is the gradual change in relative intensities of some of the diffraction peaks in the patterns as the occupancies of the sites within the structure vary.

Looking at lattice parameters determined for β-TCP in previous work, values of a/b=10.439 Å, c=37.375 Å [10], a/b=10.44 Å, c=37.38 Å [11] and a/b=10.4352 Å,

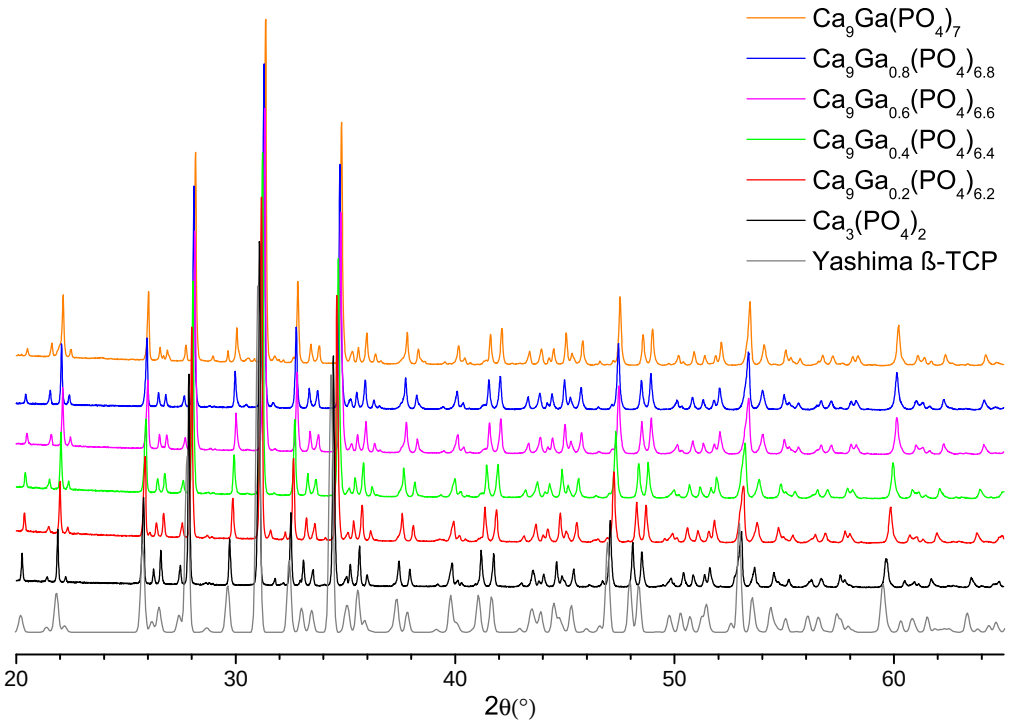

Figure 5-1 X-ray diffraction patterns of Ga substituted β-tricalcium phosphate along with pattern produced by Yashima *et al.* [24].

c=37.4029 Å [24] have been obtained. Comparing with this work, where the values obtained are a/b=10.41 Å and c=37.39 Å, the c lattice parameter falls within the range of given values, whereas the a lattice parameter is seen to be significantly smaller in this case. The reason for this is unknown but it may mean that the sample in this study is not phase pure, and instead contains a small amount of impurity substituted into the β-TCP phase. The lattice parameters obtained for the $Ca_9Ga(PO_4)_7$ sample can be compared with those obtained by Golubev *et al.* [15], where the c lattice parameter is consistent between the two studies and the a and b lattice parameters being slightly smaller in this case (10.321 Å here *cf.* 10.338 Å in [15]). A larger value could be explained by the additional phases present in the sample, therefore one explanation for the difference is that the sample produced by Golubev may also be Ga deficient or contain some impurity.

In order to describe the structures present in these materials more quantitatively, Rietveld refinement was performed on the diffraction patterns obtained. To begin with, the patterns were indexed to a β-TCP structure published by Yashima *et al.* [24] and initially just the lattice parameters and atomic positions refined. After refinement of

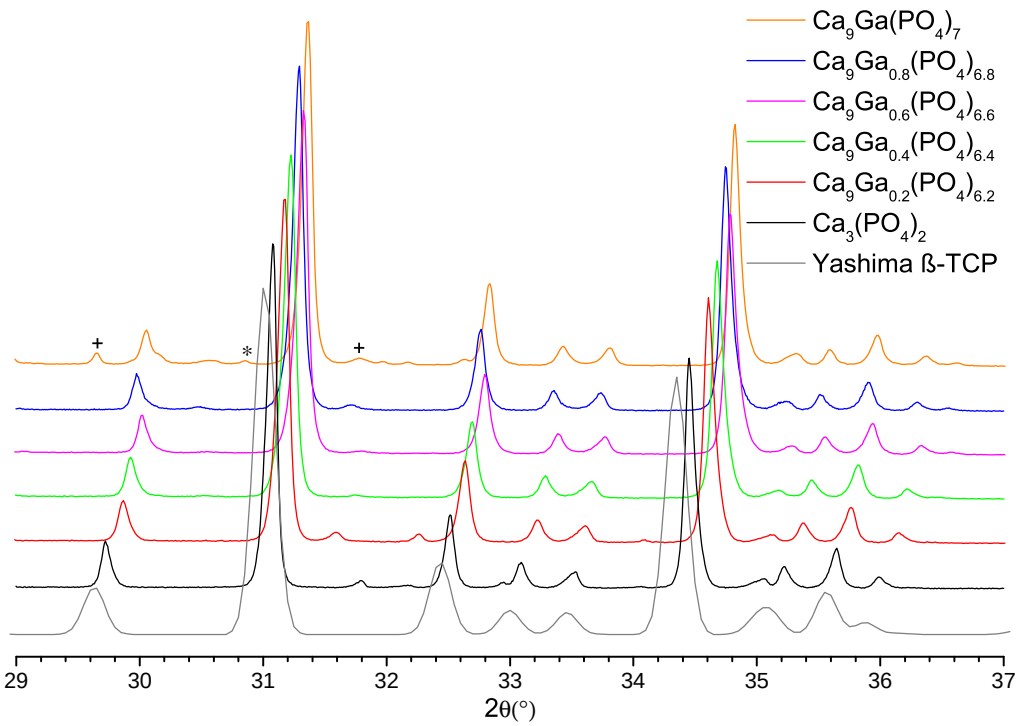

Figure 5-2 X-ray diffraction patterns of Ga substituted β-tricalcium phosphate indicating the region $29 - 37°$, where + represents β-$Ca_2P_2O_7$ and $*$ represents $GaPO_4$.

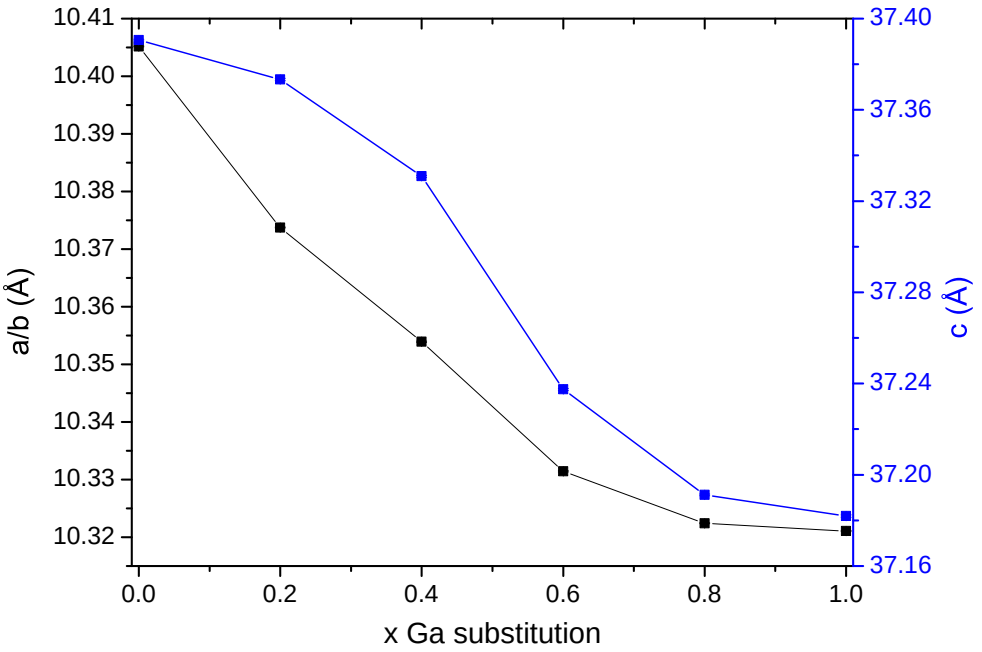

Figure 5-3 Lattice parameters of Ga substituted β-tricalcium phosphate as determined by Rietveld refinement. Error bars smaller than symbols used.

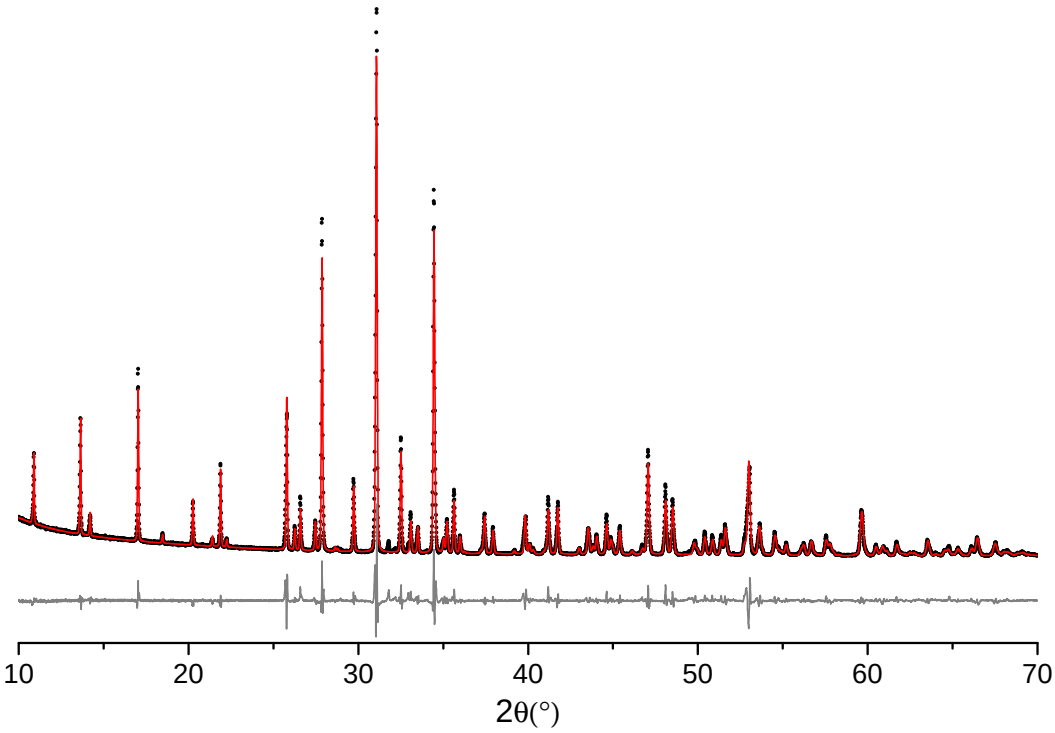

Figure 5-4 Powder x-ray diffraction pattern (·), Rietveld refinement (–), and difference plot (–) for $Ca_3(PO_4)_2$.

the atomic positions, occupancies of the Ca sites and isotropic thermal parameters were also refined.

For the 'pure' β-TCP sample, the occupancies of the five Ca sites were refined and resulted in occupancies close to 1 for all but the Ca(4) site which had an occupancy, slightly higher than predicted, of 0.52 ± 0.01. The fit of this sample can be seen in Figure 5-4, where it is apparent that some features of the pattern have not been well reproduced. This difference between fit and data mainly manifests itself as a mismatch in the asymmetry of some of the diffraction peaks, as illustrated in Figure 5-5, and indicates a possible problem in the peak shape parameters used. However, there is also a decrease in intensity of some of the fitted peaks compared with the data, possibly due to incorrect occupancies or thermal parameters, or even disorder within the system. Another explanation for the imperfect fit could be that the sample is not phase pure; given the prevalence of uptake of other ions into β-TCP, it would be easy to assume that any contaminants along the production route could be accommodated into the structure.

The same procedure was followed for the gallium substituted samples, but in this case Ga was allowed to freely refine on the Ca sites. For the Ca(1), Ca(2) and Ca(3)

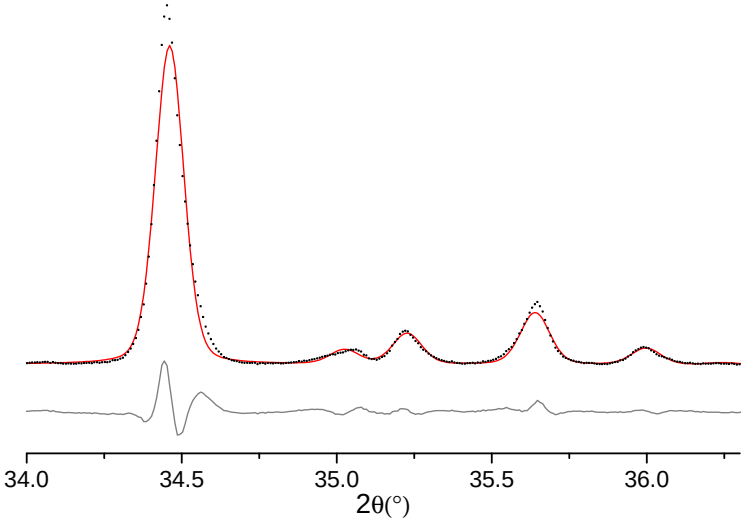

Figure 5-5 Powder x-ray diffraction pattern (·), Rietveld refinement (–), and difference plot (–) for $Ca_3(PO_4)_2$, illustrating peakshape problem encountered.

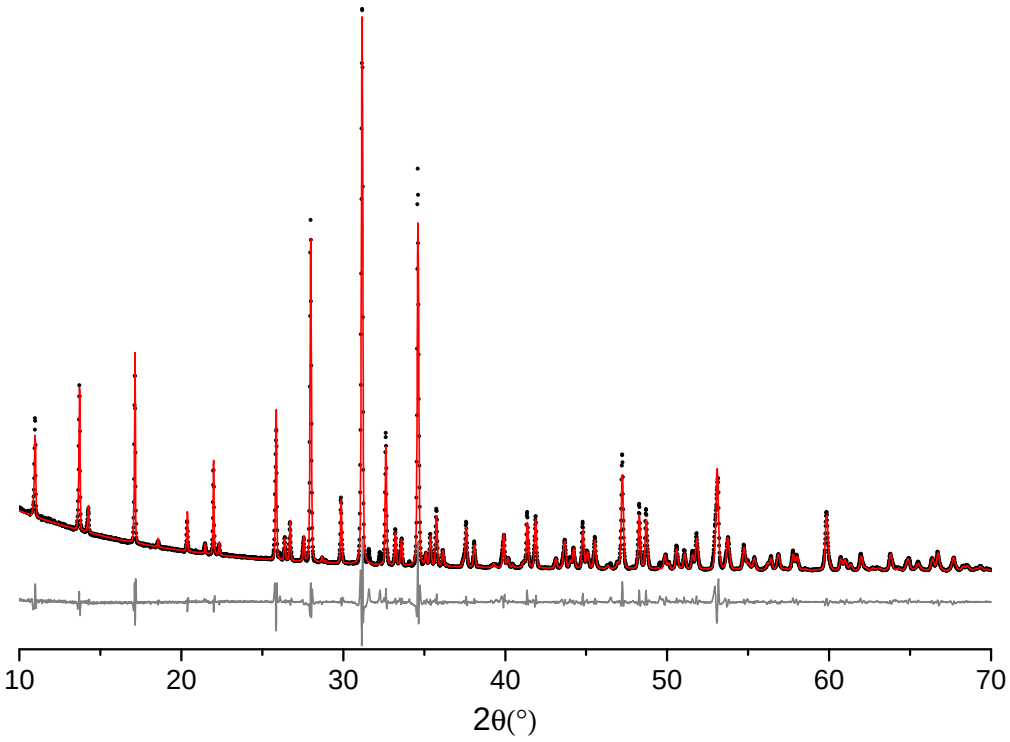

Figure 5-6 Powder x-ray diffraction pattern (·), Rietveld refinement (–), and difference plot (–) for $Ca_9Ga_{0.2}(PO_4)_{6.2}$.

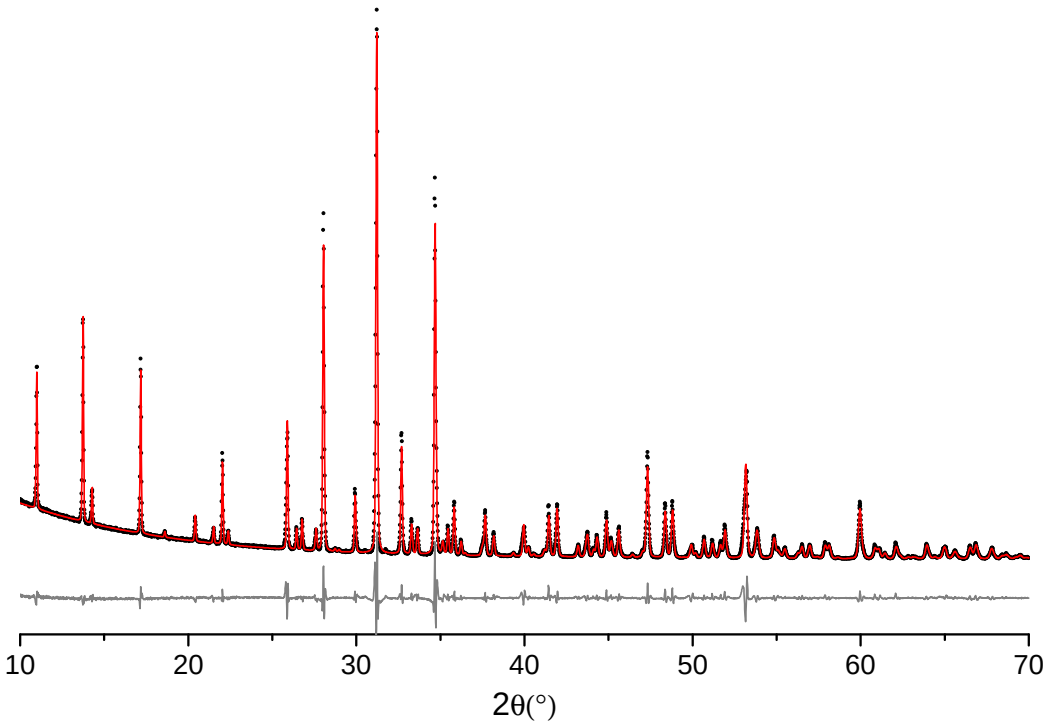

Figure 5-7 Powder x-ray diffraction pattern (·), Rietveld refinement (–), and difference plot (–) for $Ca_9Ga_{0.4}(PO_4)_{6.4}$.

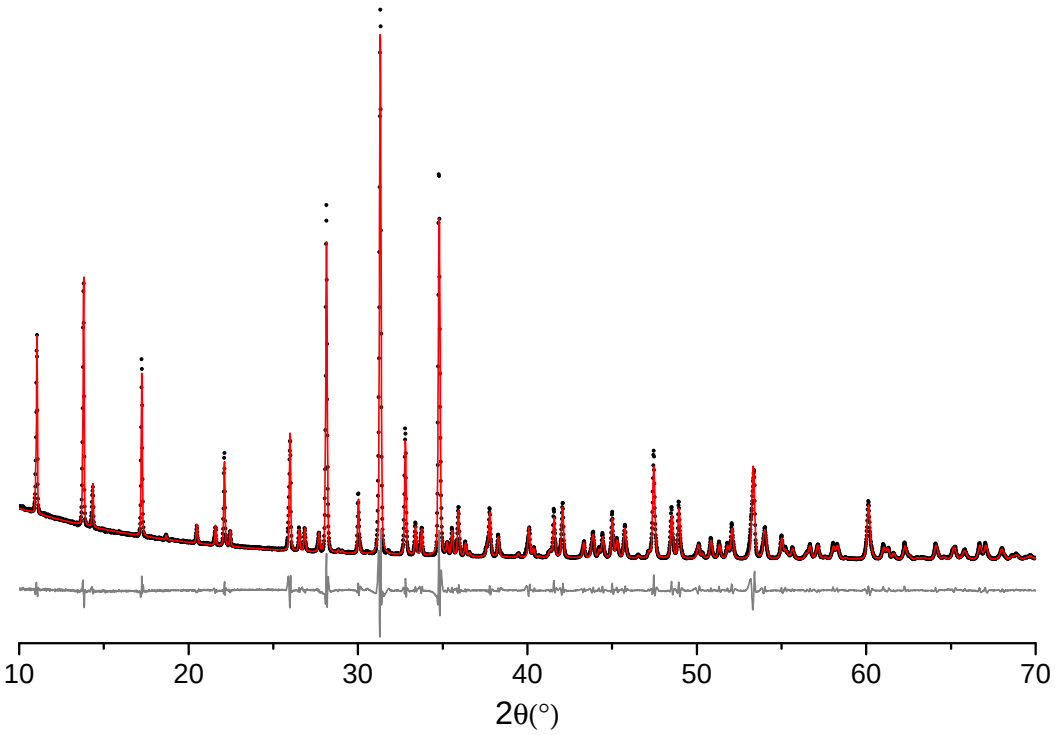

Figure 5-8 Powder x-ray diffraction pattern (·), Rietveld refinement (–), and difference plot (–) for $Ca_9Ga_{0.6}(PO_4)_{6.6}$.

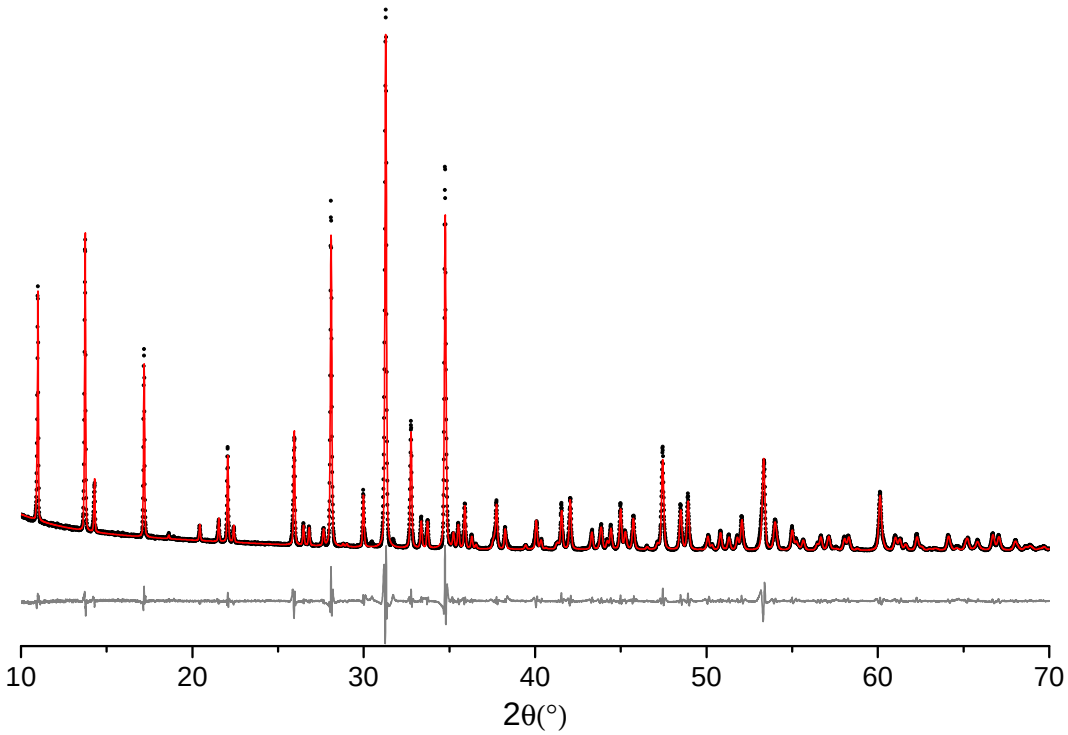

Figure 5-9 Powder x-ray diffraction pattern (·), Rietveld refinement (–), and difference plot (–) for $Ca_9Ga_{0.8}(PO_4)_{6.8}$.

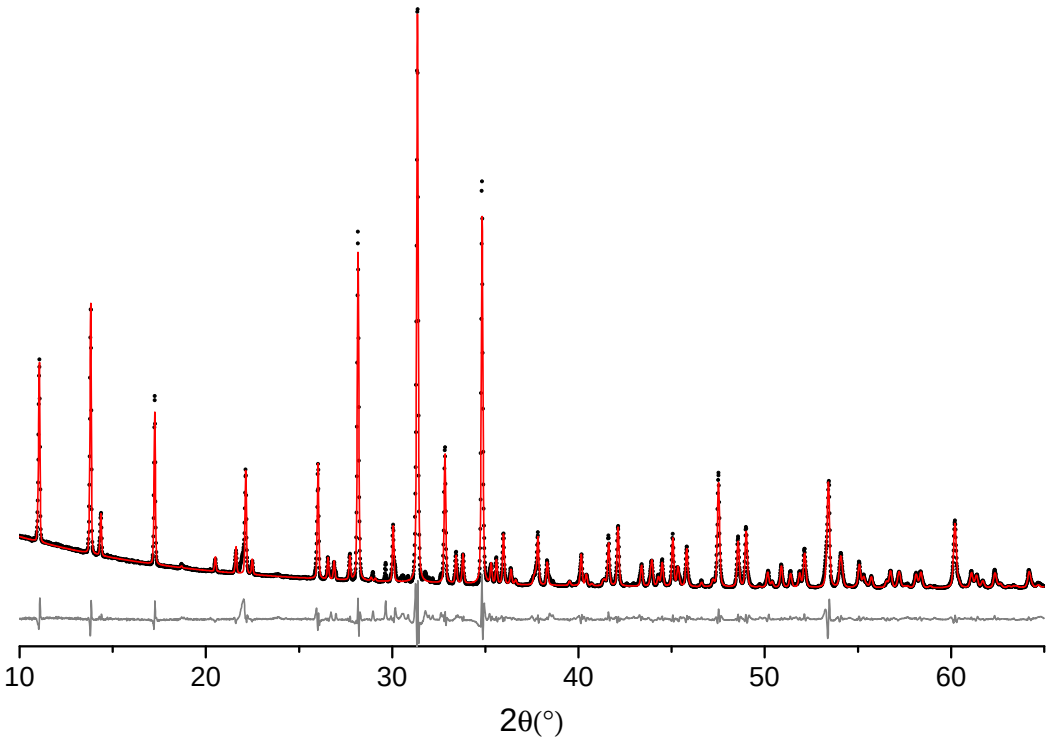

Figure 5-10 Powder x-ray diffraction pattern (·), Rietveld refinement (–), and difference plot (–) for $Ca_9Ga(PO_4)_7$.

Table 5-1 Occupancies of Ca(4) and Ca(5) sites as determined by Rietveld refinement of x-ray diffraction data.

	Expected		Observed				
				Ca(5)		Total	Total
x	Ca(4)	Ca(4) +Ca(5)	Ca(4)	Ca	Ga	Ca(5)	Ca(4)+Ca(5)
0	0.5	1.5	0.524(8)	1		1	1.524
0.2	0.4	1.4	0.484(8)	0.86(16)	0.16(11)	1.02	1.504
0.4	0.3	1.3	0.374(7)	0.75(14)	0.23(9)	0.98	1.354
0.6	0.2	1.2	0.281(7)	0.36(14)	0.54(9)	0.90	1.181
0.8	0.1	1.1	0.210(5)	0.07(9)	0.76(6)	0.83	1.04
1.0	0	1	0.226(9)	0.03(16)	0.80(10)	0.83	1.056

sites the Ga occupancy was 0 and the Ca occupancy was within a few percent of 1 and consistent with being fully occupied within errors. Because of this, the Ca occupancies of the Ca(1), Ca(2) and Ca(3) sites were then fixed at 1 to aid the refinement. For the Ca(4) site the Ga occupancy was again 0 but this time the Ca occupancy decreased from the initial half occupancy. For the Ca(5) site the Ga occupancy increased with x as the Ca occupancy decreased, although the total occupancy of the site did begin to deviate from 1 above x=0.4. Refinements are shown in Figures 5-6 to 5-10, with occupancies of the Ca(4) and Ca(5) sites shown in Table 5-1, where the occupancies on the Ca(5) site appear to have considerably larger errors. This may be due again to the lineshape problems or the considerations mentioned previously in the refinement of the 'pure' sample and means that the occupancies on the Ca(5) site can really only be used as a guide, with further information being needed to accurately determine the occupancies.

From the Ca(5) site occupancies it can be seen that, for the most part, the Ga occupancy is as expected within errors. The main exceptions are the x=0.4 and x=1.0 samples. The obvious cause for the Ga occupancy of the x=1.0 sample being too low is due to the $GaPO_4$ second phase shown to be present, although this may not fully account for the discrepancy. The errors on the values do, however, mean that it is impossible to infer the actual composition of this site. Errors on the Ca(4) site are of an acceptable level, however the values obtained are again not as expected. There is a trend of decreasing Ca occupancy with composition but it does not follow the expected values of $0.5 - x/2$. The reason for this could be due to the ways in which the different refined parameters affect the simulated pattern, with the extra occupancy of the Ca(4) site pos-

sibly being compensated for by another parameter, such as the Ca(5) site occupancies being different than expected. The deviation of the fits away from the data could also explain the unexpected values and the large errors associated with them. What could also be the case is that, as substitution takes place, Ca is removed from the Ca(5) site in addition to the Ca(4) site, leaving the Ca(4) site occupancies higher than expected and lowering the Ca(5) site occupancies.

5.3 Neutron diffraction

5.3.1 Time of flight neutron diffraction

Time of flight neutron diffraction data have been acquired on the GEM diffractometer for the 'pure' and x=0.8 samples. Rietveld refinement was performed on the data in order to extract more information about the structure. The diffraction pattern from bank 4 for the 'pure' sample was refined to the structure published by Yashima *et al.* [24], with a good fit being obtained after refinement of atomic positions and anisotropic displacement parameters (Fig. 5-11). However, occupancy of the Ca(4) site was found to be 0.62 ± 0.08, considerably higher than the expected value and that obtained using x-ray diffraction. There is some discrepancy between the fit and data at longer TOF, corresponding to larger d-spacings in the structure. The cause of this may be that there is some variation in the long range structure, such as disorder of the Ca(4) site vacancies, which cannot be easily modelled using Rietveld refinement.

For the Ga substituted sample, bank 4 was again used for refinement but in this case the starting point was the structure produced earlier from the Rietveld refinement of the x-ray diffraction data. A reasonable fit was produced from this structure, with the addition of anisotropic displacement parameters further improving it. Atomic positions and Ca(4) and Ca(5) site occupancies were then allowed to refine independently to produce the fit seen in Figure 5-11. The simulated pattern can again be seen to fit well at short TOF but deviates at longer times as in the undoped case. There were some problems in the refinement of the occupancies, where the Ca(4) site occupancy refined to 0.99 ± 0.40, much higher than allowed and far from the expected value of 0.1. The Ca and Ga occupancies of the Ca(5) site refined to the more reasonable 0.11 and 0.78 respectively, closer to the expected values of 0.2 and 0.8. However, in this case, the

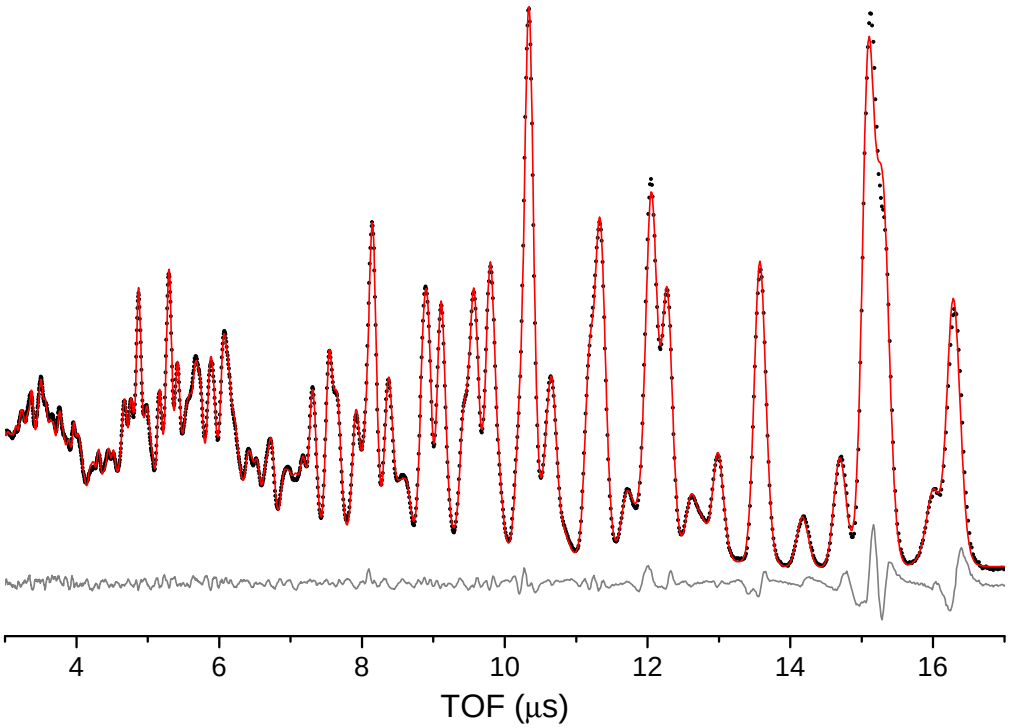

Figure 5-11 Powder neutron diffraction pattern (·), Rietveld refinement (–), and difference plot (–) for $Ca_3(PO_4)_2$ at room temperature taken from bank 4 of GEM diffractometer.

errors were of the order of 10^6, suggesting a problem with the software or possibly that too much information is trying to be extracted from the diffraction pattern.

5.3.2 Total correlation functions

Total correlation functions obtained for the undoped and x=0.8 samples are shown in Figure 5-13. Peaks in the $T(r)$ plots can be related to their corresponding atom-atom correlations via the bond valence parameter calculations performed by Brese and O'Keeffe [14]. In both plots the peak at ~1.54 Å corresponds to the P–O bonds in the P tetrahedra. The peak appears narrow and symmetrical, indicating a symmetric and well ordered environment. The large peak between 2.2 and 2.8 Å covers the majority of the Ca–O bond lengths along with many of the O–O correlations. This range corresponds to 6, 7 and 8-coordinated Ca with calculated bond valence parameters of 2.373, 2.431 and 2.480 Å respectively. Due to the number and nature of the Ca sites it is difficult to infer any more information about the sites. The peak visible around 3.1 Å comes mainly from the 3 longer Ca–O bonds on the Ca(4) site of 3.12 Å. The additional peak in the

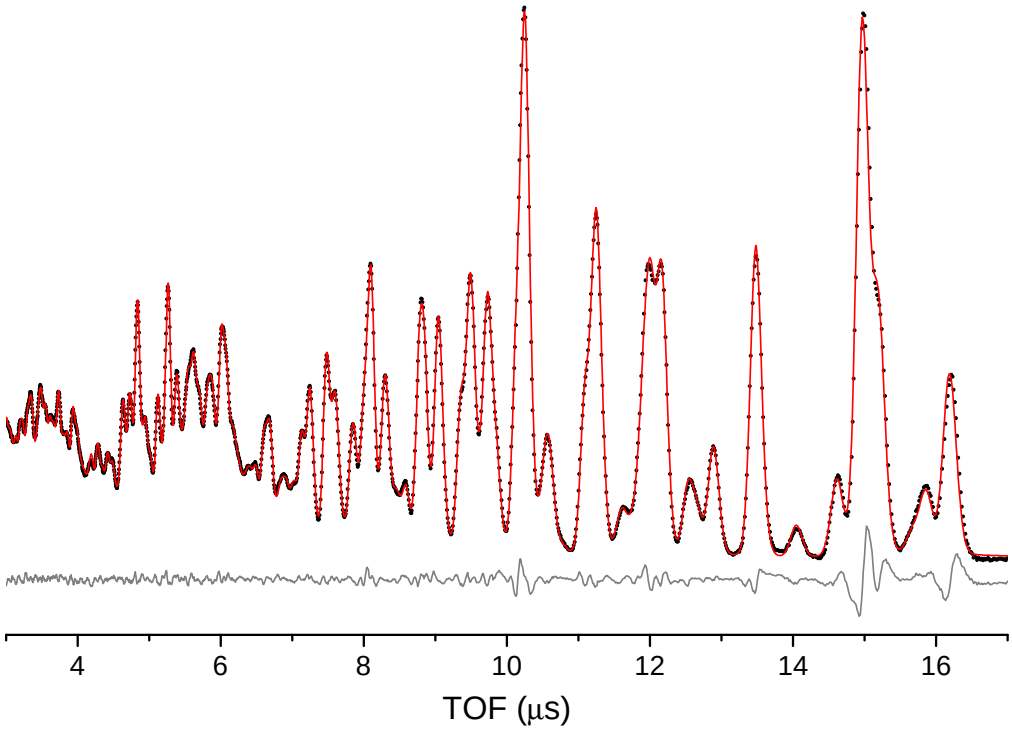

Figure 5-12 Powder neutron diffraction pattern (·), Rietveld refinement (–), and difference plot (–) for $Ca_9Ga_{0.8}(PO_4)_{6.8}$ at room temperature taken from bank 4 of GEM diffractometer.

plot for the Ga doped sample is due to Ga–O bonds and appears at ~1.99 Å, close to the calculated value of 1.986 Å for 6-coordinated Ga and consistent with Ga substituting onto the Ca(4) or Ca(5) sites.

5.4 Nuclear magnetic resonance

5.4.1 ^{71}Ga nuclear magnetic resonance

^{71}Ga NMR was undertaken on the $Ca_9Ga_{0.8}(PO_4)_{6.8}$ sample by Zhehong Gan on the 820 MHz spectrometer at NHMFL, Tallahassee. The spectrum obtained shows what appears to be one slightly asymmetric resonance centred around −50 ppm (Fig. 5-14). This shift is consistent with 6-coordinated Ga, seen to fall in the chemical shift range −80 to −42 ppm [25, p. 654]. This indicates that Ga is most probably substituting onto the smaller Ca(4) or Ca(5) sites, however, as they are both 6-coordinated sites it is impossible to deduce which one. Relatively poor signal to noise ratio means that any

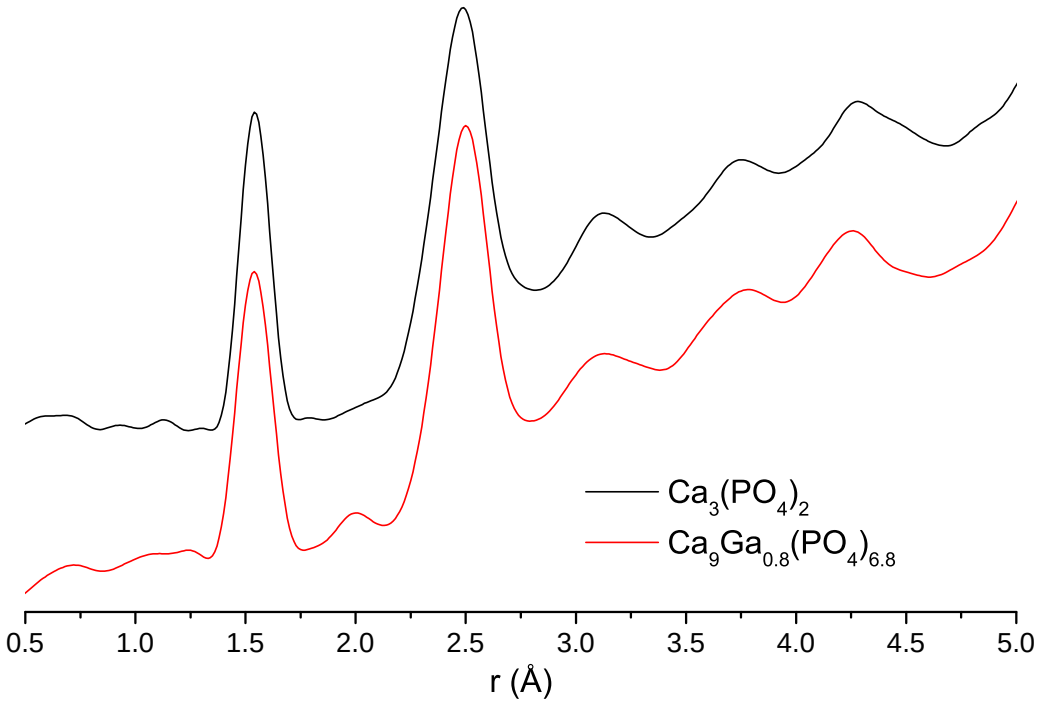

Figure 5-13 $T(r)$ for $Ca_3(PO_4)_2$ and $Ca_9Ga_{0.8}(PO_4)_{6.8}$ samples.

other features, such as any broader components to the spectrum or small amounts of second phase, cannot be identified, if present.

5.4.2 ^{31}P nuclear magnetic resonance

^{31}P MAS NMR was undertaken on the 500 MHz spectrometer for the entire range of samples, with spectra shown in Figure 5-15. The addition of Ga^{3+} causes dramatic changes in the observed spectra showing most noticeably what appears to be a transferral of intensity from the peaks around 5 ppm to a new set of resonances at approximately −2 ppm. This change is most likely due to the next-nearest neighbours of the P atoms changing from Ca on the Ca sites to either Ga or a vacancy. A progressive shift upfield is also noticeable, indicating increased electronic shielding of the nuclei, possibly due to the reduction in unit cell volume. Another point of note is that the 'pure' β-TCP sample varies distinctly from that published by Jakeman *et al.* [18], with the spectrum in this work containing much broader features and a slightly different overall lineshape.

In the sample with the highest gallium content, $Ca_9Ga(PO_4)_7$, another set of resonances can be seen between −7 and −11 ppm. This sample was run on the 360 MHz

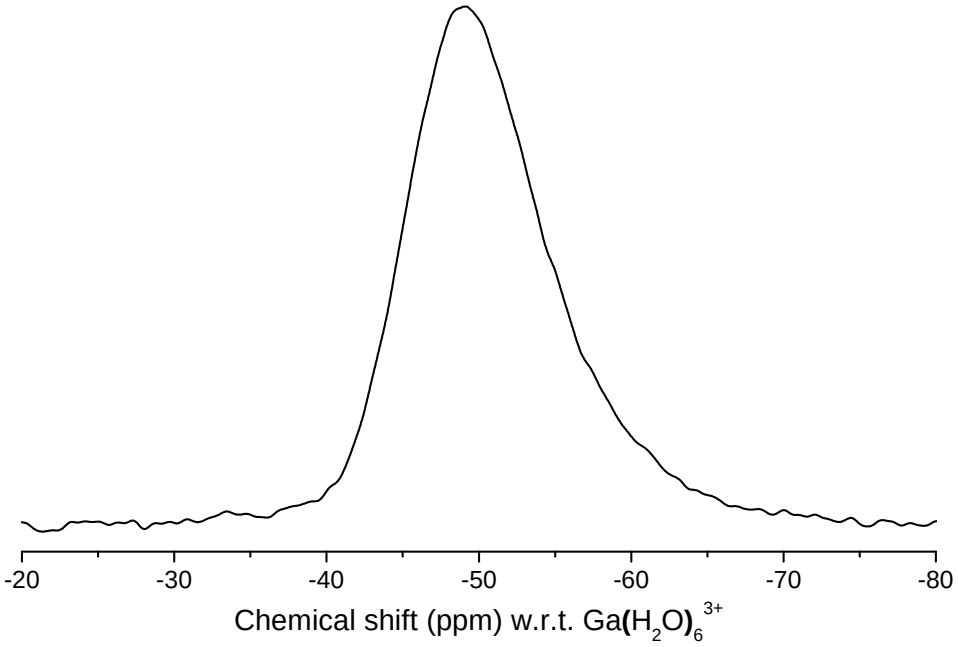

Figure 5-14 ^{71}Ga NMR spectrum of $Ca_9Ga_{0.8}(PO_4)_{6.8}$ sample.

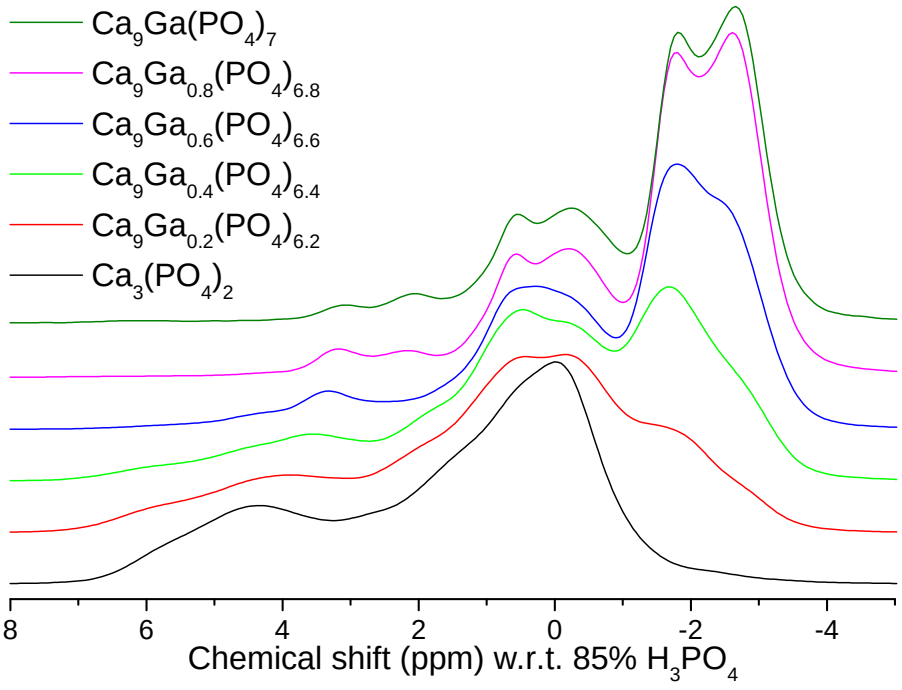

Figure 5-15 ^{31}P NMR spectra of Ga substituted β-tricalcium phosphate normalised to spectrum area.

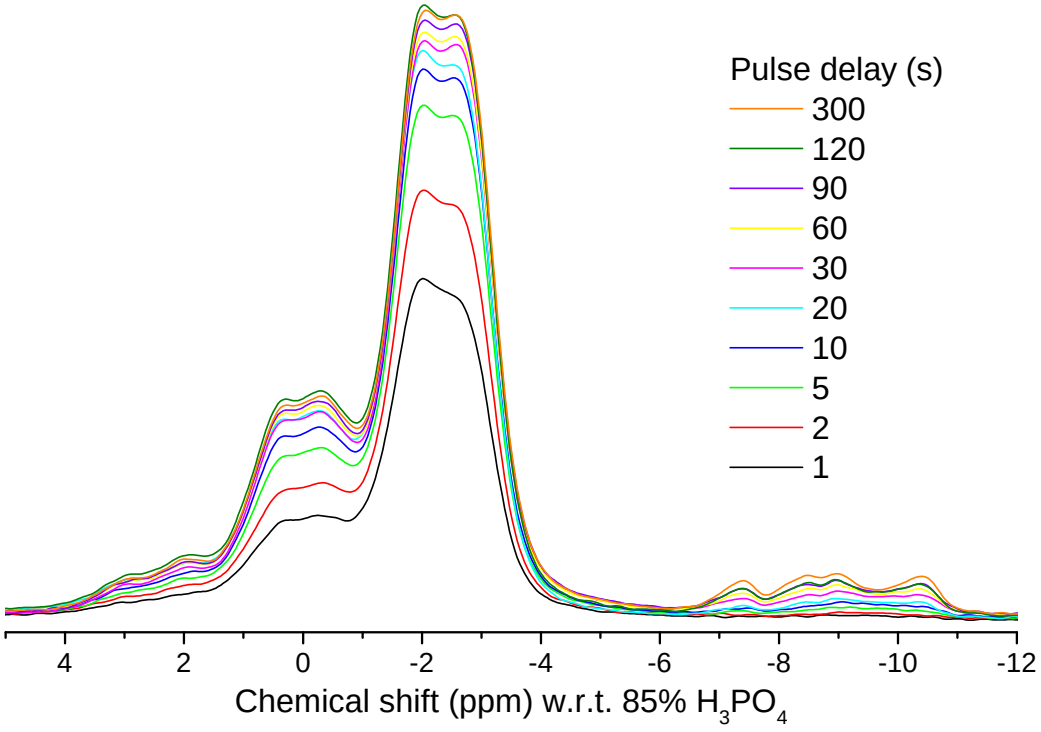

Figure 5-16 ^{31}P NMR spectra of $Ca_9Ga(PO_4)_7$ with pulse delays ranging from 1–300 s.

spectrometer with a range of pulse delays, the results of which can be seen in Figure 5-16. The intensity of this second resonance increases at a slower rate than the β-TCP resonance, indicating a secondary phase is present. Whereas for β-TCP the intensity plateaus by a pulse delay of 120 s, the intensity of the second phase appears to increase even beyond a pulse delay of 300 s. This difference is due to an increased T_1 relaxation time of the secondary phase(s) present in this sample. These resonances represent ~6 % of the total intensity and they can be fitted successfully with an ~3:1 molar ratio of β-$Ca_2P_2O_7$:$GaPO_4$ which leads to a composition for the Ga-doped TCP phase of approximately x=0.93, suggesting that the maximum gallium loading may lie somewhere around this point. This also suggests that the main phase is likely to be CaO rich (unless there are additional non-phosphate phases present).

If the Ga^{3+} ions are substituted onto the Ca(5) sites, as size considerations suggest, then this should lead to 3 new resonances appearing due to the division in occupancy of the Ca(5) site between the Ca^{2+} and Ga^{3+} ions. This is consistent with the idea that the Ga^{3+} ions are substituted into the Ca(5) sites causing a splitting of the resonances due to the different occupancies of the Ca(5) sites, along with the splitting already present

from the partial occupancy of the Ca(4) sites, as described in Section 3.4.2.

Spectra were fitted to a maximum of 8 peaks with mixed Gaussian/Lorentzian lineshapes being used. As the x=0.8 spectrum appears the most well defined over the entire lineshape, this spectrum was used as a basis for fitting. The spectrum was initially fit manually to 8 peaks before letting the software refine the position, intensity, width and Gaussian/Lorentzian ratio further. Spectra of consecutive samples were fit based on parameters of the previous sample, with fits being done down to x=0 then back up to x=0.8 and x=1 for consistency. Peak areas were then calculated and plotted against composition in order to determine which environment each peak belongs to by comparing them with the model produced earlier (Fig. 3-5). Upon assignment of the peaks the fits of the spectra were then modified slightly in an attempt to bring the peak areas closer to the expected values without compromising the fits too much. The resulting modified fits were allowed to refine once more with the final fits shown in Figure 5-17.

The fractional intensities of the fitted peaks are plotted against x in Figure 5-18 where they are compared with the functions predicted by the model. For the x=1.0 sample the recalculated value of 0.93 is used to account for the additional phases present. Good agreement to the model is obtained, supporting the idea that Ga is substituting onto the Ca(5) site with more vacancies appearing on the Ca(4) site. There is some deviation in places but the complexity of the lineshape makes it impossible to obtain an unambiguous fit. Peak positions are plotted in Figure 5-19, showing a roughly linear shift upfield of each of the fitted peaks, further supporting the validity of the fits.

There were, however, some problems in the fitting of the spectrum of 'pure' β-TCP (Fig. 5-17), which requires 7 resonances rather than the 5 predicted. The additional resonances account for ~3 % of the total intensity of the spectrum, suggesting that the 'pure' sample may in fact contain some impurity. Assignment of the peaks to the P environments also differs from those suggested by Jakeman *et al.* [18], although they are consistent with the fitting of the Ga substituted spectra. Upon inspection, it appears impossible to fit the spectrum produced in this work to the simulated fit of Jakeman (Fig. 5-20), with the 43 % P(3) resonance needing to take up the entire right hand shoulder of the spectrum in this work. What appears likely is that there is also some impurity in the sample produced by Jakeman, although greater than the 3 % observed in this work. This could also explain the differing widths between the β-TCP spectra,

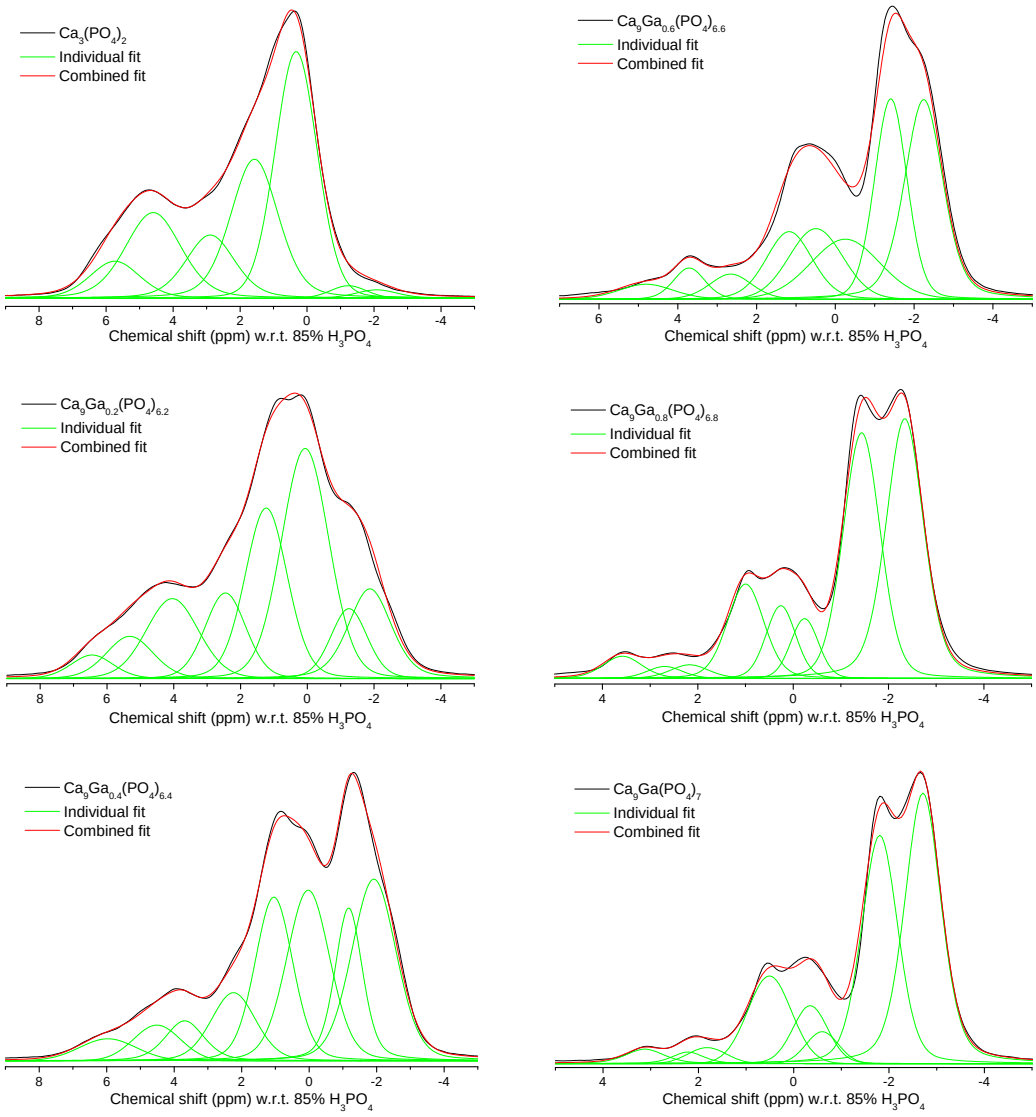

Figure 5-17 Fits of ^{31}P NMR spectra of Ga substituted β-tricalcium phosphate.

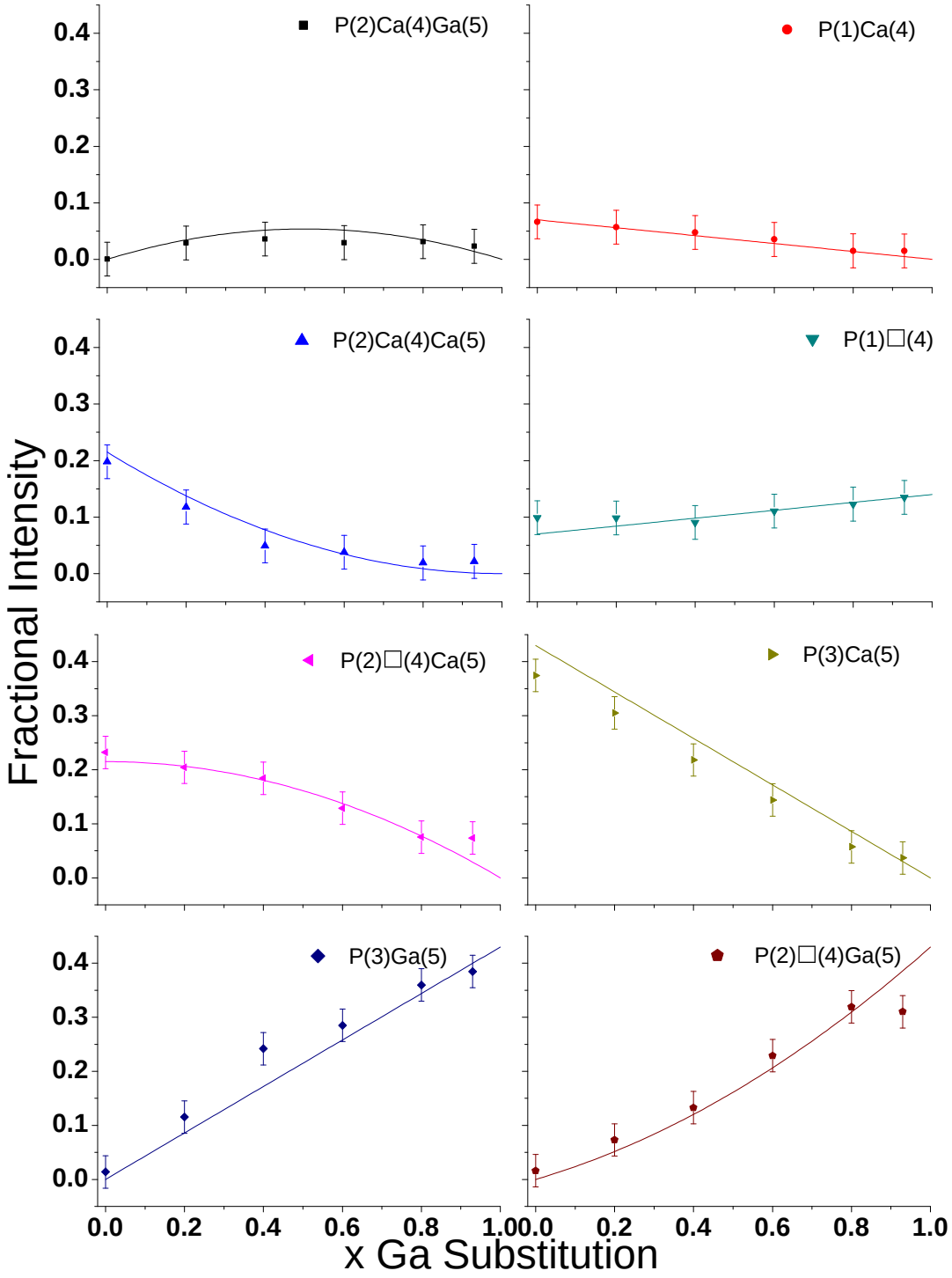

Figure 5-18 Integrated intensities of fitted peaks (solid symbols) against composition along with proposed substitution model (lines) for gallium system.

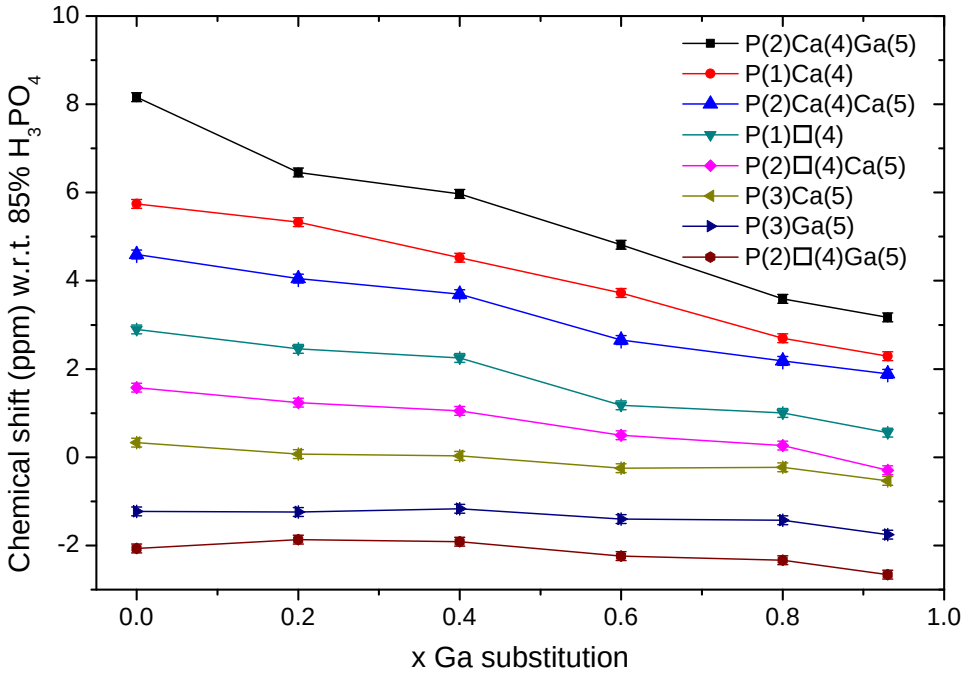

Figure 5-19 Peak positions of fitted peaks for Ga substituted β-tricalcium phosphate.

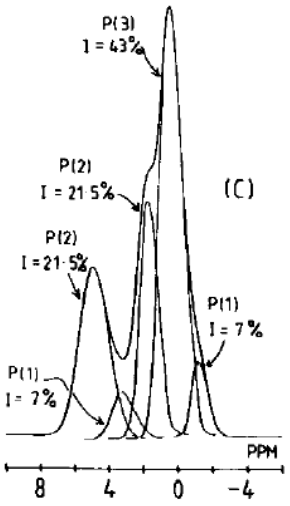

Figure 5-20 Fit of β-tricalcium phosphate predicted by Jakeman *et al.* [18].

as substitution into β-TCP does appear to greatly affect the widths of ^{31}P spectra.

5.4.3 ^{43}Ca nuclear magnetic resonance

Natural abundance ^{43}Ca MAS NMR was undertaken on the 'pure' β-TCP sample on the 850 MHz spectrometer at Warwick and on the $Ca_9Ga_{0.4}(PO_4)_{6.4}$ sample by Zhe-

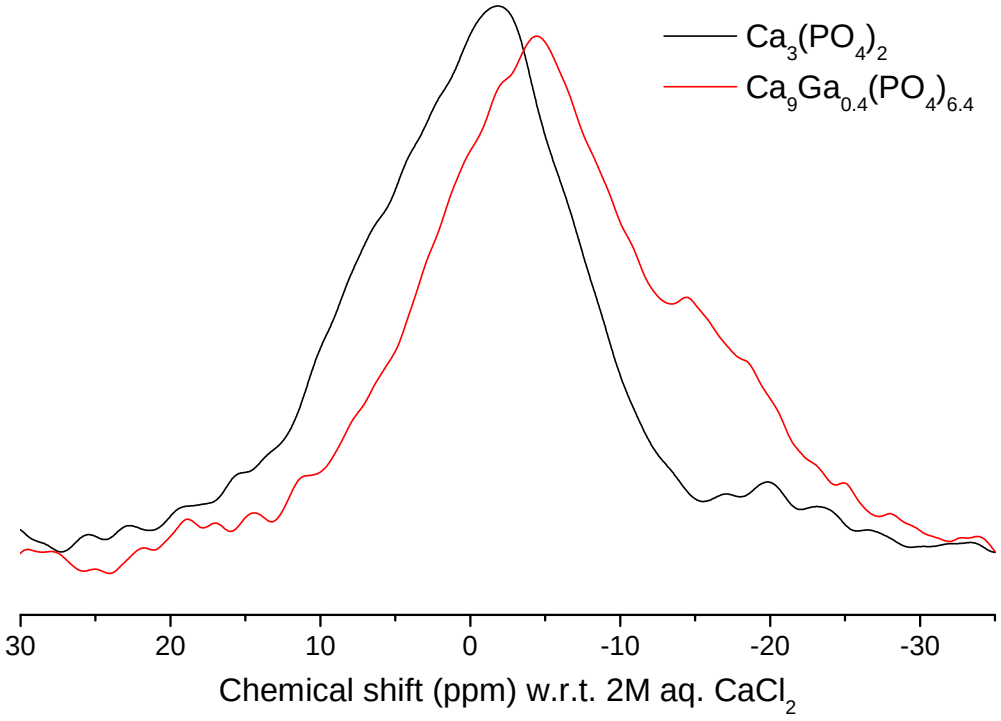

Figure 5-21 ^{43}Ca NMR spectra of $Ca_3(PO_4)_2$ and $Ca_9Ga_{0.4}(PO_4)_{6.4}$ samples, normalised to peak area.

hong Gan on the 820 MHz spectrometer at NHMFL. Spectra are shown in Figure 5-21, where a noticeable difference can be seen between the resultant lineshapes. The Ga substituted sample appears broader, more than could be explained by the differing fields, and suggests that either more variation between the different sites is present or there is additional disorder in the system in general.

Due to the poor signal obtained and broadness of the lineshapes, spectra were fitted to a series of Gaussian lineshapes in order to reduce the number of variables involved. An attempt was made to fit the 'pure' β-TCP sample to five peaks, with their order dependent on the average Ca-O bond length of the sites (Sec. 3.4.1) [23], and their relative intensities as predicted earlier (Tab. 3-3). After manually fitting the spectrum, the software was allowed to refine the peaks in order to ensure the local maximum in the fitted intensity had been reached. The fit is shown in Figure 5-22 with details of the fit in Table 5-2. A reasonable fit has been obtained, even with the poor signal, and is consistent with the predicted appearance.

The $Ca_9Ga_{0.4}(PO_4)_{6.4}$ sample was then fitted starting with the parameters from the 'pure' sample. Peaks were then manually adjusted to obtain a better fit before letting the

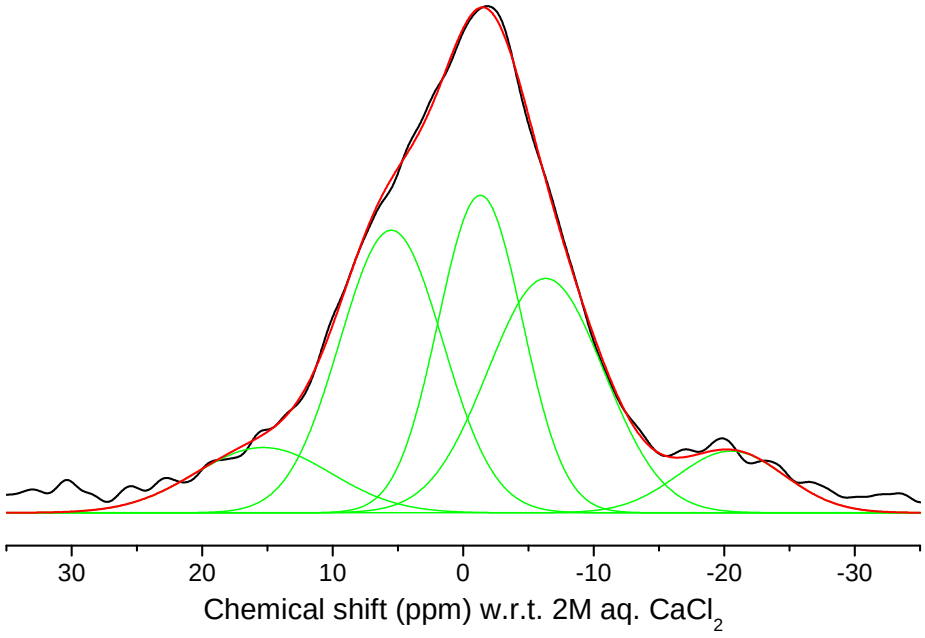

Figure 5-22 Fit of ^{43}Ca NMR spectrum of $Ca_3(PO_4)_2$ sample.

Table 5-2 Fit parameters of ^{43}Ca NMR on $Ca_3(PO_4)_2$ sample.

Site	Peak position ppm ±1	Peak width Hz ±50	Occupancy % ± 3	
			Predicted	Observed
5	15.4	700	9.5	9.0
1	5.5	530	28.6	29.6
2	−1.3	430	28.6	27.1
3	−6.3	600	28.6	27.6
4	−20.5	550	4.7	6.7

software automatically refine the resultant lineshape to further improve the fit (Fig. 5-23). Details of the fit are shown in table 5-3 where the extra column shows normalised occupancies modified to account for the proportion of Ca left in the system in an attempt to compare more easily to the undoped case. Occupancies of the Ca(1), Ca(2) and Ca(3) sites appear unchanged, with the occupancies of the other two sites suggesting the Ga is substituting onto the Ca(5) sites as predicted. Actual values for occupancies of the Ca(4) and Ca(5) sites would be 2.8 % and 5.7 % respectively for Ga substituting onto the Ca(5) site and more vacancies being present on the Ca(4) site, meaning the values obtained are consistent within errors.

Comparing the two spectra more closely there is a noticeable move to a more neg-

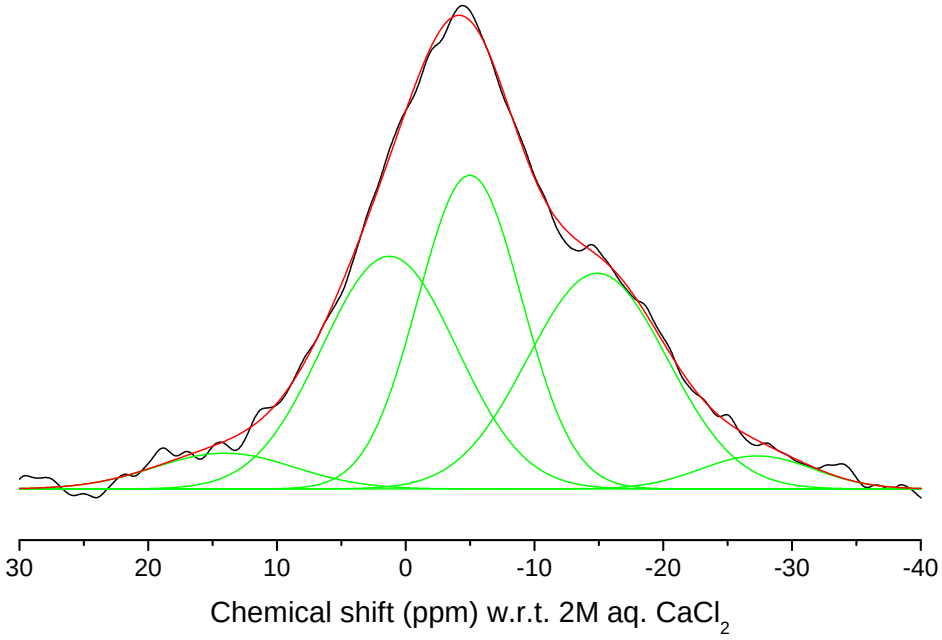

Figure 5-23 Fit of ^{43}Ca NMR spectrum of $Ca_9Ga_{0.4}(PO_4)_{6.4}$ sample.

Table 5-3 Fit parameters of ^{43}Ca NMR on $Ca_9Ga_{0.4}(PO_4)_{6.4}$ sample.

Site	Peak position ppm ±1	Peak width Hz ±50	Occupancy % ± 3		
			Undoped	Observed	Normalised
5	14.1	730	9.5	5	4
1	1.3	710	28.6	30	28
2	−4.9	540	28.6	32	29
3	−14.9	730	28.6	29	27
4	−27.3	590	4.7	4	3

ative chemical shift in the Ga substituted sample. The widths of the fitted peaks in the spectrum for the Ga substituted sample are also much broader than the undoped spectrum, suggesting a larger electric field gradient or possibly some disorder within the system.

5.5 Summary

Ga appears to readily substitute into β-tricalcium phosphate, with x-ray diffraction patterns of samples produced maintaining the β-TCP structure postulated by Yashima *et al.* [24]. Rietveld refinement of x-ray and neutron diffraction patterns suggest that Ga is

substituting onto the Ca(5) site with the Ca(4) site occupancy decreasing. Large errors on these values and their deviation from the values predicted mean that more information is needed to adequately describe the substitution process. Total correlation functions of the x=0 and x=0.8 samples reinforce this idea, with the Ga substituted sample showing 6-coordinated Ga present, meaning substitution is taking place on the Ca(4) or Ca(5) site. ^{71}Ga NMR gives a resonance corresponding again to 6-coordinated Ga, however it is impossible to determine whether it is on the Ca(4) or Ca(5) site in this case. ^{31}P NMR gives a series of spectra which can be fitted to the model of substitution predicted, showing substitution onto the Ca(5) site. Although broad and noisy, the ^{43}Ca NMR gives a lineshape consistent with substitution onto the Ca(5) site, however the poor signal to noise ratios mean a definitive answer cannot be obtained.

Chapter 6

Al substitution

6.1 Sample preparation and characterisation

Samples were prepared by final year undergraduate project students Richard Beckett and Laura Good under the supervision of the author, by grinding together stoichiometric amounts of $CaH(PO_4)$, $CaCO_3$ and Al_2O_3 according to the general formula $Ca_9Al_x(PO_4)_{6+x}$ with samples of x=0.2, 0.4, 0.6, 0.8 and 1.0 being produced. The resulting mixture was then heated at a rate of 10 °C/min up to 1050 °C and held for 4 h. This was then repeated further times to help ensure phase purity.

6.2 X-ray diffraction

X-ray diffraction patterns of the final firings of the range of samples were obtained as shown in Figure 6-1. A shift of the diffraction peaks to lower angles is observed initially, before a progressive shift to increasing 2θ at higher Al content. This shift to lower angles is not expected since the Al ions have a much smaller 6-coordinated ionic radius (0.535 Å) compared to Ca (1.00 Å) [44]. This suggests that the Al ions are somehow distorting the Ca sites rather than being simply accommodated into the structure and replacing the Ca ions. The shift can be better seen in the enlarged section in Figure 6-2, where a slight broadening of the diffraction peaks can also be observed, with calculated full width at half maximum of the main diffraction peaks shown in Figure 6-3. From Figure 6-2, a small impurity phase is noticeable in the x=0.2 sample. This was identified as hydroxyapatite ($Ca_5(PO_4)_3(OH)$), with the x=1.0 sample containing some $AlPO_4$, visible at ~21.5° in Figure 6-1.

To investigate the broadening further, x-ray diffraction patterns of two different firings of the x=0.6 and x=0.8 samples were obtained as shown in Figure 6-4. From this, a dramatic change in the widths of the diffraction peaks can be observed between fir-

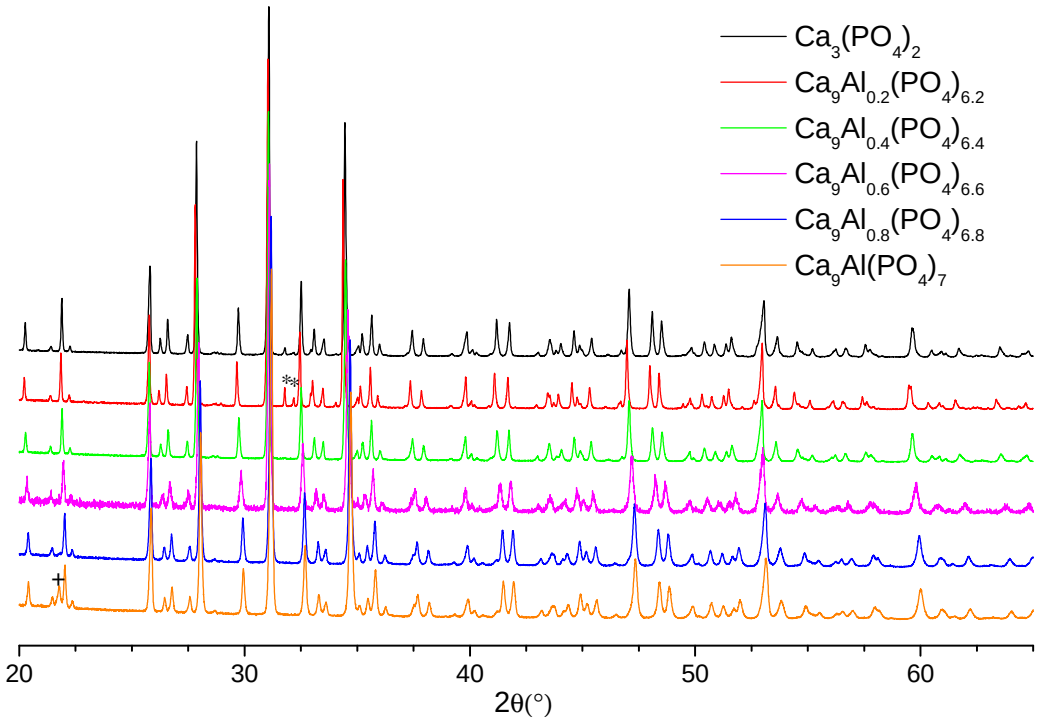

Figure 6-1 X-ray diffraction patterns of Al substituted β-tricalcium phosphate, where + represents $AlPO_4$ and $*$ represents hydroxyapatite.

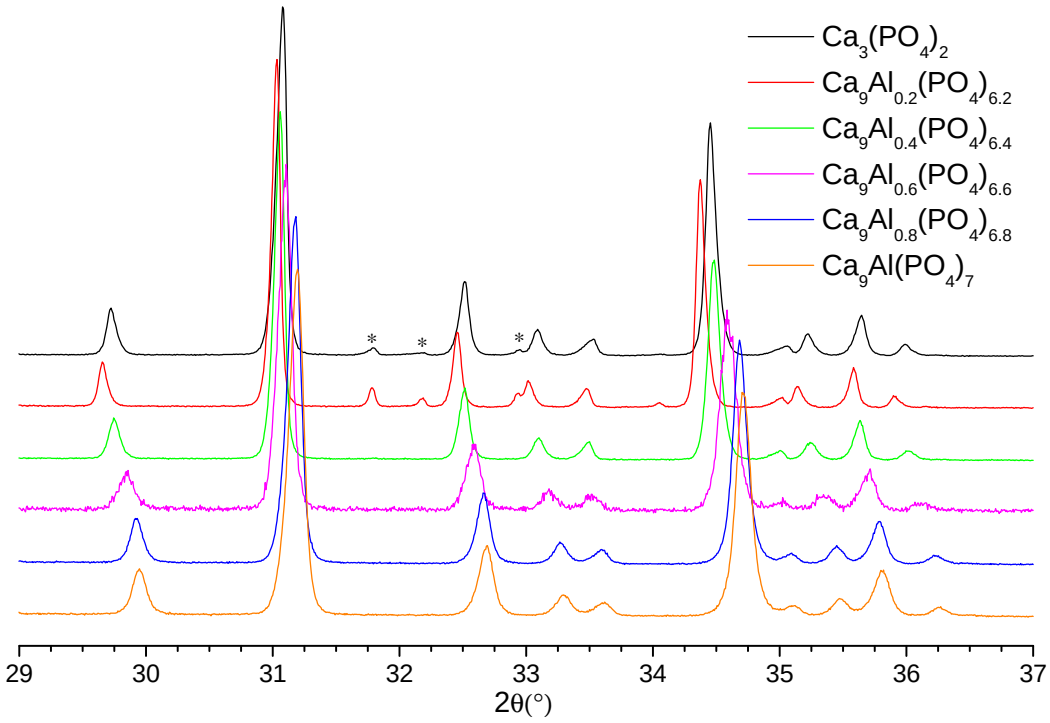

Figure 6-2 X-ray diffraction patterns of Al substituted β-tricalcium phosphate indicating the region 29 – 37°, where $*$ represents hydroxyapatite.

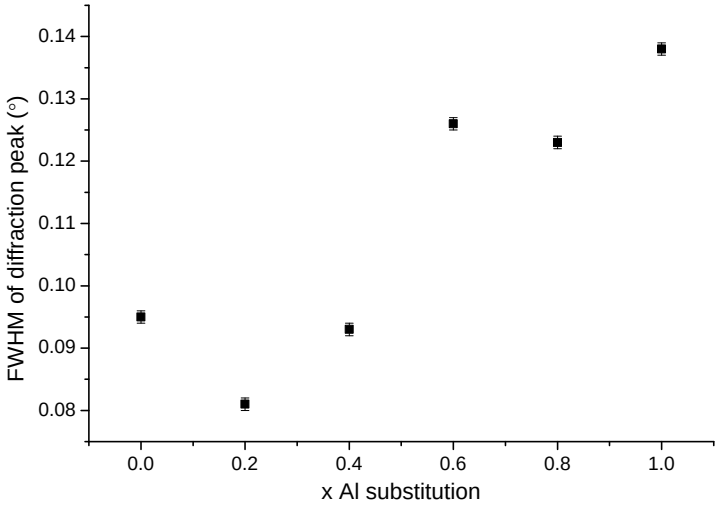

Figure 6-3 Full width at half maximum of main diffraction peak from Al substituted β-tricalcium phosphate.

ings, along with a change in the intensities of some of the diffraction peaks. However, the peak positions remain constant, implying that the underlying structure is consistent in each case. This suggests that either there is some disorder present within the structure, possibly also explaining the unexpected shift in diffraction peaks, or that what is actually being observed is a mixture of multiple closely related phases.

If what is observed were a result of multiple phases then the areas of the diffraction peaks should be the same for each firing. This does not appear to be the case and so there must some amount of disorder present. The difference in the peak widths does however appear to increase at higher angles, which could indicate some other related phases are also present, as with peak splitting (i.e. from different lattice parameters) the difference in angle between corresponding peaks would increase at higher angles, resulting in what would appear to be wider peaks.

Lattice parameters were obtained by Rietveld refinement of the x-ray diffraction data and are shown in Figure 6-5. An initial increase in all axes can be seen here, before the a/b lattice parameters decrease linearly with composition. Things are very different along the c-axis, with the c lattice parameter following a linear increase until approximately x=0.5 before decreasing linearly afterwards. This increase may again be due to some disorder within the system and, if this is the case, suggests that there is some mechanism increasing the disorder until around x=0.5, where the system then starts to become more ordered and the unit cell contracts as expected. Comparing the

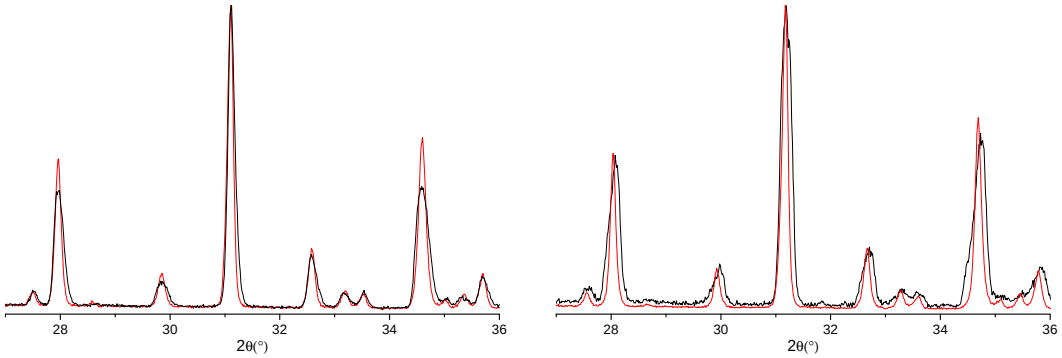

Figure 6-4 X-ray diffraction patterns of $Ca_9Al_{0.6}(PO_4)_{6.6}$ (left) and $Ca_9Al_{0.8}(PO_4)_{6.8}$ (right), showing initial (–) and refired (–) samples.

lattice parameters to work done on $Ca_9Al(PO_4)_7$ by Golubev *et al.* [15], the *a* lattice parameter of 10.335 Å is reasonably close to the published value of 10.319 Å, especially considering the $AlPO_4$ second phase present. However, the *c* parameter here is 37.36 Å, much greater than the published 37.20 Å. If it is assumed that the samples in the literature were phase pure and that the lattice parameters are varying linearly, then this difference is much larger than could be explained by the additional phase present as, if the Golubev data is used as a reference, the expected composition from the measured *c* lattice parameter is a little over x=0.1. A difference in stoichiometry is likely not the cause since the *a* lattice parameter is close to the published value. This suggests that either the Golubev value is wrong or there is some other mechanism affecting the lattice parameters, probably also causing the broadening issues observed.

Rietveld refinement was then performed on the x-ray diffraction patterns from Figure 6-1. This was done in a similar way to the previous chapter with the β-TCP structure published by Yashima *et al.* [24] being used as a basis. Initially, just the lattice parameters and atomic positions were refined, before the occupancies of the Ca sites and isotropic thermal parameters were also refined. The final refinements obtained are shown in Figures 6-6 to 6-10.

For the Ca(1), Ca(2) and Ca(3) sites, refinement of the occupancies gave values close to 1 for Ca occupancy and 0 for Al. Because of this, the occupancies of these three sites were fixed at 1 throughout the rest of the refinement. Both the Ca(4) and Ca(5) sites showed a decrease in Ca occupancy on the site and an increase in Al occupancy. This was quite surprising as Al was not expected to be substituting onto the Ca(4) site.

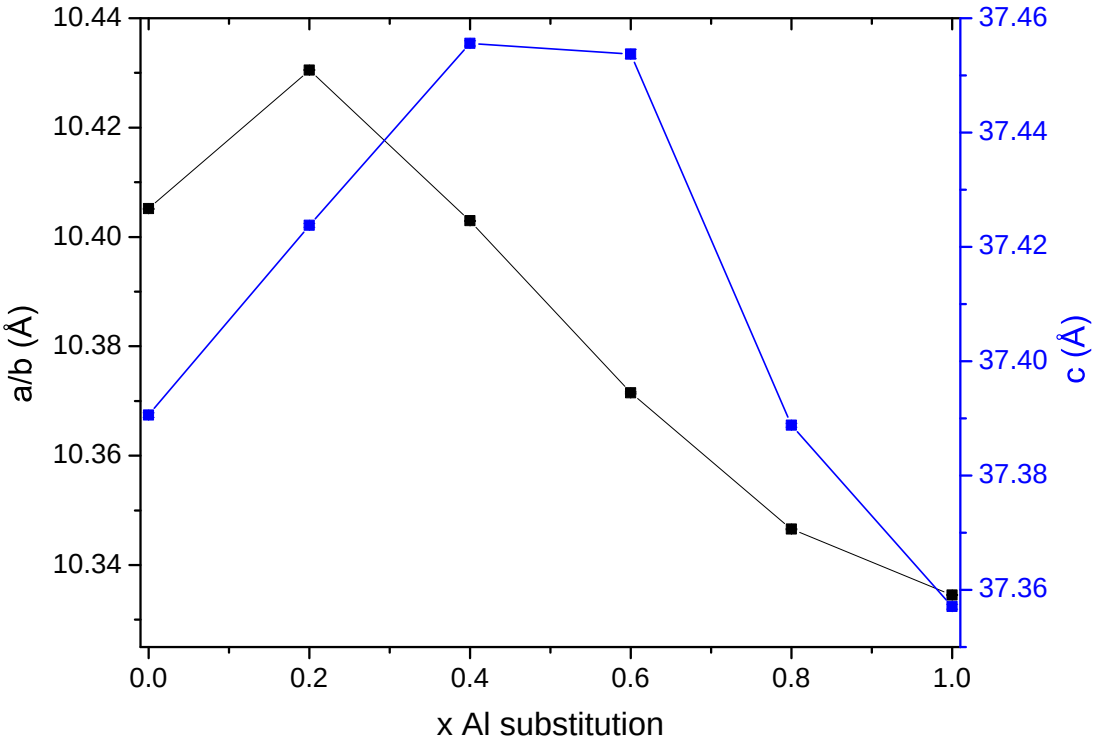

Figure 6-5 Lattice parameters of Al substituted β-TCP as determined by Rietveld refinement of x-ray diffraction data. Error bars smaller than symbols used.

After this, further refinement was performed, with the final occupancies of the Ca(4) and Ca(5) sites shown in Table 6-1.

What is apparent from this table is that the total occupancy of the Ca(4) and Ca(5) sites is initially much higher than that of undoped β-TCP, and always greater than expected from the increased number of vacancies which should be present at higher Al content. Looking at the individual sites, there is not much change in the Ca occupancy of the Ca(4) site, although Al occupancy on the site is seen to be present at lower Al content and decreasing with composition. On the Ca(5) site, the Ca occupancy decreases erratically from an occupancy close to 1 at x=0.2, with no Al shown to be present except in the x=0.4 sample. Part of the reason for this could be due to Al and Ca having reasonably similar scattering factors, especially considering the complexity of the structure. However, a more likely explanation is that the disorder or mixed phase problem is causing large errors to appear in the refinements. Also present is the lineshape issue identified in the previous chapter which could be further detrimental to the fits.

By examining how the data and fits change with composition it may be possible to

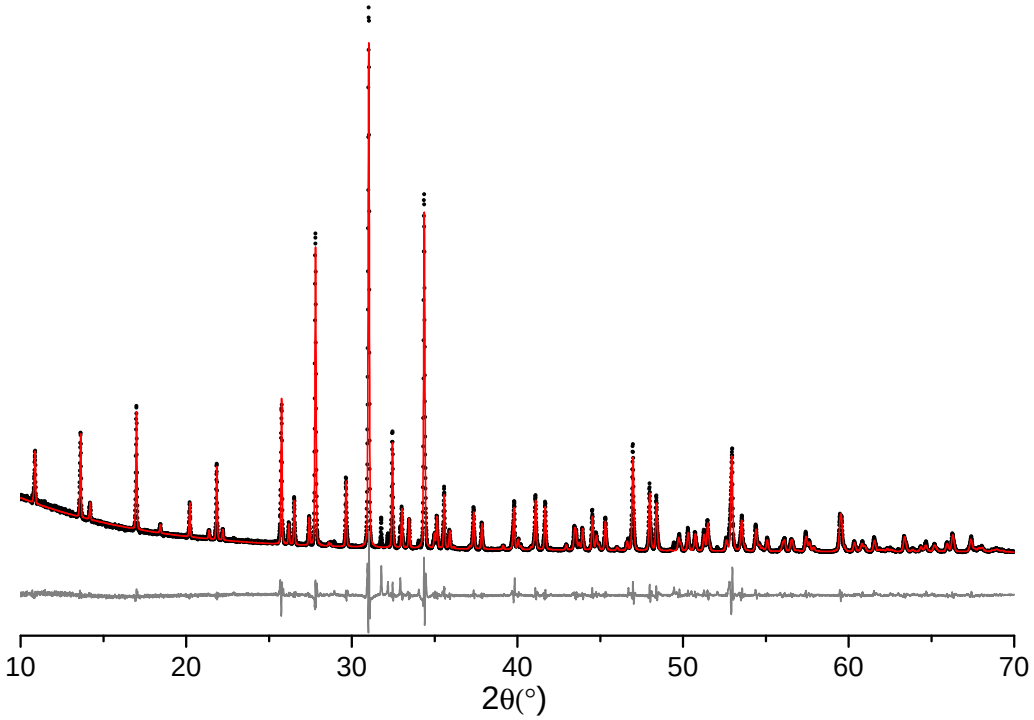

Figure 6-6 Powder x-ray diffraction pattern (·), Rietveld refinement (–), and difference plot (–) for $Ca_9Al_{0.2}(PO_4)_{6.2}$.

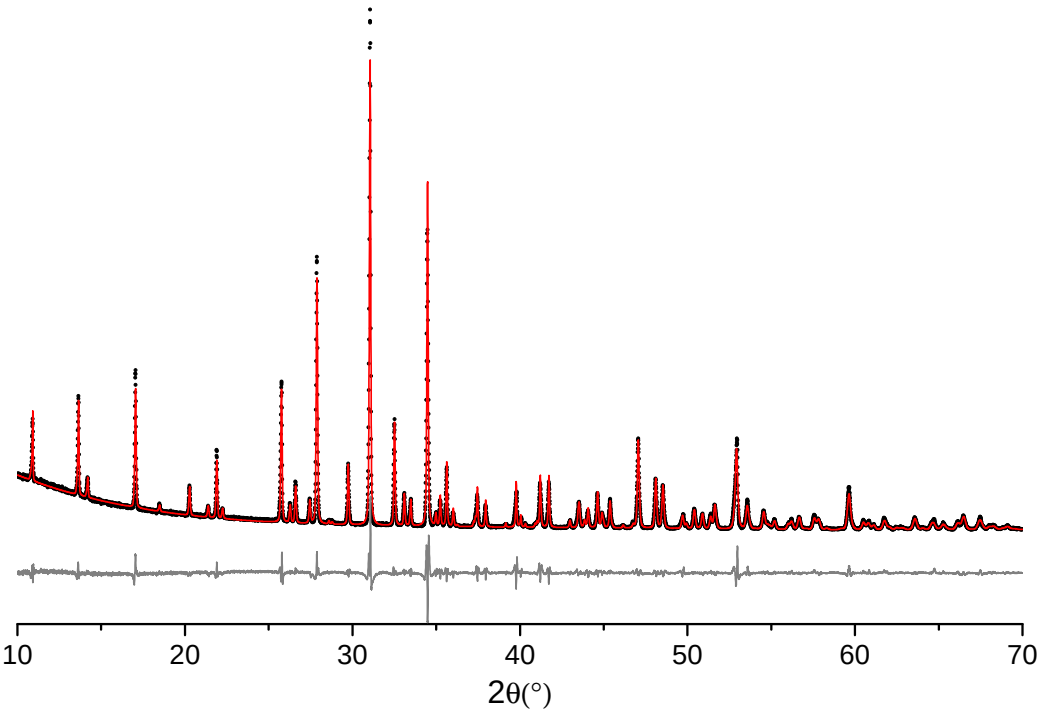

Figure 6-7 Powder x-ray diffraction pattern (·), Rietveld refinement (–), and difference plot (–) for $Ca_9Al_{0.4}(PO_4)_{6.4}$.

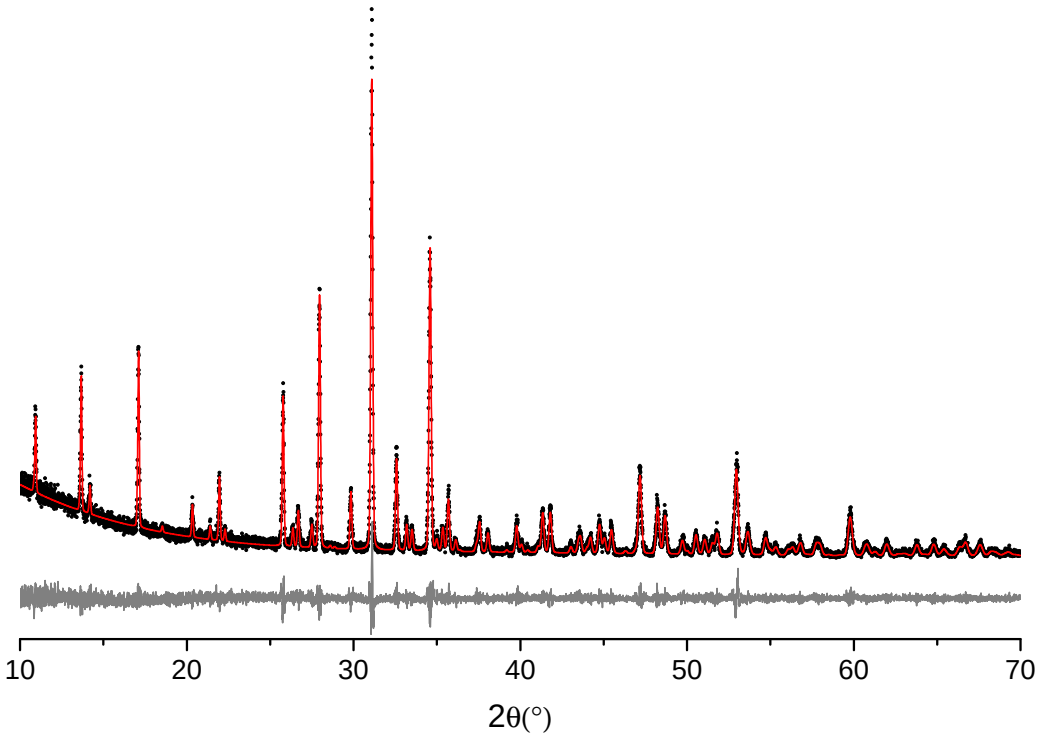

Figure 6-8 Powder x-ray diffraction pattern (·), Rietveld refinement (–), and difference plot (–) for $Ca_9Al_{0.6}(PO_4)_{6.6}$.

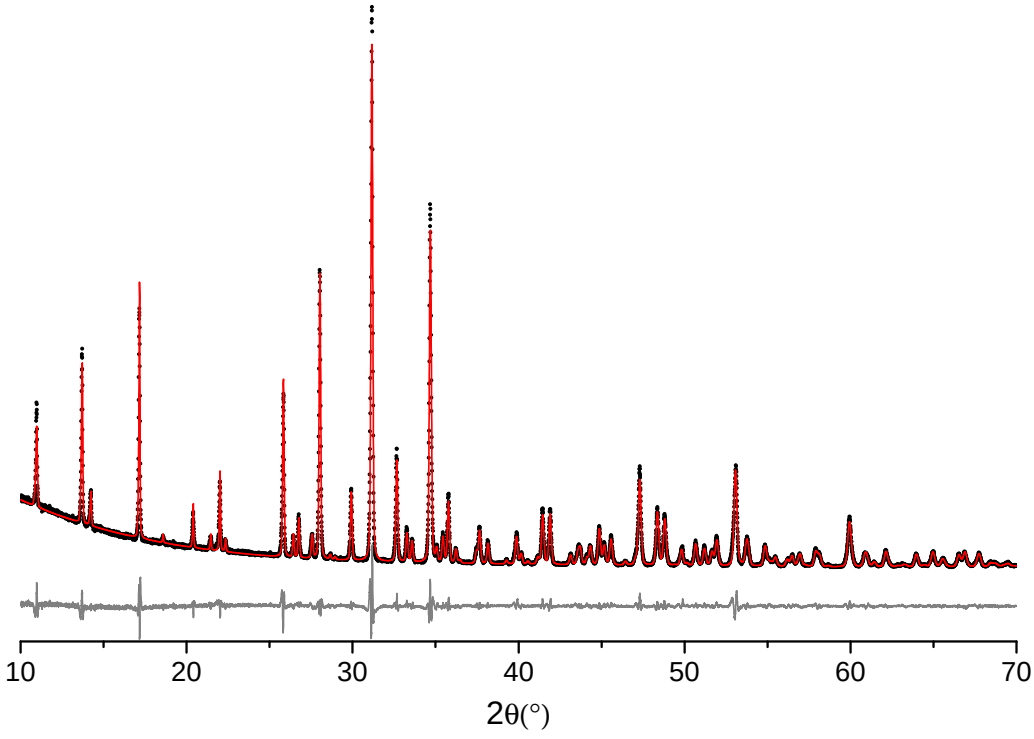

Figure 6-9 Powder x-ray diffraction pattern (·), Rietveld refinement (–), and difference plot (–) for $Ca_9Al_{0.8}(PO_4)_{6.8}$.

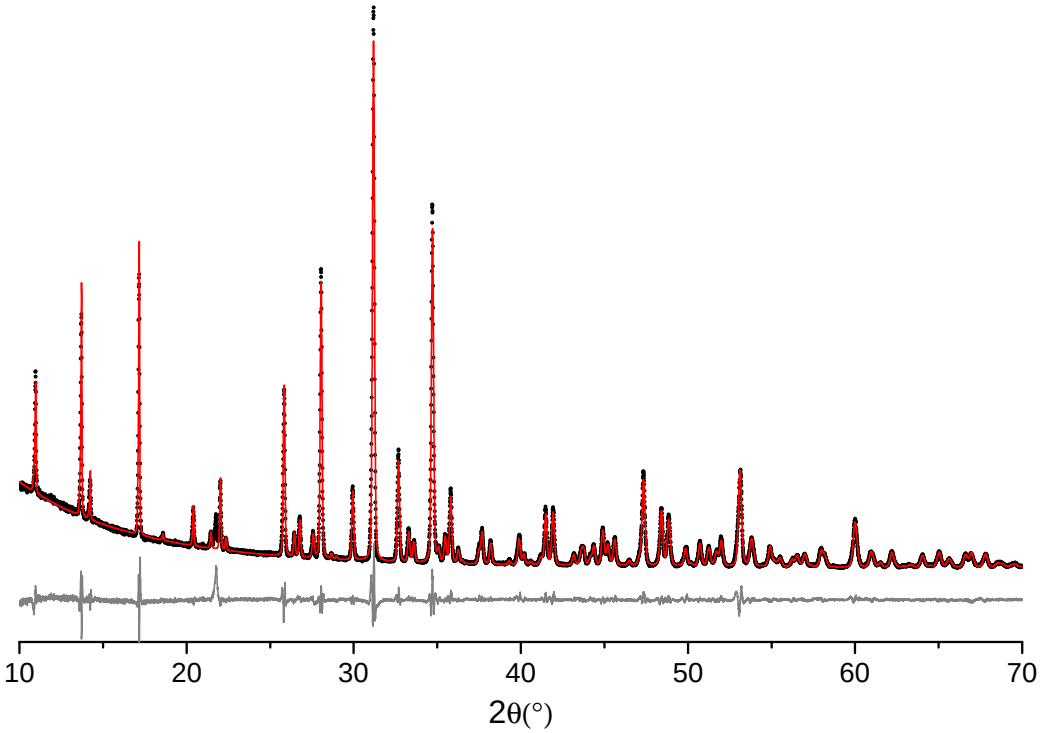

Figure 6-10 Powder x-ray diffraction pattern (·), Rietveld refinement (–), and difference plot (–) for $Ca_9Al(PO_4)_7$.

Table 6-1 Occupancies of Ca(4) and Ca(5) sites as determined by Rietveld refinement of x-ray diffraction data. Occupancies are to two decimal places with errors in parentheses.

	Ca(4)		Ca(5)		Total	Theoretical
x	Ca	Al	Ca	Al	Ca(4)+Ca(5)	total
0.2	0.46(11)	0.19(18)	1.02(10)	0.00(16)	1.67	1.4
0.4	0.43(10)	0.08(17)	0.81(10)	0.22(16)	1.54	1.3
0.6	0.45(18)	0.01(31)	0.95(16)	0.01(26)	1.42	1.2
0.8	0.42(11)	0.01(19)	0.91(07)	0.00(12)	1.34	1.1
1.0	0.39(13)	0.01(22)	0.89(08)	0.00(13)	1.29	1.0

determine the cause of the differences between the observed and calculated patterns. For the most part, it is thought that either substitutional disorder or a mixture of multiple slightly different phases are the cause of the mismatch in lineshape and intensity. Another factor which could cause changes is if there were some distribution in the position of the Ca(5) site, especially if there is substitutional disorder or multiple phases also present. The fact that the refined occupancies obtained vary greatly from what is expected will also have some effect.

If multiple, closely related phases were present then what would be observed is a contribution from each of those phases. If that is the case here then the phases present must be very similar, otherwise splitting of the peaks or additional peaks would be observed. Differences in site occupancy between phases would result in a change in intensity of some of the diffraction peaks but since this should be a linear change, and what is observed is an average, then overall the pattern would be unchanged if this is the only mechanism involved. A variation in lattice parameters would not cause a change in intensity but would result in the positions of the diffraction peaks of a single phase to change. Averaged over a sample this would cause a broadening of the peaks, occurring to a greater extent at larger angles, but with the overall intensity of each peak remaining constant. The combination of these two effects could result in asymmetric peaks but with peak intensities the same as for a single phase sample of the average composition.

A distribution of phases of this nature would cause a change in all of the diffraction peaks present which, by looking at the residuals from Rietveld refinement in Figures 6-6 to 6-10, is obviously not the case here. However, a distribution in atomic positions, especially if just on a small number of sites, would cause changes to the peaks coming from the reflections associated with those sites and may not change linearly. This effect could result in a change in the relative intensities of the peaks but may be very hard to determine the exact nature.

In order to investigate the effect that a change in atomic position may have on the diffraction patterns, simulated patterns have been produced based on one of the more likely sites to change position, the Ca(5) site. The refinement of β-TCP from Figure 5-4 was used as a starting point before varying the fractional z position of the Ca(5) site from the starting point of 0.7336 for β-TCP down to 0.72, slightly below the lowest measured for any of the systems. The refinement software was then used to produce the simulated

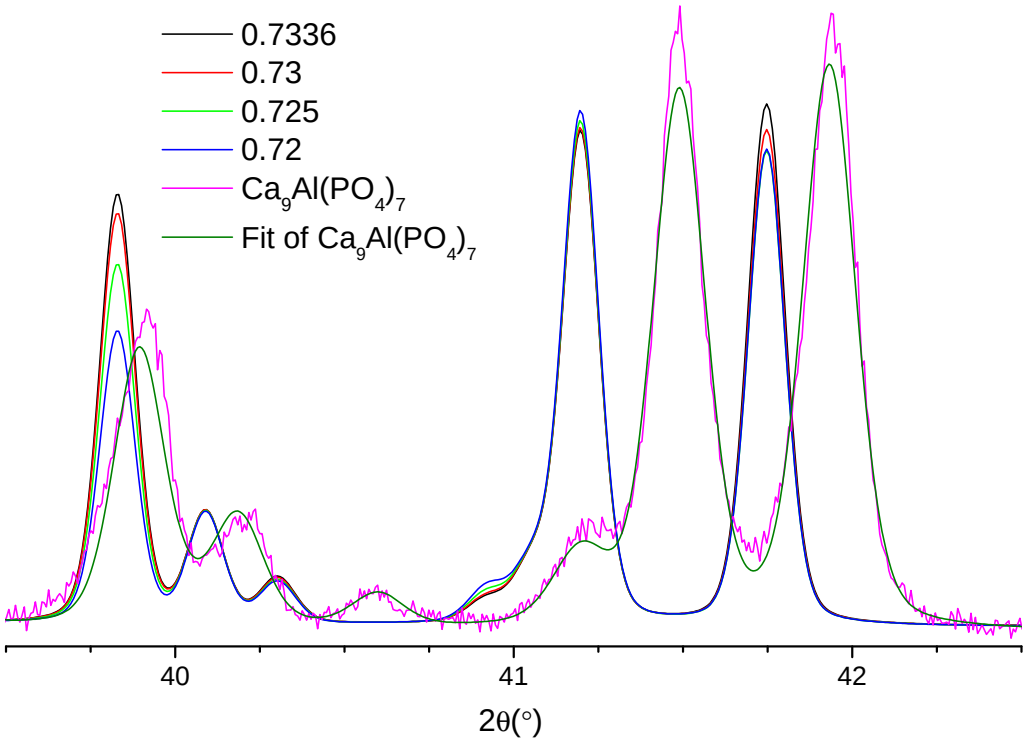

Figure 6-11 Simulated x-ray diffraction diffraction patterns showing the effect of varying the z-axis position of the Ca(5) site in β-tricalcium phosphate, along with collected diffraction pattern and fit of $Ca_9Al(PO_4)_7$ sample normalised to unchanged peak.

patterns by fixing all of the parameters, this should give patterns comparable to the rest of the refinements produced and an enlargement from a section of the simulated patterns can be seen in Figure 6-11 along with the pattern and fit from the x=1.0 sample.

From this figure is is obvious that varying the position has a distinct, often non-linear, effect and can cause a change in the relative intensities of the diffraction peaks. Looking at the peak at 39.38° it can be seen that a small change in atomic position can have a very large effect on the intensity of diffraction peaks resulting from that site. If it is assumed that the changes in atomic positions result in the same direction of variation in the peak heights irrespective of other considerations then this must not be the only factor causing the discrepancies in peak heights in this case as the peaks vary in both directions, whereas the fit to the x=1.0 pattern is always lower than the collected data in this region. This mechanism alone could be contributing to the poor fits, however coupled with a mixture of phases, especially one with a distribution in lattice parameters, the non-linearity of the changes may result in some additional asymmetry appearing in

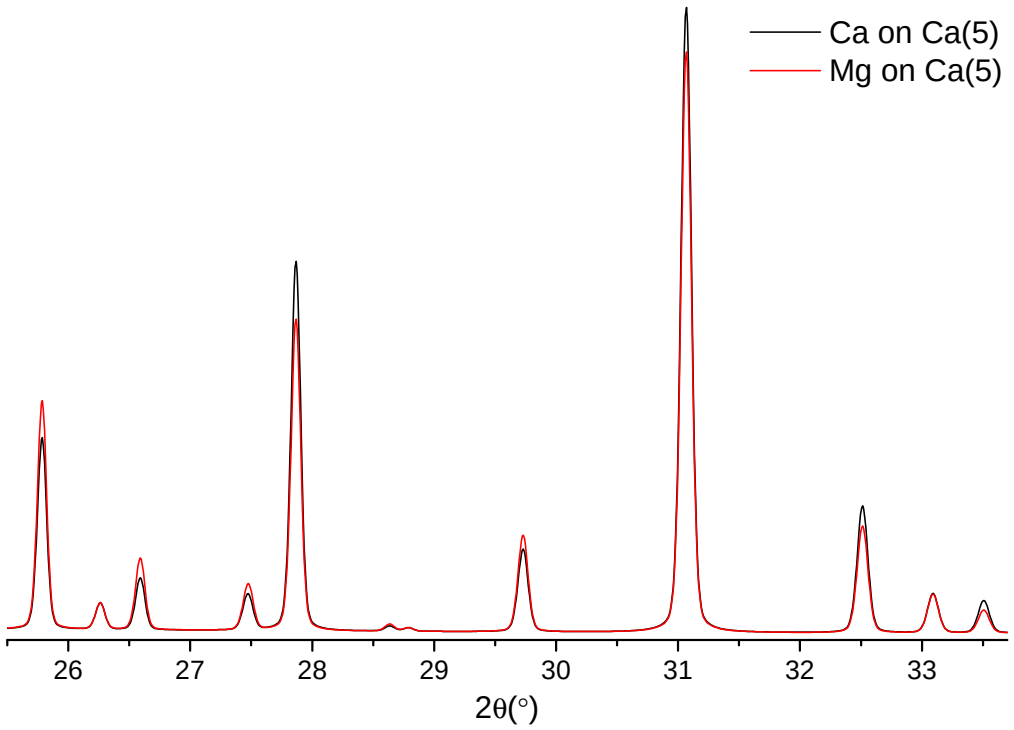

Figure 6-12 Simulated x-ray diffraction diffraction patterns showing the effect of changing the atom on the Ca(5) site in β-tricalcium phosphate.

the patterns.

The other mechanism thought to be causing problems with the fits is substitutional disorder. This would be disorder in how the ions and vacancies are distributed throughout the structure, and if disorder were occurring it would cause a reduction in the intensity of reflections involving the disordered sites as the ordering of the structure reduces. To help visualise what may be happening, a simulation of β-TCP has been produced with Mg in place of Ca on the Ca(5) site but with everything else remaining the same to show which peaks would be affected by changes in the occupancy of that site. Since Mg has the same valence and similar form factor to Al then this should be possible without having to worry about other effects which may be introduced, e.g. due to charge-balancing vacancies. This is compared with the refinement of β-TCP in Figure 6-12. If substitutional disorder was present then a decrease in intensity should be observed in those peaks seen to change under Mg substitution as the lack of order would prevent the reflections from being observed more strongly.

Bringing this all together it can be seen that there are many mechanisms which can change the observed patterns, some of which have very similar effects. It may be

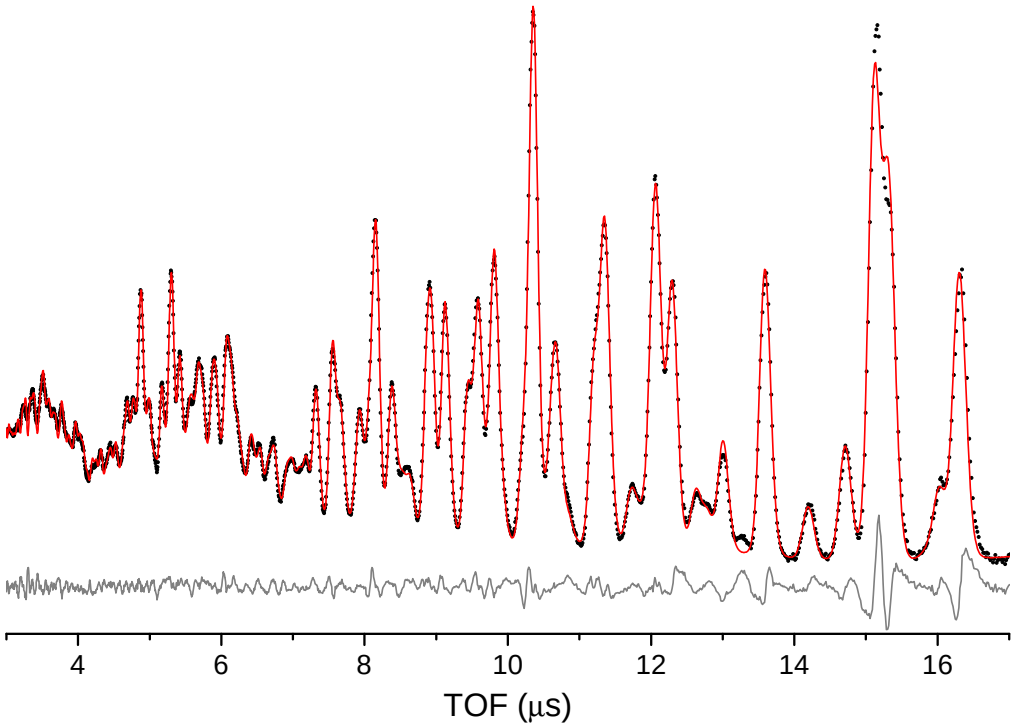

Figure 6-13 Powder neutron diffraction pattern (·), Rietveld refinement (–), and difference plot (–) for $Ca_9Al_{0.2}(PO_4)_{6.2}$ at room temperature.

possible to determine what exactly is happening from how the patterns differ but in this case the number of variables involved and the lack of confidence in some aspects of the refinements would make it very difficult without additional information.

6.3 Neutron diffraction

6.3.1 Time of flight diffraction

Time of flight neutron diffraction data have been acquired on the GEM diffractometer for the entire range of samples with Rietveld refinement being performed on bank 4 of the data. Good fits were obtained, as shown in Figures 6-13 to 6-17, with the main variations between data and fit being at longer TOF. As with Ga substitution in the previous chapter, structures obtained from Rietveld refinement of the x-ray diffraction patterns were used as a starting point, with these structures being further refined before anisotropic displacement parameters were added to improve the fits.

After further refinement of the Ca(4) and Ca(5) site occupancies, the values shown

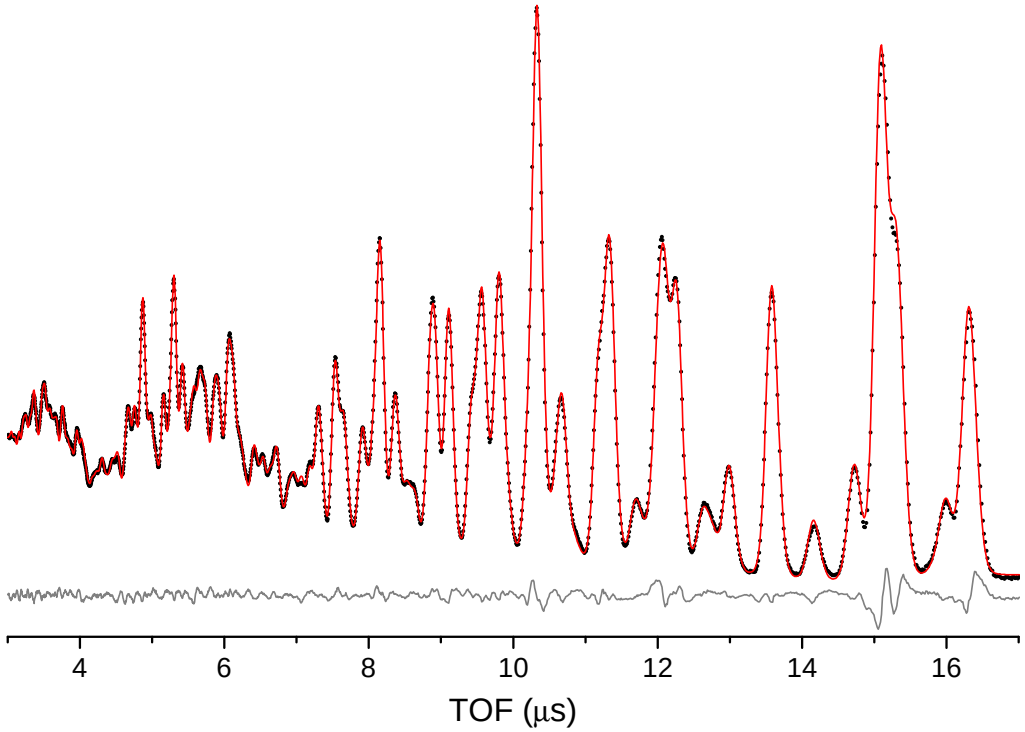

Figure 6-14 Powder neutron diffraction pattern (·), Rietveld refinement (–), and difference plot (–) for $Ca_9Al_{0.4}(PO_4)_{6.4}$ at room temperature.

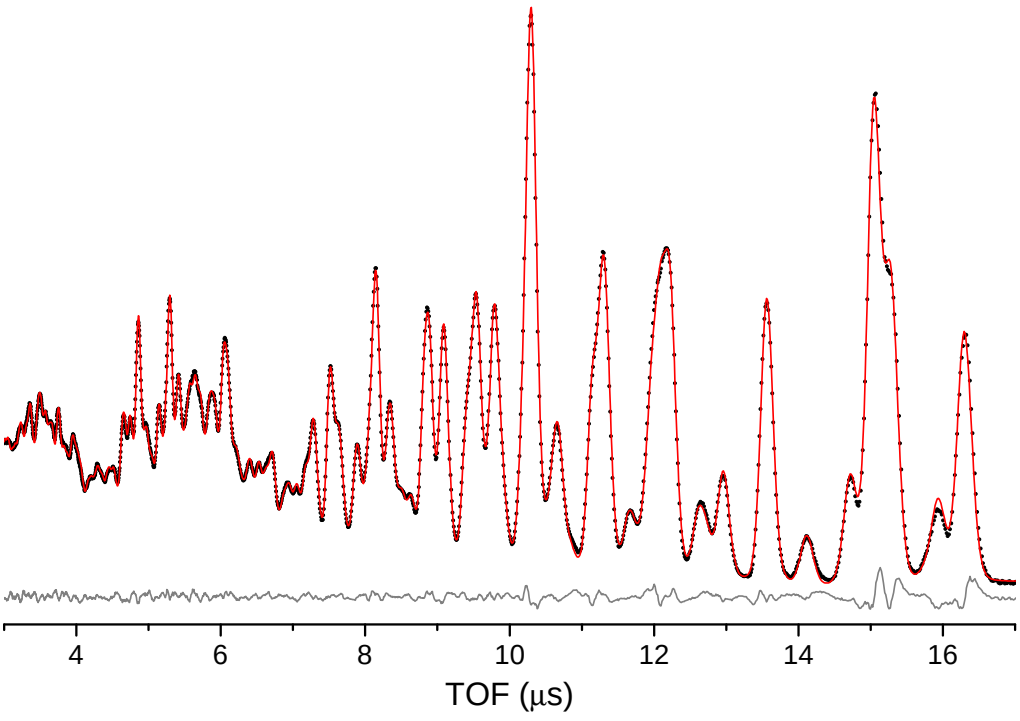

Figure 6-15 Powder neutron diffraction pattern (·), Rietveld refinement (–), and difference plot (–) for $Ca_9Al_{0.6}(PO_4)_{6.6}$ at room temperature.

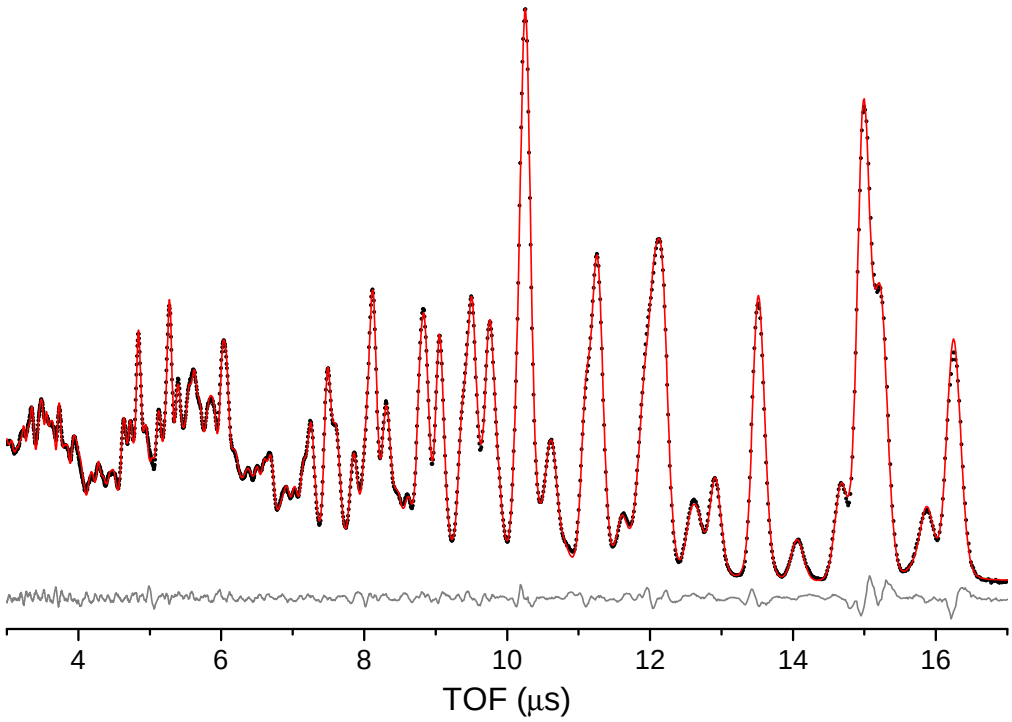

Figure 6-16 Powder neutron diffraction pattern (·), Rietveld refinement (–), and difference plot (–) for $Ca_9Al_{0.8}(PO_4)_{6.8}$ at room temperature.

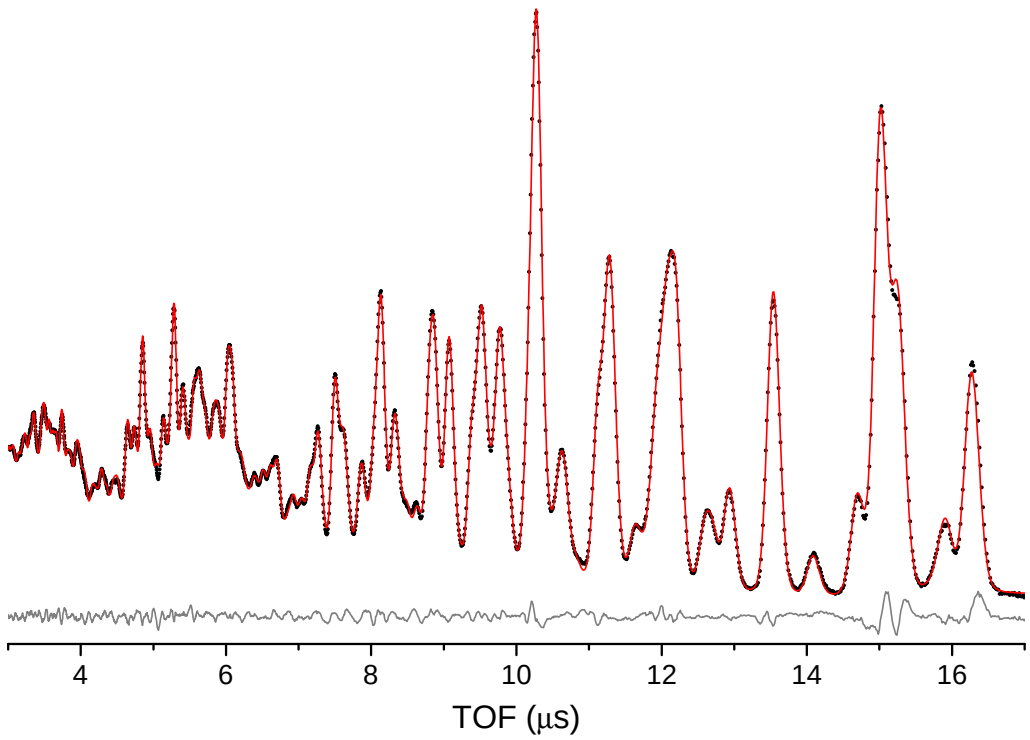

Figure 6-17 Powder neutron diffraction pattern (·), Rietveld refinement (–), and difference plot (–) for $Ca_9Al(PO_4)_7$ at room temperature.

Table 6-2 Occupancies of Ca(4) and Ca(5) sites as determined by Rietveld refinement of neutron diffraction data.

	Ca(4)		Ca(5)		Total	Theoretical
x	Ca	Al	Ca	Al	Ca(4)+Ca(5)	total
0.2	0.49	0.24	1.06	0.05	1.84	1.4
0.4	0.44	0.10	0.81	0.23	1.58	1.3
0.6	0.42	0.16	0.95	0.02	1.55	1.2
0.8	0.43	0.02	0.94	0.04	1.43	1.1
1.0	0.42	0.05	0.95	0.09	1.51	1.0

in Table 6-2 were obtained. Much like the XRD data, the values obtained are far from expected. In this case, the total occupancy of the two sites is almost consistently higher than that of undoped β-TCP, with the x=0.2 sample reaching a combined occupancy of 1.84. The actual occupancies of the sites are very similar to those found through refinement of the XRD data, except in this case there is a larger amount of Al present on the Ca(4) site and the Al occupancies of the Ca(5) site are also slightly higher. This suggests that there may actually be Al present on the Ca(4) site, however the errors on the occupancies are, as in the Ga case, of the order of 10^6. This, combined with the unusually high occupancies, makes it difficult to determine exactly how the Al is substituting onto the Ca sites. As with the XRD, Al and Ca have similar scattering lengths (3.45 fm for Al *cf.* 4.70 fm for Ca [45]), making it more difficult to discriminate between the two cations. The disorder or mixture of phases thought to be present from analysis of XRD data could also greatly influence the site occupancies, giving the unexpected values obtained.

6.3.2 Total correlation functions

Total correlation functions were obtained for the range of samples and are shown in Figure 6-18 alongside that of the 'pure' β-TCP sample. Looking at these plots, the main P–O and Ca–O/O–O peaks appear unchanged, which is to be expected as 4-coordinated to 6-coordinated Al lie within the region 1.76 to 1.91 Å [14]. The main feature visible between these peaks is an additional broad peak at around 1.92 Å, consistent with 6-coordinated Al which would be expected on the Ca(4) or Ca(5) sites.

In the x=0.2 sample there is another peak visible at 1.77 Å, at a distance expected for

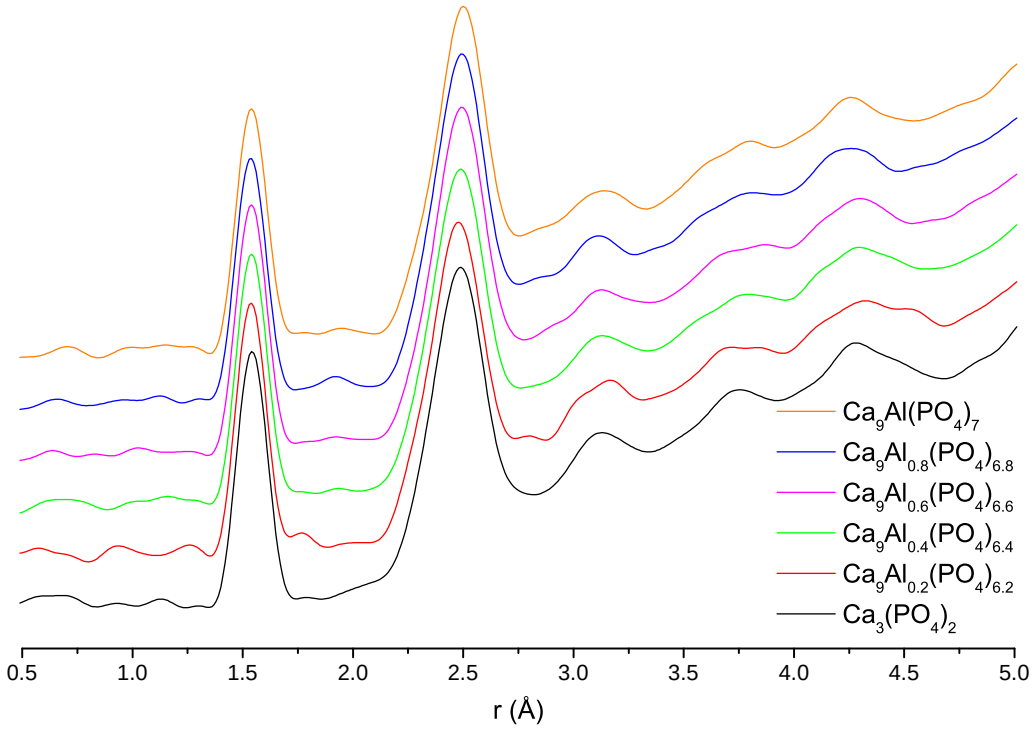

Figure 6-18 $T(r)$ for Al substituted β-tricalcium phosphate samples.

4-coordinated Al. No $AlPO_4$ was detected in this sample, however there was hydroxyapatite present in the XRD pattern meaning this peak may be a result of the presence of this phase. There are also other differences between the x=0.2 and other samples, further suggesting an additional phase may be present.

6.4 Nuclear magnetic resonance

6.4.1 ^{27}Al nuclear magnetic resonance

^{27}Al NMR was performed on the whole range of samples with spectra shown in Figure 6-19. An attempt was made to relate the features observed to the samples produced by referring to work by Mackenzie and Smith [25, p. 273]. The large main peak at around −10.4 ppm is due to 6 co-ordinated Al in a phosphate environment, as would be expected for Al on the Ca(4) or Ca(5) sites. The other main peak at 40 ppm corresponds to 4 co-ordinated Al in a phosphate environment, coming from the $AlPO_4$ second phase present in the samples. There are also two quite broad features visible, a slightly larger one present in all samples between 20 and 0 ppm and a less intense one, mostly observed

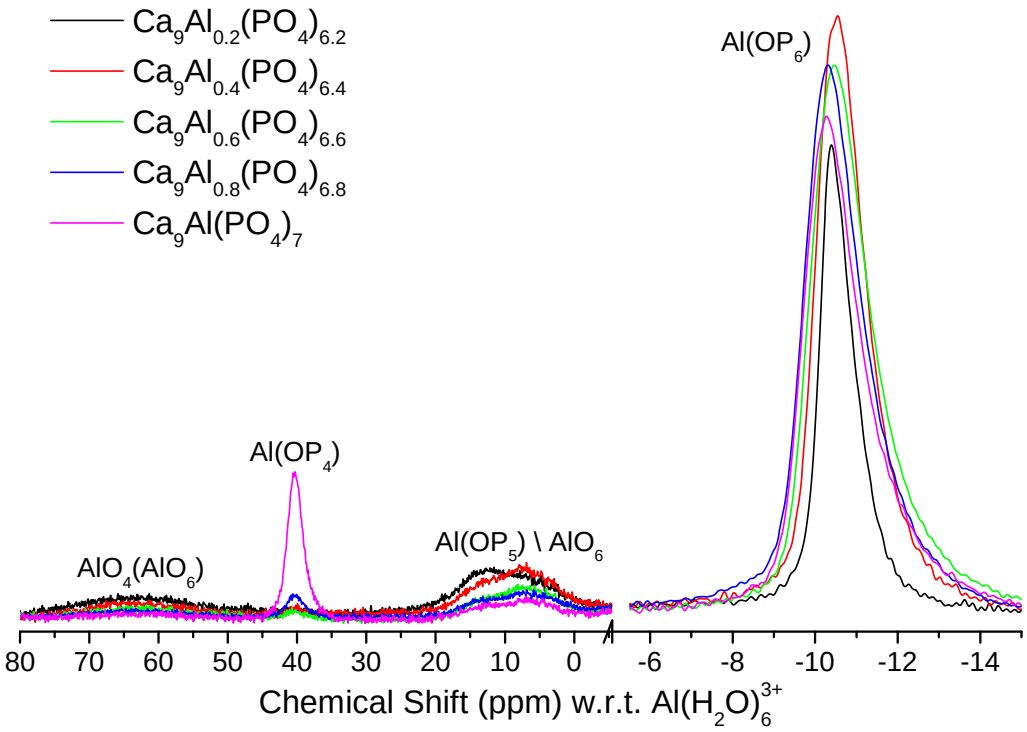

Figure 6-19 ^{27}Al NMR spectra of Al substituted β-tricalcium phosphate, normalised to area of central transitions of main peaks. Peak assignments are those given by Mackenzie and Smith [25, p. 273].

in the lower Al content samples, between 80 and 50 ppm.

The larger peak exists in the region corresponding to either AlO_6 or $Al(OP)_5$. This could be the result of some kind of distortion of the Al environment on either the Ca(4) or Ca(5) site. Since the Ca(4) site is initially quite distorted, with 3 short bonds and 3 long bonds (Tab. 3-1), if Al were to substitute onto the site it could cause further disorder or perhaps even distortion into what would appear to be a 5-coordinated site. This peak is also quite asymmetrical in the lower Al containing samples, suggesting it is caused by either more than one environment or that the site causing it not symmetric, leading to a quadrupolar lineshape. The other broad feature corresponds to $AlO_4(AlO_6)$. This feature, along with another peak at 15 ppm, is more than likely due to Al within the rotors used, explaining its prevalence at low Al content where the experiment times were much longer. Acquiring a spectrum of an empty rotor would confirm this. However the presence of the additional peaks was only noticed long after the acquisition of the other spectra.

Areas of the four regions were measured, and the relative intensities of each site

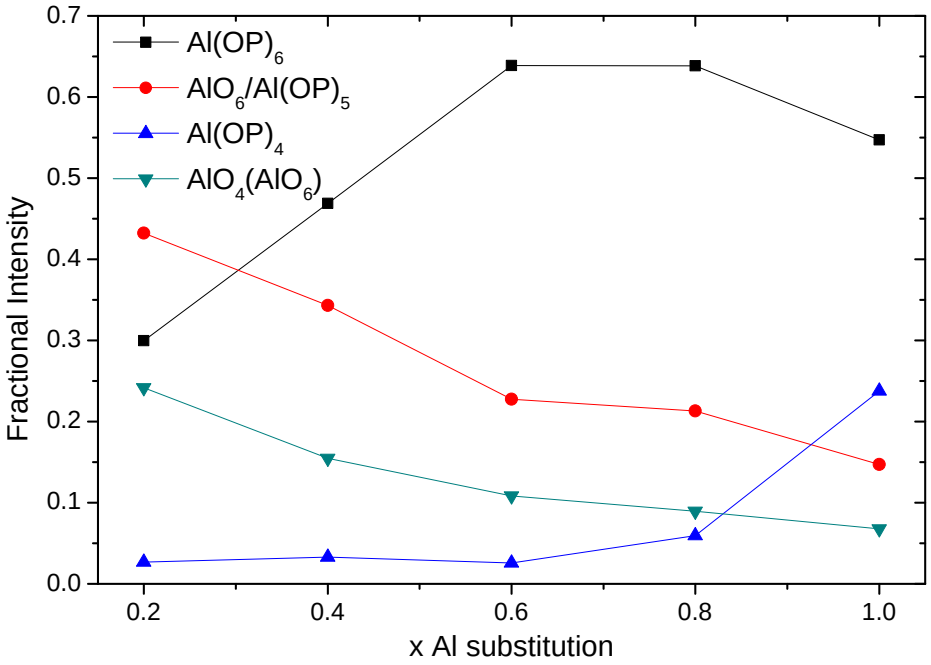

Figure 6-20 Fractional peak intensities of central transitions from ^{27}Al NMR spectra of Al substituted β-tricalcium phosphate.

are shown in Figure 6-20. For the 6-coordinated peak, only the central transition was measured since the sidebands extend beyond the spectral width, meaning that the actual intensity of that site would be substantially greater. Taking this into account it can be seen that the 6-coordinated peak is the dominant one present, indicating that most of the Al is within the standard Ca(4) or Ca(5) sites. The $AlPO_4$ peak is only really significant in the x=1.0 sample, suggesting that the maximum Al substitution may be around that point. The relative proportions of the other two peaks present decrease linearly at similar rates, with the $AlO_6/Al(OP)_5$ peak being around twice as large as the $AlO_4(AlO_6)$ peak throughout. This may just be coincidence, considering the errors in measuring the areas of the broad peaks, implying that the $AlO_4(AlO_6)$ peak may actually be less intense than shown.

If the Al is indeed substituting onto the Ca(4) site, with ions from this site also being removed for charge balancing, then what would be expected is an initial increase in the Al occupancy of the Ca(4) site until it becomes wholly Al at an occupancy of 0.25, before starting to decrease as Al starts to be removed from the site. The fractional intensity of the '5-coordinated' Al peak is not quite that which would be required, but does show a trend of decreasing intensity with increasing substitution levels.

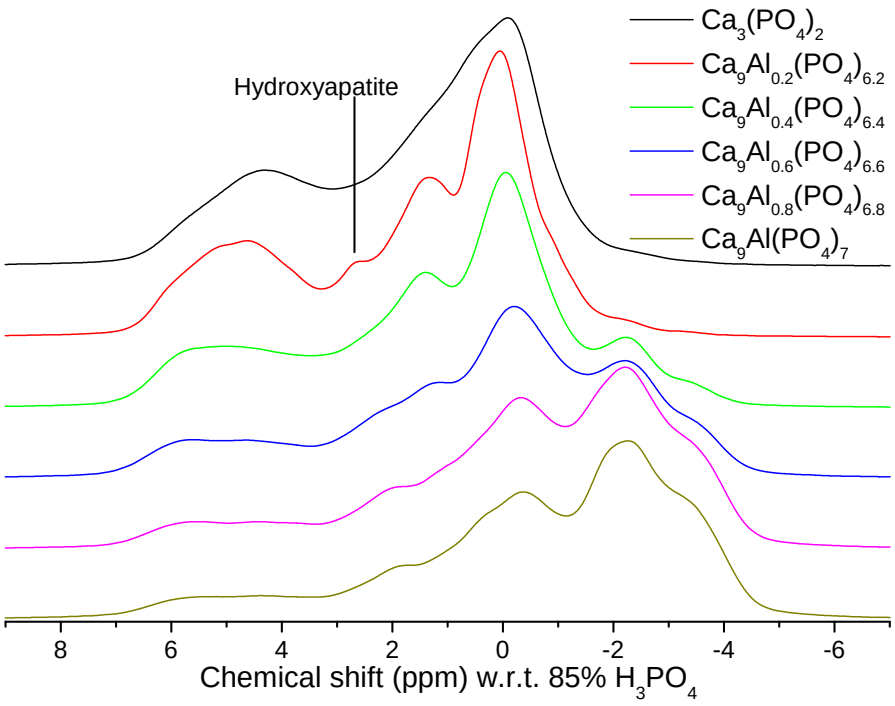

Figure 6-21 ^{31}P NMR spectra of Al substituted β-tricalcium phosphate.

6.4.2 ^{31}P nuclear magnetic resonance

^{31}P MAS NMR was undertaken on the 500 MHz spectrometer for the entire range of samples with spectra shown in Figure 6-21, alongside the spectrum obtained from the 'pure' β-TCP sample. Addition of Al into the system appears to cause distinct changes across the whole of the spectrum. The peak around 0 ppm seems present throughout, along with some of the features across the left of the spectrum. However, multiple extra resonances are visible, be they new peaks or some existing ones with more definition. There also appears to be a slight shift upfield in some of the resonances, although this may just be due to the intensities of some of the peaks changing relative to each other.

The small extra peak observable at 2.7 ppm in the x=0.2 sample is due to the hydroxyapatite within the sample, shown to be present from XRD data. The x=0.8 and x=1.0 spectra appear fairly similar, most likely due to the $AlPO_4$ present in the x=1.0 sample, but the progression in peaks suggests that a true $Ca_9Al(PO_4)_7$ sample would just include the resonances present between 1 and −4 ppm, possibly also with the additional peak at 2 ppm.

In order to fit the spectra, either well defined peaks need to be present or some idea of the number or distribution of different peaks needs to be known. Neither is true in

this case as the spectra appear broad and complex and, from all the previous data, the exact substitution site is not yet known. Two main possibilities exist, either substitution is taking place on the Ca(5) site, as in the Ga case and discussed in Section 3.4.2, or there is also Al present on the Ca(4) site (substitution solely onto the Ca(4) site would require vacancies on the Ca(5) site which contradicts the data obtained and has therefore been discounted). For substitution onto the Ca(5) site it has been shown that up to 8 peaks would be needed to fit the ^{31}P spectra (Fig. 3-4). For substitution onto the Ca(4) and Ca(5) sites, and assuming the Ca(5) site remains fully occupied, the distribution of environments would be similar to the case of substitution onto the Ca(5) site but in this case the additional presence of Al on the Ca(4) site will cause further splitting of the environments of the P sites with Ca(4) next nearest neighbours and resulting in up to 11 peaks being required in fitting.

As a result of this, each spectrum was fitted to both 8 and 11 peaks, with the resultant fits shown in Figure 6-22. The fitting was performed by initially fitting by eye the x=0.2 sample, as that appears to have the most distinct features, before letting the software refine the fits. The same procedure was then followed for the remaining spectra but the initial fitting was done to give peaks in similar places to the previous fits. The additional peak in the 8 peak fit of the x=0.2 sample is to account for the hydroxyapatite present.

Looking closely at the fits, neither method of fitting appears to adequately model the spectra. It might be expected that the 11 peak fits would produce a superior fit due to the increased degrees of freedom allowed but that is obviously not the case as with most spectra both fitting methods give similar fits. The fact that neither method appears to work suggests that the problems encountered in the previous sections are reoccurring here. Simple disorder in the systems should cause an increase in the widths of the fitted peaks, however, distortions of the Ca(4) sites or the presence of multiple phases could cause many different changes to the spectra. These are uninterpretable without further details.

6.4.3 ^{43}Ca nuclear magnetic resonance

Natural abundance ^{43}Ca NMR was performed on the $Ca_9Al_{0.6}(PO_4)_{6.6}$ and $Ca_9Al(PO_4)_7$ samples by Dr. Thomas Kemp at Warwick. The $Ca_9Al_{0.6}(PO_4)_{6.6}$ was measured on the 600 MHz spectrometer, and the $Ca_9Al(PO_4)_7$ sample on both the 600 MHz and

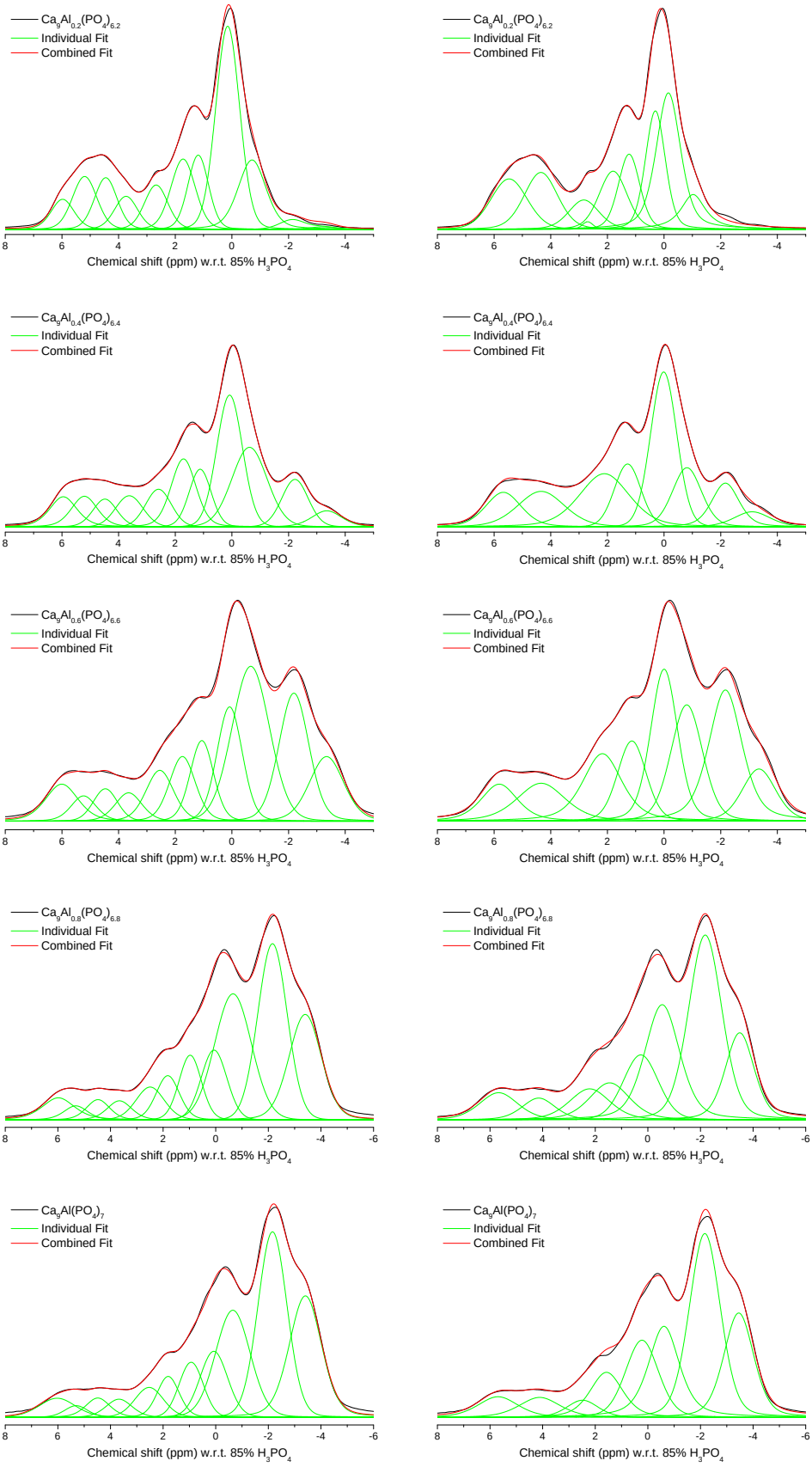

Figure 6-22 Fits of ^{31}P NMR spectra of Al substituted β-tricalcium phosphate to 8 and 11 peaks.

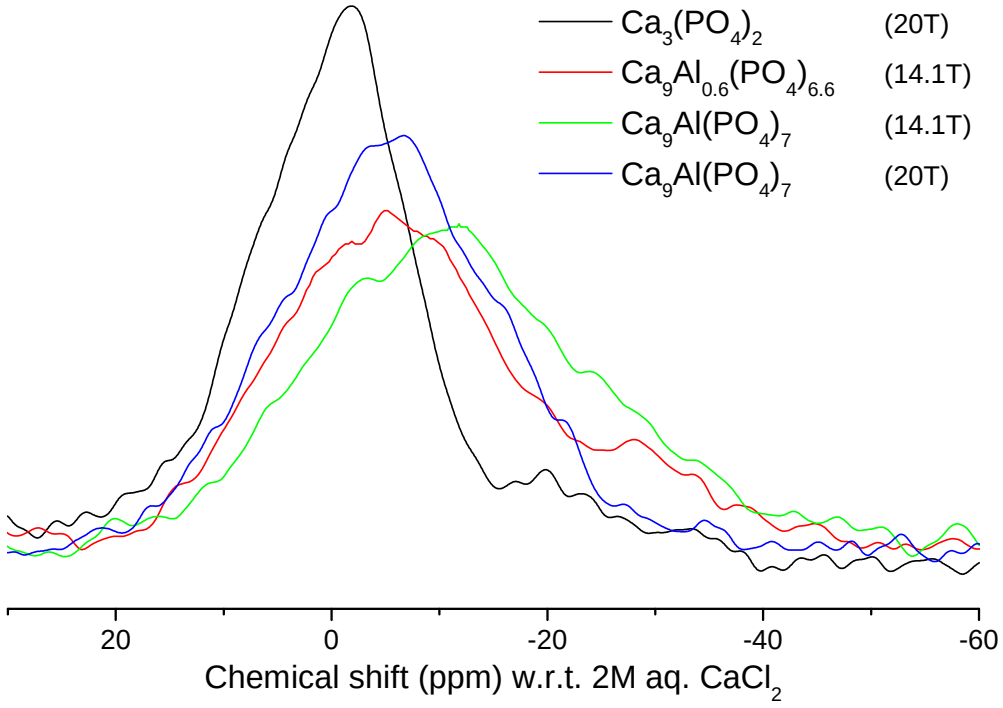

Figure 6-23 ^{43}Ca NMR spectra of Al substituted β-TCP samples, normalised to peak area.

850 MHz spectrometers. Spectra are shown in Figure 6-23 along with the 'pure' β-TCP spectrum. An increase in linewidth at lower fields is the most noticeable feature, with a shift downfield with increasing Al content and decreasing field also observed. Comparing the actual lineshapes, the main difference under Al substitution appears to be a decrease in the right hand side of the peaks, identified as the position of the Ca(4) peak. Due to the broad nature of the spectra, any changes in the other peaks are difficult to identify without fitting.

As in the Ga case, the spectra were fitted to five Gaussian lineshapes starting from the fit of the 'pure' β-TCP sample (Fig. 5-22). Since substitution is thought to take place on the Ca(4) and Ca(5) sites, an attempt was made to produce fits that followed this. However, the combination of poor signal to noise ratios and the intensities of the Ca(4) and Ca(5) sites being low to begin with made this difficult. The final fits are shown in Figures 6-24 to 6-26.

From these fits the occupancies were calculated and are shown with other fit parameters in Tables 6-3 to 6-5. The fits of the spectra from the x=1.0 sample at both fields show a decrease in the intensity of the peaks associated with the Ca(4) and Ca(5)

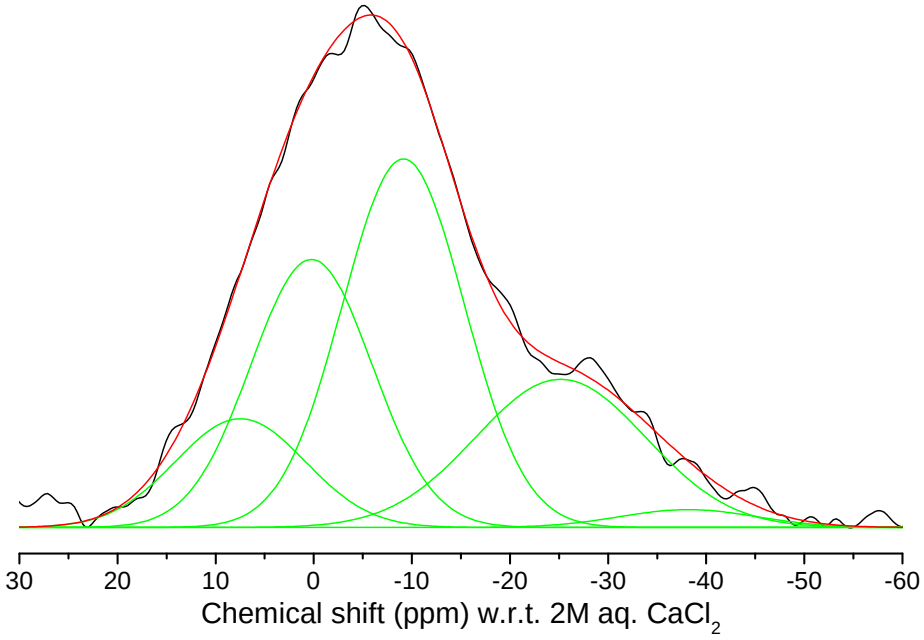

Figure 6-24 Fit of ^{43}Ca NMR spectrum of $Ca_9Al_{0.6}(PO_4)_{6.6}$ sample at 14.1 T.

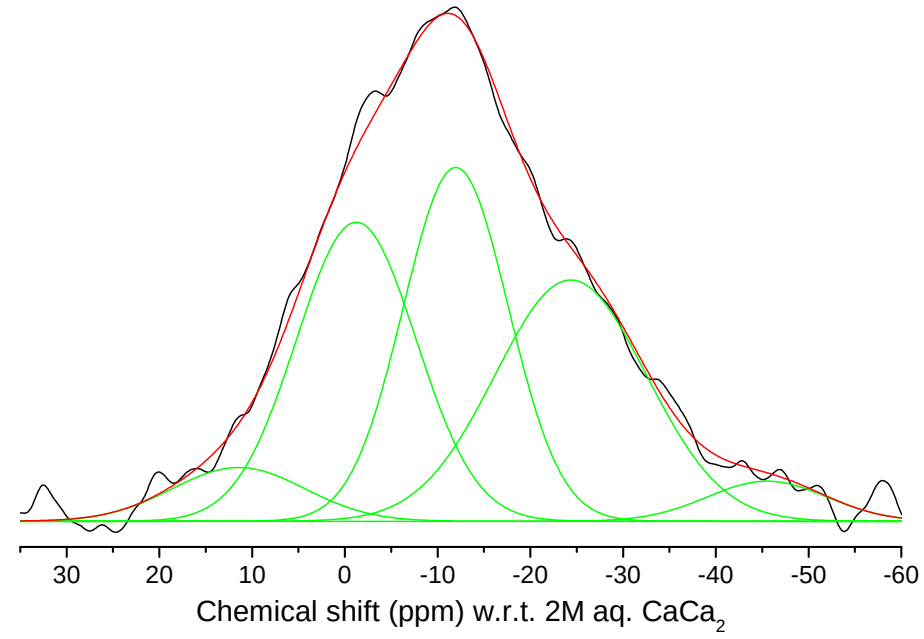

Figure 6-25 Fit of ^{43}Ca NMR spectrum of $Ca_9Al(PO_4)_7$ sample at 14.1 T.

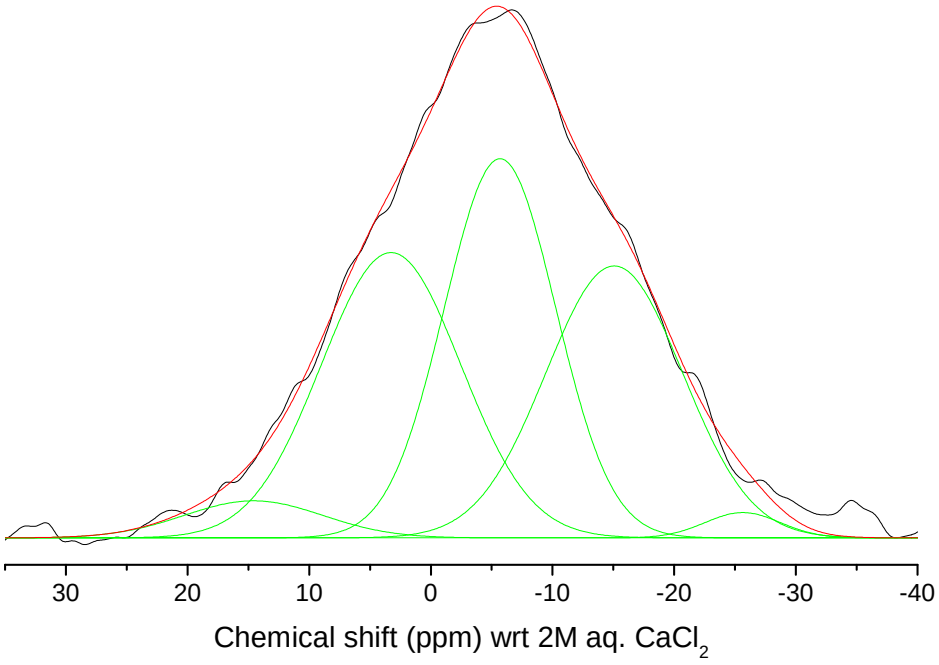

Figure 6-26 Fit of ^{43}Ca NMR spectrum of $Ca_9Al(PO_4)_7$ sample at 20 T.

sites as would be expected. Also observed is a decrease in the widths of all 5 peaks at the higher field. Things are slightly more complicated with the x=0.6 sample, where the peak from the Ca(2) site is dominant in the spectrum. The intensity of this peak is far greater than should be allowed, with the increase in intensity coming from the, in this case much smaller, Ca(3) site peak. This could mean that quadrupolar lineshapes are needed to fit this spectrum, although doing so would give a far from unambiguous fit. Alternatively, some form of disorder could again be present around the Ca(4) site, which would be more apparent for the mid-composition samples, and could potentially cause disorder within more than just the Ca(4) site, possibly explaining some of the problems with fitting.

6.5 Summary

Al substituted β-tricalcium phosphate samples have been produced which have been shown to be, in most cases, phase pure, with the exception of two samples, one of which contained hydroxyapatite and one, the highest Al containing sample, $AlPO_4$, indicating that this may be at the substitution limit of the system. Rietveld refinement of x-ray and neutron diffraction patterns seems to indicate substitution is taking place onto the Ca(4)

Table 6-3 Fit parameters of ^{43}Ca NMR on $Ca_9Al_{0.6}(PO_4)_{6.6}$ sample at 14.1 T.

Site	Peak position ppm ±1	Peak width Hz ±50	Occupancy % ± 3		
			Undoped	Observed	Normalised
5	7.9	890	9.5	12	11
1	0.6	830	28.6	27	25
2	−8.8	840	28.6	38	35
3	−24.8	1170	28.6	21	19
4	−37.7	940	4.7	2	2

Table 6-4 Fit parameters of ^{43}Ca NMR on $Ca_9Al(PO_4)_7$ sample at 14.1 T.

Site	Peak position ppm ±1	Peak width Hz ±50	Occupancy % ± 3		
			Undoped	Observed	Normalised
5	11.6	960	9.5	6	5
1	−1.2	870	28.6	29	25
2	−11.8	760	28.6	31	26
3	−24.2	1100	28.6	30	26
4	−45.3	870	4.7	4	3

Table 6-5 Fit parameters of ^{43}Ca NMR on $Ca_9Al(PO_4)_7$ sample at 20 T.

Site	Peak position ppm ±1	Peak width Hz ±50	Occupancy % ± 3		
			Undoped	Observed	Normalised
5	14.7	770	9.5	4	3
1	3.4	770	28.6	32	27
2	−5.5	620	28.6	33	29
3	−15.0	760	28.6	29	25
4	−25.5	420	4.7	2	1

or Ca(5) sites. However, the combination of unexpected values for the occupancies, and peculiar peak shapes, suggest that something more complex may be occurring, such as disorder within the system or a mixture of similar phases being present. Total correlation functions do not aid much in the assessment, with only 6-coordinated Al being observed.

^{27}Al NMR is possibly the most helpful in identifying the state of the Al, with the main feature being a 6-coordinated resonance corresponding to Al on the Ca(4) or Ca(5) site. Also present is another large resonance, this time associated with the $AlPO_4$ phase. However, the most interesting feature is a broad peak between the 4 and 6-coordinated resonances. The position of this peak is in a region corresponding to either AlO_6 or $Al(OP)_5$ [25] and may be the result of some kind of distortion of one or both of the 6-coordinated Ca sites. Interesting trends can be observed in ^{31}P spectra of the samples but fitting is difficult without knowing more about how the substitution is taking place. ^{43}Ca NMR spectra show a change in position and width of the lineshape with varying field, and an attempt can be made to fit them, however the lineshape may be more complex than initially thought, leading to an unphysical outcome in the fitting of the x=0.6 sample.

Chapter 7

La substitution

7.1 Sample preparation and characterisation

Samples were prepared at Warwick by vacation student Alex Marsden under the supervision of the author, by grinding together stoichiometric amounts of $CaH(PO_4)$, $CaCO_3$ and La_2O_3 according to the general formula $Ca_9La_x(PO_4)_{6+x}$ with samples of x=0.2, 0.4, 0.6, 0.8 and 1.0 being produced. The resulting mixture was then heated at a rate of 10 °C/min up to 1050 °C and held for 4 h. This was then repeated further times in an attempt to produce phase pure samples.

7.2 X-ray diffraction

X-ray diffraction patterns were collected by Alex Marsden for the entire composition range and are shown in Figure 7-1. The main diffraction peaks appear to shift slightly to increasing 2θ initially before shifting to a greater extent to smaller angles upon further La substitution. This appears counter intuitive as it is expected that the larger La ion (1.16 Å *cf.* 1.12 Å for Ca, for 8-coordination [44]) would cause an expansion of the unit cell and thus a shift in the diffraction peaks to decreasing 2θ. Upon closer inspection (Fig. 7-2), it can be seen that there are additional peaks present in all of the La doped samples. The main impurity phase was identified as monazite ($LaPO_4$), with the x=0.6 sample additionally containing hydroxyapatite ($Ca_5(PO_4)_3(OH)$). This implies that at least some of the La present is not within the β-TCP phase, possibly explaining the unexpected shifts in the diffraction peaks.

A series of x-ray diffraction patterns were also collected for different length firings of the x=1.0 sample. These can be seen in Figure 7-3, where, after only 4 hours of firing, monazite appears to be a major phase. Two more 4 h firings bring the amount of monazite present down considerably, however, even 123 h of firing is not sufficient

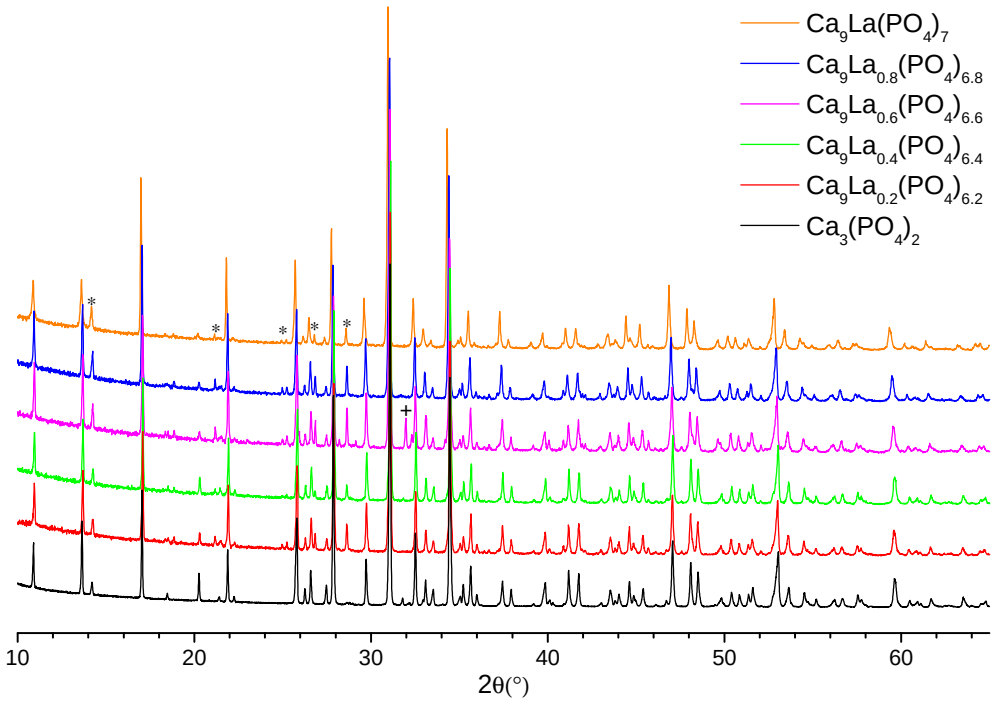

Figure 7-1 X-ray diffraction patterns of La substituted β-tricalcium phosphate, where $*$ represents monazite and + represents hydroxyapatite.

to remove all of the monazite. It is also apparent that, as the proportion of monazite decreases, the diffraction peaks shift to lower angles. This is consistent with the La substituting into the β-TCP structure and causing an increase of the unit cell size as expected.

Lattice parameters, obtained using Rietveld refinement, are shown in Figure 7-4 plotted against compositions calculated in Section 7.4.1. The trend here is not quite as expected from the observation of the diffraction patterns earlier or from the size of the substituting La ions. In Figure 7-1, an increase in the observed angle of the diffraction peaks can be seen initially before the decrease at higher La content, whereas the a/b and c lattice parameters never drop below the values for the 'pure' β-TCP sample. This unexpected trend is most likely due to the ~0.13° difference in the refined zero error of the La substituted samples compared to the 'pure' β-TCP sample run several months earlier, implying that either the diffractometer was not aligned properly or the sample height was consistently off by a similar amount.

This does not, however, explain the dip in the lattice parameters for the x=0.4 sample. The most obvious cause for this would be that most of the La present is within the

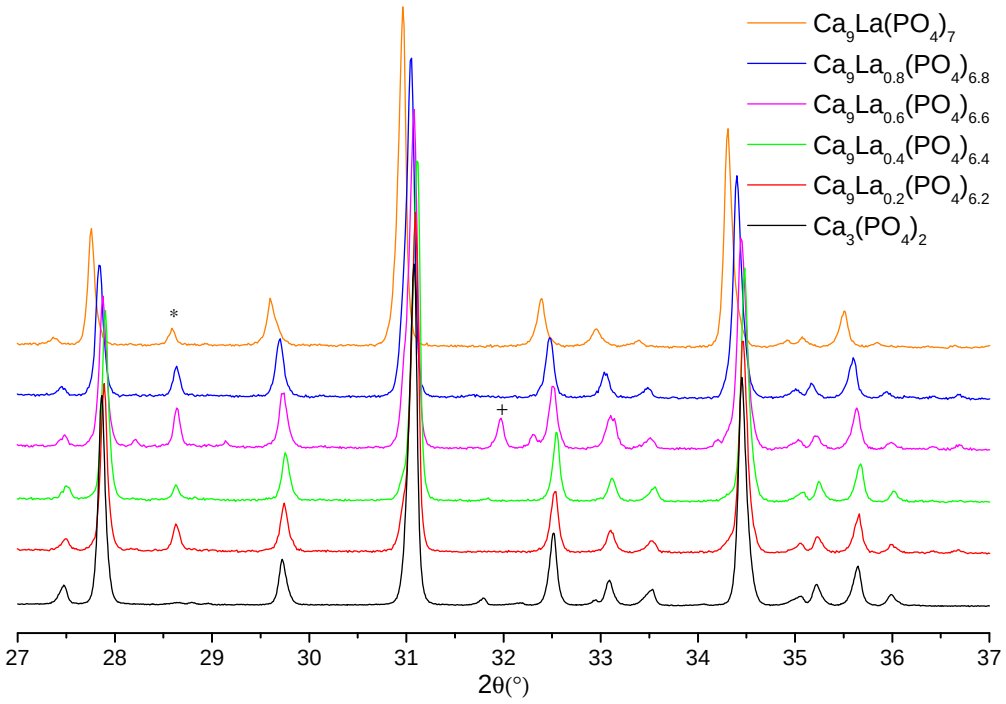

Figure 7-2 X-ray diffraction patterns of La substituted β-tricalcium phosphate indicating the region $27-37°$ illustrating shift in peak positions, where $*$ represents monazite and + represents hydroxyapatite.

monazite phase but by looking again at the diffraction patterns, the proportion of monazite in the x=0.4 sample appears less than for neighbouring compositions. Another explanation could be that there are different degrees of ordering within the samples, possibly causing changes in the sizes of the Ca sites. This is however just speculation and more information in necessary to determine what actually is happening here.

Comparing the lattice parameters to work done on $Ca_9La(PO_4)_7$ by Golubev and Lazoryak [12], the c lattice parameter is the same in each case, with a value of 37.55 Å. There is however a difference in the a and b lattice parameters, where the slightly smaller value of 10.456 Å was obtained, compared with 10.492 Å in the study by Golubev. This is much like in the Ga case, where here a smaller value could be explained by the additional phases present in sample, meaning again that the sample produced by Golubev may be La deficient or contain some impurity.

Rietveld refinement was performed on the x-ray diffraction patterns following the same procedure as in Chapters 4 and 5 with the patterns initially indexed to the β-TCP structure published by Yashima *et al.* [24]. Only the lattice parameters and atomic po-

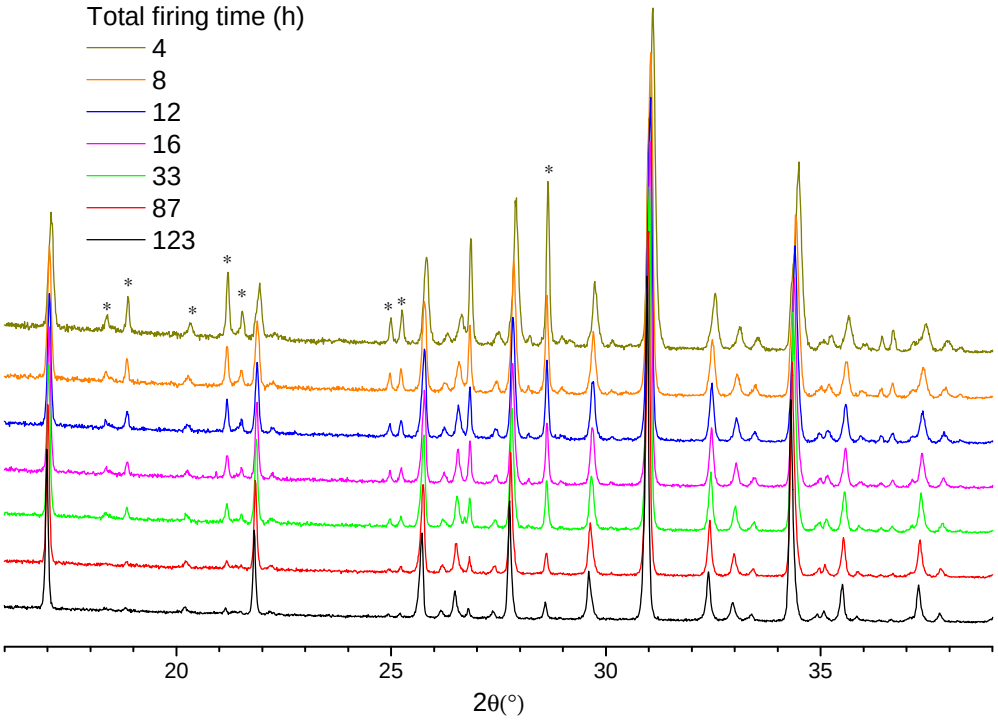

Figure 7-3 X-ray diffraction patterns of 4 – 123 h firings of $Ca_9La(PO_4)_7$ indicating the region 16 – 39°, where ∗ represents monazite.

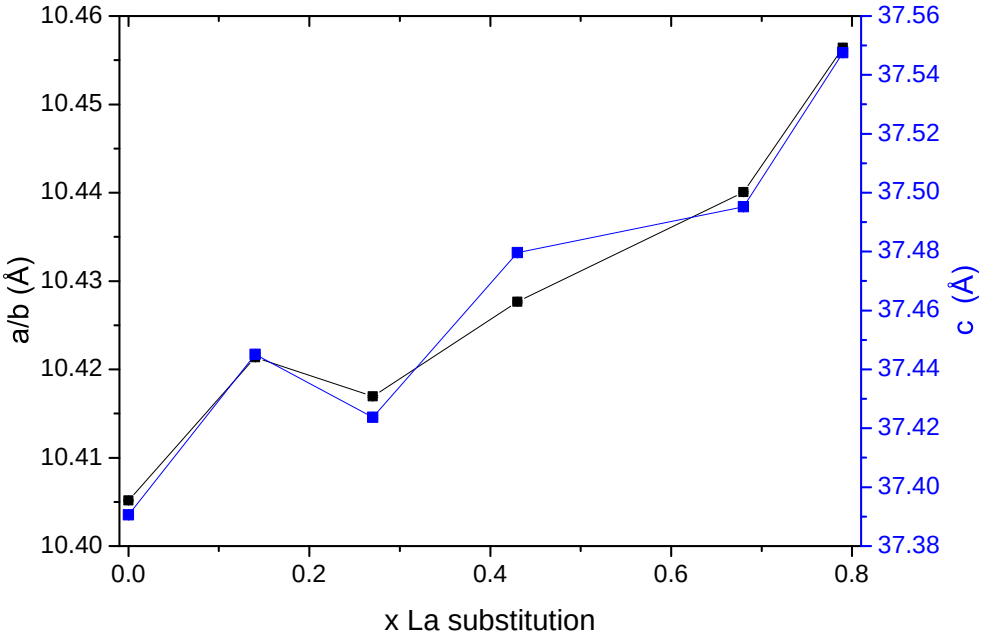

Figure 7-4 Lattice parameters of La substituted β-tricalcium phosphate as determined by Rietveld refinement of x-ray diffraction data. Compositions used are those calculated in Section 7.4.1. Error bars smaller than symbols used.

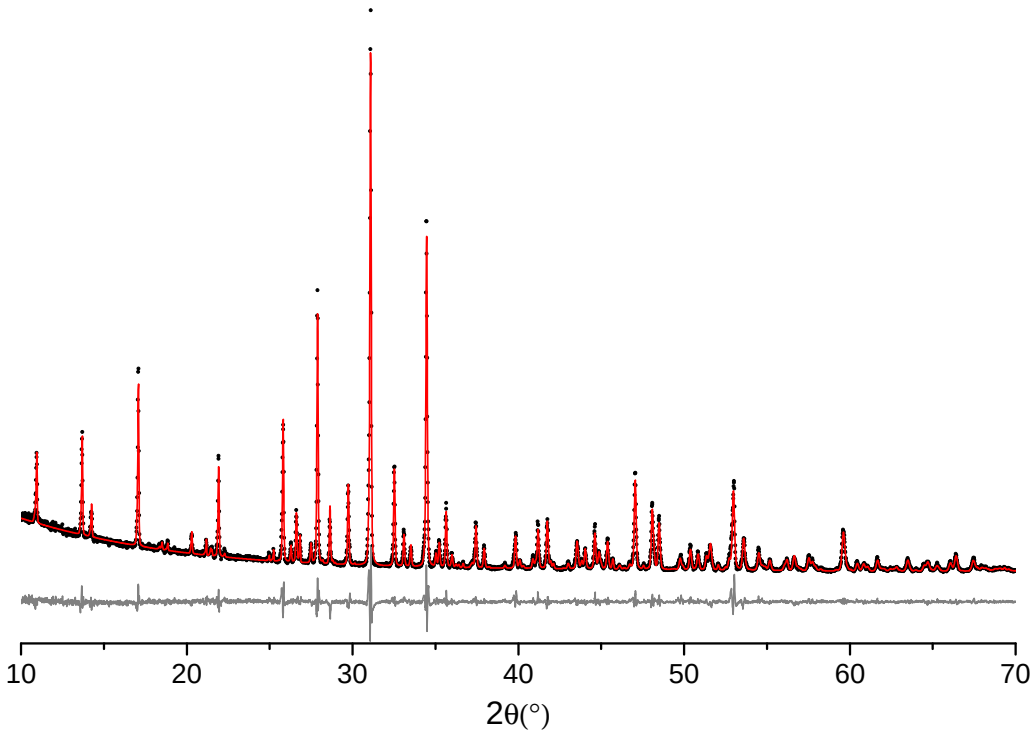

Figure 7-5 Powder x-ray diffraction pattern (·), Rietveld refinement (–), and difference plot (–) for $Ca_9La_{0.2}(PO_4)_{6.2}$.

sitions were refined at first before the occupancies of the Ca sites and isotropic thermal parameters were also refined. Finished refinements are shown in Figures 7-5 to 7-9.

For the refinement of the Ca site occupancies, La was allowed to freely refine on each Ca site. For the Ca(1) and Ca(2) sites the Ca occupancy was within a couple of percent of fully occupied with the La occupancy taking values of around 0.1 %. The Ca(3) site again showed a Ca occupancy of around 1 but in this case the La occupancy was at least 1 % after the initial refinement of the site. For the Ca(4) and Ca(5) sites the La occupancy remained at 0 with the Ca occupancy reducing slightly as expected for the Ca(4) site and staying around 1 for the Ca(5) site. From this it was decided to fix the Ca(1), Ca(2) and Ca(5) sites to have Ca occupancies of 1 and let the Ca(3) and Ca(4) sites freely refine with both Ca and La for the Ca(3) site and just Ca for the Ca(4) site.

Structures for monazite and, in the x=0.6 case, hydroxyapatite were added to the refinement in an attempt to both improve the fit and to identify the proportions of these phases present. Occupancies of the Ca(4) and Ca(5) sites along with weight percentages of the additional phases present are shown in Table 7-1. Here we can see that monazite makes up a fairly large proportion of the samples produced, especially in the lower La

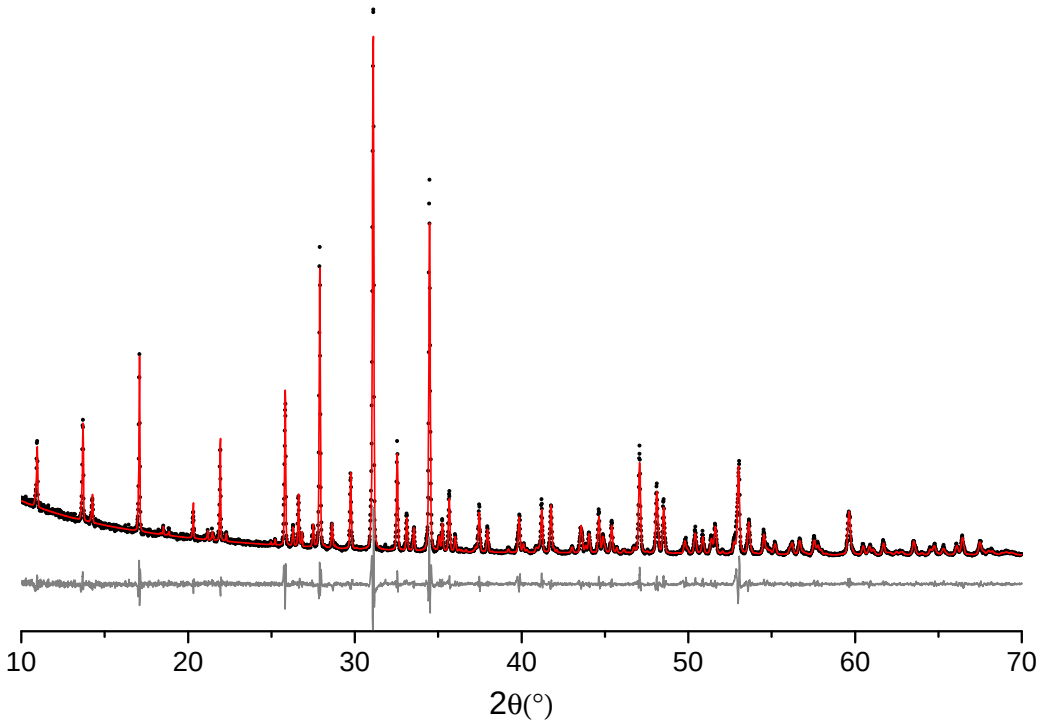

Figure 7-6 Powder x-ray diffraction pattern (·), Rietveld refinement (–), and difference plot (–) for $Ca_9La_{0.4}(PO_4)_{6.4}$.

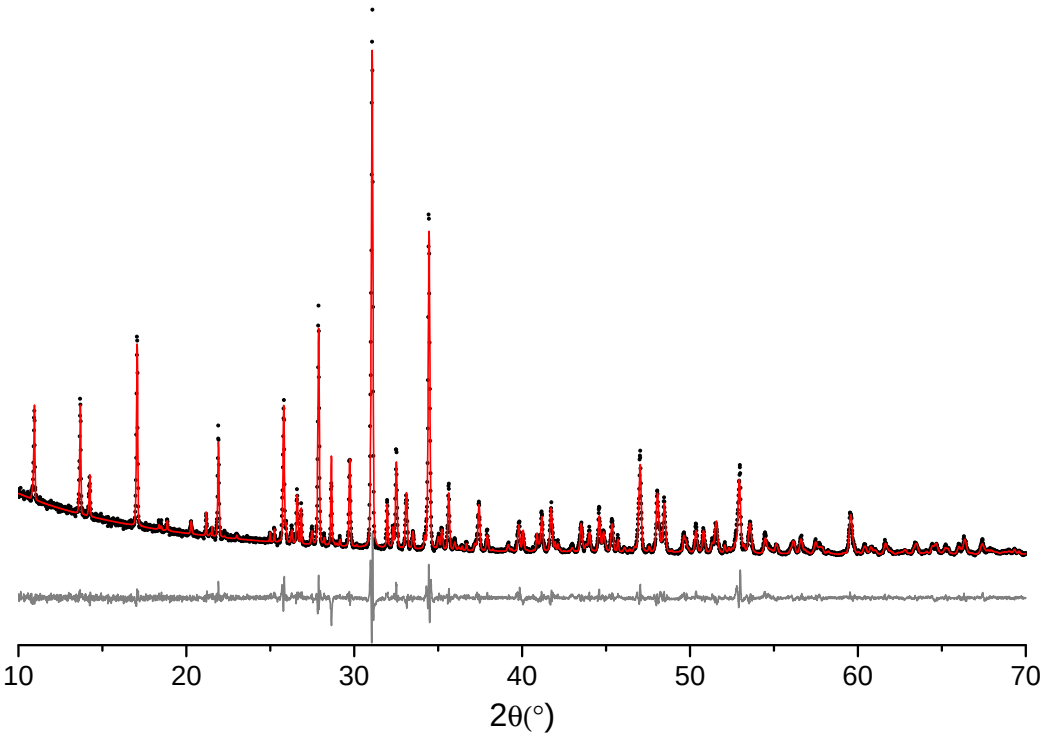

Figure 7-7 Powder x-ray diffraction pattern (·), Rietveld refinement (–), and difference plot (–) for $Ca_9La_{0.6}(PO_4)_{6.6}$.

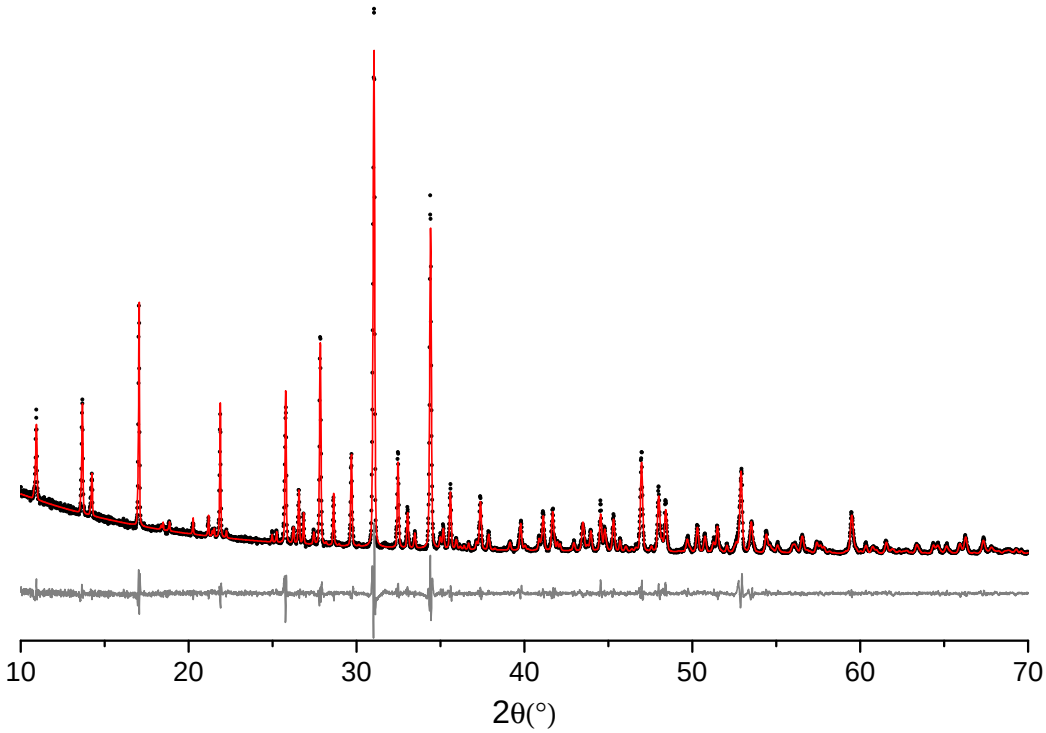

Figure 7-8 Powder x-ray diffraction pattern (·), Rietveld refinement (–), and difference plot (–) for $Ca_9La_{0.8}(PO_4)_{6.8}$.

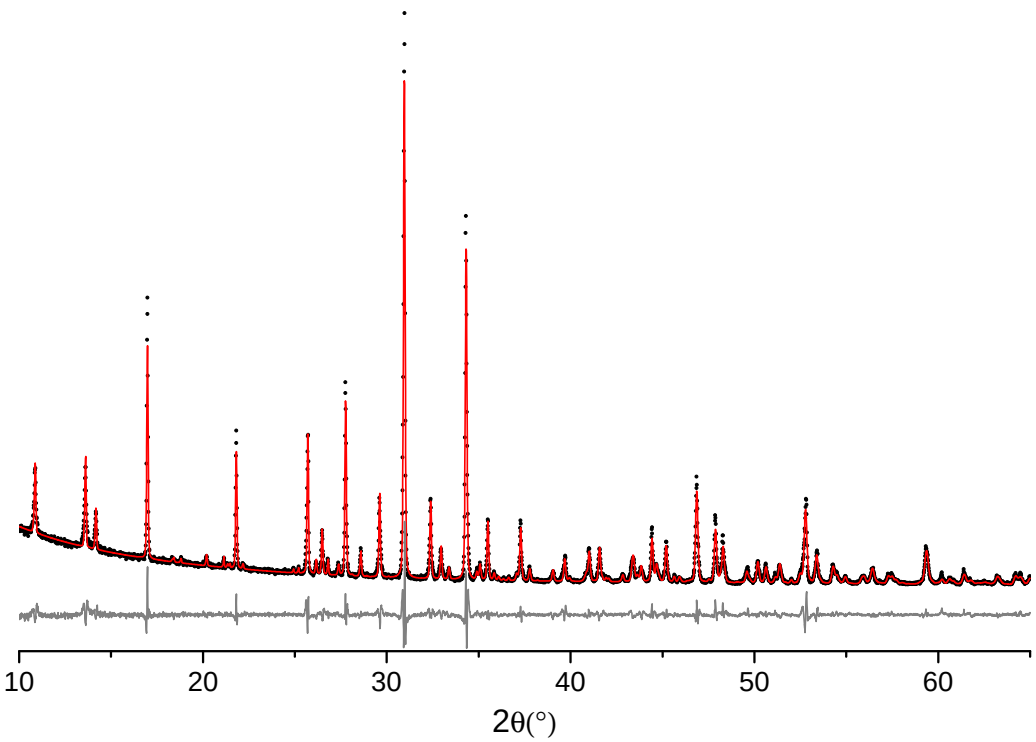

Figure 7-9 Powder x-ray diffraction pattern (·), Rietveld refinement (–), and difference plot (–) for $Ca_9La(PO_4)_7$.

Table 7-1 Occupancies of Ca(3) and Ca(4) sites along with weight percent of phases present as determined by Rietveld refinement of x-ray diffraction data, where HA represents hydroxyapatite, $Ca_5(PO_4)_3(OH)$.

	Firing	Ca(3)				wt% phases		
x	(h)	Ca	La obs.	La exp.	Ca(4)	β-TCP	$LaPO_4$	HA
0.2	12	1.08(15)	0.02(5)	0.07	0.450(9)	97.59(8)	2.41(8)	
0.4	12	1.02(15)	0.03(5)	0.13	0.478(9)	98.78(7)	1.22(7)	
0.6	16	1.00(17)	0.07(6)	0.20	0.39(1)	91.8(2)	2.36(7)	5.8(2)
0.8	20	1.01(13)	0.05(4)	0.27	0.42(1)	97.23(7)	2.77(7)	
1	123	1.00(16)	0.05(5)	0.33	0.38(1)	98.53(9)	1.48(9)	

containing samples. The apparently consistent amount of monazite in the samples is due to the samples with higher La content having longer firing times, which was shown earlier to improve the phase purity (Fig. 7-3).

Looking at the occupancy of the Ca(3) site, it can be seen that the Ca occupancy is often higher than allowed and always higher than expected, although there are rather large errors on these values. La occupancy on the Ca(3) site is, in most cases, very much lower than expected, even with the quantities of monazite also present. For the Ca(4) sites, the occupancies are also greater than expected from both the compositions and the observed La occupancy on the Ca(3) site. These unexpected values could be due to the lineshape problems mentioned for the other two systems or in this case it may also be that the proportions of the additional phases present are slightly wrong, leading to inaccurate fits.

7.3 Neutron diffraction

7.3.1 Time of flight diffraction

Time of flight neutron diffraction data have been acquired on the GEM diffractometer for the x=1.0 sample with Rietveld refinement being performed on bank 4 of the data. A good fit was obtained (Fig. 7-10), although there was some variation between data and fit for some of the peaks at longer TOF. As with the other systems, the structure obtained from refinement of the x-ray diffraction pattern from the same sample was used as a basis with anisotropic displacement parameters added to improve the fit. Occupancy of the Ca(3) site was close to that found using XRD with a Ca occupancy of 0.99 and a

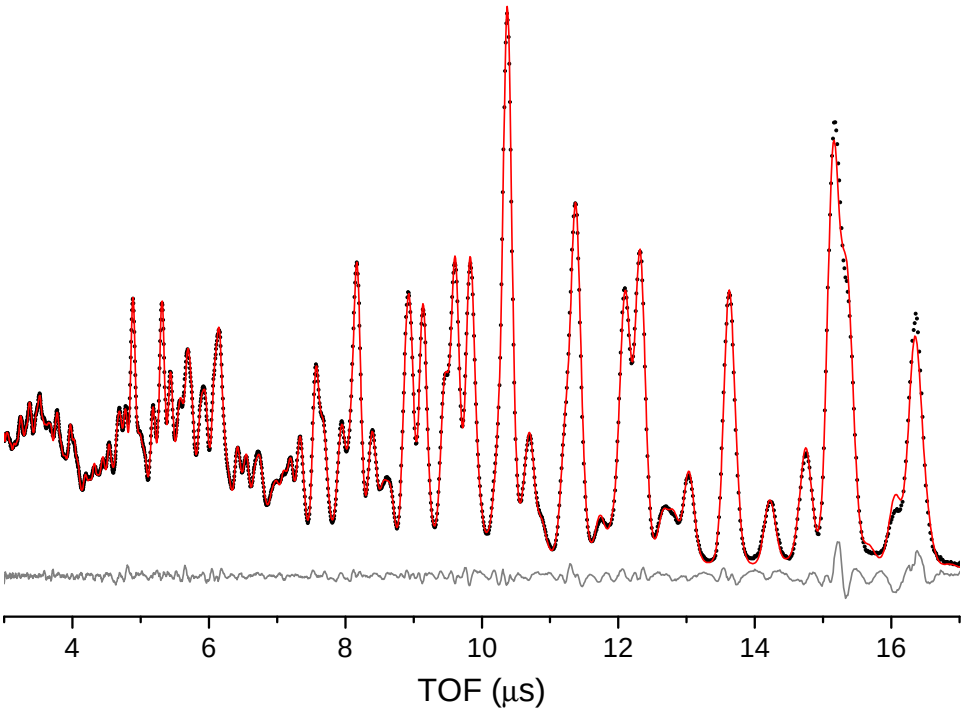

Figure 7-10 Powder neutron diffraction pattern (·), Rietveld refinement (–), and difference plot (–) for $Ca_9La(PO_4)_7$ at room temperature taken from bank 4 of GEM diffractometer.

La occupancy of 0.05. However, errors in these occupancies were again of the order of 10^6, suggesting that, again, there are some problems arising in the software. The Ca occupancy of the Ca(4) site was much higher than in the XRD case and of that expected, with a value of 0.64 ± 0.03. Some of this difference in occupancy could be due to the monazite phase present, where a larger proportion than in the XRD case of 6.55 wt.% was identified.

7.3.2 Total correlation functions

The total correlation function obtained for the x=1.0 sample is shown in Figure 7-11 alongside that of the 'pure' β-TCP sample. No additional features appear to be present, which is as expected since 6-coordinated to 8-coordinated La would lie in the region 2.43 – 2.54 Å [14], within the area covered by the main Ca–O correlations. This also means that no additional insight may be obtained into the environment of the La ions from the $T(r)$ plot. La in any monazite present would be 9-coordinated and located around 2.58 Å, also within the main Ca–O peak. The overall shapes of the peaks in the

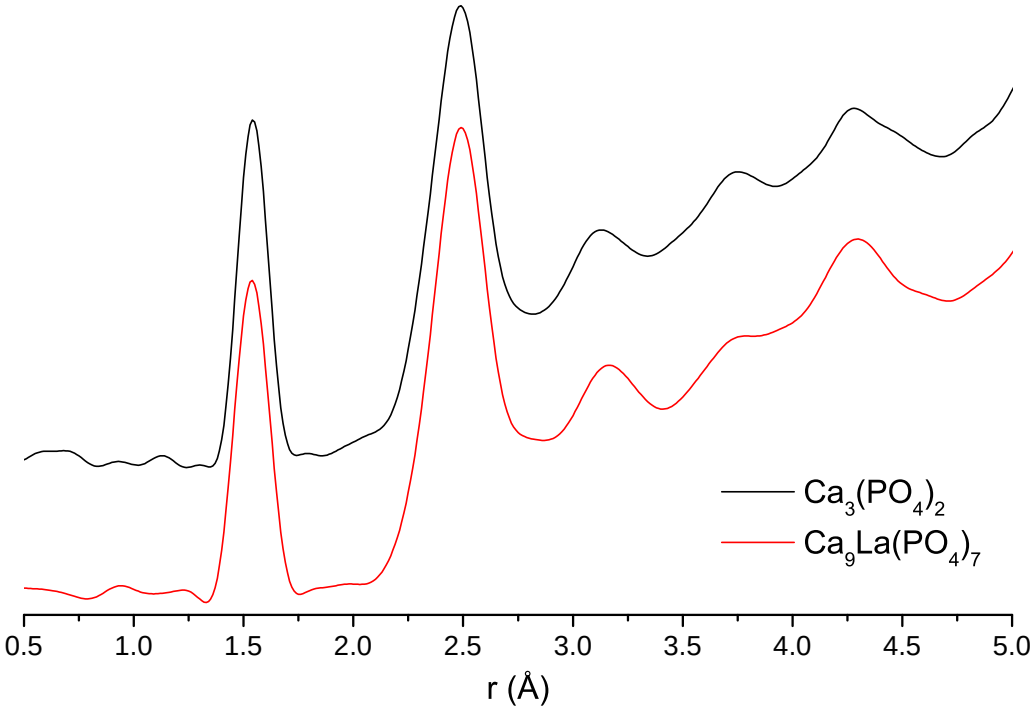

Figure 7-11 $T(r)$ for $Ca_3(PO_4)_2$ and $Ca_9La(PO_4)_7$ samples.

two plots appear very similar, indicating that the structure of the La substituted sample is close to that of the 'pure' β-TCP.

7.4 Nuclear magnetic resonance

7.4.1 ^{31}P nuclear magnetic resonance

^{31}P MAS NMR was undertaken on the 500 MHz spectrometer for the entire range of samples with spectra shown in Figure 7-12, alongside the spectrum obtained from the 'pure' β-TCP sample. La substitution appears to cause the peaks between 7 and 3 ppm to greatly decrease in intensity with new resonances between approximately 0 and −3 ppm taking their place. The positions of the peaks remain fairly constant throughout the samples, suggesting that the La has little effect on the P environments unless within close proximity. The small peak visible in all spectra around −4.5 ppm is due to the monazite phase present with the sharp peak at 2.8 ppm in the x=0.6 sample being due to hydroxyapatite.

The x=1.0 sample was run with pulse delays ranging from 1 − 720 s in order to

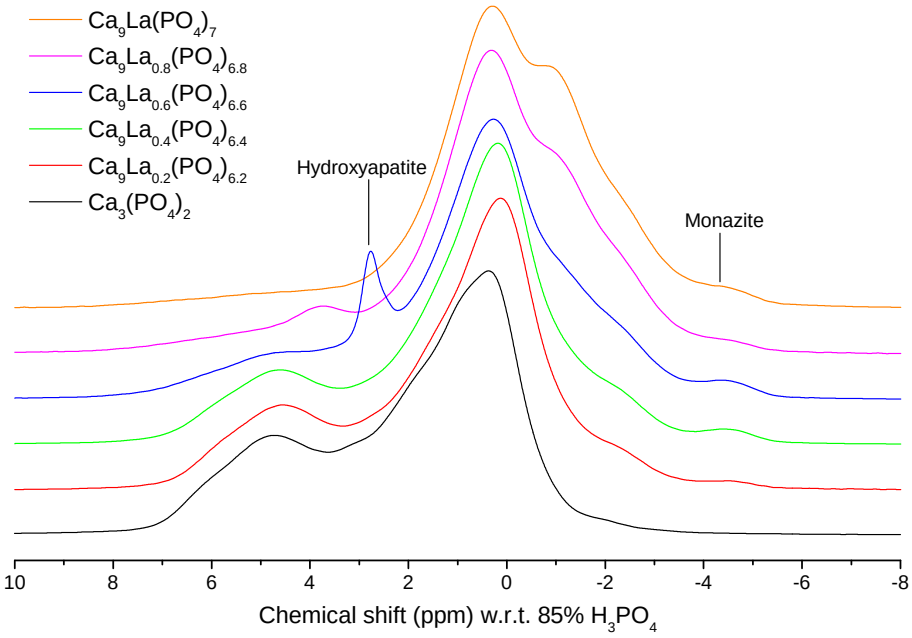

Figure 7-12 ^{31}P NMR spectra of La substituted β-tricalcium phosphate normalised to spectrum area.

confirm that the peak at −4.5 ppm is indeed due to an additional phase being present. Spectra are shown in Figure 7-13, where it is obvious that the additional peak has a much longer T_1. The rest of the spectrum appears to contain no other phases, with an increase at a consistent rate throughout the spectrum. The β-TCP phase can be seen to have a shorter T_1 than in the Ga case, with the maximum intensity being reached by approximately 30 s.

From these spectra, an attempt can be made to calculate the T_1 of the $LaPO_4$ phase in order to determine how much $LaPO_4$ is actually present. The fractional intensities of $LaPO_4$ were calculated for each spectrum, and have been plotted against the pulse delays in Figure 7-14. An attempt was then made to fit the data to the inverse exponential function $c - exp(-t/T_1)$, as would be expected for the decay of intensity (Eq. 4-6), where c should give the actual $LaPO_4$ fraction and T_1 the longitudinal relaxation time. In this case a poor fit was obtained. However, fitting to two of these functions gives the fit shown in Figure 7-14, indicating that some intensity from the main β-TCP phase was also present in the fits. From the fitted curve, values of 48 ± 7 s and 550 ± 620 s were obtained for T_1 of the two materials. The value obtained for the β-TCP phase is slightly higher than expected, since from Figure 7-13 it can be seen that the maximum intensity

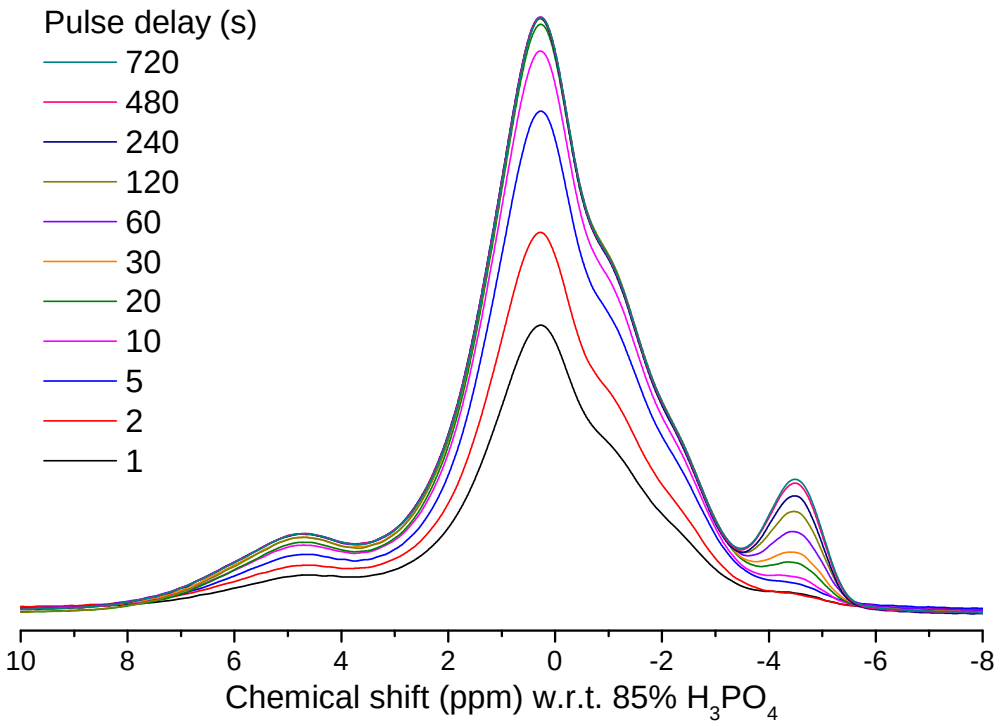

Figure 7-13 ^{31}P NMR spectra of 16 h firing of $Ca_9La(PO_4)_7$ with pulse delays ranging from 1–720 s.

for that phase is reached by around 30 s. The values for the $LaPO_4$ phase seem acceptable, with the intensity of that peak continuing to increase even above 720 s. However, there is a very large uncertainty on this value, probably due to large number of variables compared to the number of data points fitted.

If this fit is assumed to be representative, then the actual proportion of $LaPO_4$ in the sample is approximately 8 %. From this, the amount of La within the β-TCP, i.e. x, can be calculated. For $Ca_9La(PO_4)_7$, we can express this as $Ca_9(PO_4)_6$ + $LaPO_4$, where it can now be seen that 1 out of every 7 P atoms is associated with a La atom, i.e. 14 %. From the value obtained in Figure 7-14, the amount of P in the $LaPO_4$ phase is 8 %, meaning that 6 % of the total P is associated with La present in the β-TCP. Now, by dividing the amount of P associated with La in β-TCP by the total amount of P associated with La (6%/14%) and multiplying by the initial amount of La (1 in this case), the amount of La within the β-TCP can be calculated, which gives a value of x=0.43 in this case. By assuming the intensities scale to the same extent in other samples, values of x can be calculated in a similar fashion. Calculations have been performed on the ^{31}P spectra with the longest firings for each sample, with values shown

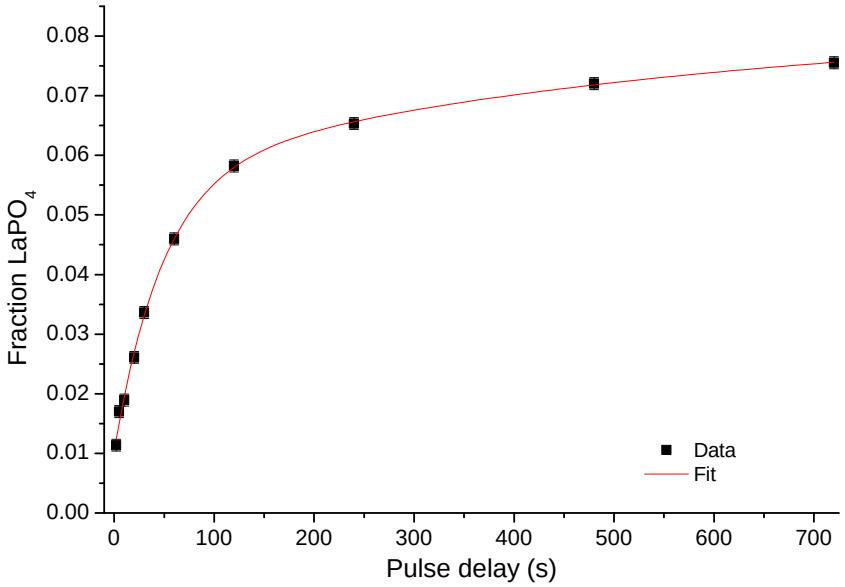

Figure 7-14 Fractional intensities of $LaPO_4$ peak in ^{31}P NMR spectra of 16 h firing of $Ca_9La(PO_4)_7$ at a range of pulse delays, along with fit to data.

Table 7-2 Recalculated sample compositions, taking into account $LaPO_4$ present in ^{31}P NMR spectra.

x	Firing time (h)	Measured % $LaPO_4$	Corrected % $LaPO_4$	Recalculated x
0.2	12	0.6	1.0	0.14
0.4	12	1.2	2.1	0.27
0.6	16	1.4	2.5	0.43
0.8	33	1.0	1.8	0.68
1	87	1.8	3.1	0.79

in Table 7-2. From these values it can be seen that between 20 and 30 % of the La is lost to the $LaPO_4$ phase. The monazite present in the samples was thought to account for the low occupancies obtained from Rietveld refinement of the XRD data, however, comparing the recalculated values of x with the occupancies in Table 7-1, the refined occupancies still appear to be much lower than expected.

The effect that the length of firing has on the materials was also investigated, with spectra from four different length firings of the x=1.0 sample being acquired (Fig. 7-15). These show a similar trend to that seen in Figure 7-12, with shorter firing times being analogous to lower La substitution. As the firing time increases the amount of monazite is reduced, causing a decrease in the peak at −4.5 ppm, with a progression

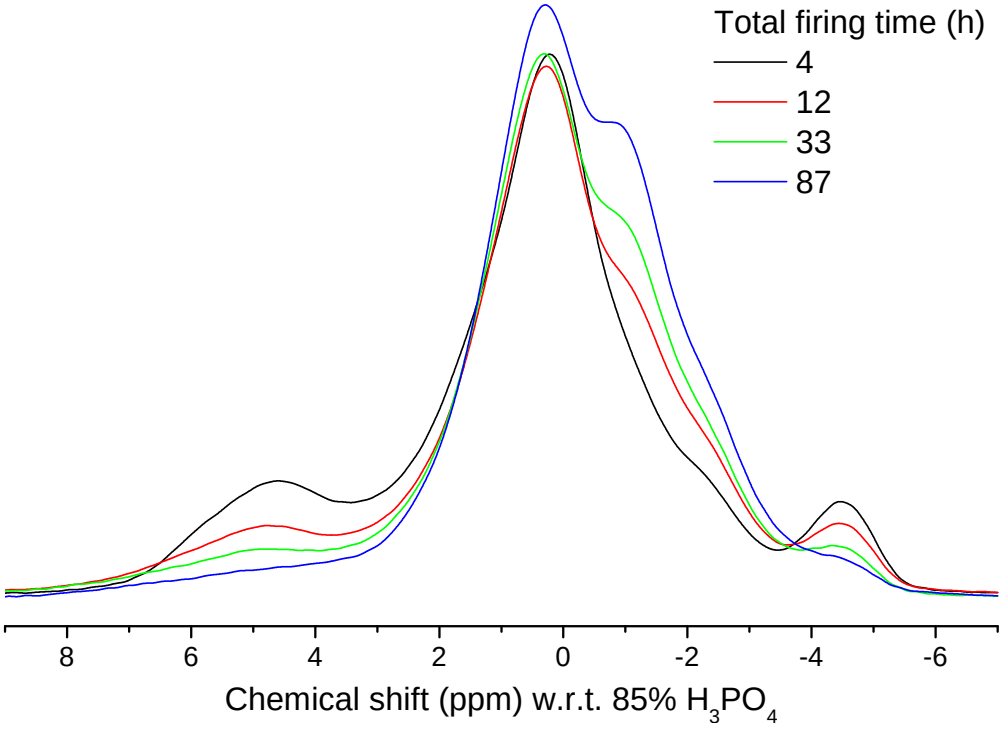

Figure 7-15 ^{31}P NMR spectra of $Ca_9La(PO_4)_7$ with a range of firing times normalised to spectrum area.

in the −1 ppm peak being observed. In this case it is more obvious that there is no shift in the spectra with increasing La substitution, again suggesting that the La has no long-range influence on the P sites.

Due to the fairly narrow lineshape some idea of the substitution mechanism is necessary in order to fit the spectra. From the XRD and ND data, it appears that the La is substituting onto the Ca(3) site. If we now look at the next-nearest neighbours of the P sites (Fig. 3-3), it can be seen that the P(1), P(2) and P(3) sites have 3, 2 and 2 Ca(3) sites respectively as next-nearest neighbours. This means that, along with the splitting of P environments from the half occupied Ca(4) site, there will be additional splitting occurring when La is present on the Ca(3) site. This could give rise to up to 28 different peaks which, due to the P–Ca(3) distances being fairly similar, could also be very close together for similar configurations. Since the spectra are also mostly featureless this makes fitting almost impossible.

7.4.2 ^{43}Ca nuclear magnetic resonance

Natural abundance ^{43}Ca MAS NMR spectra were obtained for the $Ca_9La_{0.4}(PO_4)_{6.4}$ and the $Ca_9La_{0.8}(PO_4)_{6.8}$ samples on the 600 MHz spectrometer at Warwick, on the $Ca_9La_{0.8}(PO_4)_{6.8}$ sample on the 850 MHz spectrometer at Warwick and also on the $Ca_9La(PO_4)_7$ sample by Zhehong Gan on the 820 MHz spectrometer at NHMFL. Spectra are shown in Figure 7-16 along with the 'pure' β-TCP spectrum. A slight upfield shift is noticeable in all of the La substituted samples, which appears to occur to a greater extent at lower fields. Spectra at lower fields are also much broader, suggesting that more quadrupolar broadening may be present.

From the x=0.8 spectra obtained at different fields, an estimate of C_Q can be made. The quadrupole induced shift (QIS), in ppm, of the peaks from their true values is given by

$$QIS = -\frac{3}{40}F(I)\frac{C_Q^2}{\nu_0^2}\left(1+\frac{\eta}{3}\right) \tag{7-1}$$

where $F(I)$ is a spin-dependent factor, equal to $5/147$ in the I=7/2 case [25]. This equation can then be rearranged to show how the QIS will vary with field to give

$$\Delta QIS = \left|\frac{3}{40}\frac{5}{147}P_Q^2\left[\frac{1}{\nu_{0_1}^2}-\frac{1}{\nu_{0_2}^2}\right]\right| \tag{7-2}$$

where $P_Q^2 = C_Q^2\left(1+\frac{\eta}{3}\right)$. Using the values for ν_0 of 40.4 MHz and 57.2 MHz and the shift in the spectra of ~5 ppm, a value for P_Q of approximately 2.53 MHz. Since the peaks here are mostly symmetric it can be assumed that $\eta \approx 0$ and therefore $C_Q \approx$ 22 MHz. This comparable to C_Q for hydroxyapatite of 2.6 MHz [46], where the sites should be fairly similar to β-tricalcium phosphate.

Due to the broad and noisy nature of the spectra an attempt was made to again fit them to Gaussian lineshapes. The fit from the 'pure' β-TCP sample (Fig. 5-22) was used as a basis for the fitting where, since substitution is thought to be onto the Ca(3) site, an effort was made to produce fits that followed this criteria before letting the software refine them. Fits are shown in Figures 7-17 to 7-20, where a good fit to the data has been obtained in each case. In the x=0.4 sample, the lineshape is similar to that of the 'pure' β-TCP and there is therefore some ambiguity in the fitting. As the La content increases, it becomes apparent that the right hand side of the main resonance, the position of the Ca(3) site peak, is both shifting upfield and reducing in intensity.

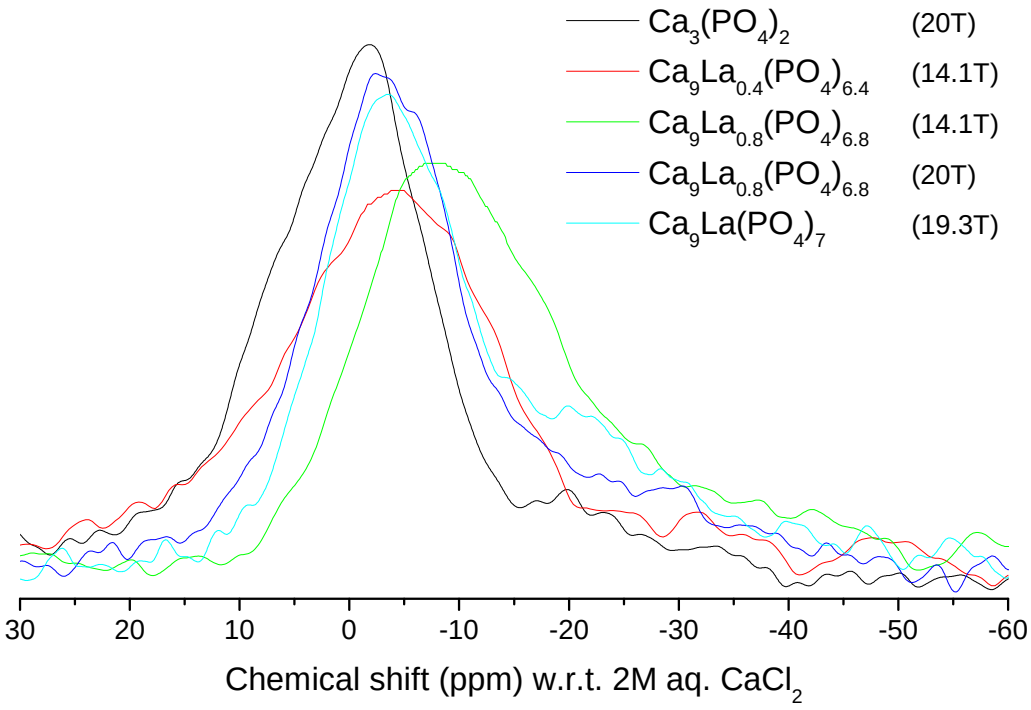

Figure 7-16 ^{43}Ca NMR spectra of La substituted β-TCP samples, normalised to peak area.

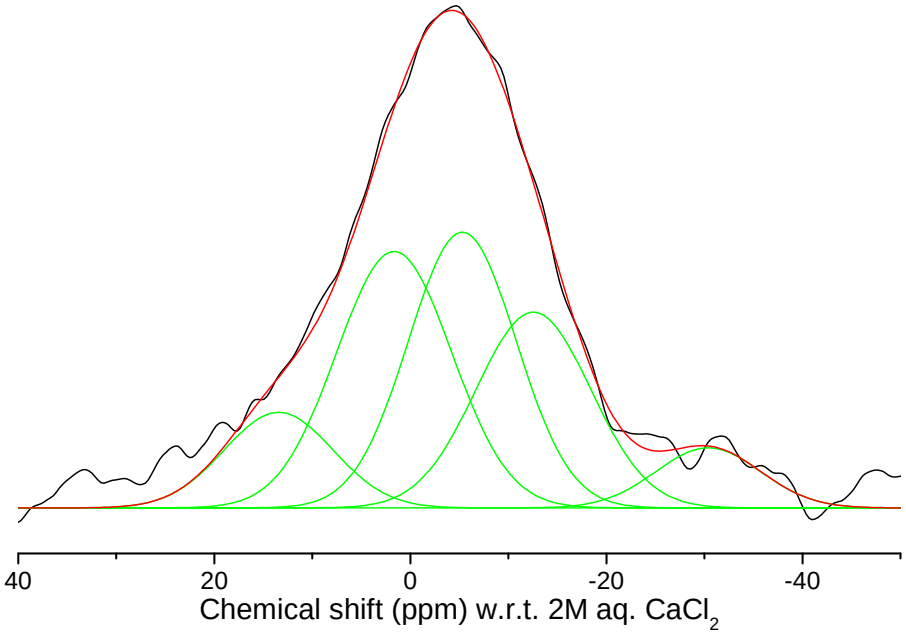

Figure 7-17 Fit of ^{43}Ca NMR spectrum of $Ca_9La_{0.4}(PO_4)_{6.4}$ sample at 14.1 T.

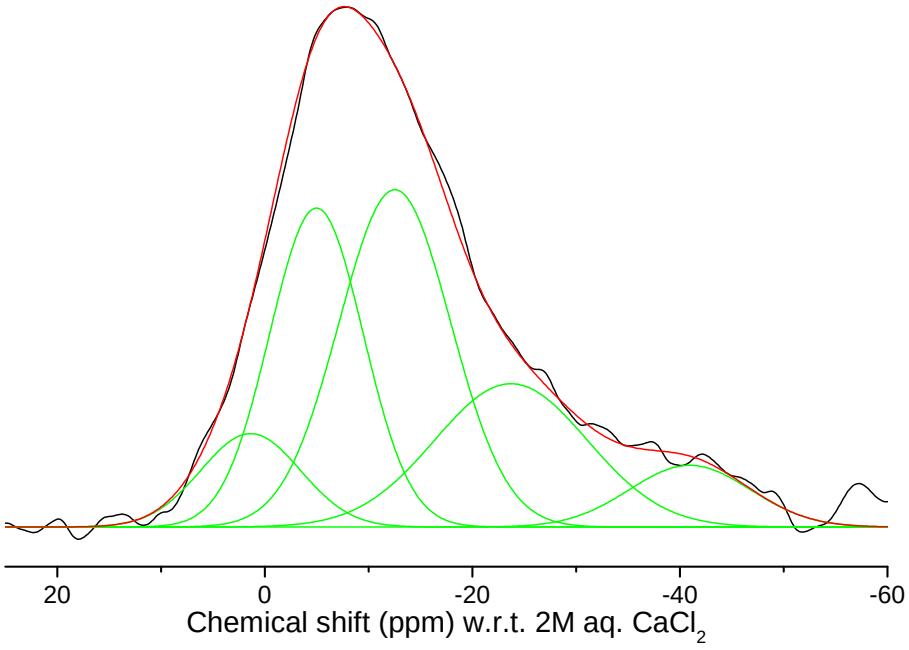

Figure 7-18 Fit of ^{43}Ca NMR spectrum of $Ca_9La_{0.8}(PO_4)_{6.8}$ sample at 14.1 T.

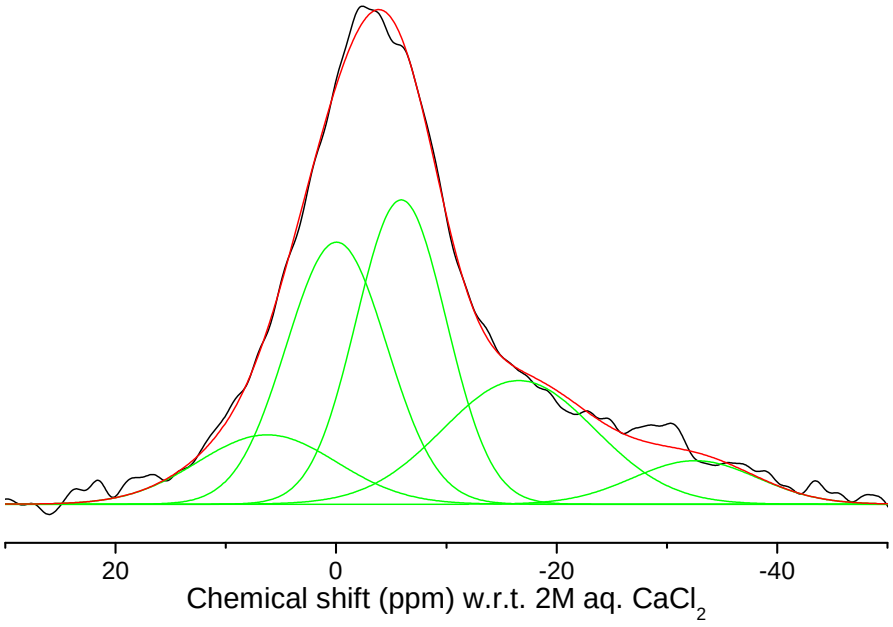

Figure 7-19 Fit of ^{43}Ca NMR spectrum of $Ca_9La_{0.8}(PO_4)_{6.8}$ sample at 20 T.

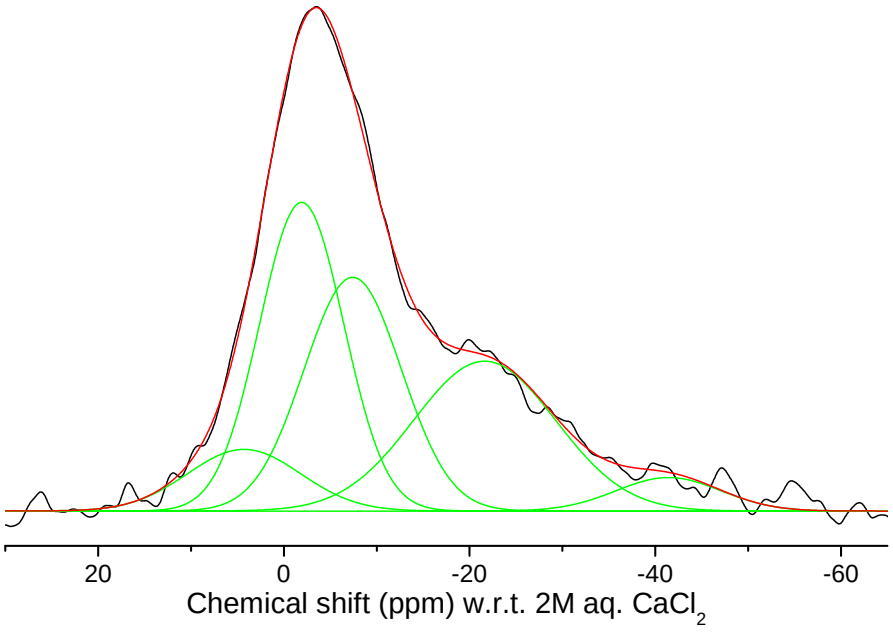

Figure 7-20 Fit of ^{43}Ca NMR spectrum of $Ca_9La(PO_4)_7$ sample at 19.3 T.

Table 7-3 Fit parameters of ^{43}Ca NMR on $Ca_9La_{0.4}(PO_4)_{6.4}$ sample at 14.1 T.

Site	Peak position ppm ±1	Peak width Hz ±50	Occupancy % ± 3		
			Undoped	Observed	Normalised
5	13.6	750	9.5	10	10
1	1.8	790	28.6	30	28
2	-5.0	740	28.6	30	28
3	-12.2	790	28.6	23	21
4	-29.9	720	4.7	6	6

Parameters from the fits are given in Tables 7-3 to 7-6. In general the site occupancies follow the expected behaviour of substitution onto the Ca(3) site, especially on the x=0.8 sample at 20 T. There are small discrepancies in some of the occupancies but this could be due to a number of factors such as poor signal to noise ratio, phasing problems or the monazite additionally present. Due to the difference in field between samples it is hard to make a comparison between the widths of the fitted peaks. For the x=0.8 sample there does not appear to be a general trend in linewidth with field, this is unexpected but understandable because of the poor signal to noise ratio.

Table 7-4 Fit parameters of ^{43}Ca NMR on $Ca_9La_{0.8}(PO_4)_{6.8}$ sample at 14.1 T.

Site	Peak position ppm ±1	Peak width Hz ±50	Occupancy % ± 3		
			Undoped	Observed	Normalised
5	1.6	650	9.5	9	8
1	-4.8	610	28.6	28	25
2	-12.3	730	28.6	36	31
3	-23.6	990	28.6	21	18
4	-40.8	780	4.7	7	6

Table 7-5 Fit parameters of ^{43}Ca NMR on $Ca_9La_{0.8}(PO_4)_{6.8}$ sample at 20 T.

Site	Peak position ppm ±1	Peak width Hz ±50	Occupancy % ± 3		
			Undoped	Observed	Normalised
5	6.3	850	9.5	11	10
1	0.1	610	28.6	30	27
2	-5.8	550	28.6	31	28
3	-16.4	930	28.6	21	19
4	-32.4	760	4.7	6	5

Table 7-6 Fit parameters of ^{43}Ca NMR on $Ca_9La(PO_4)_7$ sample at 19.3 T.

Site	Peak position ppm ±1	Peak width Hz ±50	Occupancy % ± 3		
			Undoped	Observed	Normalised
5	4.4	820	9.5	9	7
1	-1.8	610	28.6	32	28
2	-7.4	710	28.6	28	24
3	-21.6	1030	28.6	26	23
4	-41.4	760	4.7	4	4

7.5 Summary

A series of La substituted samples have been produced which have been shown to have the β-TCP structure. The synthesis route does, however, lead to formation of other phases, most notably monazite. These additional phases are seen to decrease with increasing firing times of the samples. Rietveld refinement of x-ray and neutron diffraction patterns suggests that substitution is taking place onto the Ca(3) site, however the total occupancies of the Ca(3) and Ca(4) sites are far from the values expected. The total correlation function produced for the x=1.0 sample gives no additional information, mostly due to the La–O correlations being within the same region as the main Ca–O peak. ^{31}P NMR shows a progressive trend in the lineshape obtained but the complexity of substitution onto the Ca(3) sites means that fitting of the spectra is not practical. ^{43}Ca NMR gives lineshapes which can be fitted, in some cases almost unambiguously, to that predicted for substitution onto the Ca(3) site.

Chapter 8

Substitution of other atoms

Several other β-TCP systems have been produced by AWE or by undergraduate students under the supervision of the author in an attempt to further understand the structure and substitution mechanisms in the material. The main focus of this work has been on co-substitution. Systems have been made of β-TCP substituted with both trivalent and monovalent cations, which should keep the cation site occupancies constant, in order to determine whether this will affect the stability of the structure under substitution. Additionally, samples have been made with co-substitution of different trivalent cations to determine whether the structure remains as predictable as the end members. Three of the more successful systems are detailed in the sections below.

8.1 Sm substitution

Samples were prepared by Dr. Shirley Fong at AWE by grinding, under acetone, stoichiometric amounts of $CaH(PO_4)$, $CaCO_3$ and Sm_2O_3 according to the general formula $Ca_9Sm_x(PO_4)_{6+x}$ with samples of x=0.2, 0.4, 0.6, 0.8 and 1.0 being produced. The resulting mixture was then heated at a rate of 10 °C/min up to 1050 °C and held for 4 h. This was then repeated a further two times to help ensure phase purity.

8.1.1 X-ray diffraction

X-ray diffraction patterns were taken for the entire composition range and are shown in Figure 8-1. Patterns appear consistent with the β-TCP pattern, with no additional phases being present. Positions of the peaks remain mostly unchanged with the most noticeable difference being a change in intensity of some of the diffraction peaks. This is unsurprising since Sm has a similar ionic radius to Ca (1.079 Å for Sm *cf.* 1.12 Å for Ca [44]) for 8-coordination, but its increased atomic number gives it a much greater

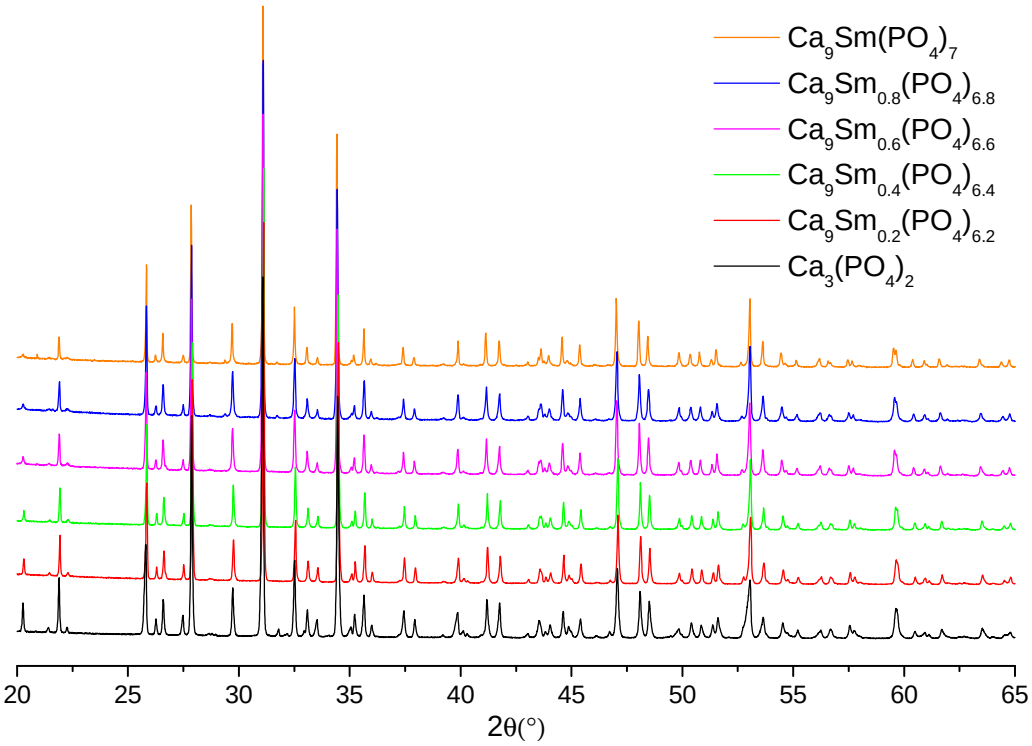

Figure 8-1 X-ray diffraction patterns of Sm substituted β-tricalcium phosphate.

scattering factor.

Lattice parameters were obtained by Rietveld refinement of the x-ray diffraction patterns and are shown in Figure 8-2. The *a* and *b* lattice parameters show little change with composition, expected from the similar ionic radius of Sm. The *c* lattice parameter appears to change erratically, although the variation is only ~0.01 Å throughout the whole compositional range. These similar atomic radii may result in little change to the β-TCP structure.

8.1.2 ^{31}P nuclear magnetic resonance

^{31}P MAS NMR spectra were obtained using the 360 MHz spectrometer for the entire range of samples, including the 'pure' β-TCP sample, with spectra shown in Figure 8-3. Due to the paramagnetic nature of Sm, its presence will cause a broadening of the resonances from any nearby P sites. This is apparent in the spectra, where an increased Sm content causes a distinct broadening across the lineshapes. The main change in the lineshapes is from either a decrease in intensity or broadening of the peak located

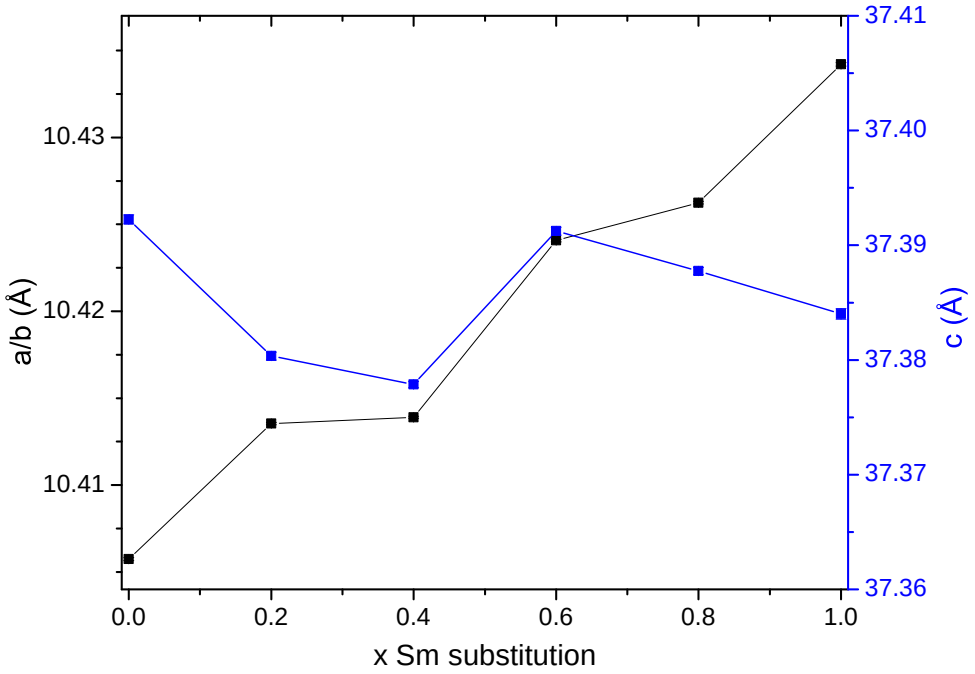

Figure 8-2 Lattice parameters of Sm substituted β-tricalcium phosphate as determined by Rietveld refinement of x-ray diffraction data. Error bars smaller than symbols used.

around 5 ppm. Also noticeable is a new and very broad set of resonances appearing between 28 ppm and the main part of the spectrum. These are most likely due to P sites with Sm next-nearest neighbours, where the proximity of the Sm ions causes a paramagnetic shift in position and extreme broadening.

From the size of Sm, it would be expected that Sm could substitute onto any of the Ca sites. However, without having some idea of the site of substitution, fitting would be difficult even in simpler cases. Even if it is assumed that Sm substitution takes place onto the Ca(5) site, which would be the simplest case, 8 peaks would be required. Fitting the spectra obtained to this many peaks cannot be done with any degree of certainty due to the broadness of the spectra.

8.2 Al/Na co-doped substitution

Samples were prepared at Warwick by vacation student Alex Marsden under the supervision of the author, by grinding together stoichiometric amounts of $CaH(PO_4)$, $CaCO_3$, Al_2O_3 and Na_2CO_3 according to the general formula $Ca_{3-x}Al_xNa_x(PO_4)_2$ with samples

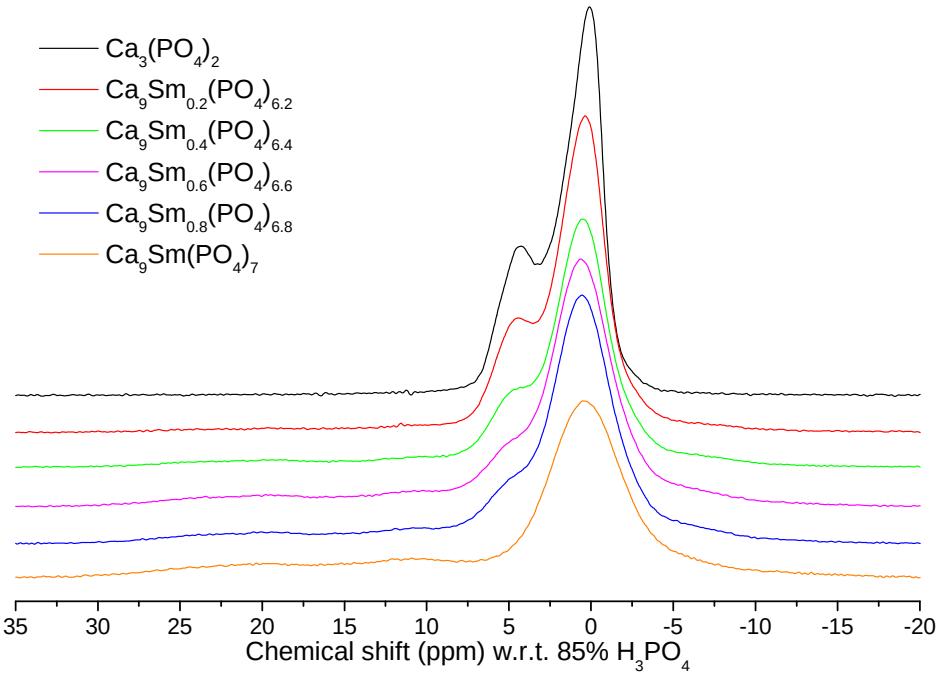

Figure 8-3 ^{31}P NMR spectra of Sm substituted β-tricalcium phosphate normalised to spectrum area.

of x=0.033, 0.066, 0.1, 0.2 and 0.3 being produced. The resulting mixture was then heated at a rate of 5 °C/min up to 1050 °C and held for 4 h. This was then repeated further times in an attempt to produce phase pure samples.

8.2.1 X-ray diffraction

X-ray diffraction patterns were taken for the entire composition range, with the x=0.066, 0.1 and 0.2 samples run on the Bruker D5005, and are all shown in Figure 8-4. The patterns appear to mostly follow the β-TCP structure, however a second phase, identified as β-$Ca_2P_2O_7$ is present in most of the samples, with a small amount of $AlPO_4$ also present in the x=0.2 and 0.3 samples. Since Al is quite small (0.535 Å) and Na (1.02 Å) is of comparable size to Ca (1.00 Å) for 6-coordination [44], a decrease in unit cell size would be expected and can be seen here in the increasing angles of the diffraction peaks with composition.

Basic Rietveld refinement was performed on the patterns in order to determine unit cell parameters which can be seen in Figure 8-5. From this, the c-axis can be seen to contract at a roughly linear rate, with the same happening for the a and b axes initially. However, at some point around x=0.2 the a/b lattice parameters decease drastically

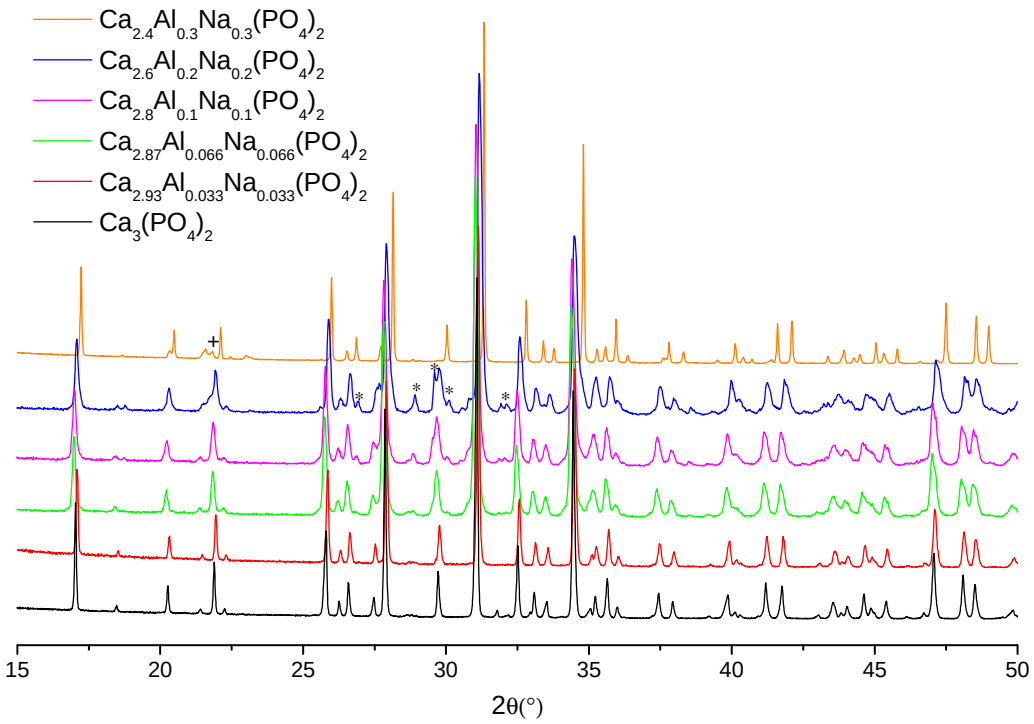

Figure 8-4 X-ray diffraction patterns of Al/Na substituted β-tricalcium phosphate, where $*$ represents β-$Ca_2P_2O_7$ and + represents $AlPO_4$.

from around 10.40 Å to 10.32 Å. This could be due to the sites onto which the cations are substituting. Work on the Al system, shown in Chapter 6, suggests that Al may substitute onto both the Ca(4) and Ca(5) sites. Since Na is larger than Al (and also Ga, shown to substitute onto the Ca(5) site in Chapter 5), it could be expected that the Na would preferentially substitute onto the Ca(5) site, however, work done by Obadia *et al.* [21] suggests that Na substitutes onto the Ca(4) site. Looking at the substitution levels, any Ca on the Ca(4) site should be fully replaced by Na by x=0.14 and the Ca(4) and Ca(5) sites should both be fully replaced by Al or Na by x=0.21. The presence of the $AlPO_4$ second phase suggests that any Al beyond this point is going into this second phase, with the β-TCP phase becoming more Na rich and potentially changing the structure. However, these predicted values may be slightly lower than would be observed due to the monovalent nature of Na. If samples are Al deficient but have the expected amount of Na, this would mean that more Ca would be needed for charge balancing in the system.

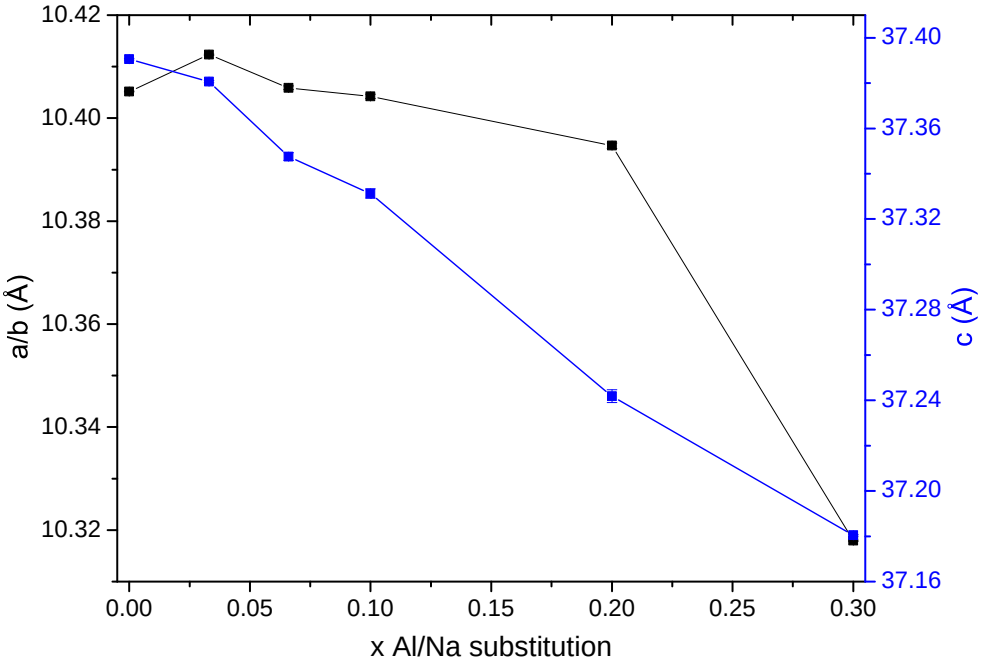

Figure 8-5 Lattice parameters of Al/Na substituted β-tricalcium phosphate as determined by Rietveld refinement of x-ray diffraction data. Error bars generally smaller than symbols used.

8.2.2 Nuclear magnetic resonance

8.2.2.1 ^{27}Al nuclear magnetic resonance

^{27}Al NMR was performed on the range of samples, with area normalised spectra shown in Figure 8-6. These spectra show similar features to those found in Figure 6-19 for the β-TCP doped solely with Al. The peak at 40 ppm is due to the $AlPO_4$ second phase known to be present in the x=0.2 and 0.3 samples, however the change in the lineshape of this peak between the two spectra is unexpected and may mean a further additional phase is present or simply a different polymorph of $AlPO_4$. The main peak present at −10.4 ppm is due to 6-coordinated Al and appears reasonably consistent throughout most of the spectra. However, in the x=0.3 sample, the width of this peak increases considerably, possibly indicating some disorder in the site responsible for it. The broad peak between 20 and 5 ppm is the, not yet fully identified, AlO_6 or $Al(OP)_5$ peak discussed in Section 6.4.1. The intensity of this peak starts to decrease from x=0.2, with the intensity mostly going into the 4-coordinated peak. The slight change at x=0.2 could be due to Na being taken up onto the Ca(5) site after x=0.14 when the Ca(4) site

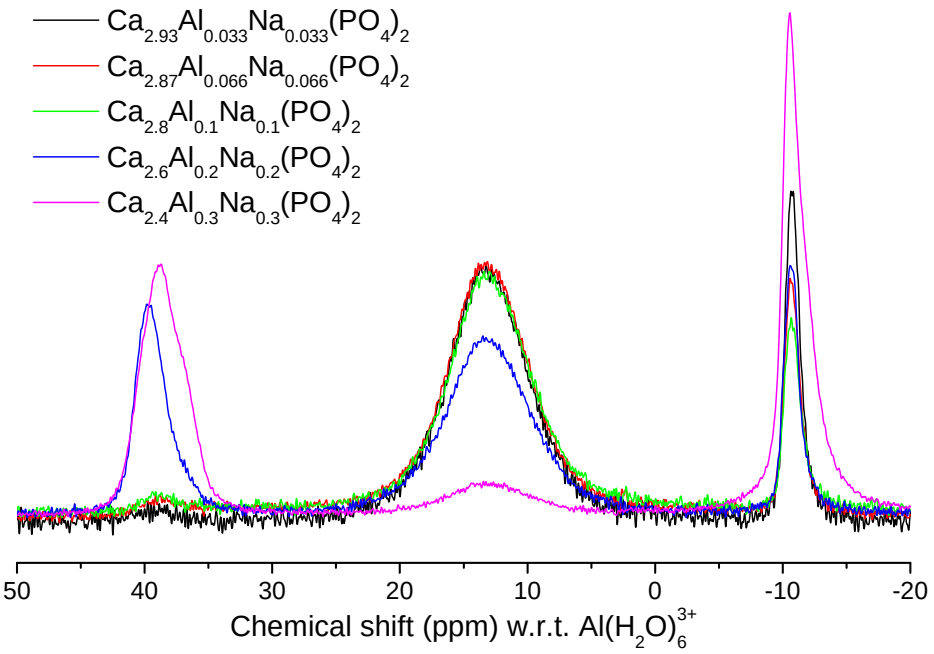

Figure 8-6 ^{27}Al NMR spectra of Al/Na substituted β-tricalcium phosphate normalised to area of central transitions.

will be full. What also may be happening is that when Ca has been fully replaced in the Ca(4) and Ca(5) sites at x=0.21, any Al present within the environment causing this peak is displaced by Na and forced out into the $AlPO_4$ second phase.

8.2.2.2 ^{23}Na nuclear magnetic resonance

^{23}Na NMR spectra were obtained for the range of samples and are shown in Figure 8-7, where the sharp peaks at 7.2 ppm are due to rotors being contaminated with the NaCl reference. Up until x=0.1, spectra appear identical, suggesting that the Na environments do not change up to this point. At x=0.2 the spectrum appears more well defined, with a distinct quadrupolar lineshape, although this could be due to this composition being above the substitution limit for Na on the Ca(4) site, resulting in an additional peak from Na on the Ca(5) site. In the x=0.3 sample a drastic change in lineshape can be seen with the peak appearing to shift downfield and become much broader. This could actually be due to a new peak appearing, possibly from the environment from which the Al is being displaced as the substitution limit is reached.

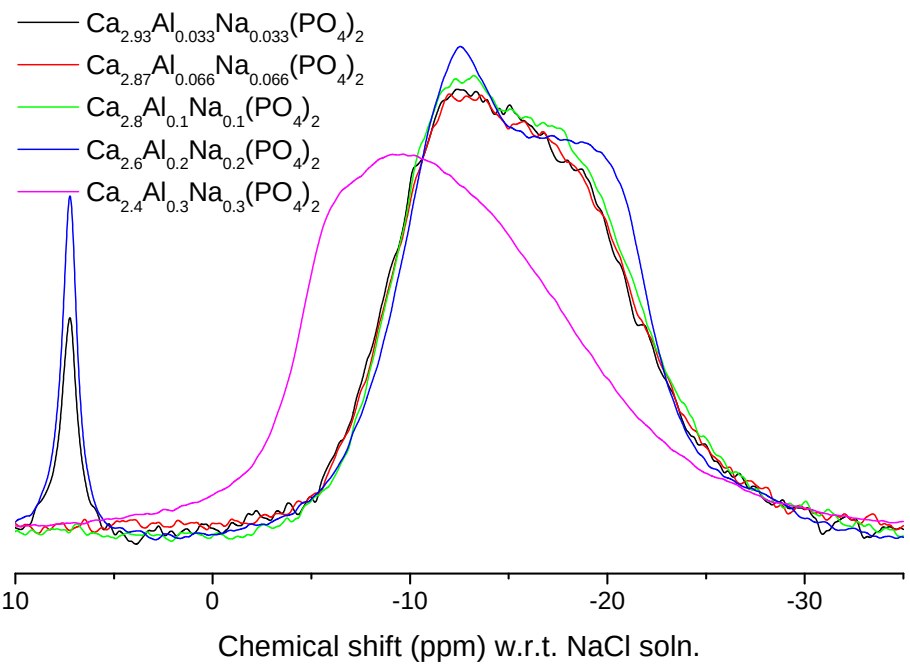

Figure 8-7 ^{23}Na NMR spectra of Al/Na substituted β-tricalcium phosphate normalised to spectrum area. Peak at 7.2 ppm due to NaCl contamination and was not included in normalisation.

8.2.2.3 ^{31}P nuclear magnetic resonance

^{31}P NMR was undertaken on the 500 MHz spectrometer for the entire range of samples with spectra shown in Figure 8-8, alongside the spectrum obtained from the 'pure' β-TCP sample. The features between −7 and −10.4 ppm are due to the β-CaP_2O_7 present with a small additional peak due to $AlPO_4$ present at −25 ppm but not shown here. Up until the x=0.1 sample there appears to be a consistent trend in peak development, with additional resonances appearing at 3.4 and 0.5 ppm and the peak at 4.7 ppm decreasing in intensity. Above this point, the resonances at 3.4 and 0.5 ppm become dominant on the left hand side of the spectra with new resonances coming in on the right. Comparing these with the spectra from the Al substituted β-TCP (Fig. 6-21), it appears that these features on the right of the co-doped spectra are consistent with the lineshapes from the high Al content single cation substitution spectra. This further supports the previous data in suggesting that there are two distinct behaviours being observed, one up until x=0.1 and a different behaviour somewhere beyond that point, possibly around x=0.14 when the Ca(5) site would be fully replaced if substitution was taking place just on that site.

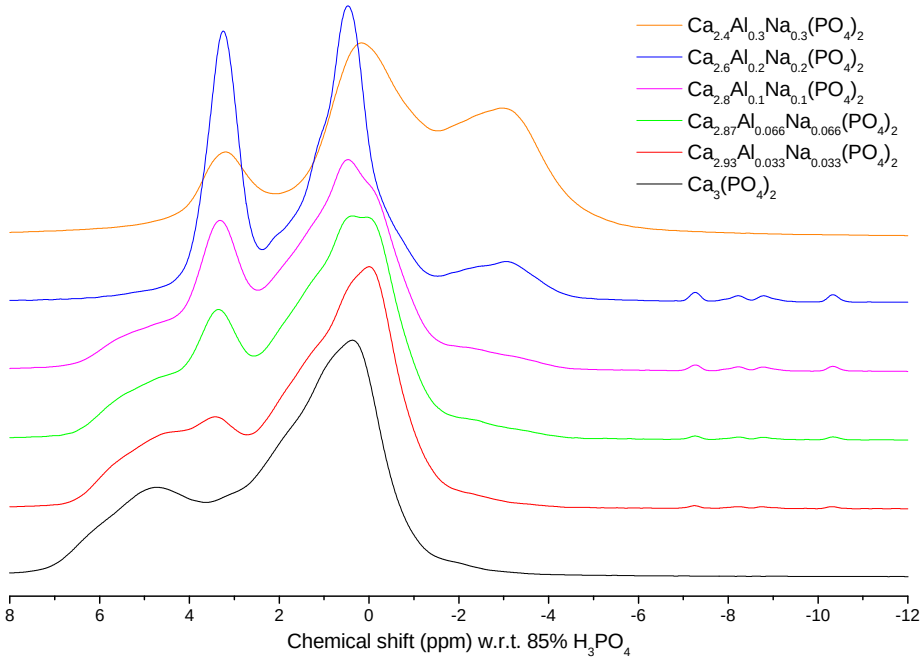

Figure 8-8 ^{31}P NMR spectra of Al/Na substituted β-tricalcium phosphate normalised to spectrum area.

8.3 Al/Ga co-doped substitution

Samples were prepared by final year undergraduate project students Michael Hardy and Arjun Zala under the supervision of the author, by grinding together stoichiometric amounts of $CaH(PO_4)$, $CaCO_3$, Al_2O_3 and Ga_2O_3 according to the general formula $Ca_9Al_{0.8-y}Ga_y(PO_4)_{6.8}$ with samples of y=0, 0.2, 0.4, 0.6, and 0.8 being produced. The resulting mixture was then heated at a rate of 10 °C/min up to 1050 °C and held for 4 h. This was then repeated further times to help ensure phase purity.

8.3.1 X-ray diffraction

X-ray diffraction patterns were taken for the entire composition range and are shown in Figure 8-9. $AlPO_4$ is seen to be present in all Al containing samples with Ga_2O_3 and β-Ca_2PO_7 also present from the y=0.4 sample and increasing with increasing Ga content. A shift to increasing 2θ can be observed with increasing Ga content, indicating a contraction in the unit cell. This is not as would be expected from the sizes of the ions (0.535 Å for Al *cf.* 0.620 Å for Ga, in 6-coordination [44]) but is consistent with the unit cell parameters determined in Sections 5.2 and 6.2.

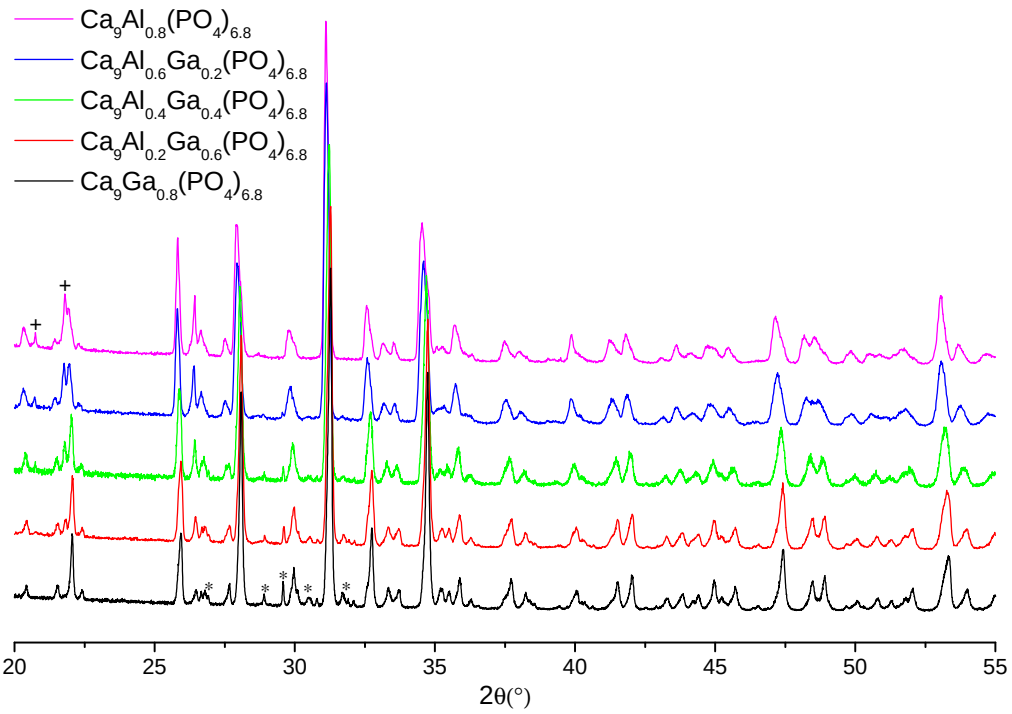

Figure 8-9 X-ray diffraction patterns of Al/Ga substituted β-tricalcium phosphate, where $*$ represents β-$Ca_2P_2O_7$ and + represents $AlPO_4$.

Lattice parameters were again obtained by Rietveld refinement of the x-ray diffraction data and are shown in Figure 8-10. They shown a linear trend across the composition range, suggesting that no major changes to the structure occur under co-substitution. The values obtained are comparable to those from singly substituted Ga and Al samples in Chapters 5 and 6, although the unit cell parameters here are slightly higher, probably due to the additional phases present.

8.3.2 Nuclear magnetic resonance

8.3.2.1 ^{31}P nuclear magnetic resonance

^{31}P NMR were obtained for the entire range of samples on the 500 MHz spectrometer with spectra shown in Figure 8-11. The features present between -7 and -10.4 ppm are due to the β-CaP_2O_7 additional phase, which appears to increase with increasing Ga content, and those present between -24 and -28 ppm being due to the $AlPO_4$ additional phase, which increase with increasing Al content. The rest of the spectra progress from a lineshape resembling the x=0.8 lineshape from Figure 5-15 in the fully Ga doped case

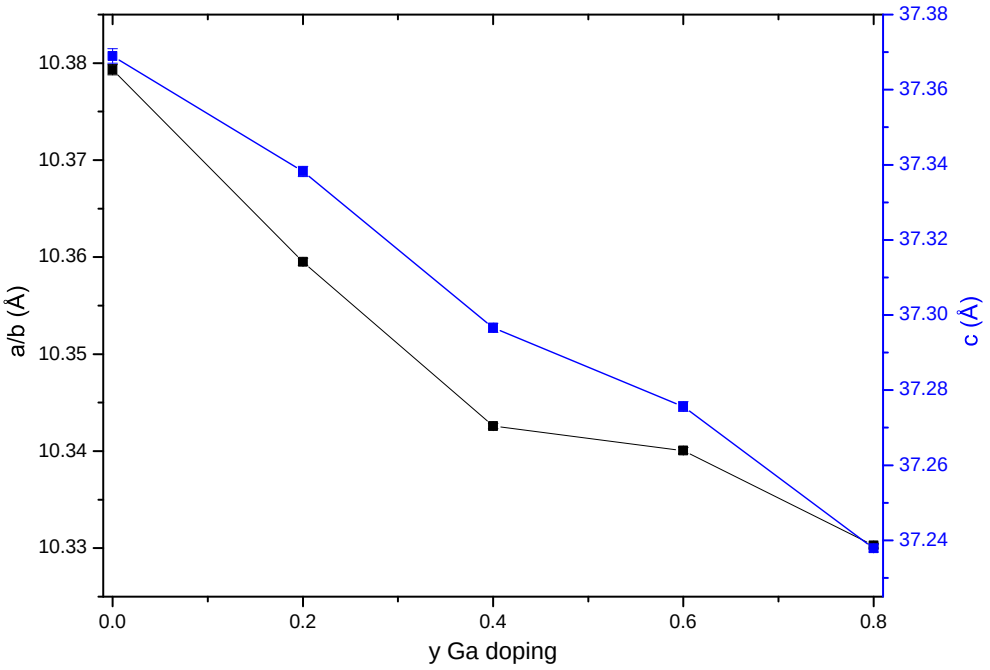

Figure 8-10 Lattice parameters of Al/Ga substituted β-tricalcium phosphate as determined by Rietveld refinement of x-ray diffraction data. Error bars generally smaller than symbols used.

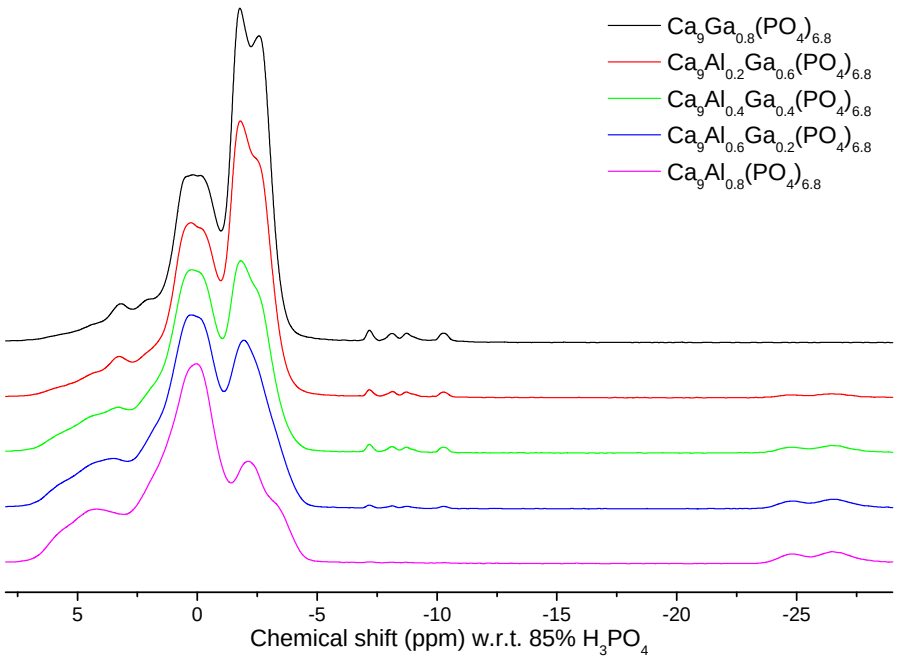

Figure 8-11 ^{31}P NMR spectra of Al/Ga substituted β-tricalcium phosphate normalised to spectrum area.

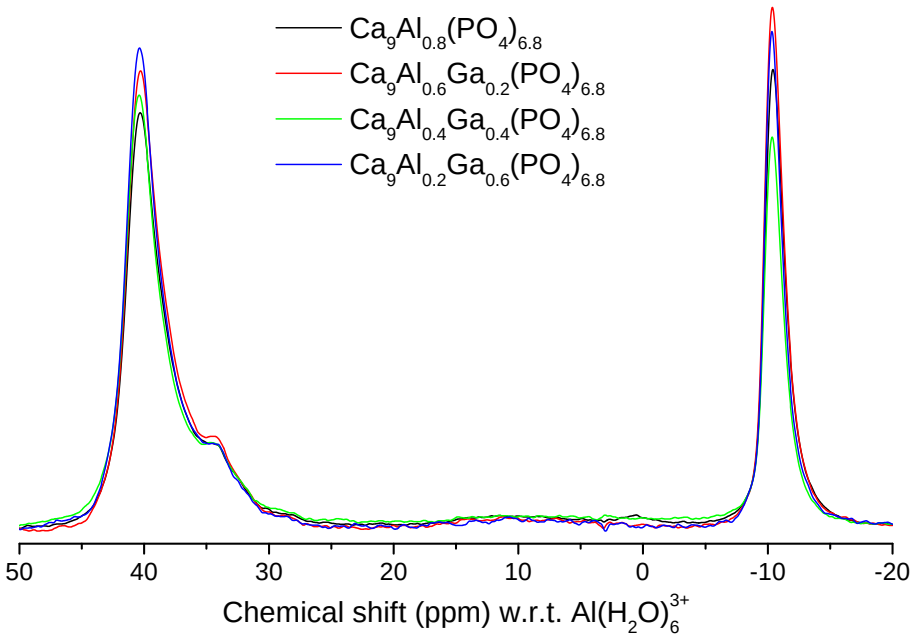

Figure 8-12 ^{27}Al NMR spectra of Al/Ga substituted β-tricalcium phosphate normalised to area of central transitions.

to one similar to the x=0.8 lineshape from Figure 6-21 in the fully Al doped sample. A consistent trend is observed throughout the spectra, further suggesting that no major changes to the structure are taking place.

8.3.2.2 ^{27}Al nuclear magnetic resonance

^{27}Al NMR was performed on the range of samples, with area normalised spectra shown in Figure 8-12. These spectra have fairly consistent lineshapes, with only slight changes in relative intensities being observed which seem to occur mostly independent of composition. The main peak at −10.4 ppm is from 6-coordinated Al present within the β-TCP structure, with the peak at 40 ppm being from the 4-coordinated $AlPO_4$, although showing a more asymmetric lineshape than in previous cases. A feature mostly absent here is the '5-coordinated' Al seen in the other Al containing samples between 20 and 0 ppm. There is a small indication of its presence, about the same as is seen in the $Ca_9Al_{0.8}(PO_4)_{6.8}$ sample in Figure 6-19. This may mean that the Ga is stabilising the β-TCP or could indicate that what is being observed is some kind of mixing of the $Ca_9Al_{0.8}(PO_4)_{6.8}$ and $Ca_9Ga_{0.8}(PO_4)_{6.8}$ samples.

8.4 Conclusions

Work in this chapter has given a significant insight into less simple substitution into β-TCP. It has been discovered that substitution of paramagnetic ions, although leaving XRD patterns unchanged, cause massive broadening to occur in NMR spectra, rendering them almost useless in the determination of site occupancies. The successful production of co-substituted samples has proven that β-TCP is able to accommodate multiple cations, with fairly predictable structures being obtained.

Chapter 9

Conclusions and future work

In this chapter comparisons of the different systems are made with respect to the different experimental techniques used. This is followed by a discussion of how this work relates to previous studies on β-TCP, before giving some suggestions of further work that could be carried out to improve our understanding of the structure and behaviour of substituted β-tricalcium phosphate.

9.1 Sample preparation

Samples of β-tricalcium phosphate substituted with Ga, Al, La, Sm and co-substituted with Al/Na and Al/Ga have all been successfully produced by solid state sintering. The dominant phase in each of the samples is the intended β-TCP phase, $Ca_3(PO_4)_2$. However, at higher substitution levels, additional phases are formed. The most common secondary phase formed is $R^{3+}PO_4$, where R^{3+} is the substituting trivalent cation, and is most prevalent in Al containing samples. Other phases occasionally formed are hydroxyapatite ($Ca_5(PO_4)_3(OH)$) and β-$Ca_2P_2O_7$, both calcium phosphate materials with similar elemental makeup to β-TCP. These additional phases have been shown to be taken up into the β-TCP structure under further firing of the samples, suggesting that β-TCP is, in many cases, the most stable phase.

9.2 X-ray diffraction

X-ray diffraction patterns were obtained for all samples produced and have been invaluable in determining the phases present within the materials and changes to the proportions of phases present after additional firings. Lattice parameters were determined from x-ray diffraction data for all of the samples produced, with those from the singly substituted samples shown together in Figure 9-1. In most cases a linear trend was ob-

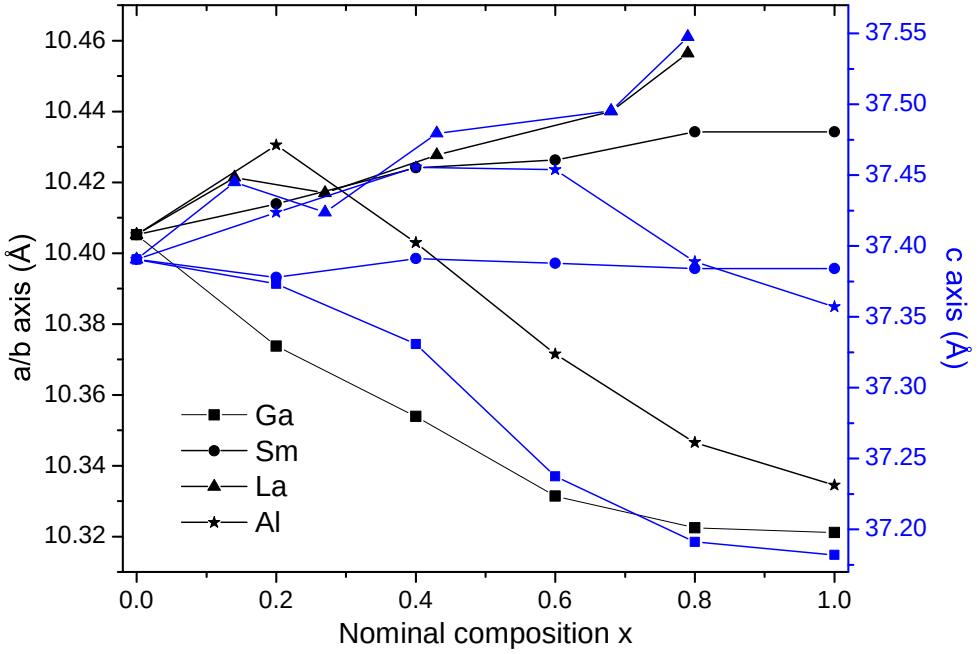

Figure 9-1 Lattice parameters of Ga, Sm, La and Al substituted β-tricalcium phosphate as determined by Rietveld refinement of x-ray diffraction data. Error bars smaller than symbols used.

Table 9-1 Metal–oxygen distances of elements used in this study.

Element	M^{n+}–O distance (Å) [14]
Al	1.651
Ga	1.73
Na	1.8
Ca	**1.967**
Sm	2.088
La	2.172

served in the unit cell parameters, with the change in unit cell size reflecting the size of the substituting ion compared to Ca^{2+} (Tab. 9-1). However, for Al-containing samples this is not the case; here an initial increase in unit cell parameters is observed before a large contraction. The reason for this is not, as yet, understood, but probably reflects the significantly smaller size of Al^{+3}. Also identified in diffraction patterns of these Al samples, is an increase in the width of the diffraction peaks compared with the 'pure' β-TCP and other systems.

Rietveld refinement was performed on x-ray diffraction patterns from Ga, Al and La substituted samples in order to further understand the crystal structures present. An

indication of the sites onto which substitution is occurring was obtained in each case, with Ga shown to substitute onto the Ca(5) site, La onto the Ca(3) site and Al onto both the Ca(4) or Ca(5) sites. With the exception of the Ga case, large differences have been seen between the actual and expected proportions of Al and La in the samples. There have also been problems in all cases with the total occupancies of the various sites, and in the errors of the values obtained for the occupancies. This is due to some features of the diffraction patterns not being correctly reproduced. The differences between fits and data have mainly appeared as a mismatch in the asymmetry of some of the diffraction peaks, indicating a possible problem in the peak shape parameters used. However, a decrease in intensity of some of the fitted peaks compared with the data obtained has also be seen, which could account for the unexpected occupancies or may be due to incorrect thermal parameters or even disorder within the systems.

9.3 Neutron diffraction

9.3.1 Time of flight diffraction

Time of flight neutron diffraction data were collected for the entire range of Al samples along with the 'pure' β-TCP, $Ca_9Ga_{0.8}(PO_4)_{6.8}$ and $Ca_9La(PO_4)_7$ samples. Rietveld refinement was performed on the data in an attempt to infer more about how the substitution is taking place. As with the refinement of the XRD data, the occupancies of the sites were far from expected, being much greater than should be allowed in each case, and often much higher than the total occupancies of the sites in pure β-TCP. There were also problems in the assessment of errors on the occupancies, with the software producing errors of the order of 10^6. As with the fits of the XRD data, there was some difference between the fits and the ND data, most noticeably at longer TOF. The cause of this may be partly due to longer range disorder in the systems, leading to incorrect assignment of the occupancies.

9.3.2 Total correlation functions

Total correlation functions were produced from the neutron diffraction data, with plots from each of the systems measured shown in Figure 9-2. Plots appear similar to the

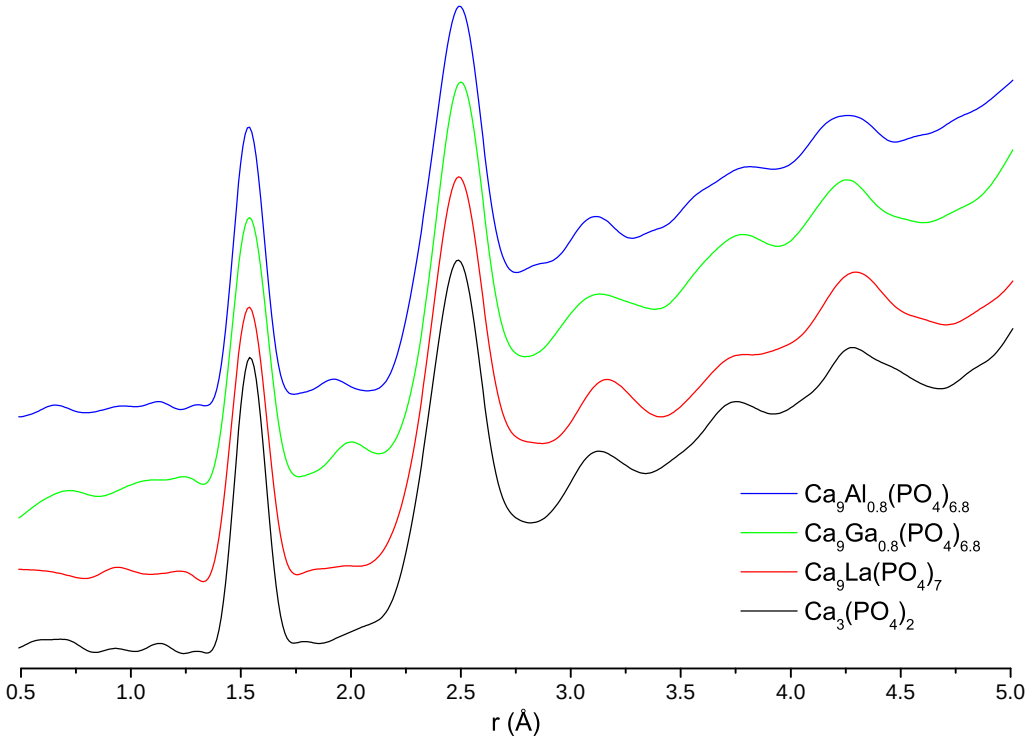

Figure 9-2 Total correlation functions for Ga, La and Al substituted β-tricalcium phosphate samples along with 'pure' β-TCP.

'pure' β-TCP plot for the Ga and La substituted samples, with only slight variations at longer distances. The Ga sample also shows a peak around 2 Å due to Ga–O bonds from 6-coordinated Ga, whereas in the La sample any La–O bond lengths would fall under the main Ca–O/O–O peak. In the Al sample, along with the small peak at 1.91 Å due to the 6-coordinated Al present, there are also other, more significant, changes to the plot at longer distances, indicating longer range changes to the structure are occurring in this case.

9.4 Nuclear magnetic resonance

9.4.1 ^{31}P nuclear magnetic resonance

^{31}P NMR has proved to be an invaluable tool in this work, as the P environments seem extremely sensitive to changes on the nearby Ca sites. ^{31}P NMR has been performed on all samples produced, and representative spectra from the Ga, Al and La systems, along with the spectrum from the 'pure' β-TCP are shown in Figure 9-3. From this, some

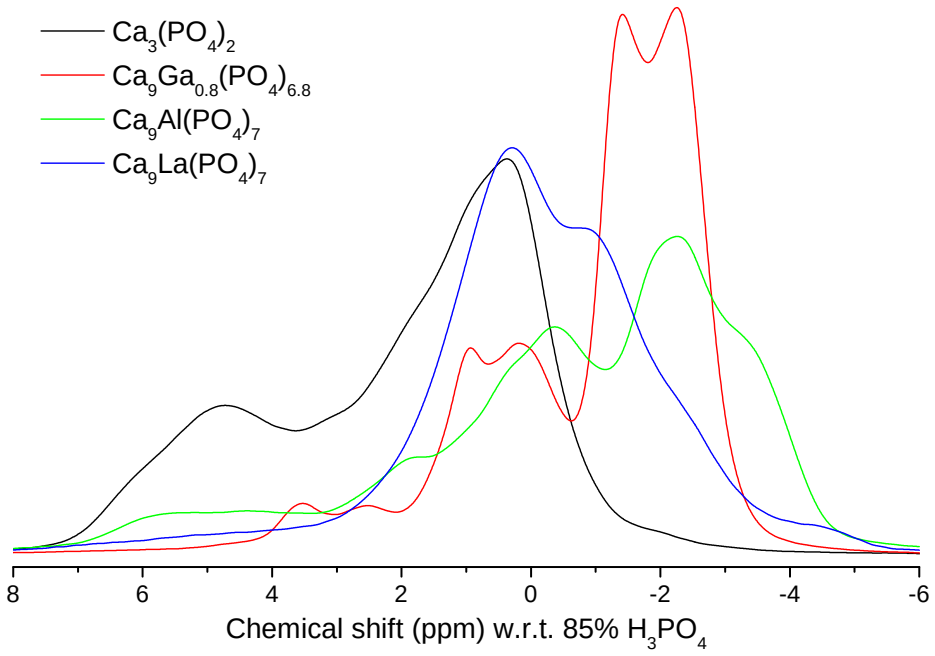

Figure 9-3 ^{31}P NMR spectra of Ga, La and Al substituted β-tricalcium phosphate samples along with 'pure' β-TCP, normalised to spectrum area.

insight into the effect that substitution of different ions into β-TCP has on the ^{31}P spectra can be obtained. The smaller Ga and Al ions, known to occupy the smaller and less abundant Ca(4) and Ca(5) sites, seem to cause new upfield resonances to appear, which are mostly separate from the main part of the spectrum, and also reduce the intensity of the downfield part of the spectra. For the larger La ion, shown to substitute onto the Ca(3) site, spectra seem to show a progression in increasing intensity of the right hand side of the spectra, although again with a reduction in the downfield resonances. This consistent reduction in the downfield part of spectra could suggest that resonances in this region are due to P with a neighbouring Ca(4) site, the resonances from which, since trivalent substitution requires the presence of more vacancies, would decrease in intensity upon increasing substitution.

9.4.2 ^{43}Ca nuclear magnetic resonance

^{43}Ca NMR, although being the most obvious nucleus to look at, has generally been the least insightful in this study. Spectra obtained contain broad peaks with considerable overlap and the poor signal to noise ratios render peak fitting ambiguous. The differing

fields used show a shift in the spectra and, in some cases, an apparent change in line-shape, implying different C_Q for each site. The fitting that has been undertaken shows that the spectra can mostly be fitted to the predicted Ca site occupancies with some confidence. The assignment of the fitted peaks is also shown to follow the trend with average Ca–O bond length as described by Gervais *et al.* [23].

9.4.3 ^{27}Al nuclear magnetic resonance

^{2}7Al NMR on the Al containing samples produces very similar spectra throughout the systems. Visible in all cases is a peak at −10.4 ppm, corresponding to 6-coordinated Al and due to Al on one or both of the 6-coordinated Ca(4) and Ca(5) sites. For those samples with an $AlPO_4$ second phase present, an additional peak at 40 ppm is visible, and is known to correspond to 4-coordinated Al. The most interesting feature is a broad peak present between 20 and 5 ppm. This was identified as coming from either an AlO_6 or $Al(OP)_5$ environment [25, p. 273], and is thought to be due to a distortion of one of the Ca sites as Al is substituted onto it.

9.5 Comparison to previous work

Of the systems studied here, limited XRD investigation has previously been performed on the $Ca_9M(PO_4)_7$ phases, where M=Ga, Al, La and Na [12, 15, 21]. For the Ga and La systems, results from the current study are consistent with the proposed substitution onto the Ca(5) [15] and Ca(3) [12] sites respectively, although a slight difference in the *a* and *b* lattice parameters is observed in each case. For the Al system, a definitive answer to the site of substitution has not been reached here, although does not discount the predicted substitution onto the Ca(5) site by Golubev *et al.* [15]. In this case it is the *a* lattice parameter which is close to the published value, whereas the *c* lattice parameter is much greater. Little work was done on the Al/Na co-substituted samples but data obtained suggest that substitution is taking place on the Ca(4) or Ca(5) sites, consistent with work done by Obadia *et al.* [21].

9.6 Future work

From the work presented in this thesis it can be seen that β-tricalcium phosphate readily incorporates trivalent ions into its structure. This is a promising step into identifying the suitability of β-TCP as an immobilisation host for radioactive waste. Much more work would need to be undertaken to determine the maximum waste loadings for combined substitution but this study could provide a valuable starting point.

This study has mainly focussed on trivalent cations, whereas there are many other elements which could be used and their behaviour observed. Co-substitution work could be continued, possibly using one ion which substitutes onto one of the larger Ca sites and one onto the Ca(5) site to identify whether they have any influence on one another or if substitution takes place independently. The main goal for AWE is to produce a material to be used in the immobilisation of radioactive ions, therefore work on radioactive samples would also need to be done at some point, probably starting from substitution of a single radioactive cation. Also possible would be increasing the number of ions substituted into β-TCP, in order to further reflect the required wasteform, in addition to investigating how the structure behaves and whether any competition effects take place, as was thought to be happening in the Al/Na co-substituted samples.

Considerable insight has been gained into the structure and substitution mechanisms of β-TCP in this work, however there are many ways in which more knowledge may be obtained. For systems where previous work has been done, many of the studies have included IR or Raman spectroscopy and it could therefore be useful to acquire IR and Raman spectra of samples used in this work in order to more directly compare the sets of samples. These would be useful tools in obtaining a better understanding of the local environments of the atoms and could complement the NMR studies. They may also indicate why some of the disagreements have arisen, if the samples being compared are not actually identical as assumed to be.

Another technique which could be of use is reverse Monte Carlo (RMC) modelling, a technique similar to the Rietveld refinement performed but with the potential to provide much more information about the structure. The basis of RMC modelling is to simulate measured data, such as diffraction patterns or total correlation functions, by calculating them from an arrangement of atoms and refine their positions in order to obtain a better fit. An advantage of RMC over Rietveld refinement is that RMC does

not need to obey symmetries enforced by space groups and so would be an ideal tool in modelling the disorder present within the systems. However, in order to produce reliable fits, a structure consisting of many unit cells is required. If 1000 unit cells were used, each consisting of around 270 atoms, this would lead to the positions of more than 10^5 atoms needing to be refined, a feat requiring massive computing power.

The main way to improve the x-ray diffraction data obtained would be to measure for longer between steps and over a wider angular range, giving improved statistics for refinement. This could give improved values for the site occupancies and, in particular, the proportions of additional phases present, to aid in the analysis of samples using other techniques. It may not, however, improve upon the peakshape obtained within the refinements and so work could be done to identify the problems arising there.

Refinement of the neutron diffraction data could be made more accurate by utilising additional banks or combining with x-ray diffraction data to further constrain the refinements. This was attempted, however, problems with the software used resulted in consistently diverging refinements and so had to be abandoned due to time constraints. If the problems could be addressed then this could be a powerful tool for determining the structure, although would still be susceptible to inaccuracies where disorder is involved. Fitting of the total correlation functions could give an estimate of the proportion of substituent atoms involved, assuming coordination number from the M–O distance.

For NMR of the samples produced, there are many, more complex, pulse sequences which can be used to further understand the environments of the nuclei. 2-dimensional NMR can show correlations between nuclei, with both homonuclear and heteronuclear techniques being available, often involving the probing of two different nuclei simultaneously. One homonuclear technique, known as POST-C7 [47], was attempted on one of the Ga containing samples. This technique was used to identify spatially close P atoms within the β-TCP, in order to relate the observed peaks to the P sites involved. Poor signal to noise ratio and difficulties with establishing the correct acquisition parameters meant that this technique was not fully explored. Heteronuclear experiments can be used to show correlations between different nuclei present, i.e. which P environments are in close proximity to Ga ions, aiding in the assignment of the resonances in the ^{31}P spectra. Some work has been undertaken at Warwick by PhD student Andrew Grigg, looking at the Al/Ga co-substituted samples, however the long experimental

times needed and poor signal to noise ratio obtained mean that no definitive conclusions have yet been drawn. Another, much simpler, method of extending the NMR study would be to istopically enrich samples with either ^{43}Ca or ^{17}O, to greatly improve their receptivities. This would require the production of new samples, however the main problem with this would be the expense in obtaining the isotopically enriched materials.

References

[1] I. Donald, B. L. Metcalfe and R. Taylor, *J. Mater. Sci.* **32**, (1997), 5851–5887.

[2] B. L. Metcalfe and I. Donald, *J. Non-Cryst. Solids* **348**, (2004), 225–229.

[3] I. Donald, B. Metcalfe, S. Fong, L. Gerrard, D. Strachan and R. Scheele, *J. Nuclear Mat.* **361** (1), (2007), 78–93.

[4] P. Trocellier, *Ann. Chim. Sci. Mat.* **26**, (2001), 113–130.

[5] S. Openshaw, S. Carver and J. Fernie, *Britain's Nuclear Waste: Siting and Safety* (Belhaven Press, 1989).

[6] B. Metcalfe, S. Fong and I. Donald, *Mat. Res. Soc. Symp. Proc.* **932**, (2006), 42.1.

[7] B. Jolliff, L. Haskin, R. Colson and M. Wadhwa, *Geochimica et Cosmochimica Acta* **51**, (1993), 4069–4094.

[8] A. Ogose, N. Kondo, H. Umezu, T. Hotta, H. Kawashima, K. Tokunaga, T. Ito, N. Kudo, M. Hoshino, W. Gu and N. Endo, *Biomaterials* **27**, (2006), 1542–1549.

[9] A. Chaudhry, J. Goodall, M. Vickers, J. Cockcroft, I. Rehman, J. Knowles and J. Darr, *J. Mater. Chem.* **18**, (2008), 5900–5908.

[10] B. Dickens, L. W. Schroeder and W. E. Brown, *J. Solid State Chem.* **10**, (1974), 232–248.

[11] K. Yoshida, H. Hyuga, N. Kondo, H. Kita, M. Sasaki, M. Mitamura, K. Hashimoto and Y. Toda, *J. Am. Ceram. Soc.* **89** (2), (2006), 688–690.

[12] V. Golubev and B. Lazoryak, *Neorganicheskie Materialy* **27**, (1991), 576–579.

[13] B. Lazoriak, V. Golubev, R. Salmon, C. Parent and P. Hagenmuller, *Eur. J. Solid State Inorg. Chem.* **26**, (1989), 455–463.

[14] N. E. Brese and M. O'Keeffe, *Acta Cryst.* **B47**, (1991), 192–197.

[15] V. Golubev, B. Viting, O. Dogadin, B. Lazoriak and R. Aziev, *Russ. J. Inorg. Chem.* **35**, (1990), 1724–1726.

[16] B. Lazoryak, N. Khan, V. Morozov, A. Belik and S. Khasanov, *J. Solid State Chem.* **145**, (1999), 345–355.

[17] A. Belik, O. Yanov and B. Lazoryak, *Mater. Res. Bull.* **36**, (2001), 1863–1871.

[18] R. Jakeman, A. Cheetham, N. Clayden and C. Dobson, *J. Solid State Chem.* **78** (1), (1989), 23 – 34.

[19] L. W. Schroeder, B. Dickens and W. E. Brown, *J. Solid State Chem.* **22**, (1977), 253–262.

[20] B. Lazoryak, V. Morozov, A. Belik, S. Stefanovich, V. Grebenev, I. Leonidov, E. Mitberg, S. Davydov, O. Lebedev and G. Van Tendeloo, *Solid State Sci.* **6**, (2004), 185–195.

[21] L. Obadia, P. Deniard, B. Alonso, T. Rouillon, S. Jobic, J. Guicheux, M. Julien, D. Massiot, B. Bujoli and J. Bouler, *Chem. Mater.* **18**, (2006), 1425–1433.

[22] V. Morozov, A. Belik, S. Stefanovich, V. Grebenev, O. Lebedev, G. Van Tendeloo and B. Lazoryak, *J. Solid State Chem.* **165**, (2002), 278–288.

[23] C. Gervais, D. Laurencin, A. Wong, F. Pourpoint, J. Labram, B. Woodward, A. Howes, K. Pike, R. Dupree, F. Mauri, C. Bonhomme and M. Smith, *Chemical Physics Letters* **464**, (2008), 42–48.

[24] M. Yashima, A. Sakai, T. Kamiyama and A. Hoshikawa, *J. Solid State Chem.* **175**, (2003), 272–277.

[25] K. Mackenzie and M. Smith, *Multinuclear Solid-state NMR of Inorganic Materials* (Pergamon, 2002).

[26] M. Levitt, *Spin Dynamics* (John Wiley & Sons, 2000).

[27] A. Kentgens, *Geoderma* **80**, (1997), 271–306.

[28] M. Duer (ed.), *solid-state NMR spectroscopy* (Blackwell Science, 2002).

[29] A. C. Hannon, in: *Encyclopedia of Spectroscopy and Spectrometry*, edited by J. Lindon, G. Tranter and J. Holmes (AP, London, 2000), vol. 2, pp. 1479–1492.

[30] A. C. Hannon, *Nucl. Instrum. Methods. Phys. Res. A* **551**, (2005), 88–107.

[31] A. C. Hannon, in: *Encyclopedia of Spectroscopy and Spectrometry*, edited by J. Lindon, G. Tranter and J. Holmes (AP, London, 2000), vol. 2, pp. 1479–1492.

[32] E. Barney, A. C. Hannon, N. Laorodphan, R. Dupree and H. D., *J. Non-Cryst. Solids* **356**, (2010), 2517–2523.

[33] H. M. Rietveld, *Acta Cryst.* **22**, (1967), 151–152.

[34] H. M. Rietveld, *J. Appl. Cryst.* **2**, (1969), 65–71.

[35] R. Young (ed.), *The Rietveld Method* (Oxford University Press, 2002).

[36] A. Coelho, Topas Academic (2007).

[37] Bruker, TopSpin 2.1 (2008).

[38] H. Kwak, S. Prasad, T. Clark and P. Grandinetti, *Solid State Nucl. Magn. Reson.* **24**, (2003), 71–77.

[39] PANalytical, X'Pert HighScore Plus (2010).

[40] International Centre for Diffraction Data, PDF-4+ Database (2010).

[41] P. Thompson, D. Cox and J. Hastings, *J. Appl. Cryst.* **20**, (1987), 79–83.

[42] S. McLain, D. Bowron, A. Hannon and A. Soper, GUDRUN: A computer program developed for analysis of neutron diffraction data (2006).

[43] F. Akeroyd, R. Ashworth, S. Johnston, J. Martin, C. Moreton-Smith and D. Sivia, OpenGENIE (1999).

[44] R. D. Shannon, *Acta Cryst.* **A32**, (1976), 751–767.

[45] V. F. Sears, *Neutron News* **3**, (1992), 26–37.

[46] J. Xu, P. Zhu, Z. Gan, N. Sahar, M. Tecklenburg, M. Morris, D. Kohn and A. Ramamoorthy, *J. Am. Chem. Soc.* **132**, (2010), 11504–11509.

[47] M. Hohwy, H. J. Jakobsen, M. Edén, M. H. Levitt and N. C. Nielsen, *J. Chem. Phys.* **108**, (1998), 2686–2694.

Appendix A

Structures obtained from Rietveld refinement

Table A-1 Structure obtained from XRD data for $Ca_3(PO_4)_2$.

R_p	6.936	R_{wp}	10.141	GOF	3.306
a	10.405138(80)	c	37.39074(38)		
site	x	y	z	occ	beq
Ca1	0.72437(42)	0.85680(57)	0.16724(24)	1	0.198(98)
Ca2	0.61884(43)	0.82189(64)	-0.03310(22)	1	0.42(11)
Ca3	0.72955(33)	0.85325(55)	0.06132(23)	1	1.01(11)
Ca4	0	0	-0.08424(34)	0.614(11)	2.54(44)
Ca5	0	0	0.73384(29)	1	1.64(16)
P1	0	0	0	1	0.71(22)
P2	0.68954(46)	0.86476(73)	0.86896(26)	1	1.05(15)
P3	0.65472(74)	0.84591(80)	0.76597(25)	1	0.97(16)
O1	0.7349(13)	-0.0892(13)	-0.09214(39)	1	2.24(38)
O2	0.7657(18)	0.7688(16)	0.85679(38)	1	2.43(40)
O3	0.7175(15)	0.0082(13)	0.84707(36)	1	0.04(37)
O4	0.5183(11)	0.7616(19)	0.86386(52)	1	2.18(32)
O5	0.5945(15)	-0.0499(13)	0.77999(41)	1	0.81(37)
O6	0.5737(14)	0.6967(13)	0.78510(36)	1	-0.49(29)
O7	0.0831(15)	0.9013(15)	0.77726(35)	1	-0.61(27)
O8	0.63033(94)	0.8307(13)	0.72753(37)	1	0.07(28)
O9	0.0108(14)	0.8602(10)	-0.01759(43)	1	3.47(32)
O10	0	0	0.03601(55)	1	1.74(56)

Table A-2 Structure obtained from XRD data for $Ca_9Ga_{0.2}(PO_4)_{6.2}$.

R_p	6.370	R_{wp}	9.539	GOF	4.536
a	10.373740(99)	c	37.37332(51)		
site	x	y	z	occ	beq
Ca1	0.72488(74)	0.85589(98)	0.16779(51)	1	-0.22(17)
Ca2	0.62155(83)	0.8224(10)	-0.03319(46)	1	0.27(19)
Ca3	0.72773(62)	0.85286(95)	0.06096(51)	1	0.29(21)
Ca4	0	0	-0.08334(64)	0.484(8)	0.60(73)
Ca5	0	0	0.73410(50)	0.86(16)	1.33(24)
Ga5	0	0	0.73410(50)	0.16(11)	1.33(24)
P1	0	0	0	1	1.71(53)
P2	0.68487(78)	0.8581(14)	0.86969(53)	1	0.91(30)
P3	0.6528(12)	0.8463(12)	0.76555(51)	1	0.51(32)
O1	0.7393(22)	-0.0896(24)	-0.09012(85)	1	2.65(71)
O2	0.7602(37)	0.7661(32)	0.85724(73)	1	4.94(87)
O3	0.7209(31)	0.0043(24)	0.84779(77)	1	1.66(76)
O4	0.5112(20)	0.7626(32)	0.86497(92)	1	0.28(49)
O5	0.6032(22)	-0.0445(23)	0.78045(70)	1	-0.86(56)
O6	0.5713(20)	0.6941(20)	0.78465(73)	1	-1.63(49)
O7	0.0787(26)	0.8998(24)	0.77512(68)	1	-0.63(53)
O8	0.6284(14)	0.8251(22)	0.72821(75)	1	-1.30(44)
O9	0.0025(26)	0.8545(18)	-0.01930(72)	1	4.35(61)
O10	0	0	0.0345(12)	1	3.7(13)

Table A-3 Structure obtained from XRD data for $Ca_9Ga_{0.4}(PO_4)_{6.4}$.

R_p	6.227	R_{wp}	8.992	GOF	3.686
a	10.353920(96)	c	37.33085(49)		
site	x	y	z	occ	beq
Ca1	0.72461(67)	0.8570(10)	0.16718(48)	1	0.20(16)
Ca2	0.62148(82)	0.8255(12)	-0.03404(41)	1	0.61(23)
Ca3	0.72413(54)	0.85270(88)	0.06024(44)	1	0.33(19)
Ca4	0	0	-0.08343(78)	0.374(7)	1.09(85)
Ca5	0	0	0.73461(45)	0.75(14)	0.51(22)
Ga5	0	0	0.73461(45)	0.23(9)	0.51(22)
P1	0	0	0	1	2.00(50)
P2	0.68407(81)	0.8592(12)	0.86947(46)	1	0.84(29)
P3	0.6516(12)	0.8464(12)	0.76524(46)	1	0.62(31)
O1	0.7369(21)	-0.0865(21)	-0.08938(80)	1	2.84(67)
O2	0.7560(33)	0.7713(30)	0.85517(61)	1	2.87(80)
O3	0.7257(28)	0.0037(24)	0.84618(71)	1	1.23(71)
O4	0.5079(18)	0.7598(29)	0.86500(89)	1	0.61(44)
O5	0.6033(23)	-0.0461(21)	0.77870(69)	1	-0.35(55)
O6	0.5781(21)	0.6958(24)	0.78393(67)	1	-0.55(57)
O7	0.0770(28)	0.9043(27)	0.77230(77)	1	1.00(53)
O8	0.6283(15)	0.8198(23)	0.72766(66)	1	-1.01(40)
O9	0.0115(24)	0.8597(16)	-0.01283(94)	1	3.51(54)
O10	0	0	0.0342(11)	1	3.9(12)

Table A-4 Structure obtained from XRD data for $Ca_9Ga_{0.6}(PO_4)_{6.6}$.

R_p	6.319	R_{wp}	9.209	GOF	4.541
a	10.331440(93)	c	37.23744(48)		
site	x	y	z	occ	beq
Ca1	0.72420(68)	0.8567(11)	0.16647(43)	1	0.42(16)
Ca2	0.62156(78)	0.8248(12)	-0.03481(39)	1	0.55(22)
Ca3	0.72248(53)	0.85119(97)	0.05930(41)	1	0.19(19)
Ca4	0	0	-0.0833(10)	0.281(7)	1.4(12)
Ca5	0	0	0.73415(43)	0.36(14)	0.65(20)
Ga5	0	0	0.73415(43)	0.54(9)	0.65(20)
P1	0	0	0	1	1.81(48)
P2	0.68383(80)	0.8573(13)	0.86949(45)	1	1.01(30)
P3	0.6524(11)	0.8457(11)	0.76446(43)	1	0.18(30)
O1	0.7418(20)	-0.0840(19)	-0.08957(75)	1	2.35(61)
O2	0.7513(36)	0.7642(33)	0.85452(57)	1	3.70(83)
O3	0.7226(28)	-0.0017(22)	0.84589(67)	1	1.25(72)
O4	0.5047(19)	0.7591(31)	0.86669(84)	1	0.10(41)
O5	0.6037(21)	-0.0448(20)	0.77848(67)	1	-0.71(53)
O6	0.5784(20)	0.6963(22)	0.78373(64)	1	-0.99(52)
O7	0.0743(29)	0.9046(26)	0.77106(68)	1	0.04(52)
O8	0.6281(13)	0.8210(21)	0.72687(61)	1	-1.77(39)
O9	0.0104(24)	0.8599(16)	-0.01457(87)	1	3.47(50)
O10	0	0	0.0377(10)	1	4.1(13)

Table A-5 Structure obtained from XRD data for $Ca_9Ga_{0.8}(PO_4)_{6.8}$.

R_p	6.686	R_{wp}	9.821	GOF	3.010
a	10.322410(70)	c	37.19121(36)		
site	x	y	z	occ	beq
Ca1	0.72265(44)	0.85788(67)	0.16690(25)	1	0.845(93)
Ca2	0.61979(42)	0.82396(68)	-0.03435(23)	1	0.49(11)
Ca3	0.72158(34)	0.85065(57)	0.06009(23)	1	0.577(94)
Ca4	0	0	-0.0823(10)	0.210(5)	4.0(11)
Ca5	0	0	0.73396(25)	0.07(9)	0.54(10)
Ga5	0	0	0.73396(25)	0.76(6)	0.54(10)
P1	0	0	0	1	1.36(23)
P2	0.68315(48)	0.85611(75)	0.86975(27)	1	0.95(15)
P3	0.65515(66)	0.84656(68)	0.76454(24)	1	0.09(15)
O1	0.7403(12)	-0.0863(11)	-0.08865(39)	1	1.18(34)
O2	0.7493(19)	0.7603(16)	0.85502(34)	1	1.61(41)
O3	0.7166(16)	-0.0023(13)	0.84731(36)	1	1.07(41)
O4	0.5020(12)	0.7570(18)	0.86920(45)	1	0.13(26)
O5	0.6010(14)	-0.0478(13)	0.77863(44)	1	0.94(35)
O6	0.5783(13)	0.6943(13)	0.78533(37)	1	-0.58(28)
O7	0.0767(15)	0.9053(14)	0.77222(33)	1	-0.75(27)
O8	0.62596(91)	0.8225(14)	0.72768(34)	1	-0.98(25)
O9	0.0111(14)	0.8608(10)	-0.01214(57)	1	3.59(33)
O10	0	0	0.04170(59)	1	2.77(67)

Table A-6 Structure obtained from XRD data for $Ca_9Ga(PO_4)_7$.

R_p	6.018	R_{wp}	9.819	GOF	4.992
a	10.321080(97)	c	37.18194(50)		
site	x	y	z	occ	beq
Ca1	0.7229(10)	0.8574(13)	0.16652(67)	1	0.74(20)
Ca2	0.61883(96)	0.8235(16)	-0.03405(61)	1	0.14(27)
Ca3	0.72051(78)	0.8504(13)	0.06058(60)	1	0.04(29)
Ca4	0	0	-0.0800(19)	0.226(9)	4.7(24)
Ca5	0	0	0.73364(62)	0.03(16)	0.27(24)
Ga5	0	0	0.73364(62)	0.80(10)	0.27(24)
P1	0	0	0	1	1.49(60)
P2	0.6842(11)	0.8554(19)	0.86928(73)	1	1.02(36)
P3	0.6594(17)	0.8498(13)	0.76469(73)	1	-0.14(39)
O1	0.7397(27)	-0.0870(27)	-0.08866(91)	1	1.02(76)
O2	0.7477(47)	0.7527(38)	0.85527(72)	1	1.49(93)
O3	0.7216(38)	-0.0023(25)	0.84923(78)	1	0.8(10)
O4	0.5004(23)	0.7559(37)	0.87069(94)	1	-1.81(45)
O5	0.5998(27)	-0.0467(29)	0.77836(96)	1	-0.45(84)
O6	0.5769(26)	0.6977(26)	0.78664(77)	1	-1.21(65)
O7	0.0744(40)	0.9009(36)	0.77362(72)	1	-0.55(62)
O8	0.6258(19)	0.8197(28)	0.72967(82)	1	-1.34(62)
O9	0.0107(26)	0.8630(18)	-0.0127(12)	1	2.70(64)
O10	0	0	0.0406(14)	1	6.0(22)

Table A-7 Structure obtained from XRD data for $Ca_9Al_{0.2}(PO_4)_{6.2}$.

R_p	7.241	R_{wp}	10.950	GOF	3.186
a	10.430530(78)		c	37.42377(35)	
site	x	y	z	occ	beq
Ca1	0.72620(53)	0.85680(73)	0.16779(46)	1	0.25(14)
Ca2	0.62073(68)	0.82345(79)	-0.03228(42)	1	0.16(16)
Ca3	0.72959(48)	0.85163(74)	0.06183(44)	1	0.54(17)
Ca4	0	0	-0.08419(53)	0.46(11)	0.30(40)
Al4	0	0	-0.08419(53)	0.19(18)	0.30(40)
Ca5	0	0	0.73365(41)	1.02(10)	1.38(21)
Al5	0	0	0.73365(41)	0.00(16)	1.38(21)
P1	0	0	0	1	2.86(47)
P2	0.68835(68)	0.8646(11)	0.86982(47)	1	2.03(24)
P3	0.6518(10)	0.84168(94)	0.76657(44)	1	0.60(21)
O1	0.7393(17)	-0.0870(19)	-0.08915(67)	1	3.29(49)
O2	0.7768(24)	0.7810(21)	0.85894(64)	1	5.23(67)
O3	0.7263(20)	0.0063(19)	0.84925(68)	1	2.64(67)
O4	0.5209(14)	0.7565(20)	0.86097(71)	1	0.21(38)
O5	0.5989(17)	-0.0446(17)	0.78123(61)	1	-1.36(44)
O6	0.5758(15)	0.6972(15)	0.78629(61)	1	-0.87(42)
O7	0.0728(19)	0.8961(18)	0.77538(57)	1	0.57(40)
O8	0.6326(11)	0.8298(16)	0.72855(60)	1	-1.22(34)
O9	0.0010(19)	0.8572(14)	-0.01631(61)	1	3.15(41)
O10	0	0	0.03370(92)	1	4.4(10)

Table A-8 Structure obtained from XRD data for $Ca_9Al_{0.4}(PO_4)_{6.4}$.

R_p	7.335	R_{wp}	10.825	GOF	3.135
a	10.40295(11)		c	37.45560(47)	
site	x	y	z	occ	beq
Ca1	0.72468(54)	0.85594(75)	0.16762(43)	1	-0.27(15)
Ca2	0.62158(70)	0.82255(94)	-0.03308(37)	1	0.29(20)
Ca3	0.72738(47)	0.85275(74)	0.06138(40)	1	-0.08(18)
Ca4	0	0	-0.08822(69)	0.43(10)	0.31(52)
Al4	0	0	-0.08822(69)	0.08(17)	0.31(52)
Ca5	0	0	0.73468(43)	0.81(10)	0.47(22)
Al5	0	0	0.73468(43)	0.22(16)	0.47(22)
P1	0	0	0	1	0.84(47)
P2	0.68743(68)	0.8590(11)	0.86905(43)	1	0.38(23)
P3	0.6512(11)	0.84876(99)	0.76711(39)	1	0.65(26)
O1	0.7323(19)	-0.0896(20)	-0.09082(67)	1	2.79(60)
O2	0.7764(27)	0.7837(21)	0.85533(56)	1	2.82(63)
O3	0.7219(18)	0.0062(19)	0.84704(58)	1	-0.63(46)
O4	0.5186(15)	0.7656(21)	0.86063(69)	1	1.28(50)
O5	0.5951(20)	-0.0526(20)	0.77778(69)	1	0.82(54)
O6	0.5795(18)	0.6926(24)	0.78239(65)	1	0.03(51)
O7	0.0811(22)	0.9035(19)	0.77278(62)	1	0.05(46)
O8	0.6253(13)	0.8240(18)	0.72859(58)	1	-0.77(39)
O9	0.0115(21)	0.8614(15)	-0.01398(78)	1	3.03(44)
O10	0	0	0.03102(87)	1	0.68(87)

Table A-9 Structure obtained from XRD data for $Ca_9Al_{0.6}(PO_4)_{6.6}$.

R_p	11.090	R_{wp}	15.324	GOF	1.141
a	10.37149(19)		c	37.45374(84)	
site	x	y	z	occ	beq
Ca1	0.72172(86)	0.8545(12)	0.16668(62)	1	-0.28(23)
Ca2	0.6206(11)	0.8217(17)	-0.03390(55)	1	0.36(27)
Ca3	0.72396(76)	0.8523(11)	0.06061(55)	1	0.21(28)
Ca4	0	0	-0.0902(11)	0.45(18)	2.8(11)
Al4	0	0	-0.0902(11)	0.01(31)	2.8(11)
Ca5	0	0	0.73463(69)	0.95(16)	1.72(38)
Al5	0	0	0.73463(69)	0.01(26)	1.72(38)
P1	0	0	0	1	1.58(73)
P2	0.6854(12)	0.8587(17)	0.86935(62)	1	0.46(38)
P3	0.6541(16)	0.8480(17)	0.76641(61)	1	0.82(42)
O1	0.7257(29)	-0.0885(29)	-0.0913(10)	1	1.97(86)
O2	0.7615(39)	0.7797(36)	0.85431(82)	1	0.42(95)
O3	0.7309(36)	0.0090(36)	0.84495(97)	1	0.73(81)
O4	0.5194(26)	0.7639(40)	0.8609(11)	1	1.33(70)
O5	0.6012(31)	-0.0473(29)	0.7766(12)	1	-0.03(77)
O6	0.5785(30)	0.6902(47)	0.7804(10)	1	0.44(85)
O7	0.0827(44)	0.9076(40)	0.7711(10)	1	1.48(79)
O8	0.6225(23)	0.8205(31)	0.72694(93)	1	0.63(62)
O9	0.0160(32)	0.8611(21)	-0.0152(12)	1	3.55(70)
O10	0	0	0.0351(13)	1	1.6(18)

Table A-10 Structure obtained from XRD data for $Ca_9Al_{0.8}(PO_4)_{6.8}$.

R_p	5.851	R_{wp}	7.876	GOF	2.323
a	10.346550(81)		c	37.38878(36)	
site	x	y	z	occ	beq
Ca1	0.72146(49)	0.85613(57)	0.16718(27)	1	-0.11(10)
Ca2	0.62026(62)	0.82180(65)	-0.03343(25)	1	0.30(13)
Ca3	0.72528(40)	0.85172(56)	0.06108(25)	1	0.31(14)
Ca4	0	0	-0.09185(53)	0.42(11)	7.33(85)
Al4	0	0	-0.09185(53)	0.01(19)	7.33(85)
Ca5	0	0	0.73403(37)	0.91(7)	1.75(17)
Al5	0	0	0.73403(37)	0.00(12)	1.75(17)
P1	0	0	0	1	0.89(31)
P2	0.68521(55)	0.86000(94)	0.86864(29)	1	1.16(19)
P3	0.65739(85)	0.85014(88)	0.76487(26)	1	0.76(20)
O1	0.7326(16)	-0.0894(17)	-0.09163(45)	1	1.81(41)
O2	0.7526(21)	0.7616(18)	0.85545(37)	1	2.04(46)
O3	0.7218(18)	0.0037(13)	0.84642(39)	1	0.20(47)
O4	0.5093(15)	0.7535(21)	0.86963(57)	1	1.32(27)
O5	0.5944(18)	-0.0505(17)	0.77802(46)	1	0.43(40)
O6	0.5770(13)	0.6967(14)	0.78259(38)	1	-1.79(30)
O7	0.0799(20)	0.9021(18)	0.77670(40)	1	1.10(41)
O8	0.6307(11)	0.8238(16)	0.72746(38)	1	0.57(37)
O9	0.0135(14)	0.85954(93)	-0.01748(49)	1	2.83(32)
O10	0	0	0.03895(68)	1	0.84(83)

Table A-11 Structure obtained from XRD data for $Ca_9Al(PO_4)_7$.

R_p	5.726	R_{wp}	8.395	GOF	2.590
a	10.334520(95)		c	37.35701(42)	
site	x	y	z	occ	beq
Ca1	0.72205(58)	0.85573(66)	0.16681(30)	1	-0.02(12)
Ca2	0.62119(71)	0.82143(75)	-0.03363(27)	1	0.40(14)
Ca3	0.72493(44)	0.85079(67)	0.06087(29)	1	0.48(17)
Ca4	0	0	-0.09291(67)	0.39(13)	8.6(11)
Al4	0	0	-0.09291(67)	0.01(22)	8.6(11)
Ca5	0	0	0.73394(44)	0.89(8)	1.85(20)
Al5	0	0	0.73394(44)	0.00(13)	1.85(20)
P1	0	0	0	1	0.89(36)
P2	0.68512(62)	0.8598(11)	0.86880(32)	1	1.12(22)
P3	0.65924(99)	0.8500(11)	0.76512(30)	1	1.15(23)
O1	0.7321(17)	-0.0892(18)	-0.09214(51)	1	1.84(47)
O2	0.7507(23)	0.7607(20)	0.85502(41)	1	1.11(50)
O3	0.7250(20)	0.0020(16)	0.84562(46)	1	0.94(53)
O4	0.5094(16)	0.7529(22)	0.86941(68)	1	1.24(31)
O5	0.5966(18)	-0.0491(18)	0.77836(51)	1	0.06(44)
O6	0.5771(15)	0.6971(17)	0.78201(45)	1	-0.92(36)
O7	0.0782(25)	0.9021(22)	0.77486(53)	1	2.09(48)
O8	0.6308(13)	0.8245(19)	0.72747(45)	1	1.09(43)
O9	0.0115(15)	0.85934(98)	-0.01867(52)	1	2.10(34)
O10	0	0	0.03952(73)	1	-0.09(88)

Table A-12 Structure obtained from XRD data for $Ca_9La_{0.2}(PO_4)_{6.2}$.

R_p	7.600	R_{wp}	10.370	GOF	1.727
a	10.421360(90)		c	37.44514(46)	
site	x	y	z	occ	beq
Ca1	0.7270(33)	0.8591(38)	0.1667(22)	1	-0.23(87)
Ca2	0.6196(35)	0.8211(44)	-0.0332(21)	1	0.26(81)
Ca3	0.7265(25)	0.8556(37)	0.0616(22)	1.08(15)	1.18(84)
La3	0.7265(25)	0.8556(37)	0.0616(22)	0.02(5)	1.18(84)
Ca4	0	0	-0.0829(34)	0.450(90)	0.450(9)
Ca5	0	0	0.7325(22)	1	1.4(14)
P1	0	0	0	1	1.5(23)
P2	0.6851(34)	0.8619(58)	0.8688(24)	1	1.1(13)
P3	0.6570(64)	0.8480(69)	0.7661(23)	1	0.9(13)
O1	0.734(10)	-0.093(11)	-0.0960(31)	1	1.7(28)
O2	0.755(13)	0.763(12)	0.8614(31)	1	3.3(30)
O3	0.7084(93)	0.0101(80)	0.8497(29)	1	-1.1(30)
O4	0.5123(88)	0.751(14)	0.8699(41)	1	3.0(21)
O5	0.587(12)	-0.055(11)	0.7846(27)	1	1.3(32)
O6	0.5806(91)	0.6945(89)	0.7859(27)	1	-1.1(25)
O7	0.083(10)	0.8968(96)	0.7811(24)	1	-1.7(19)
O8	0.6356(68)	0.8358(81)	0.7287(32)	1	-1.7(20)
O9	0.0122(97)	0.8647(75)	-0.0194(28)	1	3.2(27)
O10	0	0	0.0368(42)	1	1.6(48)

Table A-13 Structure obtained from XRD data for $Ca_9La_{0.4}(PO_4)_{6.4}$.

R_p	7.811	R_{wp}	10.682	GOF	1.786
a	10.41694(10)		c	37.42375(50)	
site	x	y	z	occ	beq
Ca1	0.72813(75)	0.85966(98)	0.16718(61)	1	-0.15(20)
Ca2	0.62114(92)	0.8232(11)	-0.03336(56)	1	-0.14(19)
Ca3	0.72758(59)	0.85450(95)	0.06161(61)	1.02(15)	1.09(21)
La3	0.72758(59)	0.85450(95)	0.06161(61)	0.03(5)	1.09(21)
Ca4	0	0	-0.08309(70)	0.478(86)	-1.35(62)
Ca5	0	0	0.73274(59)	1	1.48(32)
P1	0	0	0	1	2.36(65)
P2	0.68749(82)	0.8648(14)	0.86904(62)	1	1.68(34)
P3	0.6557(15)	0.8455(15)	0.76570(61)	1	0.75(30)
O1	0.7370(25)	-0.0931(30)	-0.09219(97)	1	3.47(80)
O2	0.7586(33)	0.7667(33)	0.85996(85)	1	3.91(86)
O3	0.7127(33)	0.0074(24)	0.84937(92)	1	1.7(10)
O4	0.5129(21)	0.7548(35)	0.8676(11)	1	2.35(47)
O5	0.5931(30)	-0.0482(26)	0.78199(74)	1	-1.17(65)
O6	0.5754(23)	0.6964(20)	0.78646(71)	1	-0.90(60)
O7	0.0814(26)	0.8988(26)	0.77976(68)	1	-0.29(58)
O8	0.6350(15)	0.8363(20)	0.72922(83)	1	-2.49(48)
O9	0.0065(24)	0.8608(19)	-0.01660(79)	1	3.83(63)
O10	0	0	0.0348(12)	1	2.7(13)

Table A-14 Structure obtained from XRD data for $Ca_9La_{0.6}(PO_4)_{6.6}$.

R_p	7.529	R_{wp}	10.375	GOF	1.741
a	10.42765(13)		c	37.47960(65)	
site	x	y	z	occ	beq
Ca1	0.7284(10)	0.8644(10)	0.16983(80)	1	0.54(24)
Ca2	0.61882(97)	0.8206(12)	-0.03100(75)	1	-0.73(20)
Ca3	0.72364(79)	0.8566(12)	0.06346(83)	1.00(17)	2.01(27)
La3	0.72364(79)	0.8566(12)	0.06346(83)	0.07(6)	2.01(27)
Ca4	0	0	-0.0775(13)	0.393(10)	0.4(12)
Ca5	0	0	0.73199(77)	1	2.71(45)
P1	0	0	0	1	2.85(82)
P2	0.68454(96)	0.8591(17)	0.87165(79)	1	1.07(41)
P3	0.6607(22)	0.8505(22)	0.76817(79)	1	1.77(42)
O1	0.7464(27)	-0.0911(39)	-0.0943(11)	1	3.6(11)
O2	0.7324(39)	0.7461(42)	0.8632(12)	1	3.76(99)
O3	0.7067(38)	0.0040(29)	0.8486(12)	1	2.1(12)
O4	0.5106(31)	0.7541(54)	0.8752(13)	1	4.73(67)
O5	0.5861(37)	-0.0482(31)	0.7854(11)	1	2.2(10)
O6	0.5767(23)	0.6916(22)	0.78894(95)	1	-2.51(61)
O7	0.0843(25)	0.9022(28)	0.78219(77)	1	-1.82(58)
O8	0.6402(19)	0.8325(27)	0.7307(12)	1	-2.51(60)
O9	0.0034(24)	0.8594(20)	-0.02137(95)	1	2.64(86)
O10	0	0	0.0452(17)	1	5.2(21)

Table A-15 Structure obtained from XRD data for $Ca_9La_{0.8}(PO_4)_{6.8}$.

R_p	7.273	R_{wp}	9.754	GOF	1.645
a	10.44007(11)		c	37.49524(55)	
site	x	y	z	occ	beq
Ca1	0.72750(84)	0.8559(14)	0.16690(64)	1	0.67(23)
Ca2	0.61838(91)	0.8168(12)	-0.03303(59)	1	-0.20(20)
Ca3	0.72190(62)	0.8563(10)	0.06053(61)	1.02(13)	0.77(22)
La3	0.72190(62)	0.8563(10)	0.06053(61)	0.05(4)	0.77(22)
Ca4	0	0	-0.0888(12)	0.419(10)	4.9(13)
Ca5	0	0	0.72986(56)	1	1.21(32)
P1	0	0	0	1	2.17(65)
P2	0.68747(87)	0.8657(17)	0.86646(58)	1	1.81(36)
P3	0.6685(18)	0.8403(21)	0.76350(57)	1	1.34(31)
O1	0.7322(28)	-0.0907(30)	-0.09324(93)	1	3.68(82)
O2	0.7515(35)	0.7503(36)	0.8569(10)	1	4.3(10)
O3	0.7131(30)	0.0098(26)	0.8469(11)	1	0.35(95)
O4	0.5139(22)	0.7522(50)	0.8649(12)	1	3.07(58)
O5	0.5830(35)	-0.0596(34)	0.77949(95)	1	0.89(95)
O6	0.5796(25)	0.6941(20)	0.78387(76)	1	-2.24(60)
O7	0.0878(29)	0.8998(30)	0.77640(69)	1	-1.28(55)
O8	0.6405(18)	0.8367(25)	0.72778(91)	1	-1.04(62)
O9	0.0192(26)	0.8649(20)	-0.01873(93)	1	4.20(74)
O10	0	0	0.0372(11)	1	1.5(14)

Table A-16 Structure obtained from XRD data for $Ca_9La(PO_4)_7$.

R_p	6.990	R_{wp}	9.508	GOF	2.125
a	10.45639(13)		c	37.54755(64)	
site	x	y	z	occ	beq
Ca1	0.7249(12)	0.8499(18)	0.16816(98)	1	0.59(34)
Ca2	0.6170(11)	0.8105(17)	-0.03106(84)	1	-0.95(28)
Ca3	0.71554(97)	0.8578(14)	0.06142(86)	1.00(16)	0.31(30)
La3	0.71554(97)	0.8578(14)	0.06142(86)	0.05(5)	0.31(30)
Ca4	0	0	-0.0871(18)	0.381(11)	4.8(19)
Ca5	0	0	0.72930(73)	1	0.35(39)
P1	0	0	0	1	1.75(83)
P2	0.6872(12)	0.8660(24)	0.86593(89)	1	0.57(44)
P3	0.6768(25)	0.8449(26)	0.76322(77)	1	2.34(50)
O1	0.7372(30)	-0.0936(44)	-0.0957(12)	1	2.59(93)
O2	0.7585(40)	0.7474(40)	0.8588(13)	1	1.1(10)
O3	0.7163(39)	0.0131(36)	0.8463(15)	1	1.1(14)
O4	0.5191(32)	0.7584(64)	0.8621(16)	1	1.80(95)
O5	0.5899(44)	-0.0715(47)	0.7816(13)	1	1.1(15)
O6	0.5873(35)	0.6867(31)	0.7851(11)	1	-2.3(10)
O7	0.0965(61)	0.9002(60)	0.7763(10)	1	-0.51(87)
O8	0.6444(23)	0.8237(45)	0.7279(14)	1	1.04(97)
O9	0.0290(39)	0.8620(29)	-0.0209(12)	1	4.61(98)
O10	0	0	0.0347(17)	1	2.7(17)

Table A-17 Structure obtained from ND data for $Ca_3(PO_4)_2$.

R_{wp}	2.633	GOF	4.975							
a	10.40997(30)		c	37.3989(16)						
site	x	y	z	occ	U_{11}	U_{22}	U_{33}	U_{12}	U_{13}	U_{23}
Ca1	0.7229(20)	0.8448(22)	0.16681(66)	1	0.0000(98)	0.000(10)	0.0000(72)	0.0107(88)	-0.0009(74)	-0.0070(88)
Ca2	0.6163(25)	0.8137(30)	-0.03367(81)	1	0.017(11)	0.034(16)	0.014(12)	0.018(14)	0.0093(95)	0.018(10)
Ca3	0.7241(15)	0.8482(23)	0.05958(60)	1	0.0000(74)	0.031(15)	0.0000(84)	-0.015(11)	0.0109(85)	-0.016(10)
Ca4	0	0	-0.0858(39)	0.62(8)	0.049(42)	0.049(42)	0.56(30)	0.024(21)	0	0
Ca5	0	0	0.7333(11)	1	0.0024(71)	0.0024(71)	0.000(11)	0.0012(36)	0	0
P1	0	0	0	1	0.0000(83)	0.0000(83)	0.000(13)	0.0000(42)	0	0
P2	0.6910(17)	0.8615(20)	0.86728(74)	1	0.0000(75)	0.0000(74)	0.0000(80)	0.0006(74)	0.0129(53)	0.0070(59)
P3	0.6568(26)	0.8494(33)	0.7643(11)	1	0.0115(92)	0.052(21)	0.026(13)	0.001(11)	0.005(12)	0.016(14)
O1	0.7222(26)	-0.0885(23)	-0.09254(65)	1	0.079(17)	0.046(14)	0.0000(92)	0.056(13)	0.0022(90)	-0.0162(80)
O2	0.7467(16)	0.7650(17)	0.85394(78)	1	0.004(10)	0.042(13)	0.057(18)	0.035(10)	-0.0093(95)	-0.016(11)
O3	0.7334(17)	0.0062(16)	0.84519(70)	1	0.048(14)	0.0016(73)	0.000(10)	0.0206(84)	-0.0227(86)	-0.0112(74)
O4	0.5183(17)	0.7701(21)	0.86279(74)	1	0.0000(61)	0.018(11)	0.0092(71)	0.0173(75)	-0.0004(48)	-0.0070(62)
O5	0.5989(16)	-0.0480(18)	0.77835(69)	1	0.0029(85)	0.0000(76)	0.0039(68)	-0.0040(72)	0.0057(56)	0.0011(65)
O6	0.5625(21)	0.6944(23)	0.78229(89)	1	0.051(12)	0.069(14)	0.0000(80)	0.061(10)	0.0147(96)	0.022(11)
O7	0.0881(22)	0.9009(18)	0.77681(81)	1	0.0354(88)	0.005(10)	0.030(10)	0.0031(79)	-0.032(12)	-0.008(11)
O8	0.6175(23)	0.8068(22)	0.72537(64)	1	0.057(12)	0.060(17)	0.0000(77)	0.040(11)	0.0306(97)	0.037(13)
O9	0.0173(17)	0.8664(13)	-0.01349(88)	1	0.0000(73)	0.0000(72)	0.060(11)	-0.0018(60)	0.0101(63)	-0.0190(68)
O10	0	0	0.04148(96)	1	0.0054(90)	0.0054(90)	0.000(14)	0.0027(45)	0	0

Table A-18 Structure obtained from ND data for $Ca_9Ga_{0.8}(PO_4)_{6.8}$.

R_{wp}	2.500	GOF	4.069							
a	10.31934(27)		c	37.1979(14)						
site	x	y	z	occ	U_{11}	U_{22}	U_{33}	U_{12}	U_{13}	U_{23}
Ca1	0.7259(18)	0.8581(25)	0.16755(79)	1	0.0051(92)	0.035(13)	0.0021(99)	0.023(10)	-0.0136(83)	0.007(10)
Ca2	0.6221(17)	0.8237(25)	-0.03380(74)	1	0.0000(85)	0.000(12)	0.0097(83)	-0.0027(81)	0.0084(89)	0.0014(88)
Ca3	0.7211(20)	0.8476(18)	0.06031(53)	1	0.033(10)	0.005(12)	0.0040(82)	0.019(12)	-0.0070(80)	-0.0139(89)
Ca4	0	0	-0.0773(71)	0.99(40)	0.42(13)	0.42(13)	0.83(43)	0.209(64)	0	0
Ca5	0	0	0.73205(94)	$0.11 \pm 6 \times 10^5$	0.0023(48)	0.0023(48)	0.0043(93)	0.0012(24)	0	0
Ga5	0	0	0.73205(94)	$0.78 \pm 4 \times 10^5$	0.0023(48)	0.0023(48)	0.0043(93)	0.0012(24)	0	0
P1	0	0	0	1	0.0094(81)	0.0094(81)	0.000(18)	0.0047(41)	0	0
P2	0.6845(19)	0.8548(25)	0.87057(64)	1	0.0000(90)	0.0026(88)	0.013(12)	0.0067(76)	0.0079(68)	0.0040(80)
P3	0.6569(26)	0.8508(20)	0.76588(60)	1	0.037(14)	0.000(11)	0.000(11)	0.009(12)	0.0061(97)	0.0065(59)
O1	0.7304(16)	-0.0870(13)	-0.09172(47)	1	0.024(11)	0.011(10)	0.0000(71)	0.005(11)	-0.0047(71)	-0.0057(63)
O2	0.7482(23)	0.7685(21)	0.85438(72)	1	0.041(16)	0.0201(88)	0.016(11)	0.022(11)	0.011(10)	-0.0097(98)
O3	0.7190(15)	-0.0013(17)	0.84722(67)	1	0.011(10)	0.0000(84)	0.018(11)	-0.0138(91)	0.0087(84)	0.0300(85)
O4	0.5063(14)	0.7602(20)	0.86855(52)	1	0.0000(84)	0.0097(83)	0.0115(75)	0.0093(86)	-0.0027(75)	-0.0071(80)
O5	0.6044(20)	-0.0466(17)	0.77824(71)	1	0.0000(94)	0.0000(90)	0.0153(76)	-0.0082(74)	-0.0046(63)	0.0021(85)
O6	0.5885(28)	0.6985(19)	0.78561(75)	1	0.020(15)	0.0290(98)	0.0063(93)	0.0148(94)	-0.004(11)	-0.015(10)
O7	0.0743(16)	0.9049(16)	0.77048(50)	1	0.0000(89)	0.0084(88)	0.011(10)	0.0029(85)	0.0138(80)	0.0125(83)
O8	0.6205(18)	0.8087(21)	0.72602(53)	1	0.0103(70)	0.0000(89)	0.0000(80)	-0.0039(65)	-0.0052(65)	-0.0004(56)
O9	0.0123(16)	0.8653(15)	-0.01121(74)	1	0.0010(68)	0.0001(95)	0.046(12)	0.0060(85)	0.0085(62)	-0.0168(86)
O10	0	0	0.04301(68)	1	0.0214(99)	0.0214(99)	0.000(18)	0.0107(50)	0	0

Table A-19 Structure obtained from ND data for $Ca_9La(PO_4)_7$.

R_{wp}	2.394	GOF	3.838							
a	10.46450(95)		c	37.5952(37)						
site	x	y	z	occ	U_{11}	U_{22}	U_{33}	U_{12}	U_{13}	U_{23}
Ca1	0.7242(26)	0.8547(39)	0.1618(23)	1	0.000(14)	0.000(19)	0.000(14)	0.019(15)	-0.004(13)	0.010(13)
Ca2	0.6220(27)	0.8220(55)	-0.0378(25)	1	0.017(21)	0.021(29)	0.000(17)	-0.019(21)	0.002(13)	-0.020(21)
Ca3	0.7221(23)	0.8606(37)	0.0559(19)	$0.99 \pm 4 \times 10^4$	0.029(14)	0.024(21)	0.000(18)	0.022(18)	-0.007(19)	0.015(21)
La3	0.7221(23)	0.8606(37)	0.0559(19)	$0.05 \pm 2 \times 10^4$	0.029(14)	0.024(21)	0.000(18)	0.022(18)	-0.007(19)	0.015(21)
Ca4	0	0	-0.0999(35)	0.64(3)	0.000(20)	0.000(20)	0.055(71)	0.0000(98)	0	0
Ca5	0	0	0.7315(34)	1	0.000(17)	0.000(17)	0.000(33)	0.0000(85)	0	0
P1	0	0	0	1	0.050(27)	0.050(27)	0.074(50)	0.025(13)	0	0
P2	0.6777(25)	0.8572(44)	0.8612(20)	1	0.000(14)	0.000(17)	0.005(17)	-0.016(15)	0.021(20)	-0.013(13)
P3	0.6590(46)	0.8436(39)	0.7606(22)	1	0.014(17)	0.003(22)	0.054(22)	0.009(13)	0.002(20)	-0.011(19)
O1	0.7329(33)	-0.0947(41)	-0.0971(23)	1	0.034(28)	0.110(38)	0.000(17)	0.037(26)	-0.016(21)	-0.018(20)
O2	0.7726(45)	0.7956(37)	0.8482(23)	1	0.031(22)	0.070(31)	0.000(18)	0.024(21)	0.003(23)	0.013(17)
O3	0.7251(36)	0.0086(38)	0.8430(22)	1	0.000(11)	0.021(18)	0.015(18)	0.025(11)	0.004(16)	0.011(17)
O4	0.5078(39)	0.7601(46)	0.8565(27)	1	0.0032(97)	0.001(21)	0.019(14)	-0.009(17)	-0.008(14)	0.005(15)
O5	0.5888(32)	-0.0698(27)	0.7749(24)	1	0.000(15)	0.012(16)	0.000(14)	0.021(14)	0.007(13)	-0.001(11)
O6	0.5896(30)	0.6857(38)	0.7785(24)	1	0.000(15)	0.000(16)	0.018(17)	-0.000(14)	0.003(19)	0.022(19)
O7	0.0858(48)	0.9004(56)	0.7737(22)	1	0.056(30)	0.006(21)	0.072(31)	0.024(18)	-0.010(25)	-0.004(22)
O8	0.6387(29)	0.8197(37)	0.7211(20)	1	0.022(17)	0.002(15)	0.000(16)	0.003(19)	0.014(13)	0.001(15)
O9	-0.0070(49)	0.8535(33)	-0.0288(21)	1	0.026(16)	0.091(44)	0.107(40)	0.009(34)	0.048(22)	0.005(33)
O10	0	0	0.0384(16)	1	0.084(33)	0.084(33)	0.038(63)	0.042(16)	0	0

Table A-20 Structure obtained from ND data for $Ca_9Al_{0.2}(PO_4)_{6.2}$.

R_{wp}	3.843	GOF	3.350							
a	10.42770(44)		c	37.4420(23)						
site	x	y	z	occ	U_{11}	U_{22}	U_{33}	U_{12}	U_{13}	U_{23}
Ca1	0.7316(26)	0.8584(29)	0.1662(13)	1	0.023(16)	0.008(13)	0.010(15)	0.020(11)	-0.008(11)	0.010(13)
Ca2	0.6274(30)	0.8290(28)	-0.0324(13)	1	0.000(15)	0.032(14)	0.000(13)	0.012(14)	0.0387(86)	0.0017(93)
Ca3	0.7313(19)	0.8495(29)	0.0616(12)	1	0.032(16)	0.000(16)	0.000(15)	0.000(15)	-0.004(13)	0.015(13)
Ca4	0	0	-0.0821(25)	$0.49 \pm 9 \times 10^5$	0.000(17)	0.000(17)	0.000(24)	0.0001(86)	0	0
Al4	0	0	-0.0821(25)	$0.24 \pm 1 \times 10^6$	0.000(17)	0.000(17)	0.000(24)	0.0001(86)	0	0
Ca5	0	0	0.7359(20)	$1.06 \pm 5 \times 10^5$	0.019(14)	0.019(14)	0.041(18)	0.0094(72)	0	0
Al5	0	0	0.7359(20)	$0.05 \pm 7 \times 10^5$	0.019(14)	0.019(14)	0.041(18)	0.0094(72)	0	0
P1	0	0	0	1	0.146(48)	0.146(48)	0.000(40)	0.073(24)	0	0
P2	0.6887(21)	0.8595(23)	0.8703(13)	1	0.0000(95)	0.014(13)	0.052(21)	0.0273(96)	0.030(11)	0.004(12)
P3	0.6519(36)	0.8416(32)	0.7679(12)	1	0.037(20)	0.064(26)	0.000(18)	0.034(17)	-0.006(12)	-0.026(14)
O1	0.7311(29)	-0.1055(44)	-0.0897(16)	1	0.080(30)	0.229(34)	0.000(14)	0.118(29)	0.021(13)	-0.028(22)
O2	0.7726(31)	0.7797(34)	0.8578(14)	1	0.039(15)	0.089(19)	0.033(16)	0.058(14)	0.011(12)	-0.047(15)
O3	0.7249(26)	-0.0009(26)	0.8478(14)	1	0.0000(95)	0.027(15)	0.000(11)	0.008(11)	-0.005(11)	-0.011(10)
O4	0.5226(32)	0.7585(53)	0.8596(17)	1	0.000(14)	0.075(26)	0.069(27)	0.002(18)	0.017(14)	-0.012(24)
O5	0.6056(24)	-0.0353(26)	0.7802(14)	1	0.000(11)	0.015(10)	0.0127(94)	0.020(10)	0.0219(82)	0.008(12)
O6	0.5793(26)	0.6900(31)	0.7843(13)	1	0.000(15)	0.060(16)	0.037(15)	0.024(13)	-0.005(16)	-0.026(16)
O7	0.0780(25)	0.9030(24)	0.7754(14)	1	0.008(12)	0.0000(90)	0.022(17)	-0.0049(84)	-0.009(11)	0.023(12)
O8	0.6343(25)	0.8415(41)	0.7277(15)	1	0.030(13)	0.124(30)	0.000(11)	0.076(18)	-0.030(11)	-0.032(16)
O9	-0.0036(38)	0.8491(34)	-0.0218(15)	1	0.042(17)	0.100(28)	0.101(30)	0.066(23)	0.059(13)	0.061(18)
O10	0	0	0.0404(14)	1	0.007(12)	0.007(12)	0.171(58)	0.0034(61)	0	0

Table A-21 Structure obtained from ND data for $Ca_9Al_{0.4}(PO_4)_{6.4}$.

R_{wp}	2.336	GOF	4.099							
a	10.38114(69)		c	37.3950(29)						
site	x	y	z	occ	U_{11}	U_{22}	U_{33}	U_{12}	U_{13}	U_{23}
Ca1	0.7244(17)	0.8479(25)	0.16650(71)	1	0.0000(97)	0.008(14)	0.0000(87)	0.0098(79)	0.0234(96)	0.021(14)
Ca2	0.6212(18)	0.8188(26)	-0.03364(78)	1	0.009(14)	0.021(15)	0.034(14)	0.006(11)	-0.0237(88)	0.006(12)
Ca3	0.7240(20)	0.8544(21)	0.05914(67)	1	0.057(15)	0.010(13)	0.000(13)	0.009(13)	-0.0003(97)	-0.0346(97)
Ca4	0	0	-0.0845(22)	$0.44 \pm 9 \times 10^5$	0.012(39)	0.012(39)	0.104(88)	0.006(20)	0	0
Al4	0	0	-0.0845(22)	$0.10 \pm 1 \times 10^6$	0.012(39)	0.012(39)	0.104(88)	0.006(20)	0	0
Ca5	0	0	0.7349(11)	$0.81 \pm 6 \times 10^5$	0.031(15)	0.031(15)	0.015(15)	0.0154(74)	0	0
Al5	0	0	0.7349(11)	$0.23 \pm 8 \times 10^5$	0.031(15)	0.031(15)	0.015(15)	0.0154(74)	0	0
P1	0	0	0	1	0.0135(81)	0.0135(81)	0.004(18)	0.0067(41)	0	0
P2	0.6923(18)	0.8590(20)	0.86864(67)	1	0.0000(91)	0.003(10)	0.029(12)	0.0101(87)	-0.0003(80)	-0.0058(98)
P3	0.6524(19)	0.8493(23)	0.76654(73)	1	0.0000(96)	0.0098(95)	0.010(13)	-0.0037(61)	-0.0103(68)	-0.0195(75)
O1	0.7288(15)	-0.0845(21)	-0.09217(78)	1	0.061(15)	0.038(16)	0.000(10)	0.019(13)	0.0030(92)	-0.032(11)
O2	0.7553(19)	0.7741(20)	0.85317(85)	1	0.015(12)	0.056(17)	0.061(19)	0.025(14)	-0.040(11)	-0.012(14)
O3	0.7194(20)	0.0049(17)	0.84663(79)	1	0.075(17)	0.032(13)	0.001(10)	0.049(13)	-0.042(12)	-0.0366(88)
O4	0.5160(20)	0.7673(21)	0.86175(71)	1	0.041(11)	0.020(14)	0.0068(83)	0.030(12)	0.0246(85)	0.0071(90)
O5	0.5979(16)	-0.0488(18)	0.77908(79)	1	0.000(10)	0.0118(85)	0.0020(69)	0.0115(89)	0.0148(57)	-0.0033(61)
O6	0.5714(21)	0.6906(17)	0.78258(89)	1	0.049(13)	0.013(12)	0.024(17)	0.020(12)	0.034(11)	0.044(12)
O7	0.0813(19)	0.8992(18)	0.77591(71)	1	0.022(10)	0.0000(95)	0.069(14)	0.020(10)	-0.009(13)	-0.037(10)
O8	0.6278(19)	0.8206(20)	0.72604(83)	1	0.047(11)	0.020(12)	0.0000(63)	0.038(11)	-0.0233(79)	-0.0156(97)
O9	0.0106(28)	0.8643(22)	-0.0102(11)	1	0.0208(94)	0.000(11)	0.041(15)	0.0002(87)	0.0001(96)	0.0032(78)
O10	0	0	0.03861(76)	1	0.064(16)	0.064(16)	0.000(13)	0.0321(79)	0	0

Table A-22 Structure obtained from ND data for $Ca_9Al_{0.6}(PO_4)_{6.6}$.

R_{wp}	2.056	GOF	3.479							
a	10.38508(63)		c	37.5139(25)						
site	x	y	z	occ	U_{11}	U_{22}	U_{33}	U_{12}	U_{13}	U_{23}
Ca1	0.7191(14)	0.8486(22)	0.16492(82)	1	0.000(11)	0.031(15)	0.0092(95)	0.0238(95)	0.0034(88)	0.013(13)
Ca2	0.6196(14)	0.8161(28)	-0.03484(77)	1	0.0000(95)	0.009(15)	0.007(14)	-0.010(11)	-0.0067(91)	-0.0120(91)
Ca3	0.7226(15)	0.8521(20)	0.05807(70)	1	0.037(12)	0.003(10)	0.000(10)	-0.0026(91)	-0.0046(82)	-0.0322(91)
Ca4	0	0	-0.0914(30)	$0.42 \pm 1 \times 10^6$	0.040(33)	0.040(33)	0.280(91)	0.020(17)	0	0
Al4	0	0	-0.0914(30)	$0.16 \pm 2 \times 10^6$	0.040(33)	0.040(33)	0.280(91)	0.020(17)	0	0
Ca5	0	0	0.7359(11)	$0.95 \pm 1 \times 10^6$	0.0034(89)	0.0034(89)	0.016(13)	0.0017(44)	0	0
Al5	0	0	0.7359(11)	$0.02 \pm 1 \times 10^6$	0.0034(89)	0.0034(89)	0.016(13)	0.0017(44)	0	0
P1	0	0	0	1	0.0000(58)	0.0000(58)	0.027(19)	0.0000(29)	0	0
P2	0.6915(16)	0.8642(15)	0.86832(74)	1	0.0043(87)	0.000(10)	0.011(12)	0.0005(91)	0.0054(59)	0.0076(91)
P3	0.6575(20)	0.8508(19)	0.76542(74)	1	0.0000(74)	0.0000(77)	0.0026(96)	-0.0067(61)	-0.0104(80)	-0.0052(75)
O1	0.7298(15)	-0.0837(17)	-0.09237(64)	1	0.0082(86)	0.039(14)	0.0000(85)	-0.0042(96)	0.0126(62)	-0.011(11)
O2	0.7484(28)	0.7694(16)	0.85336(83)	1	0.032(13)	0.041(16)	0.007(10)	0.023(13)	-0.0041(79)	0.0001(99)
O3	0.7225(15)	0.0008(18)	0.84460(79)	1	0.017(10)	0.0001(73)	0.0000(64)	0.0082(75)	-0.0151(64)	-0.0297(52)
O4	0.5144(17)	0.7642(20)	0.86211(61)	1	0.0228(85)	0.0030(92)	0.0213(92)	-0.0039(93)	-0.0030(79)	-0.0100(62)
O5	0.6008(14)	-0.0453(17)	0.77796(76)	1	0.0012(72)	0.0238(87)	0.0135(79)	0.0151(69)	-0.0174(68)	-0.0287(75)
O6	0.5724(22)	0.6915(18)	0.78204(87)	1	0.026(10)	0.0121(79)	0.0027(94)	0.0092(84)	0.0086(98)	0.0125(79)
O7	0.0817(16)	0.9022(21)	0.77427(67)	1	0.0104(83)	0.0060(83)	0.068(11)	0.0140(79)	-0.0290(92)	-0.0424(71)
O8	0.6254(15)	0.8202(21)	0.72530(69)	1	0.053(11)	0.016(10)	0.0000(81)	0.032(10)	-0.0077(57)	-0.0113(79)
O9	0.0120(21)	0.8643(15)	-0.0104(11)	1	0.025(11)	0.0000(80)	0.034(13)	-0.0025(79)	0.0031(92)	-0.0129(84)
O10	0	0	0.03993	1	0.047(13)	0.047(13)	0.087(33)	0.0236(67)	0	0

Table A-23 Structure obtained from ND data for $Ca_9Al_{0.8}(PO_4)_{6.8}$.

R_{wp}	2.202	GOF	3.975							
a	10.34760(65)		c	37.4138(25)						
site	x	y	z	occ	U_{11}	U_{22}	U_{33}	U_{12}	U_{13}	U_{23}
Ca1	0.7267(16)	0.8546(17)	0.16697(65)	1	0.0000(81)	0.0000(68)	0.0000(77)	0.0107(71)	0.0003(76)	-0.0018(79)
Ca2	0.6262(15)	0.8163(26)	-0.03330(64)	1	0.032(14)	0.037(16)	0.0047(85)	0.000(13)	0.057(11)	0.0026(74)
Ca3	0.7220(18)	0.8453(18)	0.05953(62)	1	0.037(11)	0.0000(88)	0.006(13)	0.0062(96)	-0.025(12)	-0.0016(98)
Ca4	0	0	-0.0879(18)	$0.43 \pm 6 \times 10^5$	0.023(27)	0.023(27)	0.000(40)	0.012(14)	0	0
Al4	0	0	-0.0879(18)	$0.02 \pm 8 \times 10^5$	0.023(27)	0.023(27)	0.000(40)	0.012(14)	0	0
Ca5	0	0	0.7273(10)	$0.94 \pm 6 \times 10^5$	0.003(12)	0.003(12)	0.026(17)	0.0013(58)	0	0
Al5	0	0	0.7273(10)	$0.04 \pm 8 \times 10^5$	0.003(12)	0.003(12)	0.026(17)	0.0013(58)	0	0
P1	0	0	0	1	0.013(11)	0.013(11)	0.000(15)	0.0065(54)	0	0
P2	0.6842(16)	0.8589(17)	0.86833(69)	1	0.0047(82)	0.041(14)	0.024(10)	0.0287(86)	-0.0112(86)	-0.0380(87)
P3	0.6524(19)	0.8483(21)	0.76536(70)	1	0.011(12)	0.000(10)	0.0192(94)	-0.0014(88)	0.0141(87)	0.0018(93)
O1	0.7248(15)	-0.0873(14)	-0.09350(55)	1	0.0000(60)	0.0322(96)	0.0000(78)	-0.0506(67)	0.0297(67)	-0.0256(67)
O2	0.7451(22)	0.7618(19)	0.85396(59)	1	0.068(16)	0.040(15)	0.0083(95)	0.043(14)	0.0004(86)	-0.0313(93)
O3	0.7204(18)	0.0033(22)	0.84384(75)	1	0.010(10)	0.029(13)	0.041(16)	-0.0028(94)	0.0098(78)	0.0427(99)
O4	0.5049(16)	0.7599(16)	0.86777(81)	1	0.0000(74)	0.024(10)	0.0105(90)	0.0160(83)	-0.0182(50)	-0.0157(75)
O5	0.5972(16)	-0.0514(18)	0.77816(76)	1	0.0176(99)	0.0000(98)	0.0102(92)	0.0124(87)	-0.0157(72)	-0.0176(84)
O6	0.5750(17)	0.6914(17)	0.78205(72)	1	0.0000(70)	0.0057(76)	0.0114(76)	-0.0121(62)	-0.0073(85)	-0.0173(85)
O7	0.0841(17)	0.9036(20)	0.77526(68)	1	0.0000(93)	0.025(12)	0.042(12)	-0.0015(69)	-0.003(10)	0.015(11)
O8	0.6256(15)	0.8205(20)	0.72553(60)	1	0.040(10)	0.0115(89)	0.0000(91)	0.0121(70)	0.0022(65)	-0.0035(77)
O9	0.0132(17)	0.8655(15)	-0.0170(10)	1	0.0000(92)	0.030(12)	0.117(12)	0.008(10)	0.0195(86)	0.033(14)
O10	0	0	0.04118(75)	1	0.041(14)	0.041(14)	0.044(27)	0.0205(70)	0	0

Table A-24 Structure obtained from ND data for $Ca_9Al(PO_4)_7$.

R_{wp}	2.239	GOF	3.855							
a	10.35500(75)		c	37.4261(31)						
site	x	y	z	occ	U_{11}	U_{22}	U_{33}	U_{12}	U_{13}	U_{23}
Ca1	0.7261(15)	0.8539(17)	0.16633(71)	1	0.0000(97)	0.000(10)	0.0000(71)	0.001(10)	-0.0093(70)	0.010(10)
Ca2	0.6276(20)	0.8176(29)	-0.03359(77)	1	0.044(15)	0.019(13)	0.008(12)	0.005(14)	0.055(12)	0.015(11)
Ca3	0.7230(16)	0.8437(20)	0.05974(73)	1	0.0070(96)	0.000(11)	0.006(11)	-0.0109(80)	0.0010(87)	0.014(10)
Ca4	0	0	-0.0870(20)	$0.42 \pm 1 \times 10^6$	0.035(34)	0.035(34)	0.000(40)	0.018(17)	0	0
Al4	0	0	-0.0870(20)	$0.05 \pm 2 \times 10^6$	0.035(34)	0.035(34)	0.000(40)	0.018(17)	0	0
Ca5	0	0	0.7279(13)	$0.95 \pm 4 \times 10^5$	0.019(12)	0.019(12)	0.017(19)	0.0094(59)	0	0
Al5	0	0	0.7279(13)	$0.09 \pm 5 \times 10^5$	0.019(12)	0.019(12)	0.017(19)	0.0094(59)	0	0
P1	0	0	0	1	0.031(15)	0.031(15)	0.000(16)	0.0157(73)	0	0
P2	0.6867(14)	0.8652(23)	0.86758(94)	1	0.004(10)	0.070(22)	0.0063(98)	0.030(16)	-0.0359(60)	-0.038(11)
P3	0.6564(22)	0.8475(19)	0.76460(93)	1	0.025(12)	0.000(13)	0.053(12)	0.020(12)	0.0362(93)	0.006(11)
O1	0.7259(17)	-0.0915(14)	-0.09446(77)	1	0.0000(73)	0.0246(97)	0.0000(69)	-0.0339(77)	0.0081(69)	-0.0267(98)
O2	0.7495(22)	0.7596(19)	0.85380(80)	1	0.028(12)	0.019(11)	0.018(11)	0.0151(83)	0.0008(74)	-0.0199(96)
O3	0.7213(21)	-0.0008(24)	0.84238(90)	1	0.020(14)	0.047(15)	0.036(19)	0.0144(96)	0.004(10)	0.034(16)
O4	0.5088(17)	0.7628(18)	0.86688(90)	1	0.0000(98)	0.002(12)	0.011(10)	-0.0088(90)	-0.0383(58)	-0.0069(71)
O5	0.6001(16)	-0.0478(20)	0.7779(10)	1	0.0095(85)	0.0110(85)	0.0155(94)	0.0248(86)	-0.0159(84)	-0.0218(88)
O6	0.5812(25)	0.6949(22)	0.78159(91)	1	0.042(11)	0.0000(90)	0.0057(94)	0.0121(91)	-0.0172(95)	-0.0179(94)
O7	0.0854(18)	0.9067(24)	0.77381(85)	1	0.000(10)	0.080(18)	0.026(14)	0.0192(97)	-0.0062(88)	0.029(13)
O8	0.6252(23)	0.8255(27)	0.72495(94)	1	0.081(15)	0.036(13)	0.006(12)	0.048(11)	0.0130(94)	-0.012(11)
O9	0.0093(22)	0.8601(22)	-0.02200(89)	1	0.031(14)	0.074(20)	0.106(16)	0.040(16)	0.0323(84)	0.072(15)
O10	0	0	0.04158(82)	1	0.0000(86)	0.0000(86)	0.052(32)	0.0000(43)	0	0